Bandwidth Compressed Waveform and System Design for Wireless and Optical Communications: Theory and Practice

A thesis submitted for the degree of Doctor of Philosophy

(Ph.D.)

by

Tongyang Xu

Communications and Information Systems Research Group

Department of Electronic and Electrical Engineering

University College London

June 2017

Statement of Originality

I, Tongyang Xu confirm that the work presented in this thesis is my own. Where information has been derived from other sources, I confirm that this has been indicated in the thesis.

Signed:

Date:

To my beloved parents.

"*Time is money.*" — Benjamin Franklin (1706 – 1790)

Abstract

This thesis addresses theoretical and practical challenges of spectrally efficient frequency division multiplexing (SEFDM) systems in both wireless and optical domains. SEFDM improves spectral efficiency relative to the well-known orthogonal frequency division multiplexing (OFDM) by non-orthogonally multiplexing overlapped sub-carriers. However, the deliberate violation of orthogonality results in inter carrier interference (ICI) and associated detection complexity, thus posing many challenges to practical implementations. This thesis will present solutions for these issues.

The thesis commences with the fundamentals by presenting the existing challenges of SEFDM, which are subsequently solved by proposed transceivers. An iterative detection (ID) detector iteratively removes self-created ICI. Following that, a hybrid ID together with fixed sphere decoding (FSD) shows an optimised performance/complexity trade-off. A complexity reduced Block-SEFDM can subdivide the signal detection into several blocks. Finally, a coded Turbo-SEFDM is proved to be an efficient technique that is compatible with the existing mobile standards.

The thesis also reports the design and development of wireless and optical practical systems. In the optical domain, given the same spectral efficiency, a low-order modulation scheme is proved to have a better bit error rate (BER) performance when replacing a higher order one. In the wireless domain, an experimental testbed utilizing the LTE-Advanced carrier aggregation (CA) with SEFDM is operated in a realistic radio frequency (RF) environment. Experimental results show that 40% higher data rate can be achieved without extra spectrum occupation. Additionally, a new waveform, termed Nyquist-SEFDM, which compresses bandwidth and suppresses out-of-band power leakage is investigated. A 4th generation (4G) and 5th generation (5G) coexistence experiment is followed to verify its feasibility. Furthermore, a 60 GHz SEFDM testbed is designed and built in a point-to-point indoor fiber wireless experiment showing 67% data rate improvement compared to OFDM. Finally, to meet the requirements of future networks, two simplified SEFDM transceivers are designed together with application scenarios and experimental verifications.

Impact Statement

The research in this thesis has contributed to the design of spectrally efficient systems with impact on applications that range from wireless link evolution from the 4th generation to the 5th generation to optical systems and millimeter wave communications. Practical systems demonstrated in the thesis, covering new wireless air interface design, 60 GHz millimeter wave communications, massive IoT connections, enhanced DSL communications, optical access network design and long haul optical fiber transmission, demonstrate for the first time the potential of the SEFDM technique in improving data rates, power efficiency and transmission distance, therefore paving the way for new research and possible implementation in future commercial wireless and wired systems.

Over the past four years, this research has demonstrated major successes in theoretical and practical studies, covering several disciplines; wireless, optical, electronics hardware and experimental testbed prototyping. I have authored or co-authored 22 papers in cross-disciplinary areas at leading international journals and conferences, allowing SEFDM to become a serious contender for future networks. There has been several international conference invitations to speak about the practical systems reported in the thesis and in 2016 two chapters covering the work were invited contributions to books on 5G systems, namely: *Signal Processing for 5G: Algorithms and Implementations (Wiley, 2016)* and *Key Enabling Technologies for 5G Mobile Communications (Springer, 2016)*. The research reported in this thesis inspires new innovations in engineering design, mathematical modelling, software simulation, hardware implementation and experimental verification. The work has already had academic impact in optical, wireless and satellite system designs at universities worldwide; in China (Fudan, BUPT and Jinan); University of Luxembourg; McGill University in Canada; St. Petersburg Polytechnic University in Russia. In 2015 we started collaboration with Chalmers University of Technology in Sweden to implement SEFDM transmission over millimeter wave. In the UK, we have collaborations with universities of Surrey (signal detector design) and Southampton (optical modulator design). A follow up of this work at UCL is ongoing with two PhD students.

There has been significant industrial interest following the 2014 paper on the first optical system implementation (the most downloaded paper of *IEEE Photonics Technology Letters*) and the wireless experiment first reported in 2015. In 2015, Aeroflex UK donated equipment to support the design and implementation of the world first fully running SEFDM wireless testbed, which led to 40% data rate improvement. We are currently working with a major cable operator on an EPSRC proposal to implement the wireless SEFDM signal in legacy twisted copper DSL to improve the capacity of existing networks. We are also working with a major equipment manufacturer on implementing SEFDM on long haul optical fiber systems. Finally in 2017, National Instruments (NI) supported us to pre-commercialize a software defined 5G transceiver with the award given by EPSRC "*Discovery to Use Impact Acceleration*" and the work was further funded by a donation of FPGAs from Xilinx in the USA through Xilinx University Program (XUP).

Acknowledgements

First and foremost I would like to thank sincerely my supervisor Professor Izzat Darwazeh for his great support, guidance and encouragement throughout my research. I am very grateful to Izzat for being my friend since I started my MSc project with him in April 2012. I have benefitted so much from his experience and knowledge not only in my research work but also in life in general. Meanwhile, I would also like to thank him for obtaining funding, which is Faculty of Engineering Sciences Scholarship, for this PhD work.

I would like to thank Dr. Ryan Grammenos for this help and guidance on hardware designs; Professor Farokh Marvasti for his help in the development of a new signal detector; Dr. Yu Chen for sharing his PhD experience during the course of my study; Dr. Paul Haigh for explaining and discussing new ideas with me that led to a joint publication; Dr. Bo Tan for sharing his rich experimental knowledge; Dr. Tianhua Xu for sharing his optical communication knowledge; Professor Chao Lu for inspiring discussions on optical systems and for connecting us with Professor Zhaohui Li and his students who collaborated with UCL in setting up optical experiments and hosting me in Jinan University in China; and Dr. Spiros Mikroulis, Mr Dhecha Nopchinda, Dr. Benn C. Thomsen and Professor John Mitchell for collaboration in the optical communication experiments, which led to several conference and journal publications. Finally, I would like to thank Mr Paul Mckenna and Ms Rhiannon Lloyd for their help and support that made my life at UCL easy and enjoyable.

I am grateful to my friends for supporting my decision to do a PhD and for creating very happy memories during my stay in London. Great thanks to my UCL colleagues and friends in Robert's 804 and MPEB 708; we together experienced many ups and downs. Much gratitude also to all my other London and UK friends for teaching me how to survive in what was a new environment.

Last but not least, my deepest thanks go to my family who supported me with patience and understanding throughout and especially during the research period spent at UCL. I am grateful to my parents for encouraging me to chase my dream at UCL.

Contents

List of Figures

List of Tables

Chapter 1

Introduction

The exponential growth in demand for broadband services is leading to increased research in new modulation formats and system architectures aiming to utilize the available, yet limited, spectrum. Long term evolution (LTE) [1] was proposed and standardized and has now been commercialized, with long term evolution-advanced (LTE-Advanced) [2] being introduced and its high data rate features demonstrated. The recent success of 4^{th} generation (4G) deployment and operation has led to growing interest in the system to follow, namely 5^{th} generation (5G). Even at these early stages work has started to appear aiming to define or possibly start the debate about defining 5G possible structure and services [3][4][5][6][7]. The main expectations of 5G are to achieve high-speed data communication and high spectral efficiency. There are a variety of methods being used to improve spectral efficiency like higher-order modulation, multiple antennas, interference cancellation and multicarrier techniques.

The physical layer of many of today's communication systems utilizes multicarrier transmission techniques as such techniques offer good spectrum utilization in frequency selective and multipath channels. Most prominent of the multicarrier systems is the orthogonal frequency division multiplexing (OFDM) where the information signal is carried on parallel orthogonal carriers (termed sub-carriers) with frequency separation equal to the symbol rate. OFDM, has its origins in the Kineplex system, originally

proposed for computer communications in late 1950s [8]. The modern variant of OFDM first appeared in the 1966 [9] and was implemented using digital techniques in the 1971 [10]. OFDM is currently the system of choice for many wire and wireless transmission systems [11].

In 4G standard, OFDM is the multicarrier technique that has been identified as the air interface of the physical layer in long term evolution (LTE) release 8 [1] since it provides better immunity against multipath fading than a single carrier system. A data stream is split into several parallel data streams with reduced data rate. Each data stream is modulated on separate overlapping but orthogonal sub-carriers. Using rectangular pulses in time domain, a slightly higher spectral efficiency can be achieved in OFDM compared to a single carrier. In order to maintain the orthogonality characteristic, the spectral efficiency of OFDM can not be improved further without changing the modulation formats. To overcome the challenge, some emerging techniques such as massive multiple input multiple output (MIMO) (space domain) [12], millimeter wave (frequency domain) [13] and beamforming (power domain) [14] are combined with OFDM to address this challenge and achieve higher data rates. However, in real world communications, OFDM is sensitive to radio frequency (RF) distortions like frequency offset which may compromise orthogonality between sub-carriers. This leads to inter carrier interference (ICI) and degrades the performance significantly. Since spectrum is a limited resource, techniques that can further improve spectral efficiency, while guarantee system performance would be in high demand. In order to use efficiently the limited spectrum, LTE-Advanced release 10 [15] was proposed and up to 100 MHz channel bandwidth is allocated to meet high data rate requirements using carrier aggregation (CA) techniques. Furthermore, many new features have been standardized such as enhanced MIMO and coordinated multiple point (CoMP).

In future 5G networks, a thousand-fold wireless traffic increase is predicted from 2020, originating from over 50 billion connected devices [16]. Such massive device connection and communication will be associated with the continuously emerging in-

ternet of things (IoT). In order to support faster data speed and provide sufficient multiple access, new waveform designs are needed. Some novel waveforms such as filterbank based multicarrier (FBMC) [17], universal-filtered multi-carrier (UFMC) [18] and generalized frequency division multiplexing (GFDM) [19] have been investigated as such techniques offer low out-of-band power leakage and avoid harmful interference to adjacent channels by using a pulse shaping filter on each sub-carrier or a group of sub-carriers. Therefore, protection guard band between two channels can be narrowed leading to an improved spectral efficiency. In 5G standard explorations [3][4][5][6][7], non-orthogonal concepts are commonly mentioned as potential candidates for the air interface. In 1975, Mazo showed that it is possible to increase the signalling rate up to 25% beyond the Nyquist rate [20]. A number of spectrally efficient multicarrier techniques have come to light with notable examples including fast orthogonal frequency division multiplexing (FOFDM) [21], m-ary amplitude shift keying (MASK) [22], Overlapped FDM (Ov-FDM) [23], spectrally efficient frequency division multiplexing (SEFDM) [24], faster than Nyquist (FTN) signalling [25] and time frequency packing (TFP) [26]. In addition, the non-orthogonal concept can be applied for multiple access scenarios such as sparse code multiple access (SCMA) [27], non-orthogonal multiple access (NOMA) [28] and multi-user shared access (MUSA) [29]. These techniques can superimpose signals from multiple users in the code-domain or the power-domain to enhance the system access performance.

A new direction for waveform design for future 5G networks is to compress signal bandwidth whilst maintaining the same transmission rate per sub-carrier. Conceptually, this is a non-orthogonal waveform technique termed SEFDM, which provides improved spectral efficiency by packing sub-carriers at frequency spacing below the symbol rate. The requirement of orthogonality is released and SEFDM is more immune to frequency offset than OFDM. This thesis focuses on SEFDM which can be traced back to 2003 [24] when the technique was firstly proposed. Since 2003 a number of researchers have worked on different aspects of SEFDM signals ranging from signal

generation and reception through their practical implementations using state-of-the-art hardware devices. Table 1.1 and Table 1.2 give an account of the key milestones achieved during the study of SEFDM signals from 2002 to 2017.

Table 1.1: History of SEFDM (2002-2012)

2002[21]	Fast OFDM: A proposal for doubling the data rate of OFDM
2003[24]	Proposal of the non-orthogonal waveform (SEFDM) concept
Sept. 2008[30]	A maximum likelihood (ML) SEFDM signal detector
Jun. 2009[31]	Complexity analysis of SEFDM receivers
Sept. 2009[32]	Investigation of semidefinite programming (SDP) signal detector
Sept. 2009[33]	An application of SEFDM in physical layer security
Sept. 2009[34]	A pruned sphere decoding (SD) signal detector
Jul. 2010[35]	An inverse fast Fourier transform (IFFT) SEFDM signal generator
Sept. 2010[36]	A joint channel equalization and detection scheme
Sept. 2010[37]	Precoded SEFDM
Nov. 2010[38]	The use of a fast constrained SD for signal detection
Mar. 2011[39]	Proposal of a truncated singular value decomposition (TSVD) detector
May. 2011[40]	Peak to average power ratio (PAPR) reduction in SEFDM
May. 2011[41]	Evaluation of fixed sphere decoding (FSD) detector in SEFDM
May. 2011[42]	A real-time FPGA based SEFDM signal generator
Sept. 2011[43]	FPGA implementation of the TSVD detector
Mar. 2012[44]	Soft cancellation MMSE Turbo equalization for n-OFDM
Apr. 2012[45]	A robust partial channel estimation (PCE) scheme for SEFDM
May. 2012[46]	A reconfigurable hardware based SEFDM transmitter
Jun. 2012[47]	A hardware verification methodology for SEFDM signal detection
Sept. 2012[48]	A hybrid DSP-FPGA implementation of the TSVD-FSD detector

Fig. 1.1 illustrates real-time spectra of SEFDM and OFDM, as measured using a Tektronix Mixed Domain Oscilloscope. The white (wider) spectrum is that of OFDM while the yellow (narrow) one is for SEFDM. It is apparent that the bandwidth of SEFDM is compressed by 40% compared with OFDM. The spectrum saving in SEFDM is achieved by deliberately overlapping sub-carriers at spacings below the symbol rate, effectively resulting in compressed sub-carrier spacing and leading to improved spectral efficiency. There are several reported methods to generate non-orthogonal SEFDM signals. A single IFFT structure was reported in [46] by adding zeros at the end of an SEFDM symbol, which is limited by bandwidth compression. After that, an efficient signal generator that employs multiple standard IFFTs was reported in [35] where the restrictions of the bandwidth compression are relaxed. Following the theoretical work,

Table 1.2: History of SEFDM (2013-2017, $'*'$ indicates the contributions in this thesis)

May.**2013**[49]*	Real-time FPGA implementation of TSVD-FSD detector
Jun. 2013[50]	A pure DSP implementation of the modified TSVD-FSD detector
Sep. 2013[51]	Frequency packing for spectral coexistence in satellite scenario
Oct.**2013**[52]*	An improved FSD detector using iterative soft decision method
2013[53]	Gabor transform to reduce the receiver side complexity
Feb.**2014**[54]*	Direct detection optical testbed demonstration
Jun.**2014**[55]*	Direct detection optical transmission experiment
Jul.**2014**[56]*	Soft demapping for different modulation schemes
Jul.**2014**[57]*	Block signal detection investigation
Oct.**2014**[58]*	A soft detector using Turbo principle
Nov.**2014**[59]*	Overview of SEFDM in 5G
2014[60]	BER performance improvement using smoothed envelope signals
May 2015[61]	Asymptotically optimal algorithm was studied
Jun.**2015**[62]*	Beyond 4G SEFDM radio over fiber transmission
Jun.**2015**[63]*	5G signal transmission experiment
Aug. 2015[64]	Nonlinear distortions caused by power amplifiers were studied
Aug. 2015[65]	Optimum envelope forms were studied
Oct. 2015[66]	The achievable capacity of SEFDM was studied
Oct. 2015[67]	Optimization of envelope forms for the duration of the signals
2015[68]	Mitigation of aliasing and ICI using ASK-manipulated signals
2016[69]*	A book chapter summarizes SEFDM technique
2016[70]*	A book chapter summarizes SEFDM technique
2016[71]*	Millimeter wave 60 GHz signal transmission experiment
Jan.**2016**[72]*	Coherent detection optical testbed demonstration
Jun.**2016**[73]*	Overview of SEFDM experiments
Jun. 2016[74]	Reduced complexity PAPR reduction algorithm for SEFDM
Jun. 2016[75]	Optical experiment using cascaded BPSK iterative detection (CBID)
Jul.**2016**[76]*	Waveform shaping for Internet of things (IoT)
Jul.**2016**[77]*	Millimeter wave 60 GHz signal transmission
Jul. 2016[78]	2.4-Gb/s WDM visible light communication (VLC) experiment
Jul. 2016[79]	Truncating OFDM signals to achieve high spectral efficiency
Jul. 2016[80]	Comparison of Turbo decoder and Turbo equalizer for SEFDM
Sep. 2016[81]	VLC experiment using RLS time-domain channel estimation
Oct. 2016[82]	Comparison study of sinc pulse and RRC pulse
Oct. 2016[83]	fractional Hartley transform for SEFDM
Dec. 2016[84]	Index modulation was applied to SEFDM
Dec. 2016[85]	Improve spectral and energy efficiency employing optimal envelope
Mar.**2017**[86]*	Precoding for digital subscriber line (DSL) communications
May2017[87]*	Transmission experiment for carrier aggregation in a wireless channel
May 2017[88]	Multiple channel coding schemes are studied
Jun. 2017[89]	Experimentally verify the capacity limit of SEFDM
Jun. 2017[90]	A new system architecture for FTN-SEFDM
Jun. 2017[91]	Multi-antenna SEFDM
Aug.**2017**[92]*	Reach enhancement in optical fiber transmission
Oct.**2017**[93]*	FPGA modelling verification on a non-orthogonal iterative detector
Oct.**2017**[94]*	Over-the-Air testing using software defined radio USRP RIO devices
Nov.**2017**[95]*	Multi-Sphere decoding of block segmented SEFDM signals

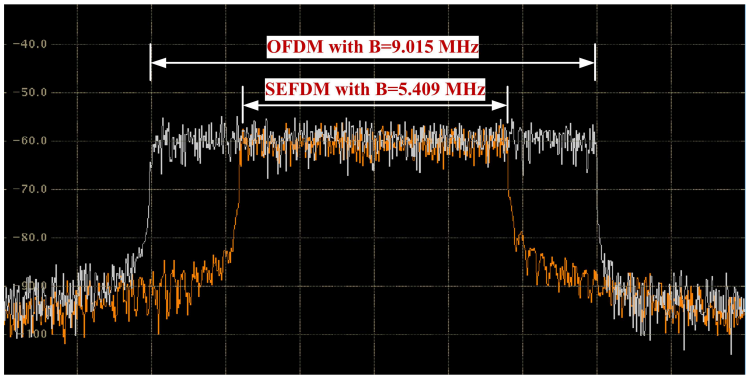

Figure 1.1: Experimental bandwidth comparisons of SEFDM ($\alpha = 0.6$) and OFDM. By transmitting the same amount of data, SEFDM requires bandwidth of 5.409 MHz while OFDM needs 9.015 MHz. Carrier frequency is 2 GHz, frequency span is 15 MHz and resolution bandwidth (RBW) is 3 KHz.

practical implementations were realized on both field programmable gate array (FPGA) [42] and designed for very large scale integration (VLSI) [46] circuit. The latter one was carried out in a 32-nm complementary metal-oxide-semiconductor (CMOS) chip. At 100 MHz clock frequency, the throughput can reach 17.4 Mbps with quadrature phase-shift keying (QPSK) modulation and up to 52.2 Mbps with 64QAM modulation with bandwidth saving up to 50% relative to OFDM. Hence, the challenge of signal generation has been resolved.

Signal detection is challenging due to the self-created ICI in SEFDM. Initially, linear detectors were evaluated such as zero forcing (ZF) [24] and minimum mean squared error (MMSE) [39]. However, these perform well only for small system sizes (i.e. small number of sub-carriers) and at high SNRs. Maximum likelihood (ML) is an optimal detection technique to recover signals subject to ICI, but it has a major drawback in the exponential growth of its complexity with the enlargement of the number of sub-carriers and modulation level. Sphere decoding (SD), an alternative to ML, was demonstrated in [38] to have an optimal performance at a much reduced complexity by searching candidate solutions within a constrained space. A key limitation is in its random complexity, which depends on noise levels and leads to impractical hard-

ware implementation. Subsequently, a hybrid detector combining TSVD with FSD was explored in [39], which offered a substantial reduction in complexity. However, the achievable error performance is still worse than the optimum ML performance. Following the theoretical work, a linear TSVD detector was verified in [43] by using FPGA. Furthermore, a hardware SEFDM detector was realized using the combination of FPGA and digital signal processors (DSP) [48].

1.1 Motivation

4G networks have been commercially set up in the UK since 2012 and they pave the way to the deployment of future 5G networks. 5G is coming with some new features. These include higher user data rate; lower energy consumption; more connected devices and lower latency. However, a standalone technique may not be able to support future 5G networks. It is expected that future 5G wireless networks will be a mixture of different backhaul and radio access technologies. In terms of future systems (5G and beyond), SEFDM would offer significant bandwidth saving advantages if used either as an air interface technique or for backhauling signals over wireless and/or wired and fiber communication channels. According to the aforementioned introduction, the existing detection techniques are all limited to small size SEFDM systems because the ICI becomes severely limiting with increased number of sub-carriers. Therefore, this thesis will investigate efficient transceiver architectures for large size non-orthogonal SEFDM systems. Meanwhile, real world experiments will be operated to verify the proposed system designs. This research work will pave the way for future wireless and wired high spectrally efficient technologies.

1.2 Organization of the Thesis

This thesis includes two parts, the first part focuses on theoretical investigations of SEFDM including detector designs and advanced SEFDM system architecture propos-

als. The second part studies practical implementations of SEFDM focusing on optical, wireless or their combination at either microwave or millimeter wave frequencies.

Chapter 2 introduces the SEFDM signal. It starts with a mathematical description followed by a summary of existing modulation/demodulation techniques. Following this, the self-created interference characteristics are analyzed to show challenges of SEFDM signal recovery. Finally, the chapter includes a summary of other spectrally efficient techniques.

In Chapter 3 efforts to simplify the signal detection are presented. Three system architectures are proposed. The first is an iterative receiver based on the FSD detector. A new linear detection algorithm termed soft demapping iterative detection (ID) is introduced. Following that, a hybrid ID together with FSD is presented to improve further the performance. The second proposal is a multi-band architecture, named block-spectrally efficient frequency division multiplexing (Block-SEFDM), for a moderate size non-orthogonal system. The new architecture decomposes the whole spectrum into several blocks. Each block can be detected separately by using an efficient detector such as SD. This technique makes it practical to detect a SEFDM signal (e.g. modulated on 128 non-orthogonal data sub-carriers). Furthermore, a detector termed block efficient detector (BED) is presented in this work and computer simulations show that the performance is significantly improved while the complexity is decreased by one order of magnitude. The third proposal investigates a new iterative detection algorithm which can simplify the detection of signals in large size non-orthogonal multicarrier systems. This work proposes a fast Fourier transform (FFT) based soft detector working alongside a standard Bahl-Cocke-Jelinek-Raviv (BCJR) outer decoder. The detector can iteratively improve the reliability of candidate solutions using forward error correction (FEC) based on the Turbo principle by exchanging soft information between the FFT detector and the outer decoder. Mathematical modelling results show the suitability of the proposed detector for use in large size (e.g. 1024 data sub-carriers) non-orthogonal multicarrier systems.

Chapter 4 presents new applications of SEFDM in optical domain. This is the first time to prove experimentally that SEFDM is applicable to optical communication systems. Two optical systems such as directed detection optical-SEFDM (DDO-SEFDM) and coherent optical-SEFDM (CO-SEFDM) are designed and evaluated. The 10 Gb/s DDO-SEFDM optical experiment can improve spectral efficiency in both electrical and optical domains while achieving the same performance when bandwidth saving is up to 20% or signalling rate is up to 25%. This is the first experimental verification of the Mazo's 25% optical faster than the Nyquist principle in the optical domain. Furthermore, results indicate that 4QAM DDO-SEFDM can replace 8QAM DDO-OFDM while achieving better performance. It is experimentally shown that a lower-order modulation format can achieve better performance by replacing a higher one. The same results were obtained in a 24 Gb/s CO-SEFDM testbed where spectral efficiency was further improved with extra signal processing efforts.

Chapter 5 reports the first experimental demonstration of LTE-Advanced SEFDM signal transmission and reception over a realistic RF environment. Carrier aggregation (CA) is a technique introduced in LTE-Advanced to achieve a higher throughput by aggregating legacy radio resources. Meanwhile, SEFDM is a bandwidth compressed technique that can pack more non-orthogonal sub-carriers in a given bandwidth. Considering the scarcity of radio spectrum, the SEFDM bandwidth compression technique can be used to enhance CA performance. The combination of two techniques results in more aggregated component carriers (CCs) in a given bandwidth. It shows that up to 7 CCs can be aggregated in a given bandwidth with guaranteed bit error rate (BER), while OFDM can only pack 5 CCs in the same bandwidth. This chapter firstly studies practical impairments in a realistic wireless communication environment. Multipath fading effect is firstly investigated followed by its compensation solutions. Then, an experimental testbed is introduced in detail. Several impairments such as imperfect timing synchronization, phase noise and sampling clock phase offset are analyzed. Furthermore, these impairments are jointly reviewed and experimentally tested. Finally,

full system description and experimental setup are given together with BER results for SEFDM and OFDM based systems using LTE-like frame and signal formats and transmitted over an LTE standard fading channel. Experimental results firstly show the suitability of the proposed detector for use in large size non-orthogonal multicarrier systems. In addition, results demonstrate the bandwidth advantages of SEFDM and confirm that the effective spectral efficiency of CA-SEFDM is much higher than that of CA-OFDM.

Chapter 6 presented a simplified interference cancellation scheme for a non-orthogonal multicarrier signal using a pulse shaping technique. In non-orthogonal multicarrier signals, higher spectral efficiency may be achieved at the expense of self-created ICI. Typically, when no pulse shaping is employed, interference, contributed by all sub-carriers, has to be minimized resulting in a receiver of significant complexity. In order to mitigate the interference effect, the work in this chapter constrains the interference to adjacent sub-carriers by shaping each sub-carrier with a root raised cosine (RRC) filter, thereby suppressing the out-of-sub-carrier power leakage. Instead of cancelling out interference from all sub-carriers, only two adjacent sub-carriers are considered in the RRC shaped scenario. Results indicate that the newly proposed scheme can achieve the same performance compared to the non-shaped one but with reduced receiver complexity. This paves the way to non-orthogonal signal detection and non-orthogonal CA system designs; both of importance to future wireless and wired communication systems. A coexistence experiment for 4G and 5G signals aggregation is operated in a realistic PCI extensions for instrumentation (PXI) environment to show the benefits such as compressed bandwidth and reduced out-of-band power leakage. Practical over-the-air testing of those proposals, targeting massive machine-type communication (mMTC), is operated on commercially developed software defined radio universal software radio peripheral (USRP) platforms. Coexistence evaluations on two USRPs show that SEFDM can significantly reduce interference when used with existing LTE signals leading to improved quality of service. Additionally, the presented pulse shaping

Nyquist-SEFDM performs well in scenarios where the spectrum is limited and in fact it outperforms pulse shaped OFDM significantly, both in terms of bandwidth saving and throughput.

Chapter 7 experimentally studies SEFDM performance in a 60 GHz millimeter-wave (mm-wave) radio-over-fiber (RoF) scenario where transmission data rate is increased without changing signal bandwidth and modulation format. Experimentally, a 2.25 Gbit/s 4QAM OFDM signal is transmitted through 250 meters of multi-mode fiber (MMF) and then it is optically up converted to 60 GHz band at the photodiode before delivery to a millimeter wave antenna for transmission over a 3 meter wireless link. The work demonstrates that when the OFDM signal is replaced by an SEFDM signal using the same modulation format and occupying the same bandwidth, the bit rate can be increased. In addition, an 8QAM OFDM signal is experimentally evaluated due to its equivalent spectral efficiency with 4QAM SEFDM of 33% bandwidth compression. The purpose is to verify that a low order modulation format may replace a higher order one and achieve performance gain.

Much work has been conceptually and practically done in terms of optimal signal detection algorithms. To summarize, the existing detectors have trade-off issues in performance, complexity and spectral efficiency. Some detectors show optimal performance but with high complexity. Some detectors have low complexity but at the cost of performance. While some detectors achieve good performance and low complexity but with reduced achievable spectral efficiency. Therefore, the topic of efficient signal detection still remains open. Existing SEFDM detectors attempt to extract useful information from distorted signals at the receiver, which would result in inaccurate signal estimate since ICI has been added to each sub-carrier. In Chapter 8, alternative solutions, focusing on transmitter side, are investigated. The first solution is to precode signals prior to the wireless channel at the transmitter, based on known ICI information. Briefly, the technique is based on modifying the data sent on individual sub-carriers according to the signal quality of each, which is based on the sub-carrier

to interference ratio (ScIR) of such sub-carrier as estimated from eigenvalue decomposition. At the transmitter, instead of modulating data on all sub-carriers, sub-carriers associated with high eigenvalues (good ScIR) are reserved for data and other sub-carriers are used for precoding redundancy. At the receiver, only the sub-carriers of high ScIR are processed for data recovery. The precoding redundancy results in apparently "wasted" sub-carriers, however, the bandwidth compression characteristic of SEFDM compensates for such "waste". Modelling is done in simple Gaussian noise channels and in a static frequency selective channel and for different modulation formats. The second solution is straightforwardly to modulate two symbols, which have the same absolute amplitude but opposite signs, on adjacent sub-carriers. In this case, interference can be cancelled mutually at transmitter side. In order to further improve performance, receiver side mutual interference cancellation could be employed without any multiplication or matrix inverse operations. The spectral efficiency is halved by using this method. Thus, achievable spectral efficiency has to be investigated by studying various modulation formats and bandwidth compression factors. In general, an optimal combination of modulation formats and bandwidth compression factors exists for each achievable spectral efficiency. Practical over-the-air testing of the self interference cancellation is operated on commercially developed software defined radio USRP platforms. It aims at ultra-reliable and low-latency communication (URLLC) scenario due to its low complexity and high efficiency in cancelling the self-created ICI.

Finally, Chapter 9 summarizes the work in this thesis and put forward some proposals for future work.

In order to provide an intuitive understanding of the thesis structure, Fig. 1.2 depicts the background and motivation of this research work. Fig. 1.3 shows the key work of this thesis being SEFDM with links between different research aspects.

This thesis includes three appendixes. Appendix A presents abbreviations used in this thesis. Appendix B attached a submitted journal paper written by the author. Appendix C shows the constellation patterns of wireless signals via radio prorogation.

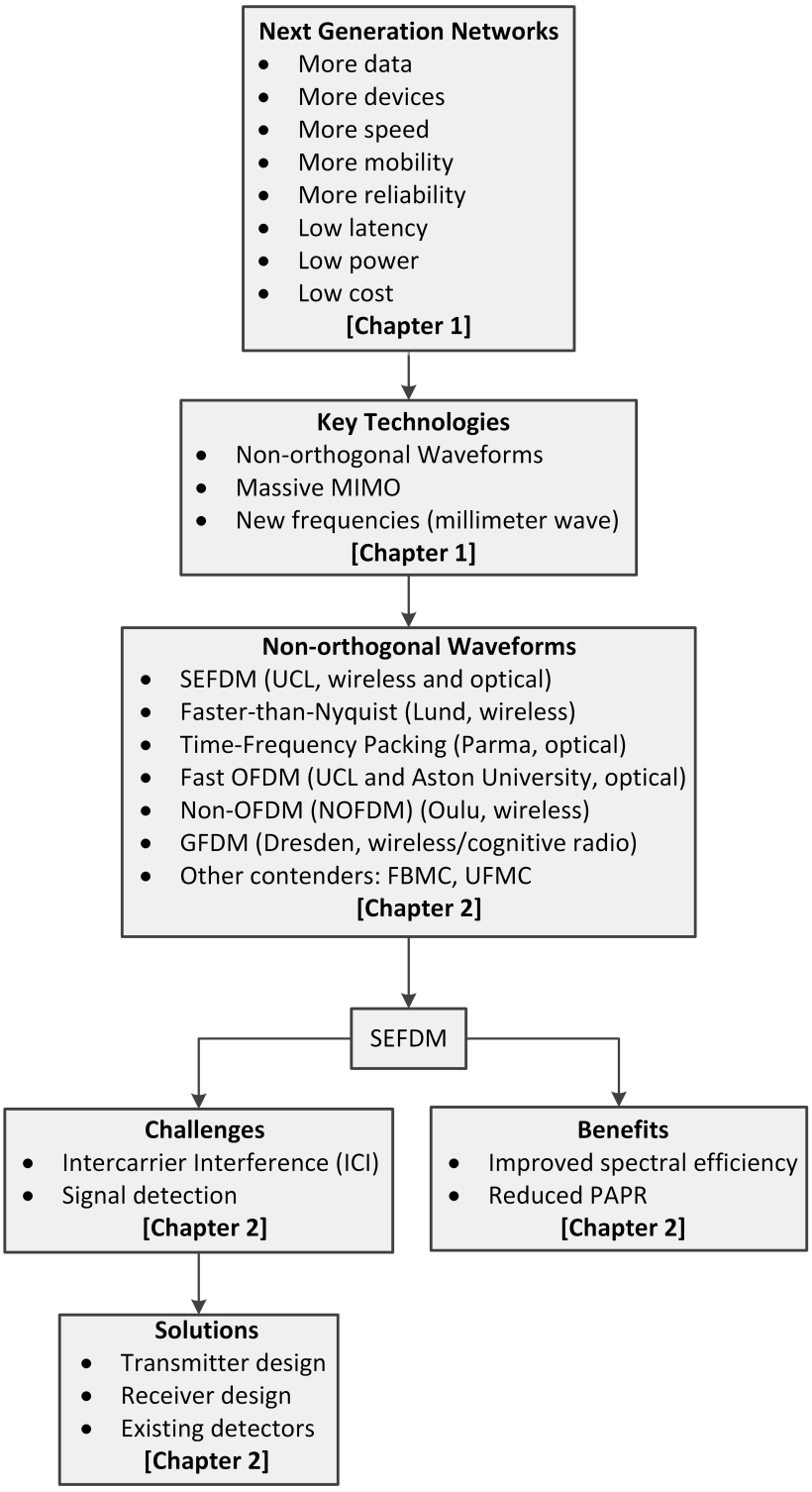

Figure 1.2: Focus of Chapters 1 and 2 (background and motivation of this work).

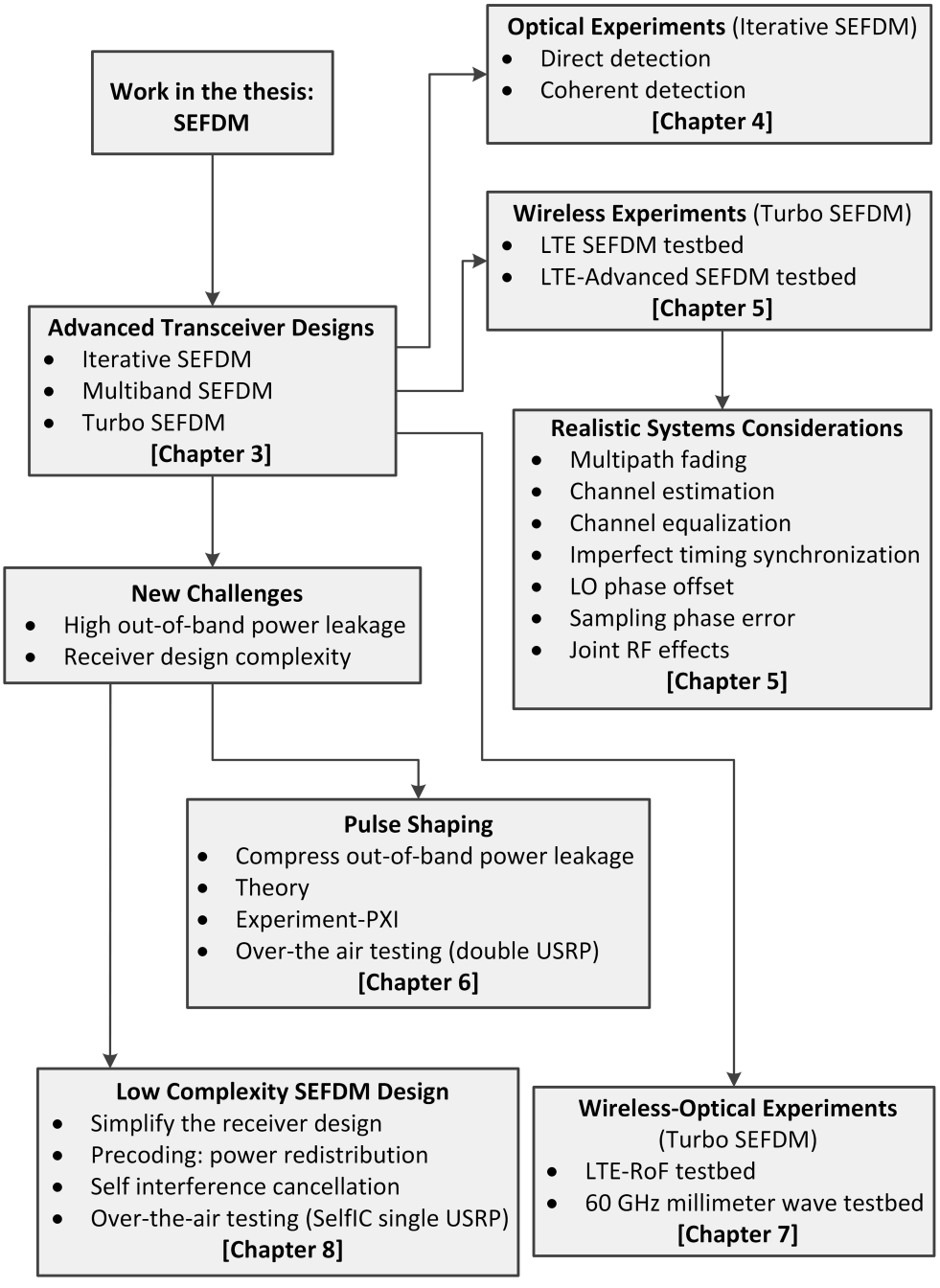

Figure 1.3: Focus of Chapters 3-8 (key work of this thesis).

1.3 Main Contributions

The work in this thesis comprises theoretical research and practical/experimental demonstration of a set of new concepts addressing implementation of SEFDM systems. This research work has contributed to the progress of SEFDM research in three areas of signal design and processing, detector design and optimisation and the first set of practical implementation of full SEFDM links in wireless and optical environments. A summary of these contributions is listed below.

- **FPGA Implementation.**

  This contribution has been published in [O01][C12] in the List of Publications (or [49][93] in List of References).

  - 2013: Designed and implemented a real time MIMO/SEFDM detector working at 1.06 Gbit/s on a Xilinx Vertex-6 FPGA chip.
  - 2017: FPGA modelling verification on a non-orthogonal iterative detector in terms of bit precision.

- **Proposal, mathematical modelling and assessment of three new non-orthogonal signal detectors for SEFDM.**

  Contributions in this area have been published in [J01][J03][C02][C03][C04][C13] in the List of Publications (or [52][58][56][57][59][95] in List of References).

  - 2013: Designed a new iterative detection scheme (ID) based on iterative demapping at the receiver and showed this scheme to outperform linear detection schemes whilst maintaining reasonable complexity.
  - 2014: Proposed a multi-band architecture, Block-SEFDM, which subdivides signal detection challenge into several blocks leading to reduced complexity and acceptable performance.

  - 2014: Designed a coding system, Turbo-SEFDM, which achieves good performance/complexity trade-off and shows its compatibility with existing mobile standards.

- **Optical Fiber Experiments.**

  Contributions in this area have been published in [J02][J04][C01][C08] in the List of Publications (or [54][72][55][73] in List of References).

  - 2014: Designed and implemented a direct detection optical testbed transmitting non-orthogonal signals at 10 Gbit/s. This is the first time to have a working experimental SEFDM transceiver.
  - 2015: Designed and implemented a dual polarization coherent detection optical testbed transmitting non-orthogonal signals at 24 Gbit/s.
  - Both experiments show that given the same spectral efficiency, a low-order modulation scheme can achieve a better performance by replacing a higher one.

- **LTE/LTE-Advanced Experiments.**

  Contributions in this area have been published in [J06][C06][C08] in the List of Publications (or [87][63][73] in List of References).

  - 2015: Seup up an LTE/LTE-Advanced experimental testbed that can reach up to 50 Mbit/s data rate using commercial PXI transceiver and Spirent VR5 channel emulator. A realistic LTE defined extended pedestrian A (EPA) wireless channel model is used.

- **Bandwidth Compressed 5G Experiments.**

  Contributions in this area have been published in [J06][C06][C08] in the List of Publications (or [87][63][73] in List of References).

  - 2015: Designed and implemented bandwidth compressed carrier aggregation wireless signal transmission at 70 Mbit/s in a realistic LTE defined EPA wireless channel. Compared to the typical LTE-Advanced testbed, a 40% data rate improvement is achieved. This is the world first time to have a fully running wireless SEFDM testbed.

- **Nyquist-SEFDM Experiments.**

  This contribution has been published in [C09] in the List of Publications (or [76] in List of References).

  - 2016: Designed a new waveform that compresses bandwidth and suppresses out-of-band power leakage. A realistic wireless platform was set up for the verification of coexistence of 4G and promising 5G signals for the first time.

- **60 GHz Millimeter Wave Non-orthogonal Radio Over Fiber Experiments.**

  Contributions in this area have been published in [J05][C05][C07][C08] in the List of Publications (or [77][62][71][73] in List of References).

  - 2015: Realized an LTE based 2.4 GHz non-orthogonal radio over fiber signal transmission and reception.
  - 2016: Designed and delivered 3.75 Gbit/s non-orthogonal signals through 250 meters multimode fiber (MMF), over 3 meters wireless link at 60 GHz mm-wave frequency. Compared to a typical 2.25 Gbit/s OFDM signal in the same scenario, the data rate is increased by 67%, which is the first attempt for SEFDM signals at millimeter wave frequency radio over fiber transmission scenario.

- **Low Complexity Transceiver Design.**

  This contribution has been published in [C10] in the List of Publications (or [86] in List of References).

  - 2017: Proposed and designed low complexity transceivers with the signal processing burden remains at the transmitter. These designs bring benefits to low power and low latency applications due to the special signal features from SEFDM.

- **Over-the-Air Testing with Software Defined Radio USRP RIO Devices.**

  This contribution has been submitted to [C11] in the List of Publications (or [94] in List of References).

  - 2017: Make use of software defined radio platform USRP and implemented an SEFDM signal based 5G testbed. It in real-time proves the Nyquist-SEFDM waveform and the applications of those low complexity transceiver designs.

In addition to all the mentioned technical contributions, I have also been awarded for Faculty of Engineering Sciences Scholarship, Association of British and Turkish Academics (ABTA) Doctoral Researcher Awards and Engineering and Physical Sciences Research Council (EPSRC) Discovery to Use Impact Acceleration award.

1.4 List of Publications

The contributions presented in section 1.3 have led to 2 book chapters, 7 journal papers of which 1 is under review, 13 conference papers of which 3 are invited. I have also contributed to related subjects one conference paper and one journal paper during my study at UCL. All publications are listed in chronological order:

- **Book Chapters:**

  [B01]. I. Darwazeh, **T.Xu**, and R. C. Grammenos, "Ch. Bandwidth Compressed Multicarrier Communication: SEFDM," Signal Processing for 5G: Algorithms and Implementations. Wiley, 2016.

[B02]. I. Darwazeh, R. C. Grammenos, and **T.Xu**, "Ch. Spectrally Efficient Frequency Division Multiplexing for 5G," Key Enabling Technologies for 5G Mobile Communications. Springer, 2016.

- **Journals:**

  [J01]. **T.Xu**, R. C. Grammenos, F. Marvasti, and I. Darwazeh, "An improved fixed sphere decoder employing soft decision for the detection of non-orthogonal signals," IEEE Communications Letters, vol. 17, no. 10, pp. 1964-1967, Oct. 2013.

  [J02]. I. Darwazeh, **T.Xu**, T. Gui, Y. Bao, and Z. Li, "Optical SEFDM system; bandwidth saving using non-orthogonal sub-carriers," IEEE Photonics Technology Letters, vol.26, no.4, pp.352–355, Feb.15, 2014.

  [J03]. **T.Xu** and I. Darwazeh, "A soft detector for spectrally efficient systems with non-orthogonal overlapped sub-carriers," IEEE Communications Letters, vol. 18, no. 10, pp. 1847-1850, Oct. 2014.

  [J04]. D. Nopchinda, **T.Xu**, R. Maher, B. Thomsen, and I. Darwazeh, "Dual polarization coherent optical spectrally efficient frequency division multiplexing," IEEE Photonics Technology Letters, vol. 28, no. 1, pp. 83-86, Jan. 2016.

  [J05]. **T.Xu**, S. Mikroulis, J. E. Mitchell and I. Darwazeh, "Bandwidth compressed waveform for 60 GHz millimeter-wave radio over fiber experiment," IEEE Journal of Lightwave Technology, vol. 34, no. 14, pp. 3458-3465, Jul. 2016.

  [J06]. **T.Xu** and I. Darwazeh, "Transmission experiment of bandwidth compressed carrier aggregation in a realistic fading channel," IEEE Transactions on Vehicular Technology, vol. 66, no. 5, pp. 4087-4097, May 2017.

  [J07]. **T.Xu**, T. Xu, P. Bayvel, and I. Darwazeh, "Reach enhancement in optical fiber transmission using non-orthogonal signals with sub-carrier spacing below symbol rate," Optics Express, 2017 (under review).

- **Conferences:**

  [C01]. I. Darwazeh, **T.Xu**, T. Gui, Y. Bao, and Z. Li, "Optical spectrally efficient FDM system for electrical and optical bandwidth saving," in IEEE International Conference on Communications (ICC), pp. 3432–3437, Jun. 2014.

  [C02]. **T.Xu** and I. Darwazeh, "M-QAM signal detection for a non-orthogonal system using an improved fixed sphere decoder," in 9th IEEE/IET International Symposium on Communication Systems, Networks & Digital Signal Processing 2014 (CSNDSP14), Manchester, United Kingdom, pp. 623–627, Jul. 2014.

  [C03]. **T.Xu** and I. Darwazeh, "Multi-Band reduced complexity spectrally efficient FDM systems," in 9th IEEE/IET International Symposium on Communication Systems, Networks & Digital Signal Processing 2014 (CSNDSP14), Manchester, United Kingdom, pp. 904–909, Jul. 2014.

  [C04]. **T.Xu** and I. Darwazeh, "Spectrally efficient FDM: spectrum saving technique for 5G?," in 1st International Conference on 5G for Ubiquitous Connectivity 2014 (5GU2014), Levi, Finland, Nov. 2014.

  [C05]. S. Mikroulis, **T.Xu**, J. E. Mitchell and I. Darwazeh, "First demonstration of a spectrally efficient FDM radio over fiber system topology for beyond 4G cellular networking," 20th European Conference on Networks and Optical Communications - (NOC), Jun. 2015, pp. 1–5.

  [C06]. **T.Xu** and I. Darwazeh, "Bandwidth compressed carrier aggregation," in IEEE ICC 2015 - Workshop on 5G & Beyond - Enabling Technologies and Applications (ICC15 - Workshops 23), London, United Kingdom, Jun. 2015, pp. 1107-1112.

  [C07]. S. Mikroulis, **T.Xu**, and I. Darwazeh, "Practical demonstration of spectrally efficient FDM millimeter-wave radio over fiber systems for 5G cellular networking," in Proc. SPIE, vol. 9772, 2016, pp. 97720I-1-97720I-8. (invited)

  [C08]. **T.Xu** and I. Darwazeh, "Experimental validations of bandwidth com-

pressed multicarrier signals," in 2016 IEEE 17th International Symposium on A World of Wireless, Mobile and Multimedia Networks (WoWMoM), Jun. 2016, pp. 1-10. (invited)

[C09]. **T.Xu** and I. Darwazeh, "Nyquist-SEFDM: pulse shaped multicarrier communication with Sub-Carrier spacing below the symbol rate," in 2016 10th International Symposium on Communication Systems, Networks and Digital Signal Processing (CSNDSP) (CSNDSP16), Prague, Czech Republic, Jul. 2016, pp. 1-6. (invited)

[C10]. **T.Xu** and I. Darwazeh, "A joint waveform and precoding design for non-orthogonal multicarrier signals," in 2017 IEEE Wireless Communications and Networking Conference (WCNC) (IEEE WCNC 2017), San Francisco, USA, Mar. 2017, pp. 1-6.

[C11]. **T.Xu** and I. Darwazeh, "Over-The-Air testing of bandwidth compressed multicarrier signals," in PIMRC 2017, Montreal, QC, Canada, Oct. 2017 (accepted).

[C12]. **T.Xu** and I. Darwazeh, "Bit precision study of a non-orthogonal iterative detector and its RTL modelling verifications," in PIMRC 2017, Montreal, QC, Canada, Oct. 2017 (accepted).

[C13]. **T.Xu** and I. Darwazeh, "Multi-Sphere decoding of block segmented SEFDM signals with large number of sub-carriers and high modulation order," in the international conference on Wireless Networks and Mobile Communications (WINCOM'17) (WINCOM'17), Rabat, Morocco, Nov. 2017 (accepted).

- **Other Publications:**

[O01]. **T.Xu**, R. Grammenos, and I. Darwazeh, "FPGA implementations of real-time detectors for a spectrally efficient FDM system," 20th International Conference on Telecommunications (ICT), pp.1–5, May 2013. (published before PhD started)

[O02]. P. Haigh, S. T. Le, S. Zvanovec, Z. Ghassemlooy, P. Luo, **T.Xu**, P. Chvojka, T. Kanesan, E. Giacoumidis, P. Canyelles-Pericas, H. L. Minh, W. Popoola, S. Rajbhandari, I. Papakonstantinou, and I. Darwazeh, "Multi-band carrier-less amplitude and phase modulation for bandlimited visible light communications systems," IEEE Wireless Communications, vol. 22, no. 2, pp. 46–53, Apr. 2015.

Chapter 2

Non-orthogonal Techniques Fundamentals

2.1 Introduction

This chapter discusses the basics of non-orthogonal signals and techniques. A block diagram of a basic OFDM/SEFDM system is shown in Fig. 2.1. A serial symbol stream is transformed into a parallel stream in the S/P module in preparation for modulation. For OFDM, signal modulation is straightforward by using IFFT. For SEFDM, since sub-carriers are no longer orthogonal, a special SEFDM modulation block instead of IFFT is used. Then, cyclic prefix (CP) is added at the beginning of each OFDM/SEFDM symbol to combat the multipath fading channel. After the digital-to-analogue conversion (DAC), up conversion, wireless channel, down conversion, analog-to-digital conversion (ADC) and CP removal, the OFDM signal is demodulated through an FFT. However, in the case of SEFDM, a special demodulation is executed due to the non-orthogonally packed sub-carriers. Finally, the demodulated but interfered SEFDM signal is recovered in the detector module, and a serial symbol stream is obtained after the P/S module. For OFDM signals, signal detection is not needed since no ICI is introduced.

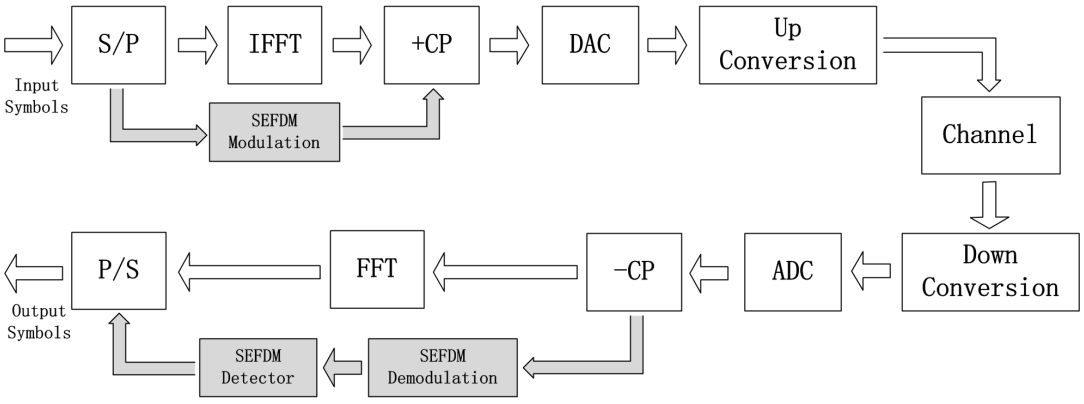

Figure 2.1: Block diagram for OFDM and SEFDM. The grey part indicates special operations for SEFDM.

SEFDM poses severed challenges in signal generation, demodulation and detection since self-created ICI is introduced. Prior to the descriptions of main achievements of this thesis, previous work on SEFDM signal generation, modulation and detection methods is introduced in this chapter to show the background of the SEFDM system. This chapter commences with introducing existing techniques of SEFDM signal generation, demodulation and detection with analysis of their limitations. Then, other spectrally efficient technologies are described to set SEFDM in context. Finally, this chapter is concluded by demonstrating the limitations of current existing SEFDM techniques and indicating potential research directions.

2.2 Orthogonality

The orthogonality is defined that if the cross-correlation of two signals is zero, then the two signals are mutually orthogonal. Meanwhile, if their auto-correlation equals one, then the signals are mutually orthonormal. The relations are given by

$$\int_0^T x_m(t)x_n^*(t)dt = \begin{cases} 0 & m \neq n \\ 1 & m = n \end{cases} \tag{2.1}$$

where $(.)^*$ denotes the complex conjugate. In a multicarrier communication system, symbols are modulated on separate sub-carriers, taking two arbitrary sub-carriers as an example, where they have frequencies f_1 and f_2, respectively, the correlation between the two sub-carriers is given by

$$\begin{aligned} CORR_{12} &= \int_0^T e^{j2\pi f_1 t}(e^{j2\pi f_2 t})^* dt \\ &= \int_0^T e^{j2\pi \Delta f t} dt \\ &= \frac{e^{j2\pi \Delta f T} - 1}{j2\pi \Delta f T} \\ &= e^{j\pi \Delta f T} \times \frac{sin(\pi \Delta f T)}{\pi \Delta f T} \end{aligned} \tag{2.2}$$

where Δf equals $f_1 - f_2$ and T is the period of one multicarrier symbol. In order to realize an orthogonal multicarrier system, the value of $CORR_{12}$ should be equal to zero. Therefore, Δf is set to be $\frac{n}{T}$ where $n \in \mathbb{Z}$. The OFDM system corresponds to $n = 1$. For SEFDM, in order to compress the bandwidth making it smaller than the OFDM one, the orthogonality is intentionally violated. Therefore, n is between 0 and 1.

2.3 SEFDM Signal Generation

The SEFDM signal consists of a stream of SEFDM symbols each carrying N complex quadrature amplitude modulation (QAM) (could be other modulation schemes) symbols. Each of the N complex symbols is modulated on one non-orthogonal sub-carrier. Therefore, the SEFDM signal can be expressed as

$$x(t) = \frac{1}{\sqrt{T}} \sum_{l=-\infty}^{\infty} \sum_{n=0}^{N-1} s_{l,n} \exp(\frac{j2\pi n \alpha (t - lT)}{T}) \tag{2.3}$$

where α is the bandwidth compression factor defined as

$$\alpha = \Delta f T \tag{2.4}$$

where Δf denotes the frequency distance between adjacent sub-carriers, T is the period of one SEFDM symbol, $\frac{1}{\sqrt{T}}$ is a scaling factor for the purpose of normalization, N is the number of sub-carriers and $s_{l,n}$ is the complex QAM symbol modulated on the n^{th} sub-carrier in the l^{th} SEFDM symbol. α determines bandwidth compressions and hence the percentage of bandwidth saving equals to $(1-\alpha)\times 100\%$. For OFDM signals $\alpha = 1$, and $\alpha < 1$ for SEFDM. Fig. 2.2 illustrates comparisons of the spectra of OFDM and SEFDM. It is clearly seen that due to non-orthogonal sub-carrier packing, SEFDM has a narrower bandwidth compared to OFDM given the same number of sub-carriers and the same modulation bandwidth per sub-carrier. The bandwidth occupations of OFDM and SEFDM are expressed in (2.5) and (2.6), respectively.

$$B_{OFDM} = \frac{(N-1)+2}{T} = ((N-1)+2)\Delta f \tag{2.5}$$

$$B_{SEFDM} = \frac{\alpha(N-1)+2}{T} = (\alpha(N-1)+2)\Delta f \tag{2.6}$$

With the increase of N, expressions in (2.5) and (2.6) can be simplified as

$$B_{OFDM} \approx N\Delta f \tag{2.7}$$

$$B_{SEFDM} \approx \alpha N\Delta f \tag{2.8}$$

where results indicate given a large number of N, the occupied bandwidth of SEFDM is approximately 'α' of that of the OFDM.

A spectral efficiency transformation table is shown in Table 2.1 where different modulation schemes are analyzed ranging from BPSK to 64QAM. The second column indicates the spectral efficiency for each modulation format. Various bandwidth compression factors are studied ranging from 0.9 down to 0.5. It is apparent that with different bandwidth compression factors spectral efficiency varies for the same modu-

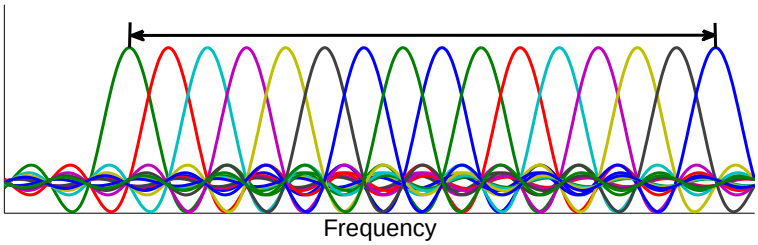

(a) OFDM Spectrum

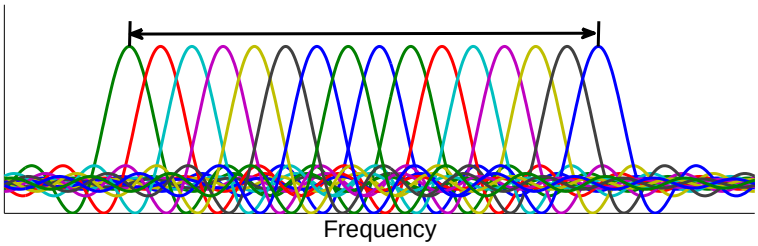

(b) SEFDM Spectrum with $\alpha = 0.8$

Figure 2.2: Spectra of 16 overlapped sub-carriers for OFDM and SEFDM.

lation format. Take BPSK as an example, using α=0.5, BPSK shows an equivalent spectral efficiency with 4QAM format. The same result is observed for the rest modulation schemes. This table provides a possible way to replace higher order modulation schemes with lower order modulation formats.

Table 2.1: Spectral Efficiency Transform.

Modulation	Modulation order	0.9	0.8	0.75	0.7	0.65	0.6	0.5
BPSK	1	1.11	1.25	1.33	1.43	1.54	1.67	2
4QAM	2	2.22	2.5	2.67	2.86	3.08	3.33	4
8QAM	3	3.33	3.75	4	4.29	4.62	5	6
16QAM	4	4.44	5	5.33	5.71	6.15	6.67	8
32QAM	5	5.56	6.25	6.67	7.14	7.69	8.33	10
64QAM	6	6.67	7.5	8	8.57	9.23	10	12

It is useful to represent the SEFDM signal in a discrete form for the purpose of signal analysis. A discrete signal is derived by sampling the first SEFDM symbol (take l=0) at T/Q intervals where $Q = \rho N$ and $\rho \geq 1$ is the oversampling factor. The discrete

SEFDM signal for $k = [0, 1, ..., Q-1]$ is represented by

$$X[k] = \frac{1}{\sqrt{Q}} \sum_{n=0}^{N-1} s_n \exp(\frac{j2\pi nk\alpha}{Q}) \tag{2.9}$$

where $X[k]$ is the k^{th} time sample of the first symbol of $x(t)$ in (1) and $\frac{1}{\sqrt{Q}}$ is a scaling factor. Furthermore, the signal can be simply expressed in a matrix form as:

$$X = \mathbf{F}S \tag{2.10}$$

where X is a Q-dimensional vector of time samples of $x(t)$ in (2.3), S is an N-dimensional vector of transmitted symbols and $\mathbf{F}$ is a $Q \times N$ sub-carrier matrix with elements equal to $\exp(\frac{j2\pi nk\alpha}{Q})$.

In a conventional OFDM system, signal generation can be realized straightforwardly by using a standard IFFT. However, due to the violation of the orthogonality property within SEFDM, the typical IFFT approach is not applicable. The direct way using equation (2.9) to address signal generation is too complex. In order to use the IFFT algorithm, two alternative algorithms are specially designed for SEFDM. Either using single IFFT [35] or multiple IFFTs [46].

2.3.1 Single IFFT Modulator

The first method is a zero padding scheme where a specific number of zeros are padded at the end of each input vector (i.e. multiple QAM symbols). The length of an original input vector becomes $U = Q/\alpha$. Therefore, for an N sub-carrier SEFDM system with the bandwidth compression factor α, it is possible to employ a single IFFT of a Q/α length where useful symbols are appended to the first N inputs and zeros are appended to the last $Q/\alpha - N$ remaining inputs such as

$$s_i^{'} = \begin{cases} s_i & 0 \leq i < N \\ 0 & N \leq i < U \end{cases} \tag{2.11}$$

where the value of Q/α has to be an integer and meanwhile the power of two $Q/\alpha \in 2^{(\mathbb{N}_{>0})}$, allowing for the IDFT to be implemented by means of the computationally efficient radix-2 IFFT. Assuming Q/α satisfies the requirement, the SEFDM signal in a new format is expressed as

$$X^{'}[k] = \frac{1}{\sqrt{U}} \sum_{n=0}^{U-1} s_n^{'} \exp(\frac{j2\pi nk}{U}) \tag{2.12}$$

where $n, k = [0, 1, ..., U-1]$. The output is truncated, only Q samples are reserved while the rest of the samples are discarded. This method has been successfully implemented on an FPGA platform in [43].

2.3.2 Multiple IFFTs Modulator

Work in [35] presents a technique to effectively generate SEFDM signals by using a multiple shorter IFFTs architecture, which relaxes the requirement for Q and α. Instead of padding zeros at the end of each input symbol, a number of zeros are interpolated. It is shown in [35] that by setting $\alpha = b/c$, where b and c are both positive integers (i.e. $b, c \in \mathbb{N}_{>0}$) and $b < c$, the rearranged input vector of length cQ can be separated into several shorter vectors where a shorter IFFT of length Q can be operated in each. Therefore, (2.9) can be rearranged and represented as

$$X[k] = \frac{1}{\sqrt{Q}} \sum_{n=0}^{cQ-1} s^{'}(n) \exp(\frac{j2\pi nk}{cQ}) \tag{2.13}$$

where $s^{'}$ is a cQ-dimensional vector of symbols as

$$s^{'}(i) = \begin{cases} s_{i/b} & i \ mod \ b = 0 \\ 0 & otherwise \end{cases} \tag{2.14}$$

by substituting with $n = i + lc$, (2.13) can be extended to

$$X[k] = \frac{1}{\sqrt{Q}} \sum_{i=0}^{c-1} \sum_{l=0}^{Q-1} s^{'}(i + lc) \exp(\frac{j2\pi k(i + lc)}{cQ}) \tag{2.15}$$

with further modifications, (2.15) can be rearranged as

$$X[k] = \frac{1}{\sqrt{Q}} \sum_{i=0}^{c-1} \exp(\frac{j2\pi ik}{cQ}) \sum_{l=0}^{Q-1} s^{'}(i+lc) \exp(\frac{j2\pi lk}{Q}) \tag{2.16}$$

Equation (2.16) shows that an SEFDM symbol is equivalent to a combination of multiple OFDM symbols. It is apparent that the SEFDM signal can be generated by using c parallel IFFT operations each of Q points. The first term on the right part of (2.16) determines the number of parallel IFFT operations. The second term indicates a Q-point IFFT of the sequence $s^{'}(i+lc)$.

Much work has been done with respect to hardware implementations of the multiple IFFTs method. An FPGA prototyping was reported in [47] and following this, a route to VLSI implementation of a reconfigurable SEFDM transmitter in 32-nm CMOS was published in [46] with the introduction of a pruned IFFT architecture. At 100 MHz clock frequency, the throughput can reach 17.4 Mbps with QPSK modulation, and up to 52.2 Mbps with 64QAM modulation, with bandwidth saving up to 50% relative to OFDM.

2.4 SEFDM Signal Demodulation

The function of a demodulator is to collect statistics of received signals by projecting the received signals onto a set of vectors defined by a basis function $b(t)$. Assume that the received signal $y(t)$ is expressed as

$$y(t) = x(t) + z(t) \tag{2.17}$$

where $x(t)$ is the transmitted analogue signal and $z(t)$ is the analogue AWGN. Defining $b_i(t)$ is the i^{th} vector where $i = 0, 1, ..., N-1$, then the collected statistics after the projection is presented as

$$r_i = \int_0^T b_i^*(t)y(t)dt \tag{2.18}$$

where $[.]^*$ indicates the complex conjugate operation, its discrete model is given by

$$R = \mathbf{M}S + Z \tag{2.19}$$

where $\mathbf{M}$ is the matrix that describes the correlation between the projection vectors and the sub-carriers. The element in the correlation matrix is defined as

$$M(m,n) = \sum_{k=0}^{Q-1} b_n^*(k) \exp(\frac{j2\pi mk\alpha}{Q}) \tag{2.20}$$

where $b_n^*(k)$ denotes the k^{th} time sample in the n^{th} vector. It is concluded that the property of basis function $b(t)$ determines the matrix $\mathbf{M}$ and further affects the quality of the collected statistics. The collected statistics are then applied in a detector to estimate the original transmitted symbols. Therefore, the proper generation of $b(t)$ is essential. In the following sections, some orthonormalization methods and a matched filtering method are introduced to generate $b(t)$.

2.4.1 Orthonormalization

Orthonormalization is a procedure to generate an orthonormal set of vectors from a non-orthonormal one. In order to make sure the collected statistics are independent, the orthonormal vectors are required to be mutually orthogonal ($\langle b_i, b_j \rangle$=0, when $i \neq j$, where $\langle . \rangle$ indicates an inner product) and the length of each vector equals one ($\langle b_i, b_i \rangle$=1). Gram Schmidt (GS) [96] is a classic orthonormalization algorithm for small size systems. With the increase of number of sub-carriers or bandwidth compression level, the performance degrades greatly due to its large rounding error. Moreover, in order to improve further the system performance, a modified Gram Schmidt (MGS) was proposed in [32] where the initial orthonormal vector is updated at each step. Work in [31] reported an iterative modified Gram Schmidt (IMGS) based on the work in [32] to

enhance the system performance by repeating orthonormalization process many times. Results in [97] confirm that MGS and IMGS have better performance than the conventional GS algorithm. However, projection onto a set of ortonormalization vectors does not avoid the ICI since the deliberate collapse of orthogonality generates significant interference between the sub-carriers. Therefore, a powerful interference cancellation detector is required after the orthonormalization process.

2.4.2 FFT Demodulator

The second demodulation method is to generate a basis function using the matched filtering principle as reported in [46]. A single FFT can be used. This is in fact an inverse operation of the single IFFT modulator described in section 2.3.1. Work in [98] has reported a reconfigurable hardware core to perform both FFT and IFFT by carrying out a few extra computations (such as conjugating input complex QAM symbols and output complex results). The conventional IFFT of length N is expressed as

$$x_n = \frac{1}{N} \sum_{k=0}^{N-1} X_k e^{\frac{j2\pi nk}{N}} \tag{2.21}$$

with some modifications, the above equation is transformed into

$$x_n = \frac{1}{N} (\sum_{k=0}^{N-1} X_k^* e^{\frac{-j2\pi nk}{N}})^* \tag{2.22}$$

where $[.]^*$ indicates the complex conjugate operation. Equation (2.21) and (2.22) are equivalent since they both obtain x_n. However, (2.21) is an IFFT realization while (2.22) gets the same result using an FFT with some modifications which include conjugating the input X_k and output of FFT. Hence, in terms of hardware implementation, IFFT and FFT can reuse the same hardware core leading to approximate 50% of resource saving. Since FFT /IFFT operations are more efficient than the complicated GS process, the matched filtering algorithm would be more practical.

Moreover, an optimized demodulator architecture which employs multiple FFTs

was introduced in [97]. This is an inverse operation of the multiple IFFTs modulator described in section 2.3.2. Complexity analysis and hardware implementation are discussed in [46].

2.5 Inter Carrier Interference Analysis

Since the matched filtering method is more efficient than the orthonormalization methods, in the following sections, the IFFT/FFT scheme is employed. At the receiver, X defined in (2.10) is contaminated by additive white Gaussian noise (AWGN) Z. The received signal is demodulated by correlating with the conjugate sub-carriers $\mathbf{F}^*$. The reception process is expressed as

$$R = \mathbf{F}^* X + \mathbf{F}^* Z = \mathbf{F}^* \mathbf{F} S + \mathbf{F}^* Z = \mathbf{C} S + Z_{\mathbf{F}^*} \tag{2.23}$$

where R is an N-dimensional vector of demodulated symbols or in other words collected statistics, $\mathbf{C}$ is an $N \times N$ correlation matrix which is defined as $\mathbf{C} = \mathbf{F}^* \mathbf{F}$, where $\mathbf{F}^*$ denotes the $N \times Q$ conjugate sub-carrier matrix with elements equal to $e^{\frac{-j2\pi nk\alpha}{Q}}$ for $k = [0, 1, ..., Q-1]$ and $Z_{\mathbf{F}^*}$ is the AWGN correlated with the conjugate sub-carriers. Interference from non-orthogonal packed sub-carriers can be defined by using the correlation matrix $\mathbf{C}$, where elements in the matrix is expressed as

$$\mathbf{C}(m,n) = \frac{1}{Q} \times \left\{ \begin{array}{ll} Q & , \ m = n \\ \frac{1-e^{j2\pi\alpha(m-n)}}{1-e^{\frac{j2\pi\alpha(m-n)}{Q}}} & , \ m \neq n \end{array} \right\}. \tag{2.24}$$

The detailed analysis of SEFDM interference can be found in work [99]. The interference caused by the off-diagonal ICI terms in the correlation matrix $\mathbf{C}$ can be evaluated by computing the cross-correlation between elements in the $\mathbf{C}$ matrix.

In order to simplify the ICI analysis, the interference to the first sub-carrier is studied here. Therefore, the first demodulated symbol $R(0)$ derived from (2.23) is given as

$$R(0) = \mathbf{C}(0,0)S(0) + \sum_{k=1}^{N-1} \mathbf{C}(0,k)S(k) + Z_{\mathbf{F}^*}(0) \tag{2.25}$$

where the first term on the right hand side indicates the desired signal and the second term is the self-created ICI component. When α=1, therefore an OFDM system, the ICI component is zero.

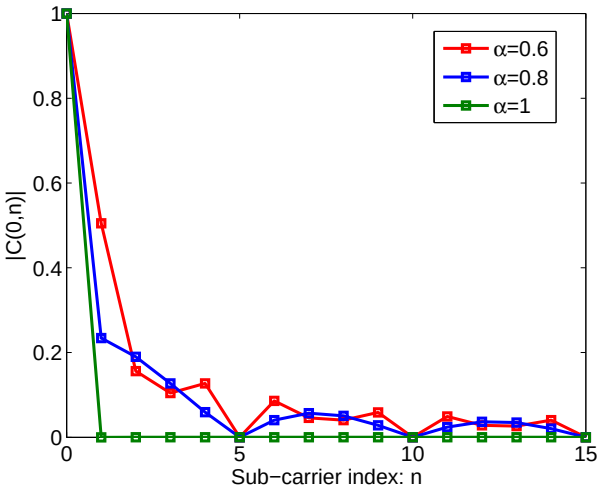

Figure 2.3: Desired and undesired power contributions to the first demodulated symbol $R(0)$.

Fig. 2.3 shows the absolute amplitude of the desired and undesired signals. It should be noted that the desired signal is located at n=0. In this section, power is normalized for desired signals. The green curve shows no ICI since all the values beyond n=0 are zeros. However, it is not the case for SEFDM signals since non-zero values fluctuate within this range. In addition, on the second sub-carrier, the red curve (i.e. α=0.6) shows a much higher absolute value than the blue curve (i.e. α=0.8). It indicates that systems of α=0.6 would result in worse performance compared with systems of α=0.8 since interference mainly comes from adjacent sub-carriers.

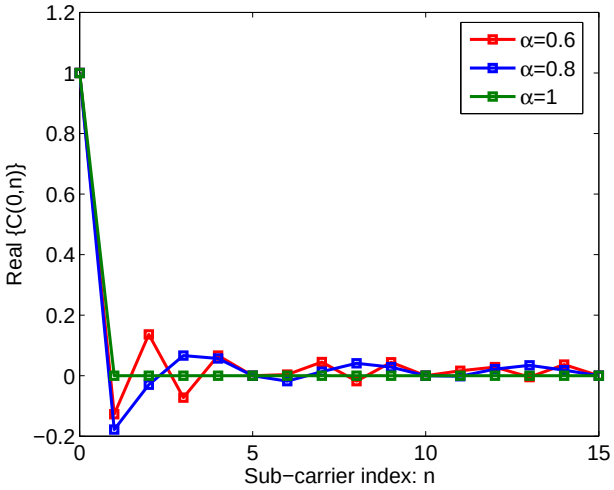

Figure 2.4: Real part of desired and undesired power contributions to the first demodulated symbol $R(0)$.

The corresponding real and imaginary part are presented in Fig. 2.4 and Fig. 2.5, respectively. It is inferred that the interference of α=0.6 systems is mainly introduced from the imaginary part, especially the adjacent interference on the second sub-carrier.

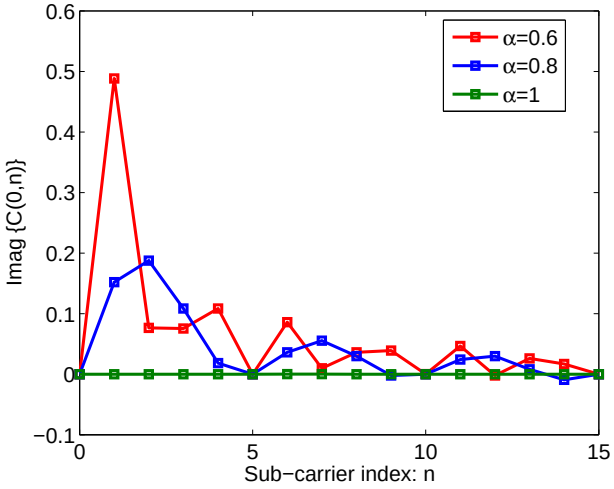

Figure 2.5: Imaginary part of desired and undesired power contributions to the first demodulated symbol $R(0)$.

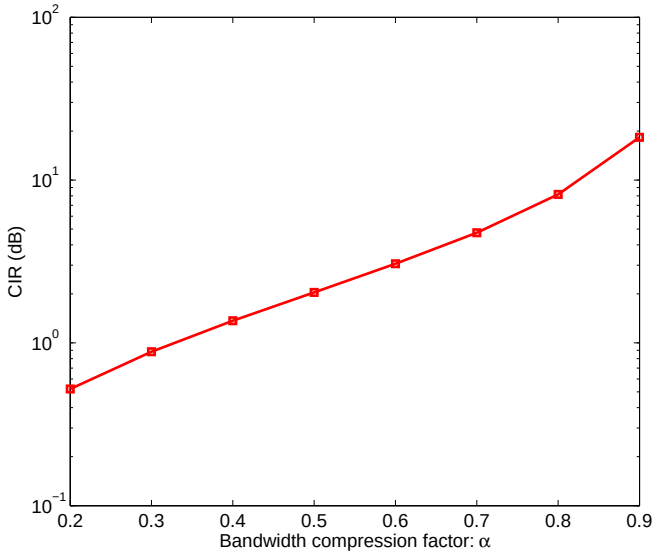

Figure 2.6: CIR for systems with N=16 sub-carriers in different bandwidth compression factors α.

As explained above, the undesired ICI component is related to α. The interference contribution can be evaluated using carrier-to-interference power ratio (CIR), which is equivalent to the ratio of the desired signal power and the ICI power. Therefore, the desired signal power on the first symbol is defined as

$$P_C = |\mathbf{C}(0,0)S(0)|^2 \tag{2.26}$$

The ICI power derived from the second term in (2.25) is given as

$$P_I = |\sum_{k=1}^{N-1} \mathbf{C}(0,k)S(k)|^2 \tag{2.27}$$

Assuming the symbol format is BPSK, therefore, the CIR is obtained as

$$CIR = \frac{P_C}{P_I} = \frac{|\mathbf{C}(0,0)S(0)|^2}{|\sum_{k=1}^{N-1} \mathbf{C}(0,k)S(k)|^2} = \frac{|\mathbf{C}(0,0)|^2}{|\sum_{k=1}^{N-1} \mathbf{C}(0,k)|^2} \tag{2.28}$$

where it is apparent that the CIR is a function of α and the numerical study of its effect

is presented in Fig. 2.6. It is noted that the CIR becomes better with the increase of α. This verifies the assumption that higher bandwidth compression (i.e. small α) introduces higher ICI.

2.6 SEFDM Signal Detection

This section describes several existing SEFDM detectors assuming an AWGN channel. Different detection techniques are compared in terms of their error performance, complexity and limitations.

2.6.1 Maximum Likelihood (ML)

The ideal performance of an SEFDM system should approach that of an equivalent OFDM. Such is shown in Fig. 2.7. Ideal performance can only be obtained using an exhaustive search method such as ML. Due to the loss of orthogonality between sub-carriers, the received signals contain serious ICI leading to increased error rates. With the aim of reducing the error rate, ML was firstly proposed as the optimal detection algorithm for SEFDM systems. The idea of ML is to test all possible combinations of input symbols for every received SEFDM symbols. The ML estimate S_{ML} of the received symbols in SEFDM can be expressed as

$$S_{ML} = \arg \min_{S \in O^N} \|R - \mathbf{C}S\|^2 \tag{2.29}$$

where $\|.\|$ denotes the Euclidean norm, S are the detected symbols, O is the constellation cardinality, N is the number of sub-carriers and therefore O^N is the set of all the possible symbols combinations. The optimum solution is the one that has the smallest Euclidean norm with the collected statistics. However, it is clearly seen from (2.29) that with the increase of the number of sub-carriers and modulation level, the ML detector complexity increases exponentially, therefore, ML is not considered as a practical

solution.

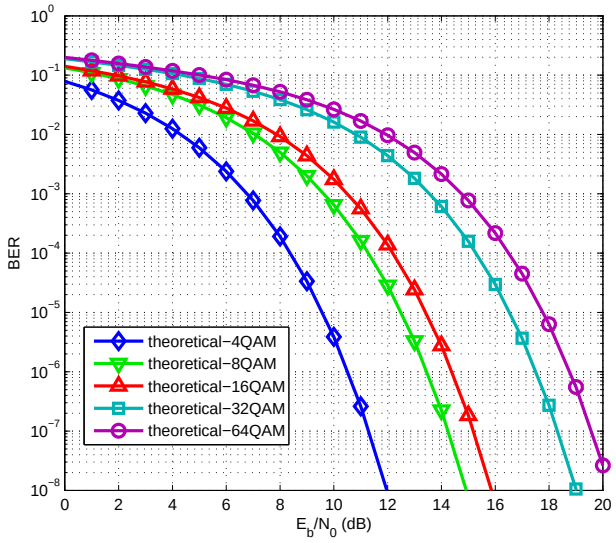

Figure 2.7: Theoretical results for M-QAM OFDM.

2.6.2 Sphere Decoder (SD)

As mentioned before, for non-orthogonal signals severely distorted by ICI in SEFDM systems, ML detection offers the optimal solution, but requires exhaustive search over all the possible combinations of transmitted symbols. In practice, ML complexity increases greatly with the enlargement of the number of sub-carriers or the order of modulation scheme. To address the high complexity level of ML detector, a complexity reduced technique called SD was proposed for SEFDM in [31]. A more detailed description and the complexity analysis of the SD were reported in [100]. Its hardware implementations can be found in work [101] [102] [103]. In addition, a reconfigurable FPGA implementation of SD was reported in [104] which allows the FPGA reconfigurable for different modulation schemes. Particularly, work in [105] demonstrated a real-time implementation of SD on a FPGA platform where signal impairments like symbol timing, imperfect channel estimation and quantization effects were taken into account. In contrast, SD algorithm achieves the ML performance by searching for the

best solution within a predefined sphere space which is constrained by an initial radius. Since the defined search space is smaller than the ML search space, SD results in significantly reduced complexity.

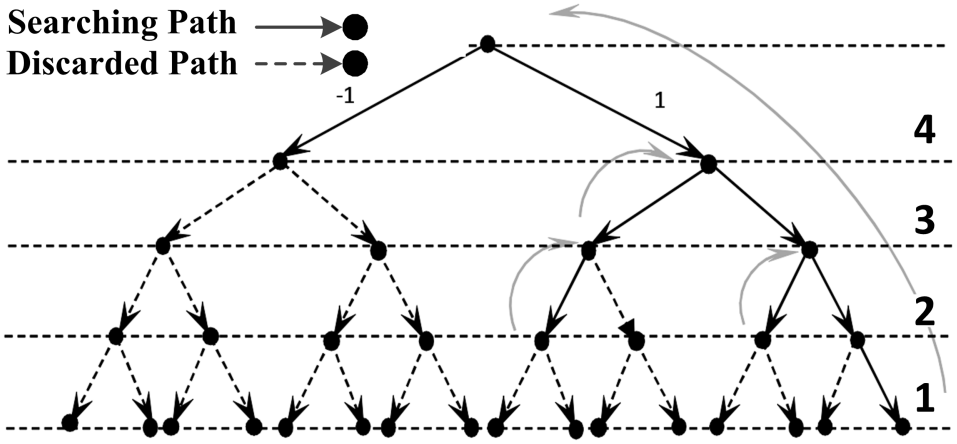

Figure 2.8: SD tree search diagram for 4 sub-carrier SEFDM systems with BPSK symbols.

Fig. 2.8 illustrates a tree search diagram in order to show how SD detection algorithm works. Each point in the tree is referred to as a node and simply represents a constellation point. The number of branches per node is equal to the constellation size (2 in the example). The number on the right at each level represents the index of sub-carriers in the SEFDM system (4 in the example). ML searches for all the nodes including both retained nodes and discarded nodes. However, SD only tests nodes within a predefined sphere space in Fig. 2.8. At each level, only points that within the sphere space are reserved while the rest nodes are discarded with all its predecessor nodes. The forward transition from a higher level to a lower level indicates the decision of one symbol; the backward transition (represented by a curved arrow) indicates the discard of one node and all its children nodes.

Initial radius determines the complexity of SD since it determines the size of the search space. However, it should be noted that a small radius would reduce the probability of finding the optimal solution since this limits the search space around a node

while a large radius will increase the complexity. There are 31 nodes in Fig. 2.8. It is clearly seen that only 9 nodes are searched, while the rest of the nodes are discarded. Therefore, the throughput of SD is much higher than that of ML.

The SD search for the best estimate S_{SD} in SEFDM is defined as

$$S_{_{SD}} = \arg \min_{S \in O^N} \|R - \mathbf{C}S\|^2 \leq g \tag{2.30}$$

where g is the initial radius which equals the distance between the received statistics R and the initial constrained estimate $S_{_{ZF}}$ where $S_{_{ZF}}$ is the zero forcing estimate which can be obtained using the rounding function $\lfloor . \rceil$ as $S_{_{ZF}} = \lfloor \mathbf{C^{-1}}R \rceil$. Then the initial radius is expressed as

$$g = \|R - \mathbf{C}S_{_{ZF}}\|^2 \tag{2.31}$$

Expanding the norm argument in (2.30) and substituting by $P = \mathbf{C^{-1}}R$ where P is the unconstrained estimate of S in (2.30) leads to

$$S_{_{SD}} = \arg \min_{S \in O^N} \{(P - S)^* \mathbf{C}^* \mathbf{C}(P - S)\} \leq g \tag{2.32}$$

In order to simplify the squared Euclidean norm calculation of (2.30), equation (2.32) can be transformed into an equivalent expression using Cholesky decomposition. The transformation is carried out using $chol\{\mathbf{C}^*\mathbf{C}\} = \mathbf{L}^*\mathbf{L}$ [39], where $\mathbf{L}$ is an $N \times N$ upper triangular matrix. Hence, (2.30) can be re-written as

$$S_{_{SD}} = \arg \min_{S \in O^N} \|\mathbf{L}(P - S)\|^2 \leq g \tag{2.33}$$

Similarly, (2.31) can be transformed to

$$g = \|\mathbf{L}(P - S_{ZF})\|^2 \tag{2.34}$$

Due to the triangular form of **L**, the detection can be divided into N consecutive steps corresponding to N dimensions (sub-carriers) of the SEFDM signal. Therefore, (2.33) can be transformed to

$$g \geq (l_{N,N}(P_N - S_N))^2 + (l_{N-1,N-1}(P_{N-1} - S_{N-1}) + l_{N-1,N}(P_N - S_N))^2 + ... \tag{2.35}$$

where $l_{i,j}$, P_i and S_i are the elements of the **L**, P and S in (2.33), respectively. In order to investigate each square term in (2.35), the N-dimension hypersphere is divided into N separate one-dimensional spheres. According to (2.35), the inequality expression for the N^{th} term is represented as

$$l_{N,N}^2(P_N - S_N)^2 \leq g_N = g \tag{2.36}$$

Therefore, the search interval for the N^{th} level is derived as

$$LB = \lceil -\frac{\sqrt{g_N}}{l_{N,N}} + P_N \rceil \leq S_N \leq \lfloor \frac{\sqrt{g_N}}{l_{N,N}} + P_N \rfloor = UB \tag{2.37}$$

where the $\lceil \cdot \rceil$ and $\lfloor \cdot \rfloor$ denote rounding operation to the nearest larger and smaller integer, respectively. Assume there is a solution S_N in this interval, the radius is updated as

$$g_{N-1} = g_N - l_{N,N}^2(P_N - S_N)^2 \tag{2.38}$$

and the inequality expression for the $(N-1)^{th}$ level is obtained as

$$(l_{N-1,N-1}(P_{N-1} - S_{N-1}) + l_{N-1,N}(P_N - S_N))^2 \leq g_{N-1} \tag{2.39}$$

Equation (2.39) can be simplified as

$$l_{N-1,N-1}^2(\xi_{N-1} - S_{N-1})^2 \leq g_{N-1} \tag{2.40}$$

where ξ_{N-1} is defined by using P_{N-1} as

$$\xi_{N-1} = P_{N-1} + \frac{l_{N-1,N}}{l_{N-1,N-1}}(P_N - S_N) \tag{2.41}$$

After that, the algorithm employes the similar enumeration scheme in (2.37) to find possible solutions in the $(N-1)^{th}$ dimension. The same process is iterated until the last dimension. General formulae for the i^{th} dimension are represented as

$$g_i = g - \sum_{j=i+1}^{N} l_{j,j}^2(\xi_j - S_j)^2 \tag{2.42}$$

$$g_{i-1} = g_i - l_{i,i}^2(\xi_i - S_i)^2 \tag{2.43}$$

$$\xi_i = P_i + \sum_{j=i+1}^{N} \frac{l_{i,j}}{l_{i,i}}(P_j - S_j) \tag{2.44}$$

Equation (2.42) and (2.43) show the process of radius update at each level. When SD reaches the last dimension $i = 1$, the solution is defined as a N-dimensional vector

that meets the condition written as

$$\|R - \mathbf{C}S\|^2 = \sum_{i=1}^{N} l_{i,i}^2(\xi_i - S_i)^2 \leq g \tag{2.45}$$

In other words, a final solution indicates that at each level, there are at least one point that meets the requirement of (2.37).

◇**An illustrative example** :

A flow chart illustrating an example of SD algorithm is shown in Fig. 2.9. This step by step example is described on the basis of Fig. 2.8. There are 8 constellation diagrams and each one represents the decision of one candidate point. Normally, the decision criterion of each candidate node is based on (2.37) where the decision space for each node is the one-dimensional interval constrained by the lower bound LB and the upper bound UB. However, in Fig. 2.9, original equations (2.36) and (2.40) are used to demonstrate the SD principle at each tree level constrained by a two-dimensional sphere which is the grey circle in Fig. 2.9. Only points that lie within this area are reserved for the following decisions while the rest of the points are discarded. The number on the right hand side represents the sub-carrier index (tree level). The decision of one point from a higher level determines the decision sphere of lower levels, which is shown in (2.38). Thus, decisions in the current level are dependent on previous estimates. At the first tree level, according to (2.36), the candidate point S_N is the point within the circle area constrained by the radius $\sqrt{\frac{g_N}{l_{N,N}^2}}$ with the center point P_N. Therefore, two points are within the decision sphere, which is shown as 4(a) in Fig. 2.9. Then, the decision threshold for the next tree level is updated according to (2.38) and illustrates in 3(a) and 3(b). However, the decision point '-1' from level 4 results in no points lying within the decision area in level 3. Therefore, S_4=-1 is discarded with its children nodes. On the other hand, S_4=1 leads to successful decisions at level 3. The algorithm continues to follow the similar procedure in (2.40) to determine S_3, S_2 and S_1. If no solution is found, the initial estimate S_{ZF} is selected to be the final solution or the initial radius g

in (2.36) has to be increased and the SD search must be executed again until a solution is found. In this example, at the last level, the final solution is '1,1,1,1'. Therefore, depending on the proper selection of a initial radius, SD can avoid exhaustive search, thus it is more computation effective than the ML algorithm.

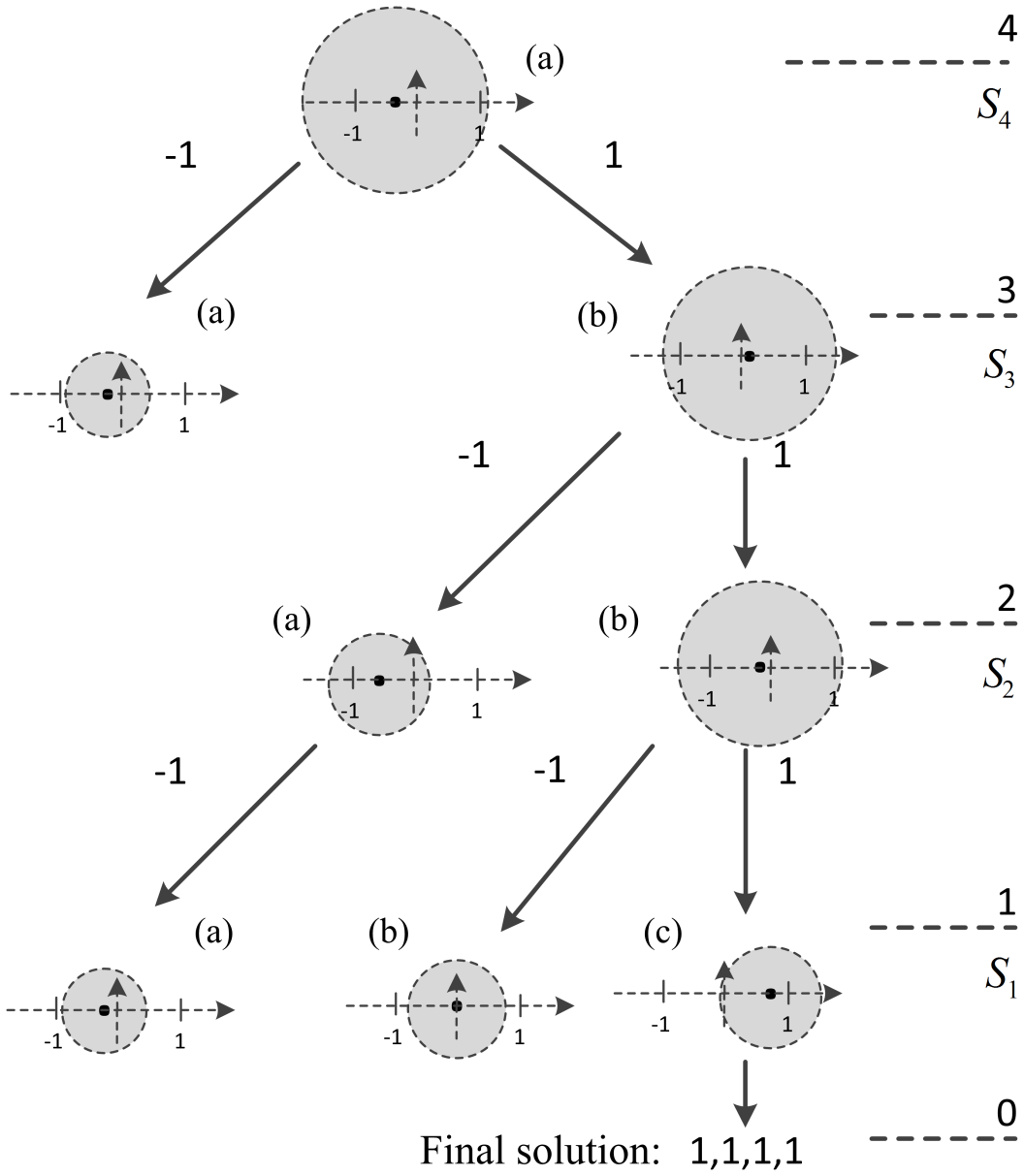

Figure 2.9: Step by step illustration of the SD algorithm. It is based on the tree diagram in Fig. 2.8. Points within the grey area are reserved as possible candidates. The modulation scheme is BPSK and the number of sub-carriers is 4.

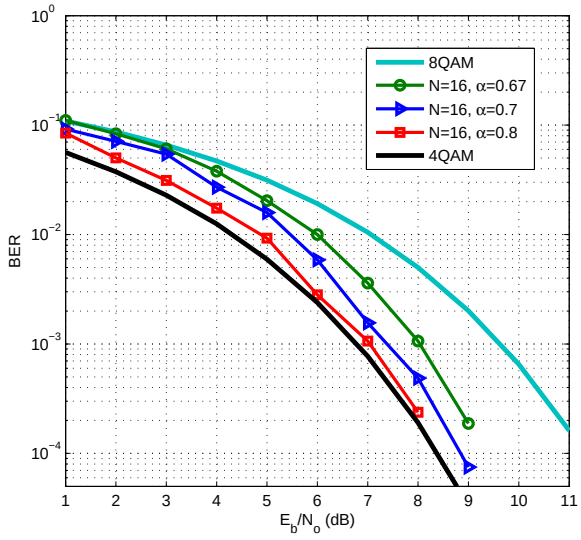

Figure 2.10: SD results for 4QAM SEFDM with various bandwidth compression factors, N=16. 8QAM has a spectral efficiency equals to '3' and 4QAM SEFDM with α=0.67 has a spectral efficiency equals to '3'.

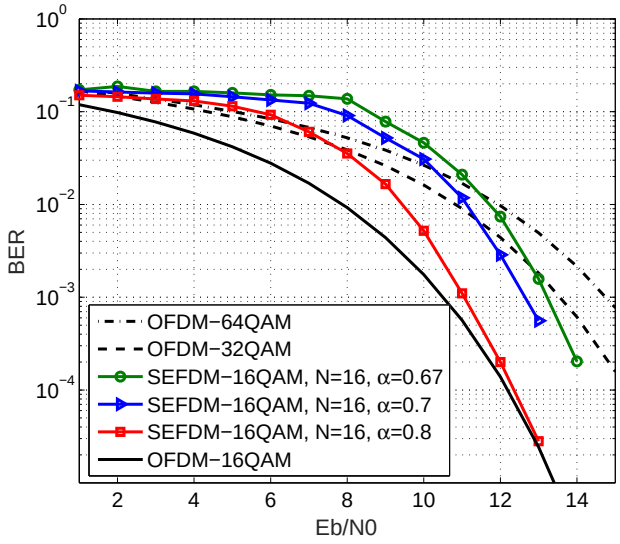

Figure 2.11: SD results for 16QAM SEFDM with various bandwidth compression factors, N=16. 32QAM has a spectral efficiency equals to '5' and 16QAM SEFDM with α=0.8 has a spectral efficiency equals to '5'. 64QAM has a spectral efficiency equals to '6' and 16QAM SEFDM with α=0.67 has a spectral efficiency equals to '6'.

In terms of BER performance, SD is a method approaches ML performance with lower complexity. However, the complexity is highly dependent on the noise in the channel and the conditioning of systems. The complexity of the SD approaches ML complexity with the increase of the number of sub-carriers and the bandwidth compression. Therefore, this detection technique is only suitable for small size systems with low bandwidth compressions. In particular, it is clearly seen from Fig. 2.9 that the SD detection is a sequential algorithm which is not practical in hardware implementation. Finally, the performance of SD for different modulation schemes is presented in Fig. 2.10 and Fig. 2.11. Results in both figures confirm that with 20% bandwidth compression the performance of SEFDM approaches the OFDM one. This is consistent with the Mazo's 25% faster than the Nyquist limit [20]. In order to demonstrate the benefits introduced by SEFDM, spectral efficiency equivalent OFDM results are included for the purpose of comparison. In Fig. 2.10, 8QAM OFDM has a spectral efficiency equals to 3 which is equivalent to that of the 4QAM SEFDM with α=0.67. It indicates that, for a given spectral efficiency, a low order modulation scheme can replace a higher one with better performance. The same benefit can be observed for 16QAM in Fig. 2.11 where the 16QAM SEFDM signal (α=0.8) outperforms 32QAM OFDM considering the same spectral efficiency beyond E_b/N_o=7dB. Furthermore, it is proved that the 16QAM SEFDM signal (α=0.67) even outperforms the 64QAM OFDM signal beyond E_b/N_o=11dB in Fig. 2.11 in the same spectral efficiency.

Although SD has a lower complexity than ML, it is still not applicable in real time communication systems due to the long computation time delay associated with the iterative process. In order to reduce the computation time, work in [106] presents a parallel architecture that can split a constellation tree into multiple sub-trees, thus, SD can be performed in each sub-tree in parallel. In particular, sub-trees can exchange updated initial radius g to tighten the sphere more quickly. Therefore, the complexity can be reduced with a faster shrinking radius. Results indicate that the processing speed is increased by 44% compared with a conventional SD. Furthermore, in order

to combine the SD with channel coding, a technique termed list SD was reported in [107][108][109]. This technique generates a list of candidates which are further used to provide soft information for channel decoder. Following theoretical analysis, a pipelined VLSI architecture for the list SD was proposed in [110]. Moreover, in [111], an increasing radius SD (IR-SD) was proposed to achieve a factor of 2.5 speed-up compared to a conventional SD. However, starting with a large initial radius may result in redundant computation. The novelty of work [111] is to set initial radius to zero at the beginning and increase radius only when no node is included within the current sphere. A technique in [112] was described to find the ML solution earlier by applying a runtime constraint scheme. A one-node-per-cycle architecture is employed to stabilize the instantaneous throughput. A decoding procedure stops after a predefined runtime constraint leading to a fixed throughput. Numerical results indicate this new SD achieves almost ML performance without severe performance degradation. More practically, work in [113] presents a multi-core SD VLSI architecture. The basic idea of the multi-core is to search multiple nodes simultaneously within a predefined search sphere. Unlike the parallel architecture reported in [106], each processing element (PE) in the multi-core has the ability to finish a complete decoding process. This architecture can efficiently improve the processing speed.

The SD is not only applicable at the receiver side, but also for signal precoding at the transmitter. In terms of the precoding scheme, the sphere decoding algorithm is termed "sphere encoder" [114] at the transmitter. The main purpose of this algorithm is to reduce receiver complexity and enhance the reliability of the transmission. In the case of multi-user scenario, mobile stations (MS) are not operating in cooperative mode. Thus conventional MIMO detectors are not applicable since the complete channel state information (CSI) is not known for each MS. An alternative way is to precode transmitted symbols on the basis of the feedback CSI from MS. Thus, it is possible to detect signals using simple linear detectors at the receiver. Following that, an FPGA implementation of a precoding technique termed vector perturbation (VP) has been

reported in [115].

2.6.3 Fixed-Complexity Sphere Decoder (FSD)

In order to solve the random complexity and sequential nature of SD, a new complexity fixed detection algorithm termed FSD was proposed for SEFDM in [39]. Unlike the depth-first search of SD, FSD is a breadth-first detection algorithm. The FSD fixes the complexity of SD by restricting the search space to a fixed size subspace, which means, at each level, a fixed number of nodes, termed tree-width, are examined. Therefore, it is more practical in terms of hardware implementation. The FSD has been studied in detail in [116] and its rapid prototyping was reported in [117]. Later, this technique was extended to a Turbo-MIMO system [118] to obtain likelihood information. However, FSD doesn't guarantee an optimal solution like SD since it enumerates a fraction of points within the sphere search space. The FSD estimate is expressed as

$$S_{FSD} = \arg \min_{S \in O^N,\ S \in M} \|R - \mathbf{C}S\|^2 \leq g_{FSD} \tag{2.46}$$

where M is the search subspace which is determined by the tree-width, $g_{FSD} = \|R - \mathbf{C}S_{ZF}\|^2$ determines the constrained space and if finally no node is found within the sphere, the initial constrained estimate S_{ZF} is taken as the solution as expressed in the equality below:

$$S_{FSD} = S_{ZF} \tag{2.47}$$

Fig. 2.12 illustrates the FSD tree search for a 4 sub-carrier system with BPSK symbols. In this diagram, the tree-width T_W is set to 2. The figure illustrates that at each level, only two nodes are reserved, while the rest of the nodes are discarded with their children nodes. Based on the aforementioned analysis, FSD has a fixed complexity (i.e. not dependent on noise) and is practical for hardware implementation. Furthermore, FSD is realized by using a parallel architecture, while SD is a sequential

architecture. This means resource utilization of FSD is relatively higher than that of SD. However, the throughput of FSD is fixed and relatively higher than that of SD. In terms of BER performance, since FSD search is restricted in a fixed search space, only a fraction of SD search space is examined, therefore, the performance is sub-optimal and is worse than SD. It should be noted that the choice of the subset M is crucial to the performance of FSD. This subset can be configured based on targeted BER performance or design complexity.

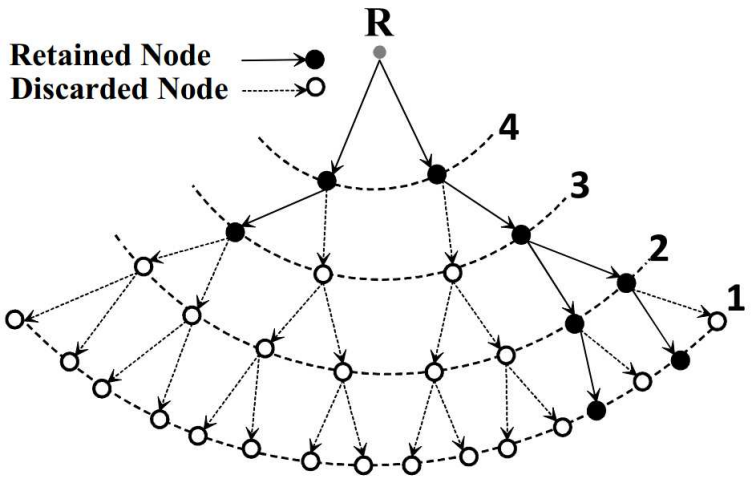

Figure 2.12: FSD tree search diagram for a 4 sub-carrier SEFDM system with BPSK symbols.

In order to cope with challenges arising from the use of FSD, several optimization methods were proposed. Work in [119] introduced an early termination FSD which makes full use of the features in FSD while preserves advantages of SD such as branch termination and radius update. Therefore, unnecessary branches are pruned leading to reduced complexity while the throughput is still fixed. The other technique named staggered SD was reported in [120] which can simultaneously search along the depth and breadth of the tree. In other words, this technique combines advantages of both SD and FSD. Results present that the throughput per unit power and per unit area is greatly improved over the parallel and sequential methods.

It should be mentioned that a technique termed K-best SD has a similar principle

to FSD. Its main idea is to keep K best nodes at each level. The K-best decoding algorithm was described in detail in [121][122]. Based on the theoretical work, a radius adaptive K-best SD with early termination was proposed in [123]. The main idea of this algorithm is to decompose the whole tree into several sub-trees and define a new tree-width to each sub-tree. The search sphere in one sub-tree is updated and used for other sub-trees. Therefore, redundant search can be avoided and the throughput is improved. Moreover, a complexity reduced technique termed sort-free K-best SD was reported in [124]. Instead of extending all the children nodes in parallel, only the child node with the minimum metric inherited from its parent node is extended. The process continues following the same criterion until all K paths have been found.

A comparison between FSD and SD are listed below:

- **BER Performance.** SD outperforms FSD substantially. FSD restricts a fixed number of searching branches in each detection and there is no update for the search space. Such detection simplification results in performance degradation. For SD, the radius is shrinking gradually in order to speed up the detection.

- **Throughput.** FSD has a fixed throughput while SD has a variable throughput. It should be noted that FSD has a higher throughput than SD as well.

- **Complexity.** The main advantage of FSD is its parallel processing structure. However, a sort unit has to be used at each level in order to find the best T_W nodes. This unit consumes a large amount of resources as mentioned in our previous work [49]. Furthermore, with the increase of the number of sub-carriers and the order of modulation scheme, the resource consumption of FSD is increased exponentially. However, SD has a lower complexity level since no sort unit is used at each level. On the other hand, it is noted that FSD has fixed complexity while SD has random complexity.

- **Power Efficiency.** SD is more power efficient than FSD. FSD searches redundant nodes in the tree diagram and results in extra power consumption.

2.6.4 Minimum Mean Squared Error (MMSE)

Nolinear detectors such as ML, SD and FSD produce competitive BER performance but at the cost of complexity. On the other hand, linear detector like ZF has a low complexity while its performance is far away from the optimal one. The mathematical expression of ZF is defined as

$$S_{ZF} = |\mathbf{C}^{-1}R| = |S + \mathbf{C}^{-1}Z_{\mathbf{F}^*}| \tag{2.48}$$

where $|.|$ is a slicer and in this thesis a QAM demapper. It is evident that the properties of the $\mathbf{C}$ matrix and its inverse will dictate the quality of the ZF estimation. In the case of small α and large number of sub-carriers N, the $\mathbf{C}$ matrix is ill conditioned leading to poor BER performance. In order to mitigate the effects of noise enhancement associated with ZF, the MMSE detector was proposed for SEFDM system in [125] where a noise whitening term is included for the purpose of optimizing the noise enhancement. The MMSE estimation is expressed in (2.49) and its detailed derivation is referred to [125].

$$S_{MMSE} = |\mathbf{C}^*(\mathbf{C}\mathbf{C}^* + \frac{1}{SNR}\mathbf{I})^{-1}R| \tag{2.49}$$

where $\mathbf{I}$ is the identity matrix. It is apparent that the estimation is related to SNR. In the case of zero noise, MMSE reduces to the ZF detection since the noise whitening term $\frac{1}{SNR}\mathbf{I}$ equals zero. Therefore, it is evident that MMSE outperforms ZF in the condition of low signal-to-noise ratio (SNR). The two detectors will have the same performance in high SNR conditions.

2.6.5 Truncated Singular Value Decomposition Detector (TSVD)

SEFDM has an ill-conditioned issue since sub-carriers are non-orthogonally packed. As the conditioning of the system worsens, the system is more sensitive to any perturbations (noise). Any solutions based on the inverse of the correlation matrix $\mathbf{C}$ result in poor performance. The TSVD [39] is a method to generate an approximated inverse of

an ill conditioned matrix to make it less sensitive to perturbations. The approximated inverse is derived by finding and truncating the small singular values which overly multiply the noise. This is accomplished by using the singular value decomposition (SVD) [1] of the correlation matrix $\mathbf{C}$ written as

$$\mathbf{C} = \mathbf{U}\mathbf{\Sigma}\mathbf{V}^{*} \tag{2.50}$$

where $\mathbf{V}^{*}$ is the conjugate transpose of $\mathbf{V}$, $\mathbf{U}$ and $\mathbf{V}$ are unitary matrices whose columns are the eigenvectors of $\mathbf{C}\mathbf{C}^{*}$ and $\mathbf{C}^{*}\mathbf{C}$ respectively and $\mathbf{\Sigma} = diag(\sigma_1, \sigma_2, ..., \sigma_N)$, for σ_i is the i^{th} singular value of $\mathbf{C}$. Then, the pseudoinverse of the truncated $\mathbf{C}_\xi$, denoted by $\mathbf{C}_\xi^{-1}$, is expressed as

$$\mathbf{C}_\xi^{-1} = \mathbf{V}\mathbf{\Sigma}_\xi^{-\mathbf{1}}\mathbf{U}^{*} \tag{2.51}$$

where $\mathbf{\Sigma}_\xi^{-\mathbf{1}} = diag(1/\sigma_1, 1/\sigma_2, ..., 1/\sigma_\xi, 0, ..., 0)$, ξ is the truncation index. The truncation index defines the number of accepted singular values and further determines the quality of the correlation matrix $\mathbf{C}$. In other words, in the calculation of pesudoinverse of $\mathbf{C}$, TSVD filters out the elements in $\mathbf{\Sigma}^{-\mathbf{1}}$ that correspond to small singular values in $\mathbf{\Sigma}$ starting from ξ+1. Then, the TSVD estimate is expressed as

$$\hat{S}_{TSVD} = |\mathbf{C}_\xi^{-1}R| \tag{2.52}$$

where $|.|$ denotes slicing operation and R is the collected statistics. It is mentioned in [39] that αN of the singular values of $\mathbf{C}$ are larger than or equal to one while the rest $(1-\alpha)N$ of the singular values are close to zero. Therefore, the truncation index could be set around αN.

Hence, TSVD can optimize the ill conditioning of the SEFDM system, and obtain

[1] Assume a non-negative scalar σ and two non-zero vectors u and v that satisfy the following relations: $\mathbf{A}v = \sigma u$ and $\mathbf{A}^H u = \sigma v$ where $[.]^H$ stands for the Hermitian transpose and denotes the complex conjugate transpose of a complex matrix. Therefore, the σ is the singular value of matrix $\mathbf{A}$; u and v indicate two singular vectors of $\mathbf{A}$.

better performance than existing linear detection algorithms like ZF and MMSE. In fact, The complexity of TSVD is similar to ZF since it only requires a special inversion of the matrix which is aided by the SVD technique.

2.6.6 TSVD-FSD Hybrid Detector

The detection of SEFDM signal is still challenging. On one hand, linear detectors provide poor performance with low complexity. On the other hand, nonlinear detectors are capable of achieving attractive performance at the cost of complexity. Combining TSVD with FSD (TSVD-FSD) [39] is a scheme that can improve both the performance and reduce the complexity simultaneously. The hybrid detector has two stages, the first stage (TSVD) is a simple linear detector which facilitates the detection of the second-stage nonlinear detector (FSD). By using the improved initial estimates from the first detector, the performance of the second stage detector can be improved. Therefore, the hybrid detector is able to obtain improved performance with reduced complexity.

2.7 Other Spectrally Efficient Techniques

2.7.1 Fast Orthogonal Frequency Division Multiplexing (FOFDM)

FOFDM was firstly proposed in [21] as a wireless technique and then adopted in optical systems [126] [127] [128]. This multiplexing scheme packs sub-carriers closer than a typical OFDM. Specifically, the sub-carrier spacing in FOFDM is half of that in OFDM. However, the orthogonality property is still maintained at the cost that only one-dimensional modulation schemes can be employed. The FOFDM signal is expressed as

$$x(t) = \sum_{k=0}^{N-1} X[k] e^{j2\pi \frac{k}{2T} t} \tag{2.53}$$

where $X[k]$ is one-dimensional modulation symbols (e.g. BPSK or MASK) and N is the number of sub-carriers. The sub-carrier spacing equals $\frac{1}{2T}$ and the center frequency for each sub-carrier is defined as $\frac{k}{2T}$. Considering two arbitrary sub-carriers, hence, the

orthogonal characteristic is verified by using the following equations.

$$\begin{aligned} corr(m,n) &= \frac{1}{T}\int_0^T X[m]X[n](e^{j2\pi\frac{m}{2T}t})(e^{j2\pi\frac{n}{2T}t})^* dt \\ &= X[m]X[n]\{sinc[\pi(m-n)] + j\cdot\frac{\pi(m-n)}{2}\cdot sinc^2[\frac{\pi(m-n)}{2}]\} \end{aligned} \tag{2.54}$$

where its real and imaginary parts are shown in (2.55) and (2.56), respectively.

$$\Re\{corr(m,n)\} = \begin{cases} X[m]X[n] & m=n \\ 0 & m\neq n \end{cases} \tag{2.55}$$

$$\Im\{corr(m,n)\} = \begin{cases} 0 & m=n \\ \frac{\pi(m-n)}{2}\cdot sinc^2[\frac{\pi(m-n)}{2}] & m\neq n \end{cases} \tag{2.56}$$

It is emphasized here that (2.55) and (2.56) are derived provided that $X[m]$ and $X[n]$ are one-dimensional modulated symbols. The auto-correlation in (2.55) is not zero while the cross-correlation is zero indicating the real part satisfies the orthogonality requirement. However, it is not the case for the imaginary part as shown in (2.56) where its cross-correlation equals zero only when $m-n=2\lambda$ where $\lambda\in\mathbb{Z}$. In other words, the sub-carrier spacing should be a multiple of $\frac{1}{T}$ leading to the same spectral efficiency as OFDM. Therefore, for real modulation symbols like BPSK or MASK, after multiplying with a complex term that has a frequency separation being $\frac{1}{2T}$, only the imaginary part of the result is distorted. The real part can be used to transmit data without any distortions. For complex modulation symbols, by multiplying a complex term, both the real and imaginary part of the result will be distorted.

To sum up, this technique can achieve the same performance as OFDM with one-dimensional modulation scheme like BPSK or MASK. With the enlargement of modulation levels, performance is degraded significantly. Therefore, by transmitting the same amount of data, the spectral efficiency is doubled since 50% of bandwidth is saved. In terms of system design, the FOFDM can directly employ IFFT and FFT at

the transmitter and the receiver, respectively.

2.7.2 M-ary Amplitude Shift Keying (MASK)

A spectrally efficient technique termed MASK was proposed in [22] where it can save 50% of bandwidth similar to the FOFDM. In this work, the author revealed a theory that if the sub-carriers differ only in frequencies or amplitudes while their phases remain the same, then the minimum required frequency spacing for the orthogonality is $\frac{1}{2T}$. Therefore, only the real part of the sub-carriers is considered in order to maintain the orthogonality. According to [22], the MASK OFDM signal is expressed as

$$x(t) = \sum_{k=0}^{N-1} X[k] cos(2\pi \frac{k}{2T} t) \tag{2.57}$$

where $X[k]$ is one of the M-ary amplitudes and N is the number of sub-carriers. The sub-carrier spacing equals $\frac{1}{2T}$ and the frequency for each sub-carrier is defined as $\frac{k}{2T}$. The orthogonal characteristic of MASK is verified in (2.58).

$$\int_0^T X[i]X[j] cos(2\pi \frac{i}{2T} t) cos(2\pi \frac{j}{2T} t) dt = 0, \quad i \neq j \tag{2.58}$$

MASK can compress bandwidth by 50% with the limitation that only one-dimensional modulation scheme can be used. A real term instead of a complex one is used for the signal modulation as shown in (2.57) leading to the discrete cosine transform (DCT) and the inverse discrete cosine transform (IDCT) based signal generation and reception. Considering system flexibility and implementation, FOFDM is superior to MASK since an efficient IFFT and an efficient FFT can be directly used in the FOFDM.

2.7.3 Overlapped FDM (Ov-FDM)

Similar to SEFDM, the Ov-FDM [23] is also a technique to pack sub-carriers closer less than the required spacing in an OFDM leading to non-orthogonal located sub-carriers. In order to directly use the IDFT at the transmitter, the signal generation

in Ov-FDM is composed of two stages. The first stage employs a precoding technique while the second stage is a conventional IDFT. The reason for this separation is due to the violation of the orthogonality in Ov-FDM. The function of the precoding stage is to generate a manipulated input signal to the second stage IDFT so that the output signal from the IDFT occupies less bandwidth. This is different compared with the signal generation in SEFDM since only one stage IDFT is required in SEFDM with a minor architecture modification. Furthermore, at the receiver, the signal detection is realized by using the optimal detector termed maximum likelihood sequence detection (MLSD) whose complexity increases exponentially. However, in SEFDM, simple linear detectors or their hybrid detectors are used as presented in section 2.6 where they all have much lower complexity than the detectors used in Ov-FDM. In addition, it is noted that the Ov-FDM is only applicable to small size systems (i.e. small number of sub-carriers) while the SEFDM can work with a large number of sub-carriers, which will be introduced in the following sections.

2.7.4 Faster Than Nyquist Signalling (FTN)

The concept of faster than Nyquist signalling was proposed by Mazo in 1975 [20]. Assuming the time period of one FTN symbol is T, in a typical Nyquist rate satisfying system, the symbol spacing is set to be T in order to avoid inter symbol interference (ISI). However, in FTN, the symbol spacing can be reduced to 0.802T (i.e. transmission faster than Nyquist rate by 25%) without any performance degradation. Recently, this idea is combined to multicarrier systems and a multicarrier FTN scheme was presented in [25]. SEFDM improves spectral efficiency by compressing bandwidth, while FTN violates Nyquist criteria, transmitting data faster than the Nyquist limit, to achieve spectrally efficient purpose. Thus, it is a time-domain technique and may be considered the dual of SEFDM. Since adjacent symbols are no longer orthogonal, the signal generation becomes challenging. An FTN transmitter was reported in [129] where an IFFT working together with an FTN mapper is applied to generate the

FTN symbols. The function of the mapper is to project the non-orthogonal symbols onto orthogonal basis functions, thus requiring the reservation of a number of sub-carriers and time domain symbols (instances) leading to a reduction in the spectral efficiency [129]. At the receiver, work in [129] introduced an iterative decoder for a 128 sub-carrier FTN system. This iterative scheme successively cancels interference caused by non-orthogonal packed symbols and sends the interference cancelled symbols to a channel decoder for data recovery. Its corresponding hardware implementation can be found in [130] [131]. It should be noted that the complexity, in terms of real hardware implementation, is much higher than an equivalent OFDM system. Inside the FTN decoder, the FTN mapper and the matched filter are the two components that consume more than 50% of the hardware resources in a 65 nm CMOS implementation. In particular, the resource consumptions of the receiver isotropic orthogonal transform algorithm (IOTA) filter and the matched filter outside the FTN decoder have not yet been taken into consideration. Numerical comparisons of SEFDM and FTN will be given in the following section.

2.7.5 Time Frequency Packing (TFP)

Time frequency packing (TFP) [26] is a technique to improve spectral efficiency in both time-domain and frequency-domain. This technique packs non-orthogonal overlapping sub-carriers and reduces spacing between adjacent transmitted symbol simultaneously. In other words, this technique is a combination of SEFDM and FTN. Its signal detection is assisted by using the low density parity check (LDPC) [132] code with an iterative scheme.

2.7.6 5GNOW (GFDM, FBMC, UFMC)

5GNOW (5^{th} generation non-orthogonal waveforms for asynchronous signalling) is an European collaborative research project supported by the European Commission within FP7 ICT Call 8. The 5GNOW aims to investigate alternative waveforms to replace the

existing LTE and LTE-Advanced. A general introduction of 5GNOW and its research achievements can be found in [4].

- **Filter Bank Multicarrier (FBMC)**

  In a conventional OFDM system, the signal is shaped using a rectangular window in time-domain resulting in a sinc shaped sub-carrier in frequency-domain. Thus, the spectral leakage of one sub-carrier introduces interference to adjacent frequency bands. Filter bank multicarrier (FBMC) [17] is an alternative technique to the conventional OFDM. It has the ability to remove out-of-band radiation to avoid harmful interference to adjacent channels by using a pulse shaping scheme on each sub-carrier. However, due to the use of pulse shaping, crosstalk from the in-phase and quadrature tributaries is introduced between adjacent sub-carriers [133]. Therefore, in FBMC, the real and imaginary parts of QAM complex symbols are separated by delaying the imaginary branch of a QAM symbol by half of symbol duration before passing through the pulse shaping filter. This approach is termed offset-QAM (OQAM) [133][134]. However, by using this modulation scheme, IFFT cannot be directly applied. Work in [135] proposed a scheme that an IFFT is applied to the real part at time kT_Q and the imaginary part at time $(k + 1/2)T_Q$ where T_Q is the duration of one QAM symbol period. FBMC is suitable for the cognitive radio, spectrum fragmentation or carrier aggregation scenarios since out-of-band interference has been significantly filtered out in FBMC.

- **Generalized Frequency Division Multiplexing (GFDM)**

  This algorithm is developed on the basis of FBMC. GFDM [19][136][137] reduces out-of-band radiation by using pulse shaping on each sub-carrier. Therefore, the sidelobe interference is mitigated. The utilization of pulse shaping at the transmitter results in non-orthogonal sub-carriers which causes self-created ICI. Noticing that the OQAM modulation scheme is adopted in FBMC to get rid

of ICI. However, in GFDM, a conventional QAM modulation is employed. The solution to eliminate ICI in GFDM is to use interference cancellation techniques.

- **Universal-Filtered Multicarrier (UFMC)**

  The aforementioned filtered techniques are defined according to different filtering locations. A filtered OFDM indicates a filtering operation over an entire frequency band; the filtering of FBMC or GFDM is done on each sub-carrier. For UFMC [18][138], combining advantages from OFDM, FBMC and GFDM, the filtering of UFMC is performed on each sub-band which comprises multiple sub-carriers. This scheme can suppress spectral leakage for one resource block (each RB consists of 12 sub-carriers). Since in both FBMC and GFDM, filtering operations are managed on each sub-carrier, therefore, the frequency response of the filter needs to be very tight leading to a long filter length compared to the length of one symbol. In the case of burst data transmission, the spectra of FBMC and GFDM requires long ramp up and ramp down areas resulting in an impractical implementation in the real world. However, the filter length in UFMC would be shorter than that of FBMC and GFDM due to the larger sub-band bandwidth.

2.7.7 Non-Orthogonal Multiple Access

SEFDM is a non-orthogonal waveform technique which provides an improved spectral efficiency. In addition, the non-orthogonal concept can be applied for multiple access scenarios such as sparse code multiple access (SCMA), non-orthogonal multiple access (NOMA) and multi-user shared access (MUSA). These techniques can superimpose signals from multiple users in code-domain or power-domain to enhance the system access performance.

NOMA [28] is a non-orthogonal multiple access scheme in the power domain. Multiple users are superimposed with different power gains and separated via a successive interference cancellation (SIC) detector at the receiver.

MUSA [29] is an advanced multi-carrier code division multiple access (MC-CDMA) which allows multiple users to transmit at the same time and frequency. Unlike the typical code division multiple access (CDMA) spreading sequence, MUSA employs non-orthogonal complex spreading sequences at the transmitter to modulate signals of each user leading to a denser deployment of existing resources. At the receiver, an advanced SIC detection algorithm is operated to remove the interference and recover each user's data.

SCMA [27] is a sparse multiple access modulation scheme, which takes advantage of CDMA and low density spreading sequence. It should be noted that each user has its dedicated codebook.

All the mentioned non-orthogonal multiple access schemes are at the multiuser scheduling level which intends to non-orthogonally superimpose multiple existing orthogonal waveforms (e.g. OFDM) from different users. On the other hand, SEFDM is a non-orthogonal waveform scheme. Therefore, by non-orthogonally superimposing several non-orthogonal SEFDM waveforms will further improve spectral efficiency. This requires a joint design of waveforms and multiple access schemes.

2.8 Conclusions

At the beginning of the chapter, basic concepts of SEFDM modulation and demodulation are introduced. Since self-created ICI is introduced in SEFDM, a standard IFFT/FFT cannot be used directly. The extended single IFFT/FFT is investigated with the design dependence on the value of α and the number of sub-carriers. Then, a multiple IFFT/FFT architecture which is proven to be the best practical solution in terms of performance and complexity is presented. At the receiver, the orthonomalization techniques which project received samples on a set of orthonormal vectors are presented. However, this technique is too complicated and performance is constrained

by α values and the number of sub-carriers. In particular, the self-created ICI is analyzed and CIR is derived with its comparison with typical OFDM signals. Furthermore, several existing detectors are described with performance/complexity analysis. Results indicate that all the existing detection algorithms are too complex for practical large size SEFDM systems. This reveals the importance of a simple but good performance detector. Finally, other spectrally efficient technologies are presented with descriptions of their advantages and limitations. The following chapters will address new detector designs and novel practical system architectures for SEFDM.

Chapter 3

Advanced SEFDM Transceiver Designs

3.1 Introduction

The key challenge arises in SEFDM relates to the self-created interference which gives rise to ICI. This interference is caused by the deliberate violation of the orthogonality rule defined for OFDM, which requires the frequency spacing to equal the reciprocal of the OFDM symbol period. Thus, the detection of SEFDM becomes more complicated. When the signal dimension is small (e.g. small number of sub-carriers or low order modulation order), exhaustive search can be operated to achieve the ML performance, at the expense of increase in detector complexity. A complexity reduced algorithm termed SD, constrained by a searching sphere, has been studied. Its random complexity is highly dependent on the noise level leading to unpractical use. In addition, several hybrid detectors with fixed complexity have been studied as well, although performance far from optimal.

In Chapter 2, it was shown that SEFDM receiver performance is dependent on obtaining good initial estimates of the data symbols before hard detection. Such initial estimates are obtained from linear detectors like ZF, MMSE and TSVD. However, these

are all limited by the noise level leading to unsatisfactory performance.

To sum up, previous detection algorithms are either too complicated for large size systems or results in unsatisfactory performance. Thus, this chapter aims to find out solutions for novel signal detector or system architecture designs.

3.2 Iterative SEFDM

In this section, an iterative soft demapping detection scheme termed iterative detection (ID) [52] [56] is introduced for the sake of iteratively cancelling the ICI and obtaining more accurate initial estimates. Following this, a hybrid soft ID together with FSD [139] which yields good complexity/performance trade-offs as a practical alternative to optimal ML and sub-optimal SD detections is investigated. The performance of square QAM modulation constellations from 4QAM up to 16QAM are evaluated. With the introduction of more accurate initial estimate from the ID detector, the overall performance will be obviously improved.

3.2.1 Iterative Detector (ID)

Notation : The tree width is denoted by T_W and v denotes the number of iterations. Matrices are denoted by bold uppercase letters, italic letters represent column vectors.

In our work [52], ID has been verified to have better immunity against interference. SEFDM signals are not only contaminated by AWGN, but also are distorted by complex interference which is described by a matrix (e.g. correlation matrix $\mathbf{C}$). Since the effects of ICI and AWGN are random, some symbols are severely interfered while others are less affected. Therefore, the main idea of ID is to firstly decide less interfered symbols and then recover the highly distorted symbols on the basis of the decided ones. The interference is removed gradually after each iteration. 4QAM was considered in work [52] yielding an error performance identical to the optimum scenario for 20% bandwidth savings. High order modulation format (e.g. 16QAM) is able to offer high spectral efficiency, however, these may be considerably less resilient to noise and interference.

This iterative interference cancellation scheme is aided by using an iterative M-QAM demapping strategy which is shown in Fig. 3.1.

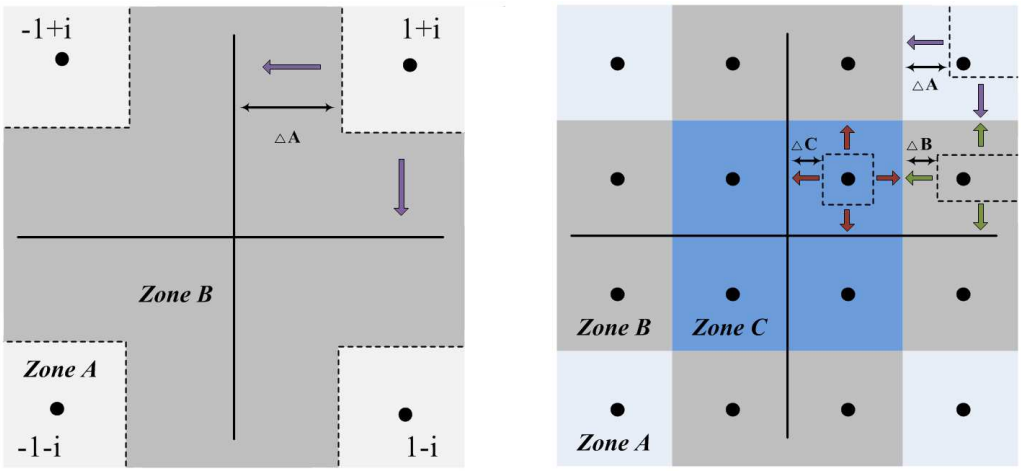

Figure 3.1: Demapping strategy for 4QAM constellation (left) and 16QAM constellation (right).

3.2.1.1 4QAM Iterative Demapping

4QAM demapping strategy is demonstrated in Fig. 3.1(left). Zone A is less susceptible to interference compared with zone B. If received symbols are within zone A, the decision of this point can be made directly. The uncertainty interval is defined by $\Delta A = 1 - m/v$, where m is the m^{th} iteration and v is the total iteration number. Only points that fall in zone A can be mapped directly to the corresponding constellation point. Points within zone B are unchanged and left to the next iteration. The interval is reduced gradually until zero in the iteration process, meaning that the effect of ICI has been cancelled. The iterative operation is shown below:

$$S_n = R - (\mathbf{C} - \mathbf{e})S_{n-1}, \tag{3.1}$$

where $\mathbf{e}$ is an $N \times N$ identity matrix, S_n is an N-dimensional vector of recovered symbols after n iterations and S_{n-1} is an N-dimensional vector of estimated symbols after $n-1$ iterations.

3.2.1.2 16QAM Iterative Demapping

In the case of 16QAM constellation, the fact that each symbol carries more bits than 4QAM makes it more difficult to demap accurately the symbols to the corresponding constellation. It is clearly seen from Fig. 3.1(right) that the whole constellation is divided into three different zones: zone A, zone B and zone C. Depending on zone a received symbol is located in, a different strategy should be employed to complete the demapping process. These are described below:

• Zone A: This zone is less susceptible to interference since only two constellation points are adjacent and directly influence the decision. Therefore, this zone should be firstly detected. The demapping strategy in this zone is very similar to that in 4QAM scheme, and the interval ΔA is set to be $1 - m/v$.

• Zone B: The interference sources of this zone come from three constellation points and thus the decision bound is set to be more rigorous. In the figure, the decision area is delimited by two horizontal and one vertical boundaries. Only points within these three boundaries are decided while other points are unreliable and reserved to the next iteration. The uncertainty interval in this zone is defined by $\Delta B = 1 - m/v$ and this criteria value is decreased in each iteration.

• Zone C: This zone is under serious interference because it is surrounded by four points. In this case, two horizontal and two vertical boundaries are added to constrain the decision area. $\Delta C = 1 - m/v$ defines the uncertain interval and decreases to zero in the last iteration.

3.2.2 Hybrid Detector (ID-FSD)

Although ID alone can effectively remove distortions through the iterative scheme, its performance can be further improved by cooperating with a second detector. This hybrid scheme is derived from TSVD-FSD where TSVD provides initial estimates to FSD which executes a more accurate signal detection. In fact, either FSD or SD can be used as the second stage detectors. However, SD is dependent on the noise level leading

to a random complexity. Therefore, in order to improve further the performance of the system and maintain relatively low and fixed complexity, a hybrid detector combining ID and FSD is proposed. The FSD algorithm simplifies ML computational effort and fixes the complexity of SD by restricting the search within a limited sub-space. Details are described in section 2.6.3. At each level, a fixed number of candidates are reserved. Fig. 3.2 depicts a block diagram for the iterative detection-FSD (ID-FSD) detector. The detailed description of each block is given in the following.

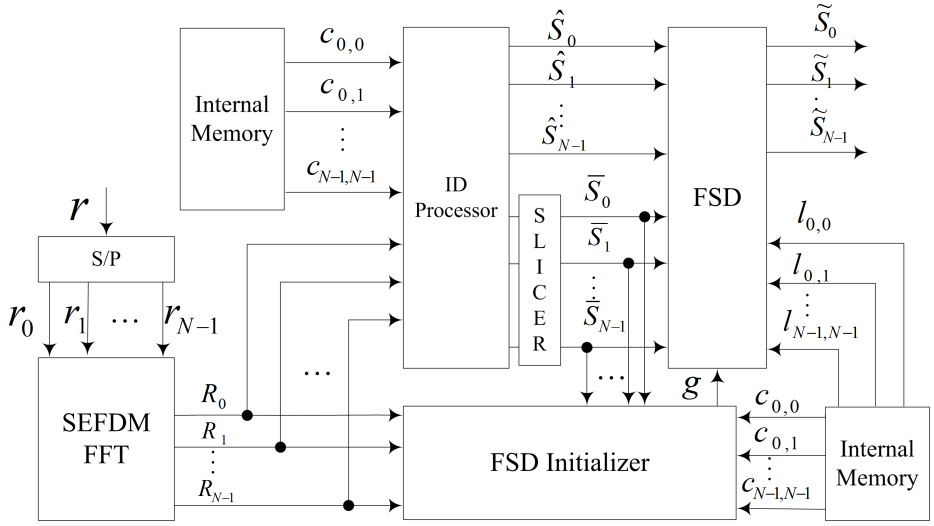

Figure 3.2: Block diagram of ID-FSD detector.

1. **ID-Processor**

   This block aims to realize the iterative function as expressed in (3.1). R is an N-dimensional vector of collected statistics derived from the FFT module. $\hat{S}$ is an N-dimensional vector of unconstrained estimated symbols which are referred to S_n at the last iteration in (3.1). Meanwhile, $\hat{S}$ is rounded or sliced to the closest integer, thus defines an N-dimensional vector of constrained estimated symbols $\bar{S}$ through the SLICER (i.e. hard decision) module. It should be noted that at the first iteration, S_1 equals R leading to inaccurate estimate due to contamination from ICI and AWGN. In the condition of small effects, they can be compensated

by ID alone while for higher ICI and noise level, a cooperative detection with FSD is required.

2. **FSD-Initializer**

   This block is responsible for generating initial radius g_{ID} which determines the size of the search sphere, as in the equation below

$$g_{ID} = \left\| R - \mathbf{C}\bar{S} \right\|^2 \tag{3.2}$$

   where $\|.\|$ denotes the Euclidean norm. The initial radius equals the distance between the collected statistics and the initial constrained estimate $\bar{S}$. Due to the ill conditioning of the SEFDM system, these initial estimates may deviate greatly from the optimal points. TSVD was previously applied in [39] to cope with this problem. However, the improvement was limited. Therefore, the contribution of ID for this module is that a more accurate initial estimate is adopted in (3.2) to calculate an improved initial radius.

3. **FSD**

   FSD has been fully explained in section 2.6.3. In this section, in order to demonstrate clearly the performance of ID initial estimate in the FSD detector, a brief re-introduction of FSD is described here. The FSD implements the SEFDM detection algorithm using equation:

$$\tilde{S}_{ID-FSD} = \arg \min_{\tilde{S} \in O^N, \tilde{S} \in M} \left\| R - \mathbf{C}\tilde{S} \right\|^2 \leq g_{ID} \tag{3.3}$$

   where $\tilde{S}$ indicates final detected symbols, O is the constellation cardinality, M is the search subspace and g_{ID} is the initial radius transferred from FSD-Initializer. If finally no node is found within the sphere, the ID constrained estimate $\bar{S}$ is

taken as the solution, as expressed in the equality below:

$$\tilde{S}_{ID-FSD} = \bar{S} \tag{3.4}$$

This is the reason why the design contains a feed of the constrained estimates from the ID-Processor to the FSD block. In order to simplify the squared Euclidean norm calculation, equation (3.3) can be transformed into an equivalent expression using Cholesky Decomposition. The transformation is carried out using $chol\{\mathbf{C}^*\mathbf{C}\} = \mathbf{L}^*\mathbf{L}$ [39], where $\mathbf{L}$ is an $N \times N$ upper triangular matrix. Hence, following the similar transform principle in (2.33) where the ZF initial estimate P is replaced by the ID initial estimate $\hat{S}$ in this case, (3.3) can be re-written as

$$\tilde{S}_{ID-FSD} = \arg \min_{\tilde{S} \in O^N, \tilde{S} \in M} \left\| \mathbf{L}(\hat{S} - \tilde{S}) \right\|^2 \leq g_{ID} \tag{3.5}$$

4. **Internal Memory**

   The correlation matrix $\mathbf{C}$ is fixed as long as the value of α and the number of subcarriers N are defined. Therefore, the elements of $\mathbf{C}$ and Cholesky decomposition elements of $\mathbf{C}$ are stored in this block. Two identical Internal Memory modules are placed in Fig. 3.2 for the sake of system demonstration. $c_{m,n}$ are the elements of $\mathbf{C}$ and are used for calculating the initial radius in (3.2) and initial estimates in (3.1). $l_{m,n}$ denotes the elements of the upper triangular matrix $\mathbf{L}$ and are used for calculating squared Euclidean norm in (3.5).

Finally, a summary of the operation of the ID-FSD is described in a mathematical format in Algorithm 1.

3.2.3 Performance and Complexity Evaluations

In this section, the performance and complexity of the proposed detector are evaluated via simulations. For the purpose of verifying the functionality, simulations were carried

out in an AWGN channel, and the iteration number is represented by v, N denotes the number of sub-carriers and T_w indicates the search tree-width.

Algorithm 1 : Hybrid ID-FSD Detection.

$[\hat{S}, \bar{S}] \Leftarrow ID(R, \mathbf{C}, \mathbf{e}, v)$;
$\bar{S} = R$;
for $m = 1$; $m \leq v$; $m++$ **do**
  $\hat{S} = R - (\mathbf{C} - \mathbf{e})\bar{S}$;
  $[\bar{S}] \Leftarrow Soft\ Demapping(\hat{S}, d)$;
  $d = 1 - \frac{m}{v}$;
  $\hat{S}_{\Re} = Real(\hat{S})$, $\hat{S}_{\Im} = Imag(\hat{S})$;
  if $\hat{S}_{\Re} > d$ & $\hat{S}_{\Im} > d$ **then**
    $\bar{S} = 1 + i$;
  else if $\hat{S}_{\Re} > d$ & $\hat{S}_{\Im} < -d$ **then**
    $\bar{S} = 1 - i$;
  else if $\hat{S}_{\Re} < -d$ & $\hat{S}_{\Im} > d$ **then**
    $\bar{S} = -1 + i$;
  else if $\hat{S}_{\Re} < -d$ & $\hat{S}_{\Im} < -d$ **then**
    $\bar{S} = -1 - i$;
  else
    $\bar{S} = \hat{S}$;
  end if
end for
$[\tilde{S}] \Leftarrow FSD(\hat{S}, \bar{S})$;
$chol\{\mathbf{C}^*\mathbf{C}\} = \mathbf{L}^*\mathbf{L}$;
$D = \left\|R - \mathbf{C}\tilde{S}\right\|^2 = \left\|\mathbf{L}(\hat{S} - \tilde{S})\right\|^2$;
$\tilde{s}_n = [1 + i, 1 - i, -1 + i, -1 - i]$;
$d = 0$;
for $m = N$; $m \geq 1$; $m--$ **do**
  $d_0 = d$;
  for $n = N$; $n \geq m$; $n--$ **do**
    $d = l_{m,n}(\hat{s}_n - \tilde{s}_n) + d$;
  end for
  $d = d^2 + d_0$;
  if $length(d) > T_W$ **then**
    $d = Sort[d]$;
  else
    $d = d$;
  end if
end for
$AED = min[d]$;
$g_{ID} = \left\|R - \mathbf{C}\bar{S}\right\|^2$;
if $AED \leq g_{ID}$ **then**
  $\tilde{S}_{ID-FSD} = \tilde{S}$;
else
  $\tilde{S}_{ID-FSD} = \bar{S}$;
end if

3.2.3.1 Performance

The convergence behaviours of ID detection algorithm in terms of 4QAM and 16QAM modulation schemes are shown in Fig. 3.3 and Fig. 3.4, respectively. The bandwidth compression factor for the aforementioned systems is set to α=0.8. Meanwhile, the theoretical results for 4QAM and 16QAM are also plotted for the sake of comparison. For 4QAM modulation format, Fig. 3.3 shows that ID doesn't work properly with small iteration numbers. However, with the increase of iteration numbers, ID yields great BER performance improvement and converges to the theoretical one when v=20. But 1dB performance loss is observed even with such a large iteration number. Then, performance of ID is examined for 16QAM with different iterations ranging from 2 to 20. Simulation results indicate that after 20 iterations, the performance of ID converges and no further improvement could be obtained. Unlike 4QAM modulation format, it is still far away from the theoretical 16QAM result. On the basis of the aforementioned

analysis, in the following simulations, the default iteration number is set to 20.

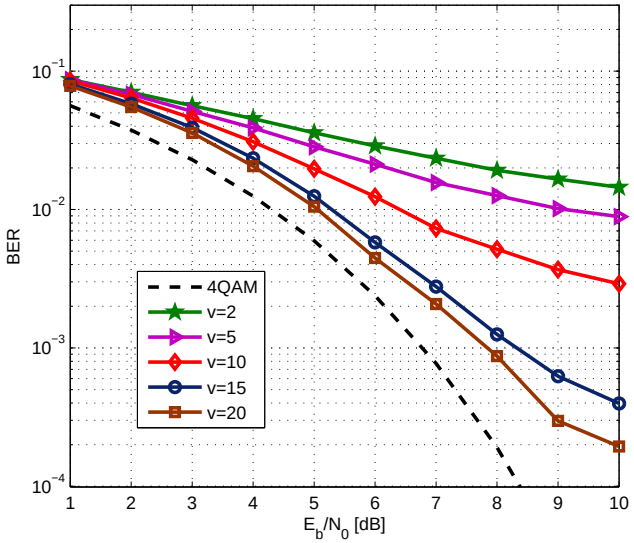

Figure 3.3: Convergence behaviour of ID detector for α=0.8 4QAM with various iterations and N=16.

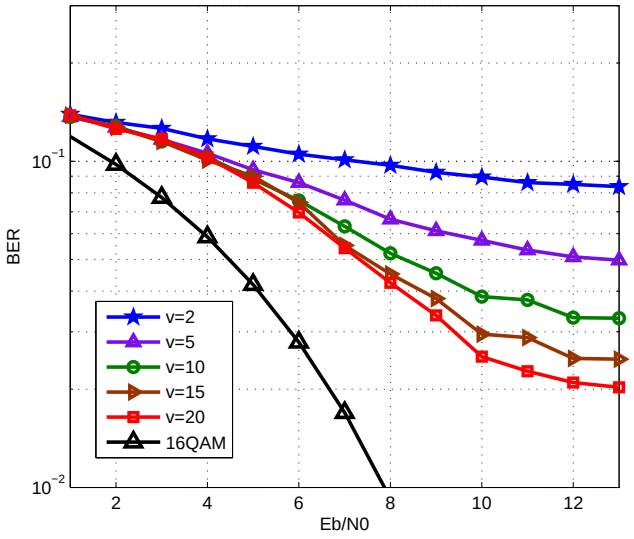

Figure 3.4: Convergence behaviour of ID detector for α=0.8 16QAM with various iterations and N=16.

Fig. 3.5 and Fig. 3.6 investigate the performance of ID under different bandwidth compressions. Both figures compare results with TSVD and theoretical curves. Fig. 3.5 depicts 4QAM results. It is evident that ID detector outperforms TSVD detector dramatically under various bandwidth compression factors. ID with α=0.7 is even better than TSVD with α=0.8. This proves that ID has a better immunity against interference. Specifically, for α=0.8, the performance gap between ID and the theoretical one is only 1 dB. However, the difference is not significant for 16QAM as illustrated in Fig. 3.6. When Eb/N0 reaches a certain value, no further improvements are observed for both ID and TSVD. An error floor occurs after Eb/N0=12 dB. It is inferred from the figure that 16QAM cannot converge to the theoretical result because of the more severe interference introduced from adjacent symbols. The increase of constellation density expectedly leads to the performance loss.

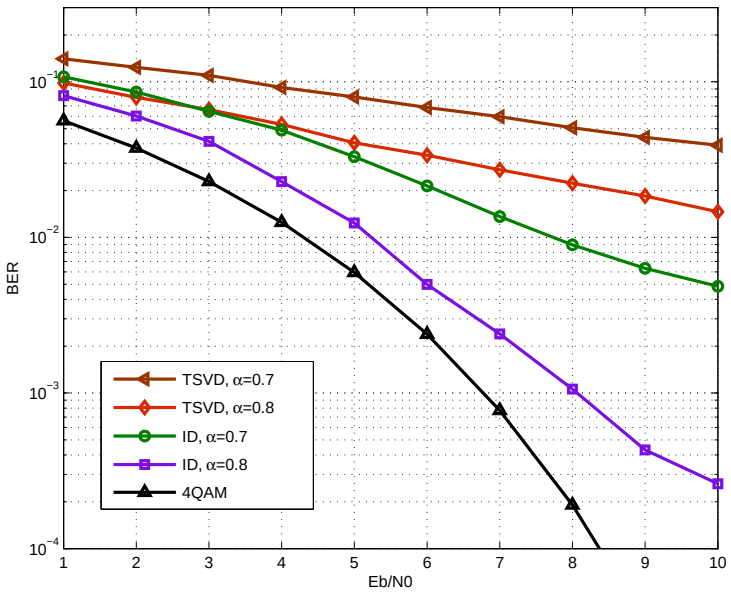

Figure 3.5: BER performance of ID detector for SEFDM systems with 16 sub-carriers carrying 4QAM with 20 iterations.

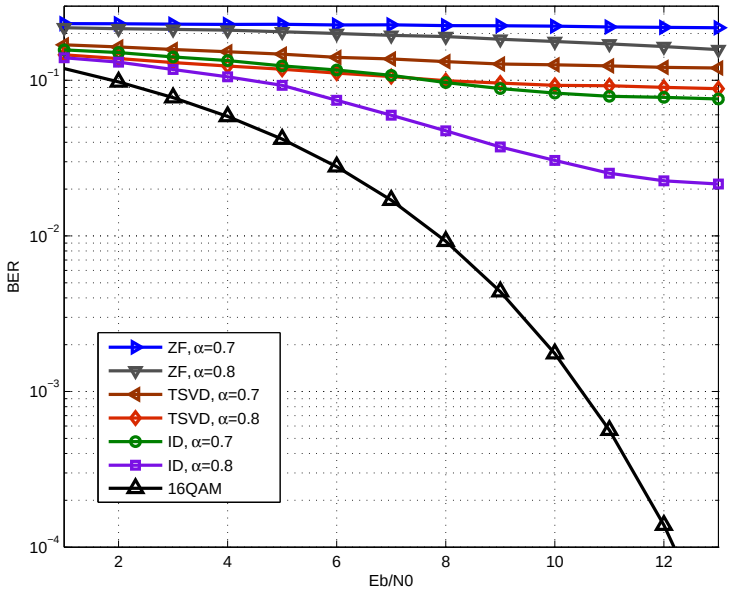

Figure 3.6: BER performance of ID detector for SEFDM systems with 16 sub-carriers carrying 16QAM with 20 iterations.

Fig. 3.7 and Fig. 3.8 illustrate the BER performance of hybrid detectors under two modulation schemes. In terms of 4QAM, we can see that the ID-FSD detector yields substantial BER reduction compared to TSVD-FSD due to the better quality of ID estimate fed to the ID-FSD detector. In the high E_b/N_o regime, for bandwidth compressions of up to 20% (α=0.8) [percentage of saving=$100 \times (1-\alpha)\%$], the ID-FSD curve approaches the theoretical 4QAM one. This proves the Mazo's theory [20] of 25% [percentage of excess=$100 \times (1/\alpha - 1)\%$] in SEFDM. In addition, there is 1 dB deviation from the theoretical performance in the low SNR regime. This is due to the performance loss from ID detection shown in Fig. 3.5. In terms of 16QAM, for bandwidth saving up to 20%, ID-FSD outperforms TSVD-FSD and ZF-FSD by 1.6 dB, which proves the proposed hybrid detector is applicable to the high order modulation scheme. However, with further compressing bandwidth to 30% ($\alpha = 0.7$), the curve of ID-FSD is close to that of TSVD-FSD and ZF-FSD, which is an expected result since higher constellation density indicates higher interference, and ID is unable to remove

such high interference. To sum up, ID-FSD outperforms conventional hybrid detectors significantly in the low order modulation scheme. In addition, it is applicable to the high order modulation scheme while its capability of removing interference is limited.

It is evident in Fig. 3.7 that ID-FSD outperforms TSVD-FSD with almost 2 dB performance gain. Meanwhile, according to the conclusion derived from section 2.6.3, the tree-width determines the performance of FSD. However, the higher value of tree-width, the higher complexity a detector requires. Therefore, in Fig. 3.9, different tree-width scenarios are tested for ID-FSD and TSVD-FSD. Fig. 3.9 shows that the much lower complexity ID-FSD detector with T_W=16 has a very close performance to that of the TSVD-FSD detector with T_W=1024. Such result is highly encouraging for achieving high performing SEFDM detection with realistic complexity. The complexity issue is further explored in the next section.

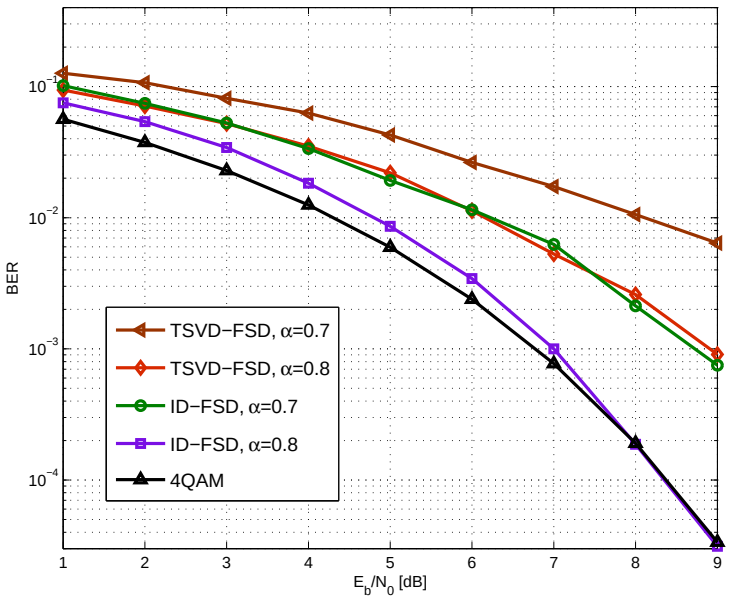

Figure 3.7: BER performance of ID-FSD detector for 16 sub-carrier SEFDM system carrying 4QAM with 20 iterations and T_W=16.

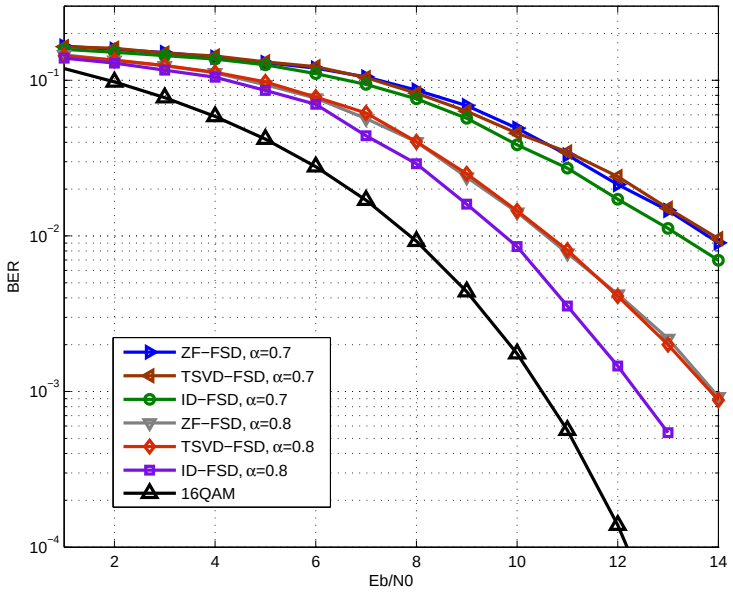

Figure 3.8: BER performance of ID-FSD detector for 16 sub-carrier SEFDM system carrying 16QAM with 20 iterations and T_W=16.

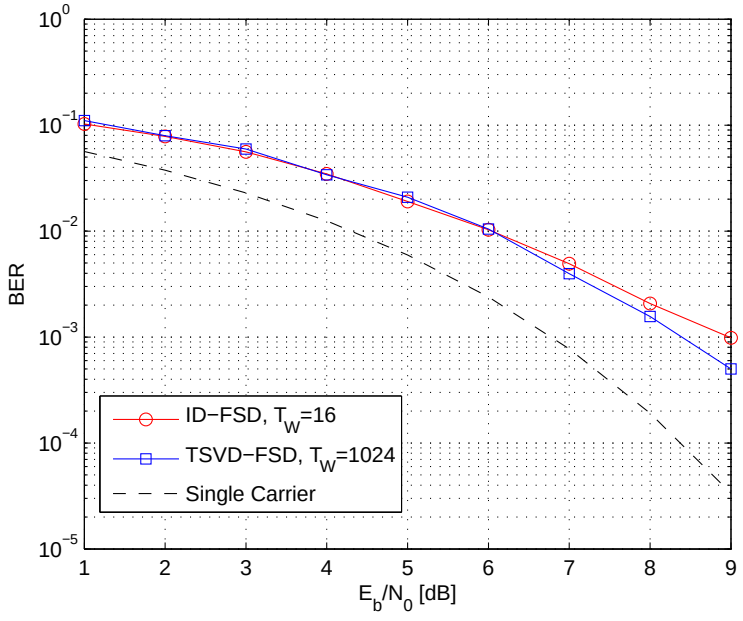

Figure 3.9: BER performance for different detectors carrying 4QAM symbols for N=16 , υ=20, α =0.7 and different tree-widths.

3.2.3.2 Complexity

We demonstrate the computational complexity in terms of real-valued multiplications and real-valued additions. For this we consider operations for detecting each symbol, not the operations required only once in the detection process (e.g. SVD for the correlation matrix $\mathbf{C}$). On the premise of practical implementation, the ID requires only one iteration calculation due to the iterative property at the cost of longer processing latency. The complexity of ID is calculated based on (3.1) while TSVD is derived by direct matrix inversion. Detailed representation of complexities are summarised in Table 3.1. It can be seen that in the case of one iteration, the required operations of ID are slightly lower than that of TSVD.

Table 3.1: Computational complexity in terms of real-valued operations for TSVD and ID

	TSVD	ID (one iteration)
Number of multiplication operations	$4N^2$	$4N^2 - 2N$
Number of addition operations	$4N^2 - 2N$	$4N^2 - 2N$

The process of FSD follows equation (3.5) where the Euclidean norm can be decomposed into two parts leading to a new expression defined as (3.6). The first part is partial Euclidean distance (PED) denoted as d_i and the second part is accumulated Euclidean distance (AED) denoted as D_{i+1}. Due to the sequential nature of FSD, unlike the SD algorithm where radius is updated at each level, FSD computes the partial Euclidean distance at each level from the top level N backward to the first level. At the last stage, the accumulated Euclidean distance D_1 is obtained and compared with the initial radius.

$$D_i = l_{i,i}^2(\xi_i - \tilde{S}_i)^2 + \sum_{j=i+1}^{N} l_{j,j}^2(\xi_j - \tilde{S}_j)^2 = d_i + D_{i+1} \tag{3.6}$$

$$\xi_i = \hat{S}_i + \sum_{j=i+1}^{N} \frac{l_{i,j}}{l_{i,i}} (\hat{S}_j - \tilde{S}_j) \tag{3.7}$$

The complexity analysis of FSD is relatively complicated. At the first $\omega = \log_2 T_W$ levels, all the nodes are fully expanded and searched, while the remaining levels are partially expanded and only T_W nodes are reserved. This is an obvious advantage of FSD over a full search since FSD fixes the throughput and makes it more practical. In addition, a sort unit is employed at each level. It should be noted that at the first ω levels, no sorting operations are needed. However, in the rest of levels, these units are required. Assuming that one comparison in a sort unit takes one addition operation, based on (3.6)(3.7), the complexity expressions in terms of real-valued operations are directly given in (3.8) and (3.9). The complexity is analyzed in our previous work in detail in [52] and practically demonstrated in [49].

$$C_{mult} = \underbrace{\sum_{n=1}^{\omega} 2^n [2n+1]}_{full\ expansion} + \underbrace{\sum_{m=\omega+1}^{2N} T_W [2m+1]}_{partial\ expansion} \tag{3.8}$$

$$C_{add} = \underbrace{\sum_{n=1}^{\omega} 2^n [2n-1]}_{full\ expansion} + \underbrace{\sum_{m=\omega+1}^{2N} T_W [2m-1]}_{partial\ expansion} + \underbrace{4T_W^2 (2N-\omega)}_{sort} \tag{3.9}$$

Table 3.2 shows the normalised delay comparison of both ID-FSD and TSVD-FSD detectors. Assuming both ID-FSD (N=16,υ=20) and TSVD-FSD (N=16) employ parallel and pipelined structures. Regarding the initial delay, ID-FSD consumes 19 more clock cycles than TSVD-FSD. In terms of the pipelined delay, both schemes consume one clock cycle.

Figure 3.10 illustrates the Matlab execution time of different detectors and for various iterations and tree-widths. We use the execution time to compare the relative complexity of detectors. This complexity figure is generated assuming TSVD-FSD

Table 3.2: Delay Comparisons (normalised values)

	TSVD	ID	FSD
Initial Delay(Clock Cycles)	1	υ	N
υ=20,N=16	1	20	32
Pipelined Delay(Clock Cycles)	1	1	1

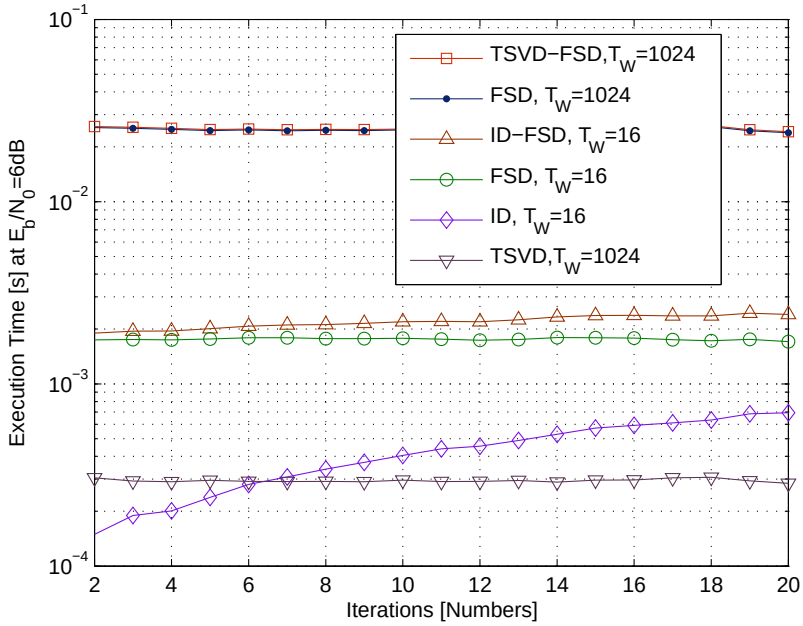

Figure 3.10: Execution Time versus iteration numbers for different SEFDM detectors carrying 4QAM symbols with $\alpha = 0.7$, N=16 and different tree-widths.

achieves the same performance with ID-FSD as illustrated in Fig. 3.9. It is apparent that the new ID-FSD detector, even with a very high number of iterations, always displays execution time one order of magnitude lower than its TSVD-FSD counterpart. This trend is consistent with the absolute numbers of Table 3.1 and equations (3.8) and (3.9). It is evident that the TSVD-FSD detector needs more computational operations than the ID-FSD detector. As a result, the ID-FSD detector takes significantly less time than the TSVD-FSD detector to complete a detection.

3.3 Block-SEFDM

In section 3.2, we examined a novel hybrid soft ID together with FSD [52] which yields much better complexity/performance trade-offs than the TSVD-FSD detector. Unfortunately, this detector is only suitable for small size systems. In realistic multicarrier systems, in order to combat with multipath fading, a large number of sub-carriers (i.e. FFT size) are preferred such as 512 in 802.11ac [140] and 2048 in LTE [1]. Thus, a simplified detector for a non-orthogonal system with a large signal dimension is highly desirable. In this section, we present a multi-band system termed Block-SEFDM [57] which divides the whole spectrum into several blocks. Symbols in each block can be detected separately by using powerful ML or SD algorithms. This technique makes it practical to detect large size non-orthogonal signals (e.g. 128 non-orthogonal sub-carriers).

3.3.1 System Model

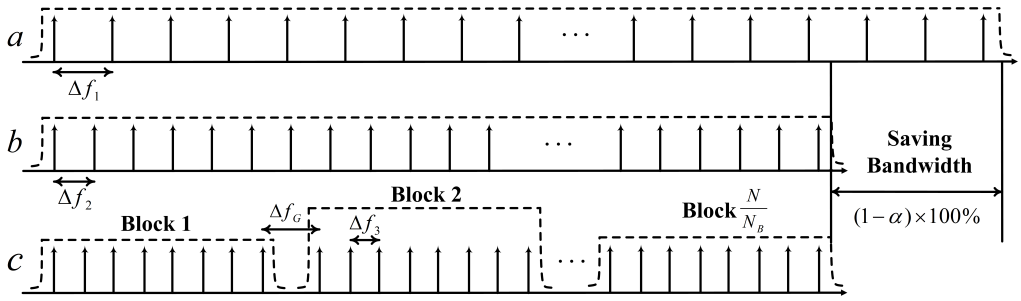

Figure 3.11: Spectra illustration for a) OFDM, b) SEFDM, c) Block-SEFDM. Each impulse indicates one sub-carrier and there are overall N sub-carriers for each system, respectively.

The general comparison between OFDM, typical SEFDM and Block-SEFDM are shown in Fig. 3.11. Fig. 3.11 (a) demonstrates a typical OFDM spectrum where the sub-carrier spacing Δf_1 equals $\frac{1}{T}$ where T is the time period of one OFDM symbol. Fig. 3.11 (b) shows a typical SEFDM system with sub-carrier spacing $\Delta f_2 = \frac{\alpha}{T}$ where $\alpha < 1$ is the bandwidth compression factor. It is apparent that the SEFDM system can

save $(1-\alpha)\times 100\%$ of bandwidth compared to a typical OFDM system. The typical SEFDM signal is straightforwardly detected using a single detector due to the single band feature. However, this kind of detector is limited by the system size. In order to simplify the detector design and maintain the system performance, multiple parallel shorter (small size) detectors are desirable. On the basis of this idea, Block-SEFDM divides the original SEFDM spectrum into several non-orthogonal blocks where a short detector is adopted in each block. The principle of Block-SEFDM is illustrated in Fig. 3.11 (c) where the entire spectrum is evenly partitioned into $\frac{N}{N_B}$ blocks where each sub-block is composed of N_B sub-carriers and every $(N_B+1)^{th}$ sub-carrier is removed. Δf_3 is the sub-carrier spacing and Δf_G is the guard band between two adjacent blocks and is equal to $2\Delta f_3$. Hence, the partitioned blocks are non-orthogonally packed. Due to the introduction of the guard band Δf_G, in order to keep the same occupied bandwidth, sub-carriers in each block are more compressed leading to a smaller Δf_3. According to Fig. 3.11, the sub-carrier spacing relationship is $\Delta f_3 < \Delta f_2 < \Delta f_1$. Considering the guard band and (2.9), the Block-SEFDM signal [57] is expressed as

$$X[k] = \frac{1}{\sqrt{Q}} \sum_{l_B=0}^{\frac{N}{N_B}-1} \sum_{i=0}^{N_B-1} s_{i+l_B N_B} \exp[\frac{j2\pi k\alpha(i+l_B(N_B+1))}{Q}] \tag{3.10}$$

where N_B is the number of sub-carriers in each block, $s_{i+l_B N_B}$ is the i^{th} symbol modulated in the ${l_B}^{th}$ block. Therefore, N_B determines the size of each block and l_B indicates the index of blocks. The product of N_B and the maximum value of l_B equals N. It should be noted that not all of the sub-carriers are evenly overlapped and therefore not all have the same levels of ICI, since there is a deleted sub-carrier (additional spacing) between adjacent blocks in order to mitigate the non-orthogonal out-of-block interference. Therefore, the in-band bandwidth compression factor (BCF) α in each block should be smaller than the effective BCF β because the removed sub-carrier between adjacent sub-bands results in reduced spectral efficiency. The bandwidth occupations of SEFDM and Block-SEFDM are given in (3.11) and (3.12), respectively.

$$B_{SEFDM} = \frac{\beta(N-1)+2}{T} = (\beta(N-1)+2)\Delta f \approx \beta N \Delta f \tag{3.11}$$

$$\begin{aligned} B_{Block-SEFDM} &= \frac{\alpha(\frac{N}{N_B}-1+N-1)+2}{T} \\ &= (\alpha(\frac{N}{N_B}-1+N-1)+2)\Delta f \approx \alpha(\frac{N}{N_B}-1+N)\Delta f \end{aligned} \tag{3.12}$$

Therefore, according to (3.11) and (3.12), the in-band BCF α is calculated as

$$\alpha = \frac{\beta N}{\frac{N}{N_B}-1+N} \tag{3.13}$$

The bandwidth compression factor transformation is provided in Table 3.3. $N_B = 8$ is selected considering the trade-off between complexity and effective BCF.

Table 3.3: Effective Bandwidth Compression Factor Transformation (N_B=8)

	Sub-carrier	In-band BCF	Effective BCF
$N_B = 8$	N=16	$\alpha = 0.612$	$\beta = 0.65$
		$\alpha = 0.659$	$\beta = 0.7$
		$\alpha = 0.753$	$\beta = 0.8$
	N=32	$\alpha = 0.5943$	$\beta = 0.65$
		$\alpha = 0.64$	$\beta = 0.7$
		$\alpha = 0.7314$	$\beta = 0.8$
	N=64	$\alpha = 0.586$	$\beta = 0.65$
		$\alpha = 0.631$	$\beta = 0.7$
		$\alpha = 0.7211$	$\beta = 0.8$
	N=128	$\alpha = 0.582$	$\beta = 0.65$
		$\alpha = 0.6266$	$\beta = 0.7$
		$\alpha = 0.7161$	$\beta = 0.8$

The multi-band SEFDM reception process is similar to the operation in (2.23). The discrete model is represented as

$$R = \mathbf{C}S + Z \tag{3.14}$$

where $\mathbf{C}$ is an $N \times N$ correlation matrix that describes the interference between the sub-carriers. However, the sub-carriers are no longer continuous since one sub-carrier is removed after every eight data sub-carriers. Therefore, the expression of interference would be different compared to a conventional SEFDM one. The sub-carrier matrix can

be derived from (3.10). Then, the new correlation matrix is obtained by correlating the sub-carrier matrix $\mathbf{F}$, with element values $f_{k,(x,l_{Bx})} = \exp[\frac{j2\pi k\alpha(x+l_{Bx}(N_B+1))}{Q}]$ with its conjugate sub-carrier matrix $\mathbf{F}^*$, with element values $f_{(y,l_{By}),k} = \exp[\frac{-j2\pi k\alpha(y+l_{By}(N_B+1))}{Q}]$ for $k = 0, 1, ..., Q-1$. The process can be expressed as

$$c[m,n] = \frac{1}{Q}\sum_{k=0}^{Q-1} f_{(y,l_{By}),k} \cdot f_{k,(x,l_{Bx})} \tag{3.15}$$

for $x, y = [0, 1, ..., N_B - 1]$ and $l_{Bx}, l_{By} = [0, 1, ..., \frac{N}{N_B} - 1]$. The distorted symbols R are then fed to a detector to get the estimate of the transmitted symbols.

3.3.2 Block Efficient Detector (BED)

The proposed spectrum segmentation scheme provides a new way to signal detection. In the proposed multi-band system, each band consists of 8 sub-carriers indicating a small size sub-system. Therefore, powerful detectors like ML or SD may be used. Taking into account the complexity, SD is employed in each block instead of ML. Remembering that SEFDM and Block-SEFDM are multicarrier modulation techniques in which the sub-carriers overlap similarly to OFDM but where the orthogonality principle defined for OFDM is deliberately violated in SEFDM in order to reduce the frequency spacing between the sub-carriers with the benefit of improved spectral efficiency. In Block-SEFDM, although one sub-carrier is reserved as a gap between two adjacent sub-bands, the interference is still challenging with high bandwidth compressions since the sub-carrier spacing is smaller and more overlapping occurs from adjacent sub-carriers. Therefore, the ID algorithm derived from section 3.2.1 is selected here as the method to alleviate the out-of-block ICI due to the non-orthogonal overlapping sub-carriers from adjacent sub-bands. Its iterative demapping scheme is referred to Fig. 3.1. The work in section 2.6.3 showed that an initial estimate determines the search space of FSD. The search space is a crucial parameter that decides which candidate points are included in the detection procedure. It has been proven in section 3.2.3 that ID has a better immunity against interference and is a more effective method which can be used to

generate a more accurate initial estimate relative to the ZF or TSVD method. In this work, we present the BED algorithm which is also assisted by the initial estimate from ID. However, the function of the initial estimate in this case is not to constrain the search space but cancel out the out-of-block interference. Therefore, at the receiver, an iterative detection ID [52] algorithm is firstly executed to remove the out-of-block interference in each block by using the iterative soft demapping scheme. Then, a typical SD [38] is adopted in each interference-clean block (e.g. Block 1, Block 2,...) to recover signals.

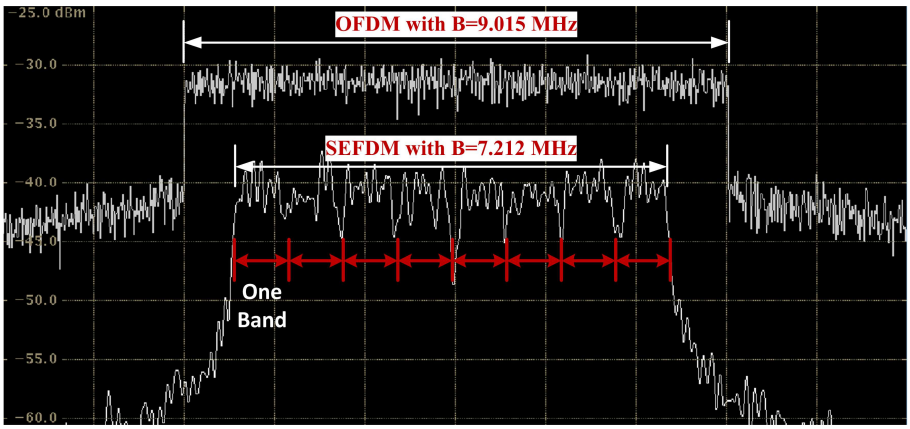

Figure 3.12: Experimental bandwidth comparisons of Block-SEFDM (effective BCF: $\beta = 0.8$) and OFDM. By transmitting the same amount of data, Block-SEFDM requires bandwidth of 7.212 MHz while OFDM needs 9.015 MHz. Carrier frequency is 2 GHz, frequency span is 15 MHz and RBW for OFDM and Block-SEFDM are 3 KHz and 60 KHz, respectively.

The measured signal spectrum of this technique [57] is shown in Fig. 3.12. It is measured from a Tektronix Mixed Domain Oscilloscope. The OFDM signal is configured on the basis of LTE release 8 [1]. The Block-SEFDM signal also follows the LTE release 8 but the sub-carrier spacing is compressed by 20%. Therefore, by transmitting the same amount of data, Block-SEFDM requires bandwidth of 7.212 MHz while OFDM needs 9.015 MHz. A Block-SEFDM signal employing 64 sub-carriers is presented here for the sake of demonstrating the multi-band SEFDM signal structure. The number of sub-carriers can be set to any values in practice. In the figure, 64 sub-carriers are

evenly divided into 8 sub-bands where each sub-band is composed of 8 sub-carriers and every 9^{th} sub-carrier is removed. At the receiver, ID is firstly executed to remove the out-of-block interference in each band by using the iterative soft demapping scheme. Then, an 8×8 SD is adopted in each interference-clean sub-band to recover signals. The description of the BED operation is presented in Algorithm 2.

Algorithm 2 : Block Efficient Detector.

$[\hat{S}, \bar{S}] \Leftarrow ID(R, \mathbf{C}, v)$
$\frac{N}{N_B}$ *Parallel Out − of − block Interference Cancellation*$(U = N_B; U \leq N; U = U + N_B)$:
One unit start
for $m = U - N_B$; $m \leq U - 1$; $m++$ **do**
  for $n = 0$; $n \leq N - 1$; $n++$ **do**
    $a[m] = c[m, n] * \bar{S}_n$
  end for
  for $n = U - N_B$; $n \leq U - 1$; $n++$ **do**
    $b[m] = c[m, n] * \bar{\bar{S}}_n$
  end for
  $I[m] = a[m] - b[m]$
  $\tilde{R}_{(U/N_B)-1} = R[m] - I[m]$
end for
One unit end
$\frac{N}{N_B}$ *Parallel SD*$(U = N_B; U \leq N; U = U + N_B)$:
One unit start
$g_{ID} = \left\| \tilde{R} - \bar{\mathbf{C}}\bar{S} \right\|^2$
$\tilde{S}_{BED} = \arg\min \left\| \tilde{R} - \bar{\mathbf{C}}\tilde{S} \right\|^2 = \arg\min \left\| \bar{\mathbf{L}}(\hat{S} - \tilde{S}) \right\|^2 \leq g_{ID}$
One unit end

The interference cancellation is decomposed into two stages. The first stage Eq. (3.16) is interference modelling and the second stage Eq. (3.17) is to cancel out the modelled interference. The entire process is expressed as

$$I[m] = \sum_{n=0}^{N-1} c[m, n] * \overline{S}_{ID}(n) - \sum_{n=U-N_B}^{U-1} c[m, n] * \overline{S}_{ID}(n) \tag{3.16}$$

$$\tilde{R}_{U/N_B-1} = R[m] - I[m] \tag{3.17}$$

where $m \in [U - N_B, ..., U - 1]$, $U = [N_B, 2N_B, ..., N]$. $U/N_B - 1$ represents the block sequence number which starts from 0 and ends with $N/N_B - 1$, $I[m]$ is an N_B-dimensional vector of the out-of-block interference and should be cancelled out in Eq. (3.17). $\tilde{R}_{U/N_B-1}$ is an N_B-dimensional vector of the interference cancelled symbols and is transferred to SD for detection.

After removing interference from each block, the ID detected symbols are fed to the SD as initial estimates. The SD algorithm has been described in detail in section 2.6.2. However, some parameters have to be modified due to the segmentation of the entire spectrum. Therefore, some basic mathematical expressions are presented here again. The recovered SEFDM signals are processed in each block by examining only points that exists within an N_B-dimensional hypersphere of radius $g_{_{ID}}$. Within one sub-band, the initial radius $g_{_{ID}}$ is taken as the Euclidean norm between the received statistics $\tilde{R}$ and the initial estimates $\bar{S}$, the equation is shown below:

$$g_{_{ID}} = \left\| \tilde{R} - \bar{\mathbf{C}}\bar{S} \right\|^2 \tag{3.18}$$

where $\tilde{R}$ is an N_B-dimensional vector of the interference cancelled received statistics, $\bar{S}$ is an N_B-dimensional vector of the hard decision symbols from the ID detector and $\bar{\mathbf{C}}$ is an $N_B \times N_B$ partial correlation matrix which is defined by $\sum_{m=U-N_B}^{U-1} \sum_{n=U-N_B}^{U-1} c[m,n]$. It is apparent that $\bar{\mathbf{C}}$ is a subset of the original $\mathbf{C}$. The detection procedure is handled by the following equation:

$$\tilde{S}_{BED} = \arg \min_{\tilde{S} \in O^N} \left\| \tilde{R} - \bar{\mathbf{C}}\tilde{S} \right\|^2 \leq g_{_{ID}} \tag{3.19}$$

where $\tilde{S}$ are detected symbols of length N_B, O is the constellation cardinality. In order to simplify the calculation of Euclidean norm, Cholesky Decomposition is employed to transform (3.19) to an equivalent expression as shown in (3.20). The transformation is accomplished by using $chol\{\bar{\mathbf{C}}^*\bar{\mathbf{C}}\} = \bar{\mathbf{L}}^*\bar{\mathbf{L}}$ [39], where $\bar{\mathbf{L}}$ is an $N_B \times N_B$ upper triangular matrix. The expansion of (3.20) and its computations have been discussed in section 2.6.2.

$$\tilde{S}_{BED} = \arg \min_{\tilde{S} \in O^N} \left\| \bar{\mathbf{L}}(\hat{S} - \tilde{S}) \right\|^2 \leq g_{_{ID}} \tag{3.20}$$

where $\hat{S}$ is an N-dimensional vector of soft estimated symbols in the last iteration of

ID.

3.3.3 Performance and Complexity Evaluations

The performance and complexity of the proposed detector are evaluated. The purpose is to test the functionality of the multi-band system. Therefore, 4QAM modulation scheme is adopted and an AWGN channel is assumed throughout the simulation. Both typical SEFDM (Fig. 3.11 (b)) and Block-SEFDM (Fig. 3.11 (c)) systems are demonstrated. For the typical SEFDM system, the ID-FSD [52] detector is employed. For the Block-SEFDM system, the proposed BED detector is used. It should be noted that β is the effective BCF in the Block-SEFDM system which is greater than α; the in-band BCF in the Block-SEFDM system. Therefore, the bandwidth saving for Block-SEFDM is calculated as $(1-\beta)\times 100\%$.

3.3.3.1 Performance

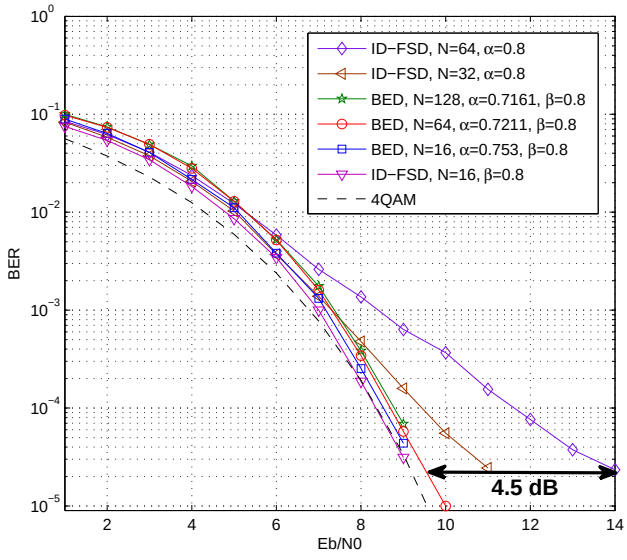

Figure 3.13: Performance comparisons of BED and ID-FSD for different $\alpha(\beta) = 0.8$ and N with $N_B = 8$. The tree-width T_W=16 and 20 iterations are used in the ID-FSD to guarantee BER performance.

Fig. 3.13 shows that ID-FSD has the same bit error rate with BED under low $Eb/N0$. However, as $Eb/N0$ increases, the BED detector outperforms the ID-FSD significantly, for example, up to 4.5 dB performance gain at BER equals 2×10^{-5}. The performance of the ID-FSD scales with the number of sub-carriers since more interference is introduced between adjacent symbols with the increase of sub-carriers. But it is not the case for BED. Simulations in Fig. 3.13 show that increasing the number of sub-carriers from 16 to 128 does not compromise the performance. In addition, it is apparent that the BED performance approaches the theoretical one independent on the system size. This figure proves that our new detector has a better immunity to interference and it is applicable to large size systems.

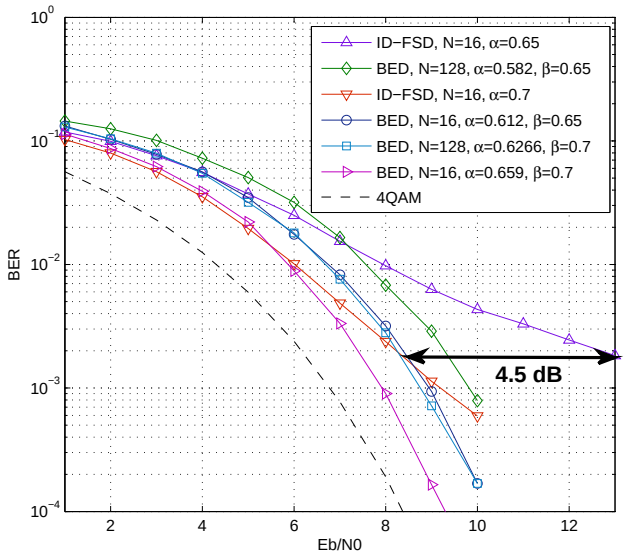

Figure 3.14: Performance comparisons of BED and ID-FSD for various $\alpha(\beta)$ smaller than 0.8 and various sub-carriers N with $N_B = 8$. The tree-width T_W=16 and 20 iterations are used in the ID-FSD to guarantee BER performance.

This performance gap is even more obvious between the BED and the ID-FSD with lower bandwidth compression factors like $\beta = 0.7; 0.65$. Their performance is shown in Fig. 3.14. It should be noted that for the same bandwidth saving, the performance of a BED detector with 128 sub-carriers is even better than that of an ID-FSD detector

with a smaller number of sub-carriers. For the same bandwidth compression factor and the same number of sub-carriers, the BED even outperforms the ID-FSD by 4.5 dB at BER equals 2×10^{-3}. Such performance improvement is attributed to the reduction of interference in the multi-band system coupled with the use of SD. Hence, one may conclude that the combination of multi-band SEFDM and BED allows practicable systems with a large number of sub-carriers and high bandwidth compressions.

However, maintain a small number of sub-carriers such as 8 in each block would degrade the system performance since the in-band BCF, calculated according to (3.13) and shown in Table 3.4, has to be small enough to get a targeted overall effective BCF. Thus, higher interference is introduced and will increase the BER. Therefore, for a large size system, the number of sub-carriers in each block has to be large enough. The new Block-SEFDM signal occupying 256 data sub-carriers is designed to use 16 sub-carriers in each block. Thus, the in-band BCF will be relatively relaxed. The effective bandwidth compression factor transformation for this special case is presented in Table 3.5.

Table 3.4: Effective Bandwidth Compression Factor Transformation (N=256, N_B=8)

	Sub-carrier	In-band BCF	Effective BCF
$N_B = 8$	N=256	$\alpha = 0.714$	$\beta = 0.8$
		$\alpha = 0.624$	$\beta = 0.7$
		$\alpha = 0.598$	$\beta = 0.67$

Table 3.5: Effective Bandwidth Compression Factor Transformation (N=256, N_B=16)

	Sub-carrier	In-band BCF	Effective BCF
$N_B = 16$	N=256	$\alpha = 0.756$	$\beta = 0.8$
		$\alpha = 0.661$	$\beta = 0.7$
		$\alpha = 0.633$	$\beta = 0.67$

The system BER performance is shown in Fig. 3.15 where five systems are tested and compared. It is clearly seen that for 20% bandwidth saving (i.e. α=0.8), the 4QAM SEFDM system shows similar BER performance with the 4QAM OFDM one. It verifies the 25% Mazo limt theory. For higher bandwidth saving such as 33% (i.e. α=0.67),

it shows worse performance than the 4QAM OFDM one but outperforms the spectral efficiency equivalent 8QAM OFDM. It proves that a low order modulation signal can achieve the same spectral efficiency as a higher order one with better performance.

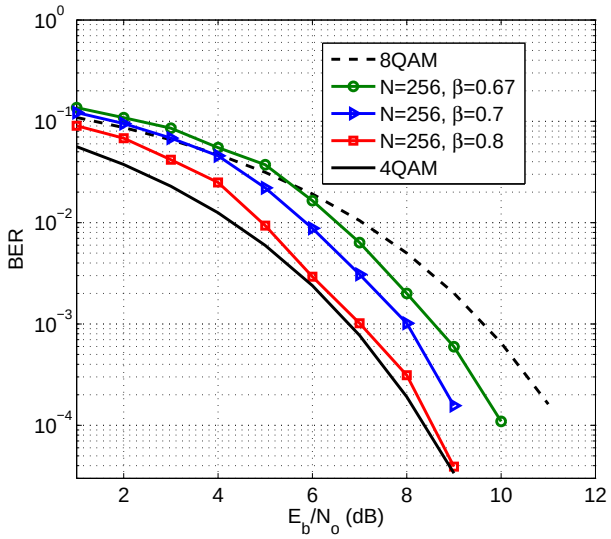

Figure 3.15: Performance comparisons of 4QAM symbol modulated SEFDM systems associated with different effective BCF β in the condition of N=256 and N_B=16.

For higher order modulation formats such as 16QAM, SD performance has been investigated in Fig. 2.11 where the 16QAM SEFDM signal with 20% saving can achieve the same performance as the 16QAM OFDM. It not only verifies the Mazo limit but also proves that a low order modulation format (i.e. 16QAM) can outperform the spectral efficiency equivalent higher order modulation formats such as 32QAM OFDM.

Table 3.6: Effective Bandwidth Compression Factor Transformation (N=64, N_B=16)

	Sub-carrier	In-band BCF	Effective BCF
$N_B = 16$	N=64	$\alpha = 0.764$	$\beta = 0.8$
		$\alpha = 0.670$	$\beta = 0.7$
		$\alpha = 0.640$	$\beta = 0.67$

However, it is not the case for the Block-SEFDM signal as illustrated in Fig. 3.16. Using 256 data sub-carriers, the performance of the 16QAM modulated SEFDM signal is no longer identical to that of the 16QAM modulated OFDM signal. The BER

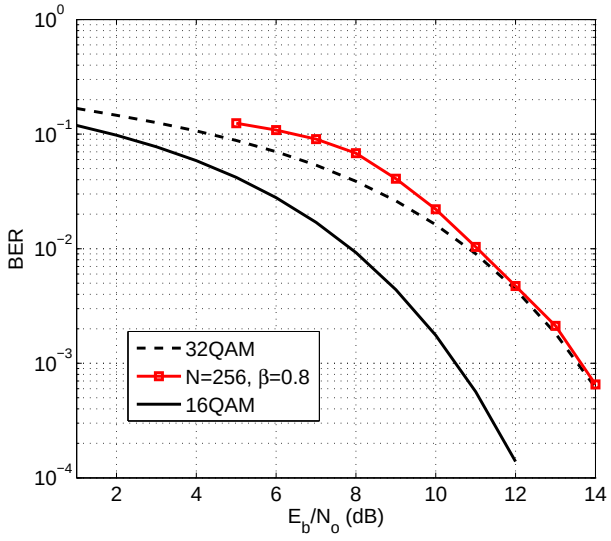

Figure 3.16: Performance comparisons of 16QAM symbol modulated SEFDM systems associated with different effective BCF β in the condition of N=256 and N_B=16.

curve overlaps with the 32QAM result. Since the 16QAM SEFDM signal with 20% bandwidth saving has the same spectral efficiency with the typical 16QAM OFDM one, it is inferred that there is no benefit in this scenario. Three reasons contribute to the reduced performance. The first one is the high in-band self-created ICI; the second is the enhanced out-of-block interference using high order modulation symbols. The last is due to the higher density of 16QAM constellation and the decision reliability is greatly affected. One solution to mitigate the out-of-block interference is to use small number of blocks, thus small number of total sub-carriers. The in-band self-created ICI and the superimposed out-of-block interference would be reduced to some extent. The simulated performance is shown in Fig. 3.17 where a total number of 64 sub-carriers are used and 4 blocks are separated with each has 16 sub-carriers. The interference level, which maybe indicated by in-band bandwidth compression factor, is presented in Table 3.6. The benefit of using SEFDM signals is obvious but with limited contributions. It is clearly seen that the 20% bandwidth saving SEFDM signal outperforms the 32QAM OFDM signal with 1 dB performance gain. However, compared with the 16QAM

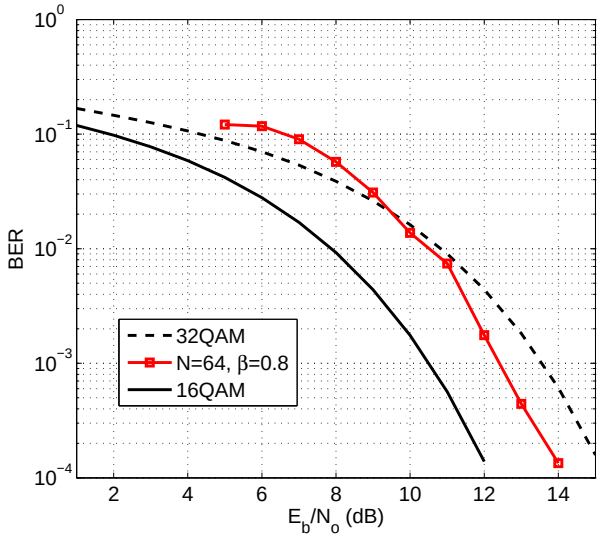

Figure 3.17: Performance comparisons of 16QAM symbol modulated SEFDM systems associated with different effective BCF β in the condition of N=64 and N_B=16.

OFDM signal, the curve is 2 dB away. Thus, it is concluded that in large size systems (e.g. large number of sub-carriers), using higher order modulation formats such as 16QAM, the Mazo limit cannot be reached easily and the low order modulation benefits are limited depending on the interference level.

3.3.3.2 Complexity

The complexity is calculated in terms of real-valued multiplications and real-valued additions. For this we consider operations for detecting each symbol, not the operations required only once in the detection process (e.g. Cholesky Decomposition). An approximated complexity of ID-FSD has been studied in section 3.2.3. However, the complexity of BED is random since the computation of SD is highly dependent on channel conditions. Therefore, it is not convincing to compare BED with ID-FSD. In this section, in order to clearly show the complexity reduction of BED, a single SD is included for the comparison. A single SD indicates a SD detector for a single SEFDM band. It should be noted that due to the random complexity of SD, all the nodes are as-

sumed to be visited in this work indicating the upper bound computational expressions in (3.21) and (3.22). However, in practice, only a portion of nodes would be searched because of the search space shrink indicating a much lower computational complexity.

$$C_{mult} = \frac{N}{N_B}(\underbrace{\sum_{n=1}^{2N_B} 2^n[2n+1]}_{full\ expansion}) \tag{3.21}$$

$$C_{add} = \frac{N}{N_B}(\underbrace{\sum_{n=1}^{2N_B} 2^n[2n-1]}_{full\ expansion}) \tag{3.22}$$

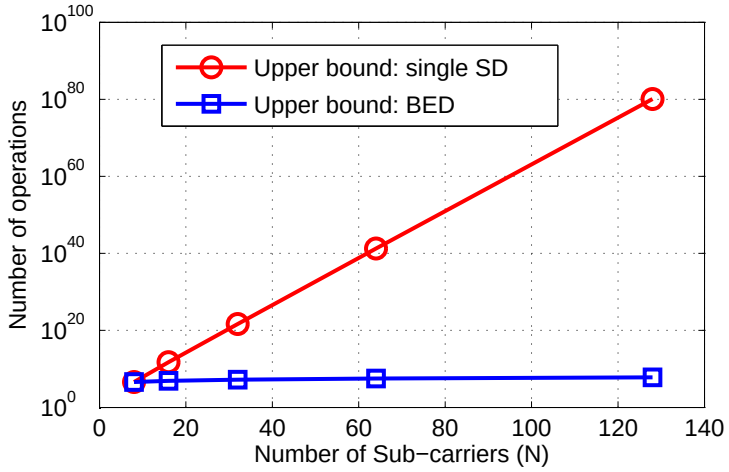

Figure 3.18: Upper bound of the required multiplication operations versus N for two detectors with $N_B = 8$.

The upper bound computational complexities in terms of real-valued multiplication operations for both the BED and the single SD are shown in Fig. 3.18. For the sake of comparison, the number of operations in Fig. 3.18 is expressed by a logarithmic scale. The starting point of x-axis is N =8 sub-carriers and then goes up to 128 sub-carriers. Comparing these two curves, it is obvious that the complexity of BED is substantially

lower than that of the single SD. The computational operations for both BED and the single SD increase with the value of N. But it is more apparent for the single SD one. It is noted that when N =8, they have the same complexity due to the size of each block in BED equals 8. However, the difference becomes more obvious when the number of sub-carriers reaches 128. Based on the previous mathematical analysis, it is evident that the complexity of BED is propositional to the number of blocks, while in terms of the single SD, its complexity is propositional to the number of sub-carriers. Therefore, it can be inferred from the figure that the multi-band structure is suitable for large size systems while the single-band would be impractical.

3.4 Turbo-SEFDM

Iterative detector is a kind of detector that can effectively remove ICI using a feedforward and feedback structure. The feedforward loop estimates original symbols and the feedback loop models interference either from RF channels or systems (e.g. SEFDM). After cancelling out the interference effect, more reliable estimated symbols are fed to the loop process until a converged symbol estimation is obtained. It can be inferred that the reliability of the modelled interference determines the accuracy of interference cancellation and further determines the system performance.

One challenge of iterative detection methods is that signal detection is dependent on previous iterations and a decision error will affect the subsequent signal decisions leading to performance degradation. The impact is more serious in SEFDM since self-created ICI is introduced in the system. With the introduction of higher interference power in SEFDM, typical ID [52] in section 3.2 or enhanced ID-sphere decoding (ID-SD) [57] in section 3.3 fail to recover signals. This is due to the fact that in the feedforward loop symbol estimation is greatly affected. The inaccurate symbol estimation results in inaccurate interference modelling in the feedback loop. Hence, the detector cannot effectively cancel out the interference. Previous reported work is either based on uncoded SEFDM systems or requires impractically high number of iterations for small

size systems. Here we explore, for the first time, a coded system with iterative detection and show that a large size SEFDM is practicable with limited complexity and good performance.

An improved interference cancellation scheme, termed Turbo equalization, can improve the reliability of interference modelling and cancellation using error correction code. In a Turbo equalizer, an inner and an outer decoder exchange soft information many times until converged performance is obtained. A detailed description of the Turbo equalization can be found in [141]. In multicarrier systems, this principle has been investigated in [25]. A block diagram of the Turbo equalizer is illustrated in Fig. 3.19.

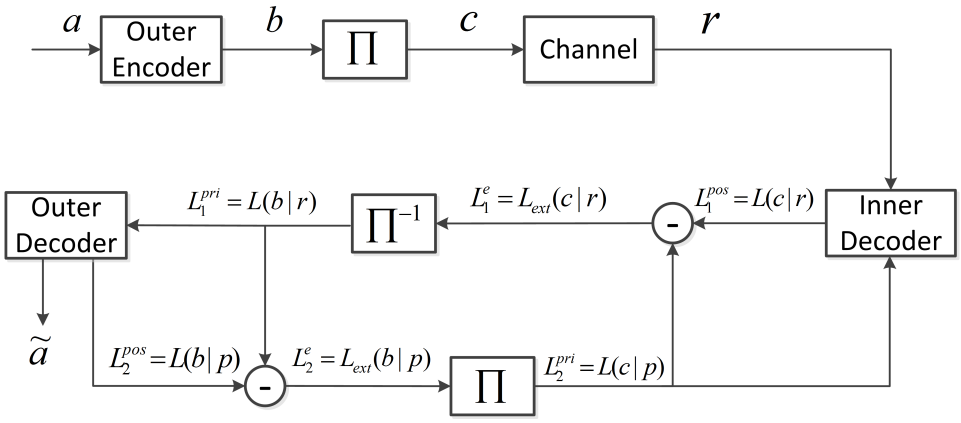

Figure 3.19: Block diagram of a generalized Turbo equalizer.

In this figure, the purpose of Turbo equalization is to update and decide symbols b not a. Note that either BCJR [142] or Turbo decoding [143] [144] can be used in the outer decoder block. Turbo decoding has a similar iterative structure like Turbo equalization. However, the updated symbols inside the outer decoder are a not b. In this chapter, the Turbo equalization concept is applied in the Turbo-SEFDM system attempting to iteratively remove the self-created ICI caused by non-orthogonally packed sub-carriers.

3.4.1 System Model

In this section, we present a Turbo-SEFDM architecture which maximizes the *a posteriori* probability (APP) for a given bit through a process of iteration. The block diagram of the Turbo-SEFDM system is shown in Fig. 3.20 where it consists of the transmitter and the Turbo equalization receiver. The Turbo principle receiver includes a feedforward and feedback loop between an SEFDM detector and a decoder. The soft information, termed extrinsic information, is updated between the SEFDM detector and the decoder in an iterative process to improve the reliability of the estimation of transmitted symbols. Detailed process within the Turbo-SEFDM system is described in the following.

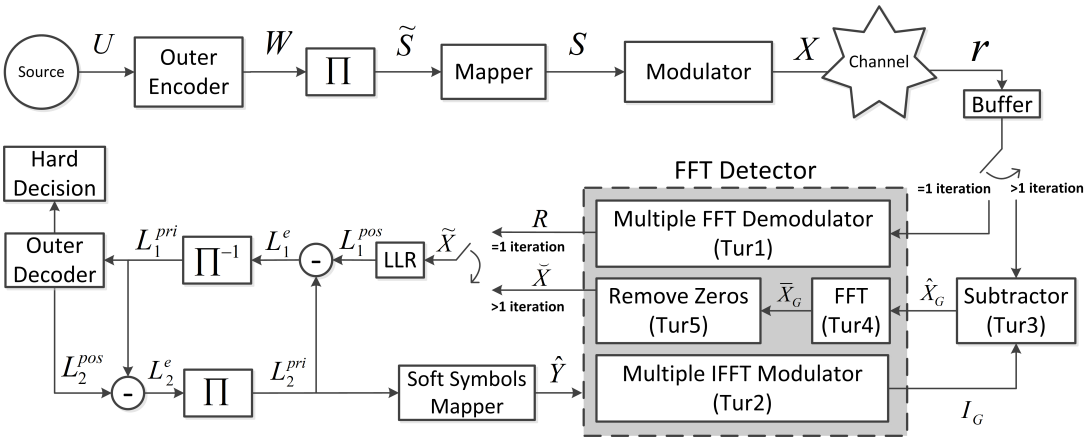

Figure 3.20: Block diagram of Turbo-SEFDM. The block labelled $\mathbf{\Pi}$ is the interleaver and $\mathbf{\Pi^{-1}}$ represents deinterleaver. Symbols in brackets (.) denote equation indexes. **Tur1** is referred to equation (3.27); **Tur2** is (3.28); **Tur3** is (3.30); **Tur4** is (3.31) and **Tur5** is (3.32).

At the source output, an M-dimensional vector of information bits $U = [u_1, u_2, ..., u_M]$ is encoded in the outer encoder. This work employs a coding rate $R_c = 1/2$ recursive systematic convolutional (RSC) code of memory 2 with feedforward polynomial $G_1(D) = 1 + D + D^2$ and feedback polynomial $G_2(D) = 1 + D^2$ [145]. The bits in the coded vector $W = [w_1, w_2, ..., w_H]$ of length $H = M/R_c$, are interleaved using a random interleaver $\mathbf{\Pi}$ with size of 2048 information bits. The interleaved bits $\tilde{S}$ are mapped to

the corresponding complex symbols $S = [s_1, s_2, ..., s_P]$ with $P = H/log_2O$, where O is the constellation cardinality. The complex coded symbols are then modulated in the modulator according to [46].

At the receiver, soft information is exchanged between the FFT detector and the outer decoder. The soft information is expressed in the form of log-likelihood ratios (LLR). The sign of the LLR value determines the sign of the bit, and its magnitude determines the reliability of the sign of the bit. The extrinsic information L^e is obtained by separating *a priori* information from *a posteriori* information written as $L^e = L_{a-posteriori} - L_{a-priori}$. In Fig. 3.20, after the first iteration, the LLR block generates *a posteriori* information L_1^{pos} based on the received $\tilde{X}$. L_1^{pos} is transformed to extrinsic information L_1^e by subtracting *a priori* information L_2^{pri}. This extrinsic information is deinterleaved and delivered to the outer decoder as the *a priori* information L_1^{pri}. The outer decoder outputs *a posteriori* information L_2^{pos} which then generates extrinsic information L_2^e. This information is interleaved and sent back to the soft symbols mapper as the new *a priori* information L_2^{pri}. Soft symbols $\hat{Y}$ is sent to the Multiple IFFT Modulator to retrieve interference I_G. Finally, the interference cancelled received symbols $\hat{X}_G$ are obtained in a subtractor for the preparation of the next iteration. The extrinsic information is updated iteratively until the performance converges to a fixed level. After a number of iterations, the final estimated bit stream is obtained after the outer decoder. It should be noted that in the first iteration the Multiple FFT Demodulator is activated while the subtractor is deactivated. After the first iteration, the reverse operations are executed. A buffer stores the received discrete symbols r during one complete symbol detection. After that, the buffer refreshes and receives new symbols.

3.4.2 Soft Detector

The demodulation of an SEFDM signal can be treated as multiple FFT operations indicating one SEFDM symbol is composed of multiple overlapped OFDM symbols.

It is apparent that one OFDM symbol is an interference signal superimposed on other OFDM symbols. Hence, the soft detector aims to remove the superimposed interference from each OFDM symbol. Note that either Bahl-Cocke-Jelinek-Raviv (BCJR) [142] or Turbo decoding [143] [144] can be used in the outer decoder block. In this section, the standard BCJR algorithm is employed in the outer decoder and its detailed description can be found in [142]. The FFT detector is a crucial component since it plays an important role in signal demodulation and ICI cancellation in the received symbols.

3.4.2.1 FFT Detector

By observing (2.9), sub-carriers are no longer orthogonal in SEFDM because of the introduction of α. Therefore, FFT and IFFT are not directly applicable. In order to cope with this issue, a multiple IFFT structure was proposed in [35] where an SEFDM IFFT operation is divided into several blocks where a standard IFFT is adopted in each block. The complexity can be reduced further by using a pruned technique in [46]. At the receiver, for demodulation, we adopt the same idea to decompose a single long SEFDM FFT operation into several small blocks where a standard FFT is applied in each one. Moreover, considering the fact that FFT can be easily extended to an IFFT by requiring extra computations like conjugating input complex QAM symbols and output complex results, we proposed a time domain interference canceller [58] which has a lower complexity compared to a standard one [52]. The time-domain interference canceller and multiple-FFT demodulator are combined to form the FFT detector. Since we use a Turbo receiver structure, the interference canceller and demodulator are not activated simultaneously, therefore, it is possible to reuse FFT/IFFT and further save resources. Hence, we propose an FFT detector which can exchange soft information with an outer decoder based on the Turbo principle. This method can effectively eliminate interference at the demodulation stage and prevents errors from spreading to the following decoder. The demodulation process is an inverse operation of the modulation in (2.9). In addition, based on (2.23), the demodulation process can be

expressed as

$$R[n] = \frac{1}{\sqrt{Q}} \sum_{k=0}^{Q-1} r(k) \exp(\frac{-j2\pi nk\alpha}{Q}) \tag{3.23}$$

where r is the received sample vector, $n, k = [0, 1, ..., Q-1]$ and n should be truncated to N if $N < Q$. Applying the same concept in [46], (3.23) can be expressed as the sum of multiple FFTs. By setting $\alpha = b/c$, where b and c are both integers and $b < c$, (3.23) can be represented as

$$R[n] = \frac{1}{\sqrt{Q}} \sum_{k=0}^{cQ-1} r^{'}(k) \exp(\frac{-j2\pi nk}{cQ}) \tag{3.24}$$

where $r^{'}$ is a cQ-dimensional vector of symbols as

$$r^{'}(i) = \begin{cases} r_{i/b} & i \ mod \ b = 0 \\ 0 & otherwise \end{cases} \tag{3.25}$$

by substituting with $k = i + lc$, (3.24) can be rearranged as

$$R[n] = \frac{1}{\sqrt{Q}} \sum_{i=0}^{c-1} \sum_{l=0}^{Q-1} r^{'}(i + lc) \exp(\frac{-j2\pi n(i + lc)}{cQ}) \tag{3.26}$$

$R[n]$ in (3.26) can be further simplified to

$$R[n] = \frac{1}{\sqrt{Q}} \sum_{i=0}^{c-1} \exp(\frac{-j2\pi ni}{cQ}) \sum_{l=0}^{Q-1} r^{'}(i + lc) \exp(\frac{-j2\pi nl}{Q}) \tag{3.27}$$

The second summation term in (3.27) is a Q-point FFT of the sequence $r^{'}(i + lc)$. Considering the first term, the demodulation of an SEFDM signal can be treated as c parallel FFT operations indicating one SEFDM symbol is composed of c parallel overlapped OFDM symbols. It is apparent that one OFDM symbol is an interference signal superimposed on other OFDM symbols. Therefore, the interference canceller aims to remove $c - 1$ parallel OFDM interference signals from one OFDM signal, through regenerating interference signals using IFFT processes applied to the soft mapped sym-

bols. Equation (3.28) is the interference superposed to the G^{th} OFDM signal with zero padding as in the condition of (3.29). $G \in [0, 1, ..., c-1]$.

$$I_G[k] = \frac{1}{\sqrt{Q}} \sum_{i=0, i\neq G}^{c-1} \exp(\frac{j2\pi ik}{cQ}) \sum_{l=0}^{Q-1} Y^{'}(i+lc) \exp(\frac{j2\pi lk}{Q}) \tag{3.28}$$

where

$$Y^{'}(i) = \begin{cases} \hat{Y}_{i/b} & i \ mod \ b = 0 \\ 0 & otherwise \end{cases} \tag{3.29}$$

The second summation term in (3.28) is a Q-point IFFT of the sequence $Y^{'}(i + lc)$. After one iteration, the interference $I_G[k]$ is subtracted from the received discrete symbols $r[k]$ to get the more reliable interference cancelled received symbols $\hat{X}_G[k]$ as shown in Eq. (3.30). It should be noted that the accurate channel estimation determines the accuracy of the interference generation. The increasing estimation errors would affect the interference generation and further degrade the following Turbo principle signal detection since errors will be passed to the next iteration.

$$\hat{X}_G[k] = r[k] - I_G[k] \tag{3.30}$$

Since the $c-1$ parallel OFDM interference signals have been removed from the G^{th} OFDM signal, therefore, only one Q-point FFT is required to demodulate the signal. Manipulation of this single OFDM signal is shown in (3.31). The first term in the bracket is the operation of getting rid of the complex exponentials. Outside the bracket is a standard FFT operation.

$$\bar{X}_G[k] = \sum_{l=0}^{Q-1} [\hat{X}_G[k] \exp(\frac{-j2\pi Gk}{cQ})] \exp(\frac{-j2\pi lk}{Q}) \tag{3.31}$$

Because the original SEFDM signal is decomposed into c parallel OFDM signals, the same interference cancellation process has to be repeated for c times. After that, we obtain a $C \times Q$ matrix $\bar{\mathbf{X}} = [\bar{X}_0, \bar{X}_1, ..., \bar{X}_{c-1}]$ which is interpolated with zeros.

Equation (3.32) removes zeros to get a single vector $\breve{X}$ composed of soft symbols

$$\breve{x}_{i/b} = \bar{x}_i, i \ mod \ b = 0 \tag{3.32}$$

where useful symbols are extracted every b positions. $\breve{x}_{i/b}$ and $\bar{x}_i$ are the elements of vector $\breve{X}$ and matrix $\bar{\mathbf{X}}$, respectively. These soft symbols are delivered to the next module for iterative recovery. Finally, after a preset iteration number, soft symbols are sliced to hard symbols as a final step.

3.4.2.2 LLR Calculations

Following [141] and [146], we calculate the log-likelihood ratio of the transmitted bit $\tilde{S}$ conditioned on the demodulation output $\tilde{X}$ as

$$L(\tilde{s}|\tilde{x}) = ln\frac{P(\tilde{s}=+1|\tilde{x})}{P(\tilde{s}=-1|\tilde{x})} \tag{3.33}$$

With a conditioned log-likelihood ratio $L(\tilde{s}|\tilde{x}) = L(\tilde{s}) + L(\tilde{x}|\tilde{s})$, the above equation can be expressed as

$$\begin{aligned} \underbrace{L(\tilde{s}|\tilde{x})}_{a-posteriori} &= ln\frac{P(\tilde{s}=+1)}{P(\tilde{s}=-1)} + ln\{\frac{\frac{1}{\sqrt{2\pi\sigma^2}}exp(\frac{-(\tilde{x}-d)^2}{2\sigma^2})}{\frac{1}{\sqrt{2\pi\sigma^2}}exp(\frac{-(\tilde{x}+d)^2}{2\sigma^2})}\} \\ &= \underbrace{ln\frac{P(\tilde{s}=+1)}{P(\tilde{s}=-1)}}_{a-priori} + \underbrace{\frac{2d\tilde{x}}{\sigma^2}}_{extrinsic} \end{aligned} \tag{3.34}$$

where σ^2 is the noise variance and d is the fading amplitude ($d = 1$ for AWGN channels). By subtracting the *a priori* information from the *a posteriori* information, the extrinsic information can be obtained as ${L_1}^e = \frac{2d\tilde{x}}{\sigma^2}$.

3.4.2.3 Soft Symbols Mapper

In order to realize the iterative principle, the complex symbols $\hat{Y}$ are required to be regenerated on the basis of the updated L_2^{pri}. The mapping function is realized in the

soft symbols mapper. L_2^{pri} is the LLR of the bit $\tilde{s}$. The two possible values of $\tilde{s}$ are $+1$ and -1. Therefore, the LLR of its two possible values are defined as

$$L_2^{pri} = ln\frac{P(\tilde{s}=+1)}{P(\tilde{s}=-1)} \tag{3.35}$$

Considering that $P(\tilde{s}=+1) = 1 - P(\tilde{s}=-1)$, and taking the exponent of both sides in (3.35), we ca get:

$$e^{L_2^{pri}} = \frac{P(\tilde{s}=+1)}{1-P(\tilde{s}=+1)} \tag{3.36}$$

Therefore, it is possible to calculate the bit probability for $\tilde{s}=+1$ and $\tilde{s}=-1$ as

$$P(\tilde{s}=+1) = \frac{e^{L_2^{pri}}}{1+e^{L_2^{pri}}} = \frac{1}{1+e^{-L_2^{pri}}} \tag{3.37}$$

$$P(\tilde{s}=-1) = \frac{1}{1+e^{L_2^{pri}}} = \frac{e^{-L_2^{pri}}}{1+e^{-L_2^{pri}}}. \tag{3.38}$$

Hence, the expectation of $\tilde{s}$, which is also the soft symbols sent back to the FFT detector, can be calculated as

$$\hat{Y} = (+1) \times P(\tilde{s}=+1) + (-1) \times P(\tilde{s}=-1) \tag{3.39}$$

3.4.3 Evaluations of Complexity and Performance

3.4.3.1 Complexity

Table 3.7 shows the complexity of various systems. For the purpose of comparisons, we assume that all the systems use the same Turbo architecture. The only different module is the shaded block in Fig. 3.20. In Turbo-SEFDM, The FFT detector has simplified demodulator (3.27) and interference generation (3.28). Additional operation is (3.31), whilst (3.32) has no computations. In terms of Turbo-General (applied to any α), the complexity of demodulator is directly computed according to (2) and the complexity of interference generation is derived in [52]. Turbo-OFDM($\alpha = 1$) is a special case of

Table 3.7: Complexity in number of complex operations per SEFDM symbol per iteration ($\rho = 1$)

	Turbo – General	**Turbo – OFDM**
Multiplications in (2)	N^2	$(N/2) \times log_2 N$
Additions in (2)	$N \times (N-1)$	$N \times log_2 N$
Multiplications in [52]	N^2	N^2
Additions in [52]	$N \times (N-1)$	$N \times (N-1)$
Total	$4N^2 - N$	$2N^2 - N + (3N/2) \times log_2 N$
	Turbo – SEFDM	
Multiplications in (3.27)	$c \times ((N/2) \times log_2 N)$	
Additions in (3.27)	$c \times (N \times log_2 N)$	
Multiplications in (3.28)	$(c-1) \times ((N/2) \times log_2 N)$	
Additions in (3.28)	$(c-1) \times (N \times log_2 N)$	
Multiplications in (3.31)	$(N/2) \times log_2 N$	
Additions in (3.31)	$N \times log_2 N$	
Total	$2c \times ((3N/2) \times log_2 N)$	

the Turbo-General. The demodulator can be realized by means of an FFT algorithm. Interference is still computed based on [52]. Results in Fig. 3.21 indicate that Turbo-SEFDM needs the least operations. When N=1024, Turbo-SEFDM saves close to an order of magnitude operations compared to Turbo-OFDM and Turbo-General.

One advantage of this technique is to reuse the same resources. The FFT detector realizes both demodulations and detections since the two functions are not activated simultaneously. The basic component in the block is FFT elements which can be easily extended to an IFFT by requiring extra computations like conjugating input complex QAM symbols and output complex results. Based on this reuse principle, complexity could be reduced in the future hardware implementations.

3.4.3.2 Performnce

In this section, a perfect CSI is assumed to be known at the receiver side in order to neglect the channel estimation effect. Noting that 1024 sub-carriers are used and no CP and pilot symbols are inserted. The oversampling factor in this section is set to be ρ=2 which indicates the IFFT/FFT size is 2048 and the interleaver size is also 2048.

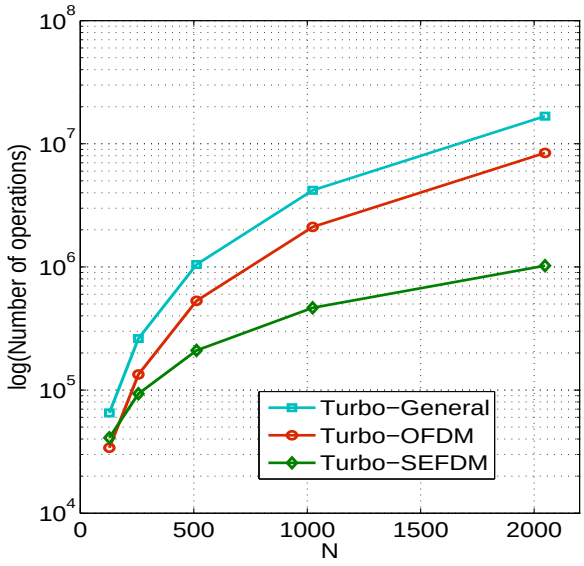

Figure 3.21: Complexity comparisons of different systems.

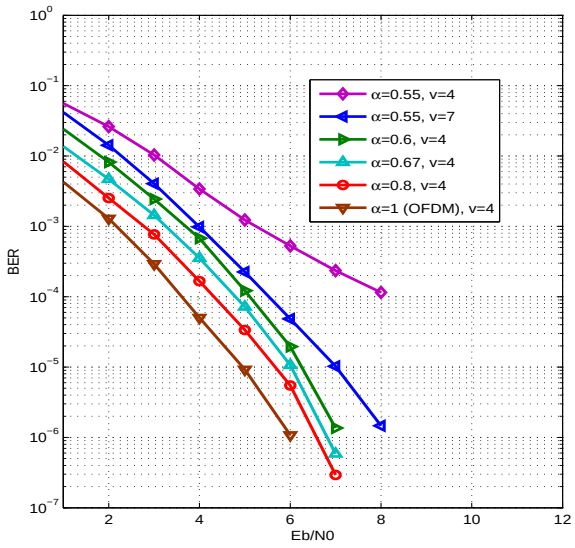

Figure 3.22: Performance of 4QAM-SEFDM in AWGN channel with N=1024 and ρ=2 at various α. The number of iterations is denoted as v.

Simulation results are given in Fig. 3.22. In this case study, 1024 sub-carriers and 4QAM modulation scheme are employed. The default iteration number is 4, while it

can be increased or decreased according to performance requirements. It is clearly seen that curves with α=0.8, 0.67, 0.6 converge at 7dB. The E_b/N_o difference at BER=10^{-6} between $\alpha = 1$ and $\alpha = 0.6$ is approximately 1 dB, and reduces to 0.5 dB with $\alpha = 0.8$. On the other hand, for $\alpha \leq 0.55$, with the same iteration number, curves cannot reach the same performance as others at 7dB. This is due to the fact that too much ICI is introduced with small bandwidth compression factors. However, this performance gap can be reduced by increasing the number of iterations. With 7 iterations, considering α=0.55, the performance gap at BER=10^{-6} is reduced to 2 dB compared to $\alpha = 1$. It is proved that this new system can save 45% of bandwidth with slight performance degradation. It also indicates that the new detector is suitable for 1024 sub-carrier SEFDM system; the highest number of sub-carriers to be considered.

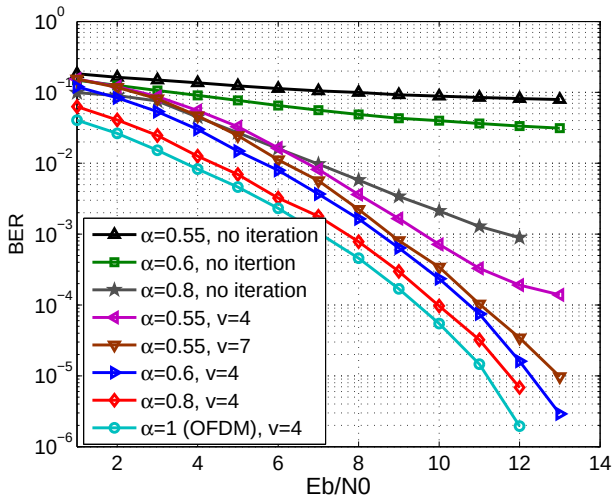

Figure 3.23: Performance of 4QAM-SEFDM in the presence of frequency selective channel with N=1024 and ρ=2 at various α. The number of iterations is denoted as v.

The performance of Turbo-SEFDM is examined in the presence of static frequency selective channel [147]. The channel impulse response is shown as

$$h(t) = 0.8765\delta(t) - 0.2279\delta(t - T_s) + 0.1315\delta(t - 4T_s) - 0.4032e^{\frac{j\pi}{2}}\delta(t - 7T_s) \quad (3.40)$$

This channel model is reserved as the default frequency selective channel for the following simulations and experiments. Assuming perfect CSI is known at the receiver. For time-varying channels, preambles can be periodically inserted to obtain accurate channel estimates. Results in Fig. 3.23 indicate that 4 iterations are sufficient to approach OFDM performance while saving up to 40% of bandwidth. As for the smaller $\alpha = 0.55$, with the same iteration number, it cannot reach the converged performance. This is due to the fact that too much ICI is introduced by using small bandwidth compression factors. However, this performance gap can be reduced by increasing the number of iterations. It is clear seen that the convergence is achieved by 7 iterations. Thus, considering a reasonable iteration number, in a multipath channel scenario, this new system can save up to 45% of bandwidth with slight performance degradation. It also indicates that the new detector is applicable for 1024 non-orthogonal sub-carrier SEFDM systems; the highest number of sub-carriers to be considered so far. In addition, it should be noted that for systems in the frequency selective channel, the performance gap is much smaller compared with systems in an AWGN channel. This can be observed by comparing Fig. 3.22 and Fig. 3.23. It is proved that our technique performs well in multipath channel scenarios.

Higher modulation schemes in the presence of AWGN and frequency selective channels are investigated in this work. Fig. 3.24(a) and Fig. 3.24(b) present the performance of SEFDM and OFDM in different channel scenarios. In the case of 16QAM modulation scheme, each symbol carry more bits than 4QAM, making it more difficult to demap accurately the symbols to the corresponding constellation. In a normal 4QAM SEFDM, the curve with α=0.8 approaches the OFDM curve. However, as the level of modulation increases, a performance degradation appears in SEFDM. It is clearly seen that the curve with α=0.8 no longer converges to the one with α=1 in both AWGN and frequency selective channels. This is because high level interference is introduced in 16QAM.

The convergence features of $\alpha = 0.6$ 4QAM-SEFDM in both AWGN and multipath

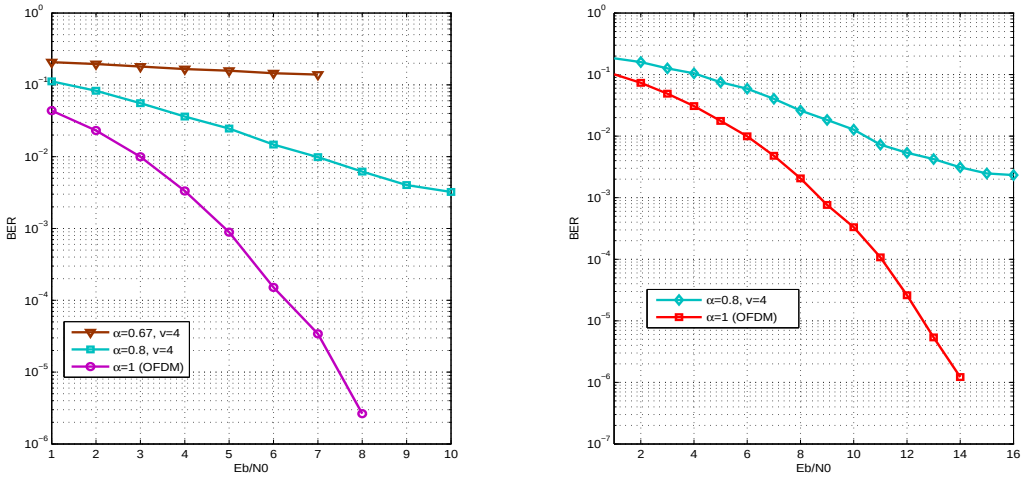

(a) AWGN channel.

(b) Frequency selective channel.

Figure 3.24: Performance of 16QAM-SEFDM in the presence of different channel conditions with N=1024 at various α. The number of iterations is denoted as v.

channels are plotted in Fig. 3.25. It is observed that the performance of both scenarios is significantly improved at the first 3 iterations. By further increasing the number to 4, the performance remains stable. It can be concluded that 4 iterations are sufficient to obtain optimal performance, showing a significant improvement on the work in [52] where a large number of iterations are required.

In Fig. 3.26, we investigate effects of different interleaving sizes for 4QAM-SEFDM systems. Both 2048 bits and 10×2048 bits are considered. The 16QAM performance is included as a reference. The performance gap between the two interleavers are very small. Considering BER=10^{-3}, by using 7 iterations, the difference is only 0.5 dB. Increasing further the iteration number to 12, the difference reduced to 0.25 dB. We note that for any iteration numbers, 2048-bit interleaver and 10×2048-bit interleaver have very similar BER performance, proving that the interleaver size has negligible effects on the performance. Therefore, it is concluded that 2048-bit interleaver is sufficient to decode symbols.

4QAM-SEFDM technique can reach the same spectral efficiency with 16QAM-OFDM. This is based on the premise that α=0.5 is employed in a 4QAM-SEFDM. In

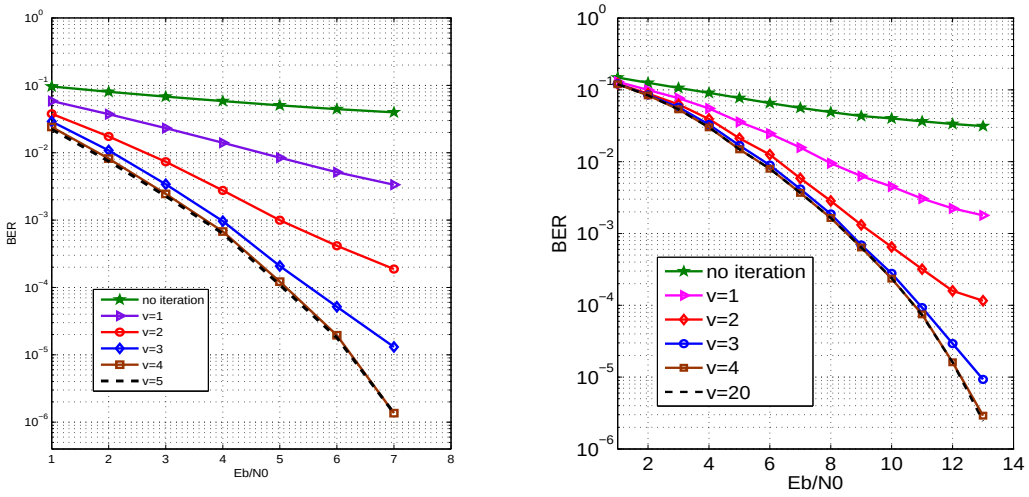

(a) AWGN channel.

(b) Frequency selective channel.

Figure 3.25: Convergence behaviour of 4QAM-SEFDM in the presence of different channels at $\alpha = 0.6$ with various iterations.

Fig. 3.27(a) and Fig. 3.27(b), $\alpha = 0.5$ 4QAM-SEFDM is compared with the spectral efficiency equivalent 16QAM-OFDM. It is apparent that the performance of 4QAM-SEFDM has the same performance with 16QAM-OFDM. However, this is achieved at the cost of large number of iterations. In Fig. 3.27(a), when 4 iterations are used, the performance of $\alpha = 0.5$ SEFDM is much worse than that of OFDM. The performance is improved by increasing it to 19. This is attributable to the fact that more efforts are required to eliminate ICI. Fig. 3.27(b) shows comparisons in frequency selective channels. 4 iterations are also not sufficient for SEFDM to approach OFDM performance. However, in this situation, only 10 iterations are required to obtain a converged performance. No performance improvement is observed with higher number of iterations.

3.4.4 Comparison of Turbo-SEFDM and FTN

The comparison is based on two aspects, which are spectral efficiency and estimated hardware complexity. For FTN, a table labelled Table I in work [131] shows an actual resource utilization for the FTN iterative decoder. However, the actual hardware

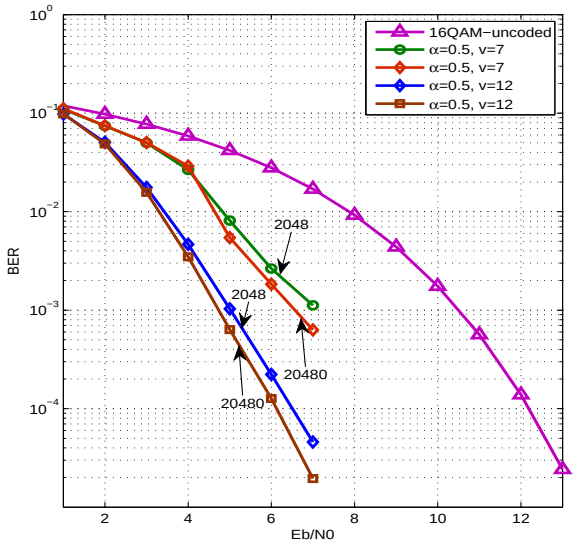

Figure 3.26: Effects of various interleaving sizes.

complexity of the SEFDM soft detector is not available.

Since it is difficult to use accurate data to do the hardware complexity comparison. Therefore, a general comparison is discussed in this section. Work in [131] shows three block diagrams of FTN transmitter (i.e. Fig. 1), receiver (i.e. Fig. 2) and signal detector (Fig. 3). In the first figure, the highlighted blocks are the FTN specific processing blocks at the transmitter side. The OQAM has a similar complexity level compared to QAM. According to the Table I of work [131], the FTN mapper occupies 94360 um^2 CMOS area. Work in [148] explains that the Tx IOTA filter occupies 109545.76 um^2 CMOS area or 2134720 um^2 CMOS area in terms of parallel structure. For an SEFDM transmitter side, it follows a typical OFDM system except for signal generation which requires multiple IFFTs.

At the receiver side, specific FTN blocks are Rx IOTA filter, matched filtering and inner decoder. The IOTA filter resource utilization is referred to [148]. The matched filter consumes 100636 um^2 CMOS area. In the inner decoder, additional FTN mapper and matched filter are used, which indicate additional resource consumptions. Other

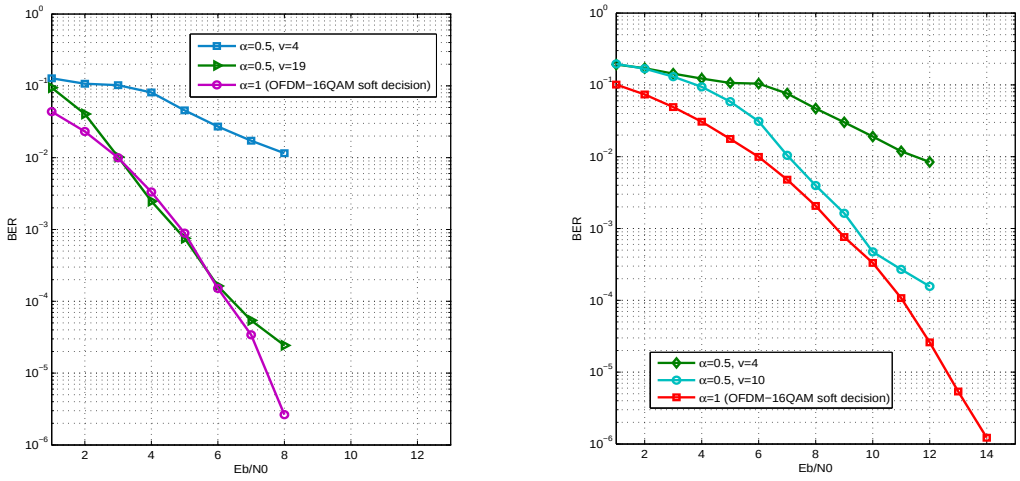

(a) AWGN channel.

(b) Frequency selective channel.

Figure 3.27: Demonstration of two spectral efficiency equivalent systems

blocks such as LLR calculation, soft output calculation, outer decoder, interleaver and deinterleaver are common blocks in the SEFDM soft detector, which are not taken into considerations.

Through a simple and rough estimate, the hardware implementation of an SEFDM system would save resources including two FTN mappers, two IOTA filters and two matched filters.

Table 3.8: Equivalent Spectral Efficiency Comparison.

α(**SEFDM**)	$\mathbf{T_\Delta}$(**FTN**)	**Actual Ratio**
0.48	0.40	2.09
0.53	0.45	1.90
0.60	0.50	1.66
0.71	0.60	1.41
0.86	0.70	1.16
1.09	0.90	0.92

Spectral efficiency can be analyzed based on Table I in work [129] and Table IV in work [130]. It should be noted that in both tables, actual spectral efficiency and theoretical spectral efficiency are presented. This is because that FTN requires time-frequency space to project non-orthogonal packed symbols to orthogonal packed sym-

Table 3.9: Equivalent Spectral Efficiency Comparison.

α(**SEFDM**)	$\mathbf{T_{\Delta}}$(**FTN**)	**Actual Ratio**
0.53	0.40	1.87
0.68	0.50	1.47
0.79	0.60	1.27
0.93	0.70	1.08
1.28	0.90	0.78

bols in order to directly use IFFT. In SEFDM systems, there is no need for the reserved time-frequency space. The actual spectral efficiency is equivalent to the theoretical one. Two comparison tables are shown. Table 3.8 corresponds to work [130] and Table 3.9 is for work [129]. Based on the tables, it is concluded that reaching the same actual ratio, SEFDM relaxes bandwidth compression factors.

3.5 Conclusions

Orthogonality is intentionally violated in SEFDM to improve the spectral efficiency. ICI is introduced since sub-carriers are not packed orthogonally. The interference is proportional to the number of sub-carriers, which poses great challenge to SEFDM since a large number of sub-carriers are required in modern multicarrier systems. In addition, due to the collapse of orthogonality, FFT/IFFT can not be directly used in SEFDM. Therefore, a large size system with attractive performance is in urgent need. This issue is addressed in this chapter.

This chapter commenced with an iterative SEFDM detector and a hybrid version of it that includes an FSD (ID-FSD), designed for different modulation schemes, 4QAM and 16QAM. For 4QAM, we show that for bandwidth compressions of up to 20%, the ID-FSD can achieve the same performance as OFDM. For higher bandwidth savings more than 20%, the complexity/performance trade-offs of the hybrid method are better than those of TSVD-FSD and soft iterative detection alone. The work clearly demonstrates that the iterative detector provides good immunity against interference and the use of a hybrid ID-FSD detector achieves quasi-optimum performance at realistic

complexity, the latter being nearly a 10% of the complexity of a similar performance TSVD-FSD detector. For 16QAM, the hybrid ID-FSD detector with the same complexity of the existing TSVD-FSD detector can reduce power penalty gap by 1.6dB, due to the improvement of using an ID relative to that of TSVD. However, the efficiency of the designed detector is limited by the number of sub-carriers. An alternative solution was developed as a multi-band technique termed Block-SEFDM, which can reduce the complexity of signal detection by separating the spectrum into several sub-bands. This technique is applicable to large size non-orthogonal systems which in this work are tested up to 128 sub-carriers. Furthermore, a low-complexity detector termed BED based on the iterative soft demapping scheme is presented and shown to achieve better performance. Compared with the earlier ID-FSD, we show that BED can bring significant performance gains while its complexity is greatly reduced when compared with a typical single SD scheme. Although the complexity has been significantly reduced using the multi-band architecture, it is still proportional to the number of signal bands. Considering low complexity and acceptable performance, an efficient soft detector composed of an FFT detector and a BCJR decoder has been designed and investigated for a large size SEFDM system. A multiple FFTs structure is employed to realize effectively both demodulation and detection in the FFT detector. The FFT detector works with the BCJR decoder to improve iteratively the system performance. Simulation results show that in the presence of a frequency selective channel, the soft detector can save up to 40% of bandwidth with 1.1 dB power penalty degradation in the case of 1024 non-orthogonal sub-carriers while maintaining acceptable implementation complexity.

In summary, the designs introduced in this chapter propose, for the first time, practical techniques that deal with the SEFDM complexity/performance challenge. These designs are used in the following chapters in practical wireless and optical systems, where their performance is evaluated through especially designed experimental systems.

Chapter 4

Optical Experimental Designs and Validations

4.1 Introduction

Optical fiber communication systems can be categorized as either coherent or non-coherent (direct detection) systems. In general, a coherent system leads to better performance in terms of receiver sensitivity and spectral efficiency when compared to otherwise equivalent direct detection system. However, a coherent system requires the use of a receiver local oscillator laser and accurate phase/frequency offset estimation at the receiver, thus increasing the complexity of both the transmitter and the receiver [149]. On the other hand, a direct detection system may operate with a single photodiode (PD) at the receiver, and does not require carrier frequency and phase offset estimation, due to the elimination of the local oscillator. Thus it is straightforward to be implemented, making direct detection systems well suited to applications where cost saving is of importance. However, in the direct detection scenario, a frequency gap [150] of the same bandwidth as a signal band is needed between an optical carrier and the signal band in order to combat the second-order intermodulation distortion (IMD) at frequencies demodulated close to the optical carrier due to square-law distortion

introduced by a PD. The drawback is that the excess bandwidth occupied by this spectrally inefficient gap cannot be used for data transmission.

The required number of sub-carriers in a wireless system is dependent on the multipath fading channel and the requirement of peak-to-average power ratio (PAPR). Generally, the higher number of sub-carriers, the better immunity against frequency selective channel, especially for a deep fading channel due to a narrow sub-carrier bandwidth and long symbol interval. However, with more sub-carriers, the effect of PAPR will be more severe. A key issue in optical systems is that of chromatic dispersion (CD) and its compensation. CD is similar to time delay spread issue, More specifically, the light consists of many components of different wavelengths. Therefore, they have different velocities. At the receiver, a delayed copy will overlap the original version leading to bit errors. Channel estimation has to be used with the assistance of CP. Hence the attraction of optical-orthogonal frequency division multiplexing (O-OFDM) with its high tolerance to CD and flexibility resulting in its consideration as one of the attractive candidates for future optical communication techniques [151]. This technique can make multiple narrow bandwidth sub-carriers overlap at orthogonal locations such as $\frac{1}{T}$ where T is the period of one OFDM symbol, thus spectral efficiency is doubled compared to a typical non-overlapping multicarrier system.

A number of multicarrier techniques have been developed with the aim of improving optical spectral efficiency. The technique termed optical-fast orthogonal frequency division multiplexing (O-FOFDM) reported in [126] follows the same idea derived from [21] where 50% of electrical bandwidth is saved by packing sub-carriers closer with a frequency separation $\frac{1}{2T}$ where T is the period of one FOFDM symbol. However, it is limited to one dimensional modulation schemes, such as BPSK and M-ary ASK. Work in [152] proposed a spectrally efficient scheme termed virtual single-sideband OFDM (VSSB-OFDM) that uses no frequency gap between an optical carrier and a signal band. Thus spectral efficiency is doubled in the optical domain. However, this achievement is at the cost of complicated signal processing at the receiver. A technique

termed dense orthogonal frequency division multiplexing (DOFDM) in [153] achieves optical bandwidth saving by narrowing the spacing between two optical sub-channels. However, the optical DOFDM is only applicable to systems with two sub-channels and in a scenario that an optical sub-channel spacing is close to an equivalent OFDM. Taking into account hardware, due to the limitation of sampling rate in DAC and ADC, data transmission speed is severely restricted. Work in [154] proposed a multi-band technique termed orthogonal band multiplexed OFDM (OBM-OFDM) where the entire spectrum is divided into several parallel sub-bands with a guard band between each. Indeed, the inspiration of this technique is similar to the carrier aggregation scenario in LTE-Advanced discussed in Chapter 5. As a special form of a broader class of multi-carrier modulation (MCM), SEFDM provides a benefit of providing enhanced bandwidth utilization by allowing the sub-carriers to be placed at closer frequency intervals while maintaining the same transmission rate per sub-carrier.

With the aim of saving bandwidth or increasing delivered bit rate, in this chapter, two different systems are demonstrated. An uncoded non-orthogonal 10 Gbit/s direct detection optical multicarrier system termed DDO-SEFDM [54] [55] is experimentally demonstrated followed by a 24 Gbit/s coherent detection CO-SEFDM [72] system. [1]

4.2 Direct Detection Optical-SEFDM

A direct detection optical OFDM/SEFDM scenario is considered in this section due to its simple receiver design. However, in the direct detection scenario, a frequency gap [150] of the same bandwidth as a signal band is needed between an optical carrier and the signal band in order to combat the second-order IMD close to the optical carrier due to square-law distortion introduced by a photodiode. The drawback is that the excess bandwidth occupied by the spectrally inefficient gap cannot be used for

[1] The direct detection experimental system in this chapter was designed by the author and constructed then tested in the Institute of Photonics Technology at Jinan university in China. The coherent experimental system was designed and constructed in UCL using the optical testbed of UCL's Optical Networks Group.

data transmission. An illustration of the drawback is shown in Fig. 4.1. The first inset shows a typical direct detection optical-OFDM (DDO-OFDM) transmission flow. Firstly, a baseband OFDM signal is up converted to an optical frequency, with a certain frequency gap from the optical carrier. At the receiver, after a photodiode operation, the optical signal is moved back to the electrical domain with the introduction of IMD which is highlighted in red. It is apparent that the reserved frequency gap is distorted by the IMD and can not be used for data transmission. Therefore, for OFDM, the bandwidth occupation is $2B$. On the other hand, the baseband spectrum is compressed by $(1-\alpha)\times 100\%$ in SEFDM further leading to the compression of the frequency gap. Therefore, by transmitting the same amount of data, the bandwidth occupation of SEFDM is $2\alpha B$. This benefit has been experimentally shown in [54].

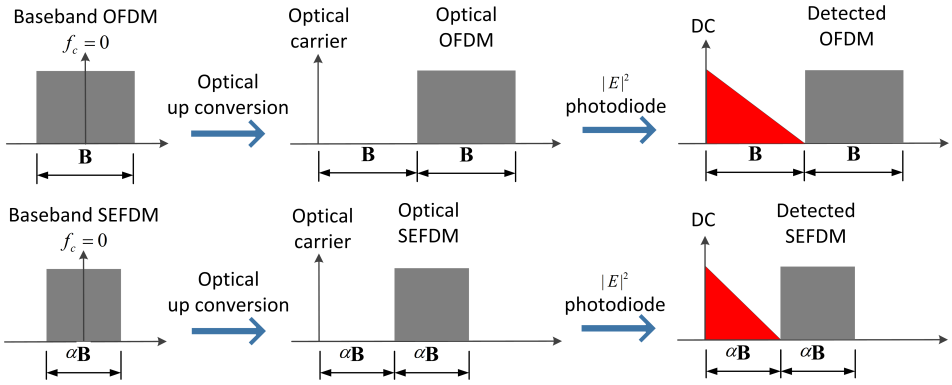

Figure 4.1: Comparison of spectrum occupation for DDO-OFDM and DDO-SEFDM.

The bandwidth saving achieved in such a non-orthogonal multicarrier system comes at the expense of interference which complicates the design of a receiver. Several detection schemes are described in section 2.6 of this thesis, where they are either too complicated or resulting in poor performance. In this work, we examine a low-complexity hybrid detector ID-FSD [52] for the DDO-SEFDM system with 16 sub-carriers. The reason for selecting 16 is due to the practical complexity. DDO-SEFDM essentially deals with spectrum saving issues both in electrical and optical domains. It should be noted that both the signal band and the frequency gap are compressed in DDO-SEFDM leading to further improved spectral efficiency.

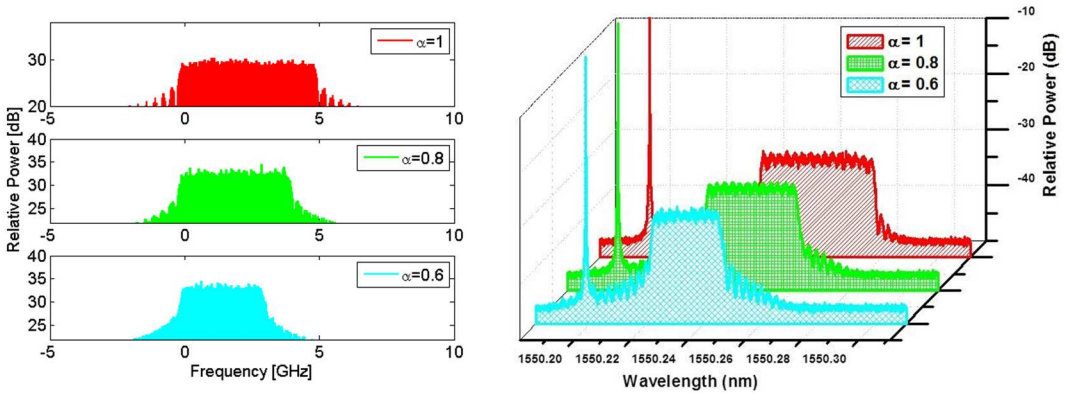

Figure 4.2: Illustration of 10 Gb/s single sideband DDO-SEFDM and DDO-OFDM with 4QAM modulation format. Electrical spectrum (left) and optical spectrum of signal and optical carrier (right).

Fig. 4.2 illustrates both the electrical and optical spectra of single-sideband (SSB) DDO-OFDM and SSB DDO-SEFDM with different levels of bandwidth saving. It is apparent in Fig. 4.2 that the bandwidth of DDO-SEFDM with $\alpha = 0.6$ occupies 60% bandwidth of an equivalent DDO-OFDM system both in the electrical and optical domains. In the second inset, the "impulses" indicate optical carriers for three systems of different bandwidth compression factors. It is evident that a frequency gap is introduced between the optical carrier and the signal band. In general, DDO-OFDM utilizes a sufficient frequency gap between the optical carrier and the signal band to prevent the signal from being interfered by the signal-signal beat interference (SSBI). The minimum frequency gap should be equal to the bandwidth of the signal band. In addition, it is shown that the frequency gap is also determined by the bandwidth compression factor. With a small α, the gap is reduced leading to spectrum saving. The reduction of α therefore further improves the spectral efficiency alas at the expense of detection complexity. Noting that the ICI introduced in DDO-SEFDM requires sophisticated signal detection, which is more complicated than that required for DDO-OFDM, where simple detectors such as ZF suffice. To maintain low receiver complexity whilst saving bandwidth, the proposed hybrid ID-FSD [52] detector is utilized in the Optical SEFDM system.

4.2.1 Intensity Modulation DDO-SEFDM System

Three different DDO-OFDM transmitter architectures have been studied in work [155]. In the first system, one DAC is required since a real valued OFDM signal is generated using IFFT. The input vector to the IFFT is constrained to have Hermitian symmetry so that the imaginary part of the IFFT output is zero. The guard band is introduced by adding zeros at the beginning and the end of the input IFFT vector. It indicates that the spectral efficiency is reduced. The benefit is the simplified transmitter design. In the second transmitter design, two DACs are introduced with an RF upconversion stage. Therefore, complex OFDM symbols can be mixed with the RF carrier before optical modulation. The guard band is determined by the RF carrier frequency. Thus, it is more spectrally efficient since all sub-carriers are used to transmit data. The third transmitter system generates an optical single side band using a signal and its Hilbert transform. A Hilbert transform can be generated directly in an OFDM transmitter by setting half of the IFFT inputs to zero. Then a single side band IFFT output signal is generated to drive an optical I/Q modulator. The guard band is introduced by setting several sub-carriers to zero, which is not spectrally efficient.

In this section, a DDO-SEFDM experimental system, employing the second transmitter architecture, is illustrated in Fig. 4.3. The distributed feedback (DFB) laser is modulated by Mach-Zehnder modulator (MZM) driven by the RF SEFDM signal to create a double sideband (DSB) optical signal. The RF SEFDM signal is generated via an IQ-Mixer which up-converts the baseband SEFDM signal to the desired carrier frequency f_{IF}. The bias for the MZM and the RF SEFDM signal power have to be carefully adjusted to maintain an optimum carrier to signal power ratio (CSPR), which is defined as the power ratio of carrier to first-order sideband [156], and to suppress the second-order components for getting the minimum required optical signal-to-noise ratio (OSNR) at a target bit error ratio (BER, usually at 3.8×10^{-3}, assuming use of forward error correction [157]). The optical single sideband (OSSB) filter is used to block one sideband and allow only one sideband together with the optical carrier to

pass, with the aim of reducing the CD effect. An erbium doped fiber amplifier (EDFA) can be added to enhance and adjust the output optical power. The optical transmission link is constructed with 80 km standard single mode fiber (SSMF) and EDFA amplification. At the receiver side, after filtering the amplified spontaneous emission (ASE) noise out of the required band, a direct detection PD is used to recover the electrical RF SEFDM signal at the cost of square-law distortion. The effect of SSBI is illustrated in the inset above the photodiode module.

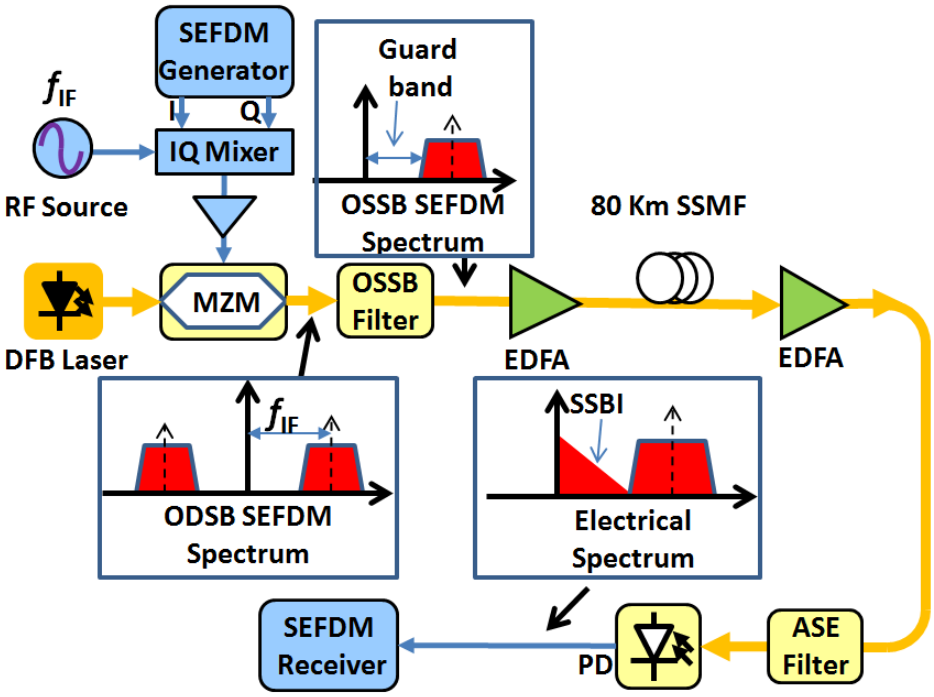

Figure 4.3: Block diagram of the single sideband DDO-SEFDM experimental system.

4.2.2 Experimental Setup

Fig. 4.4 shows the experimental setup of single sideband DDO-SEFDM with 16 subcarriers and the bandwidth compression factor may be varied from 1 down to 0.7. At the transmitter side, an initial signal is generated through 4QAM symbol mapping, inverse fractional Fourier transform (IFrFT)[31][158], 1/16 CP addition and parallel to serial conversion which are all operated offline on a computing platform. Then, the

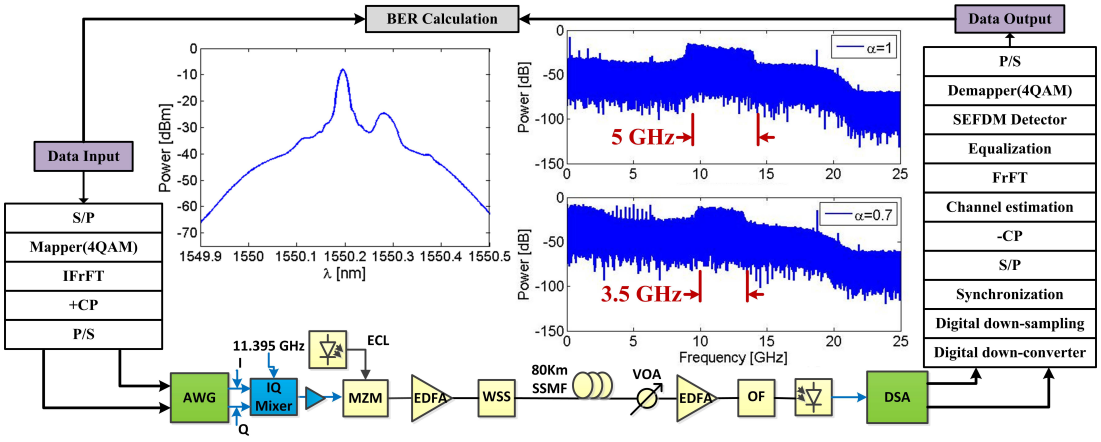

Figure 4.4: Experimental setup and measured spectra of 10 Gb/s DDO-SEFDM system. Optical spectrum (left) and electrical spectra for OFDM (top right) and SEFDM (bottom right)

real and imaginary part of the SEFDM signal are uploaded into a Tektronix arbitrary waveform generator (AWG) 7122B operated at 10 GS/s. To avoid second-order IMD due to the square-law PD, the SEFDM spectrum is separated from the optical carrier by a frequency gap. An IQ mixer is used, with an 11.395 GHz RF signal which can both combine I/Q parts and up-convert the baseband signal. After amplification, the signal is modulated, onto an optical carrier generated from an external-cavity laser (ECL) at 1550.196 nm and fed into a MZM, to generate a double sideband optical signal. A single sideband DDO-SEFDM signal (Fig. 4.4, left spectrum plot) is generated by using a wavelength selective switch (WSS) 4000S with 20 GHz optical filter bandwidth and then passed through 80 km of SSMF to get 10 Gb/s DDO-SEFDM signals. An optical EDFA is used to compensate for the loss of optical link. At the receiver, an optical filter (OF) is used to suppress ASE. A photodiode with a bandwidth of 20 GHz is used to detect the optical signal. The detected RF signal is then fed into a Tektronix real-time scope; acquired at 50 GS/s and processed off-line. The retrieved signal (Fig. 4.4, bottom right spectrum) is then transferred to a computing platform for offline processing. The signal after down-conversion and down-sampling is then synchronized and delivered to a serial-to-parallel (S/P) transform module. The CP is stripped away

and the fractional Fourier transform (FrFT) module demodulates the signal. Due to CD, phase distortion is introduced and this impact is equalized in an equalizer. The compensated SEFDM symbols are then detected in the SEFDM detector and data is recovered into a serial bit stream before BER evaluation.

4.2.3 Experimental Results

Measurements of a 10 Gb/s DDO-SEFDM system, in both back-to-back (B2B) and 80 km SSMF scenarios, are taken. The implementation of the ID-FSD requires setting the number of iterations, which for this experiment was conservatively set to 20. The channel estimation was done by sending 1000 SEFDM training symbols, only once at the start of measurements.

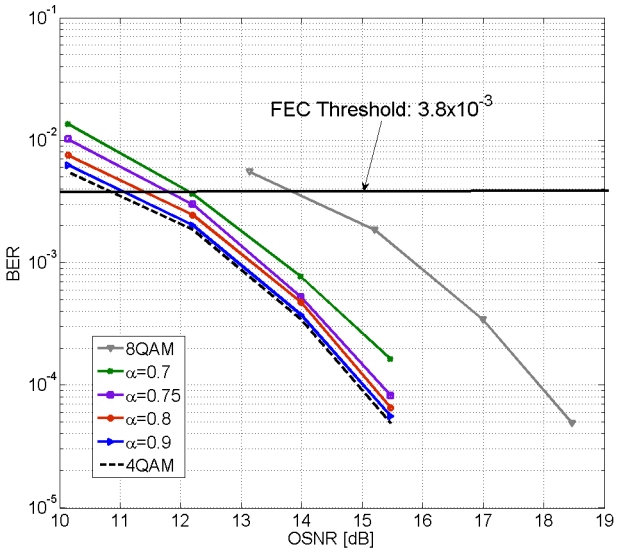

Figure 4.5: BER versus OSNR for B2B experiment, N=16.

Fig. 4.5 depicts the B2B measurement of the BER performance, assisted by the ID-FSD detector, for different values of α. The figure shows that when α=0.8, the curve is virtually the same as the theoretical one, which indicates the hybrid detector has quasi-optimum performance. Additionally, this result proves Mazo's 25 percent

limit theory in the optical domain. It should be noted that 4QAM DDO-SEFDM with $\alpha = 0.7$ has a similar spectral efficiency (SE=2/0.7=2.86) to an 8QAM DDO-OFDM (SE=3). The OSNR difference at BER $= 3.8 \times 10^{-3}$ between $\alpha = 0.7$ and $\alpha = 1$ is approximately 1 dB. For the same bit rate, the DDO-SEFDM system with $\alpha = 0.7$ outperforms an 8QAM DDO-OFDM system by 1.6 dB. This experimentally proves that a lower modulation scheme can achieve a better performance by replacing a higher one of equivalent bandwidth.

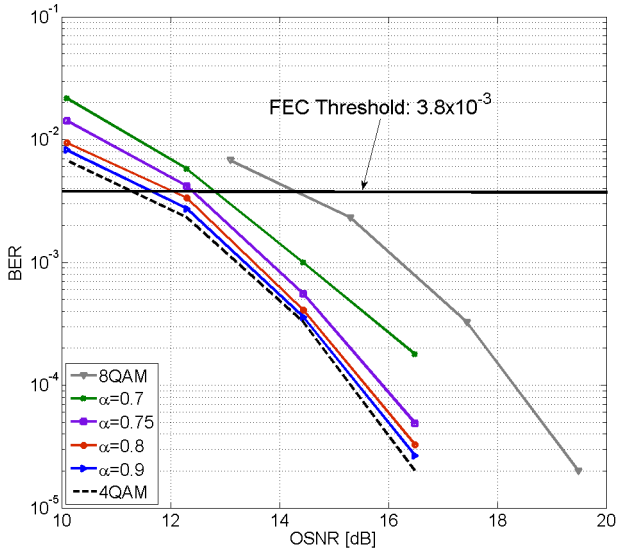

Figure 4.6: BER versus OSNR for 80 km experiment, N=16.

Figure 4.6 shows the performance of the 80 km transmission experiment. With the introduction of a fiber, it is clear that a balance exists between bandwidth saving and OSNR values required for a given bit error rate. For example, 20% bandwidth saving ($\alpha = 0.8$) the OSNR penalty of 0.7 dB is observed whilst for 30% bandwidth saving ($\alpha = 0.7$) the OSNR penalty becomes 1.5 dB. The proposed technique still performs better than standard 8QAM by 1.6 dB, again verifying the DDO-SEFDM system operation and practically demonstrating that bandwidth may be saved with limited compromise of error performance.

4.3 Coherent Detection Optical-SEFDM

The notable benefit of a direct detection system is its low implementation complexity. However, its spectral efficiency is reduced due to the gap introduced between an optical carrier and a signal band. In order to improve further the spectral efficiency, a dual polarization coherent detection scheme is designed and demonstrated in this section.

4.3.1 Principle and Key Digital Signal Processing

In a coherent optical system, the received signal is impaired by the frequency offset between the optical transmitter and the local oscillator (LO) within the coherent receiver, and combined phase noise of both lasers. The received signal, $y(t)$, is represented as

$$y(t) = x(t)exp[j(2\pi\Delta ft + \phi(t))] + z(t) \tag{4.1}$$

where x(t) is an OFDM signal, Δf is the frequency offset between the incoming signal and the LO, $\phi(t)$ is the time-varying combined phase noise of the transmitter and LO lasers, and $z(t)$ is AWGN.

Carrier frequency offset and phase noise are mitigated using optical carrier phase estimation where both the amount of frequency shift, and the time varying phase can be estimated. In addition, as both polarizations are used independently, the effects of polarization rotation and polarization mode dispersion (PMD) that occur during transmission must be addressed at the receiver. In conventional OFDM, a frame header is usually used to estimate and correct the frequency offset and the channel response is estimated using a training sequence. Furthermore, some sub-carriers are used as pilots for symbol phase correction. In SEFDM systems, these approaches to symbol phase correction and channel estimation do not work because of the inherent ICI.

To overcome this problem we use the specially designed transmission frame shown in Fig. 4.7, which consists of two OFDM timing synchronization symbols transmitted on a single polarization, followed by 20 dual polarization (DP)-OFDM training symbols

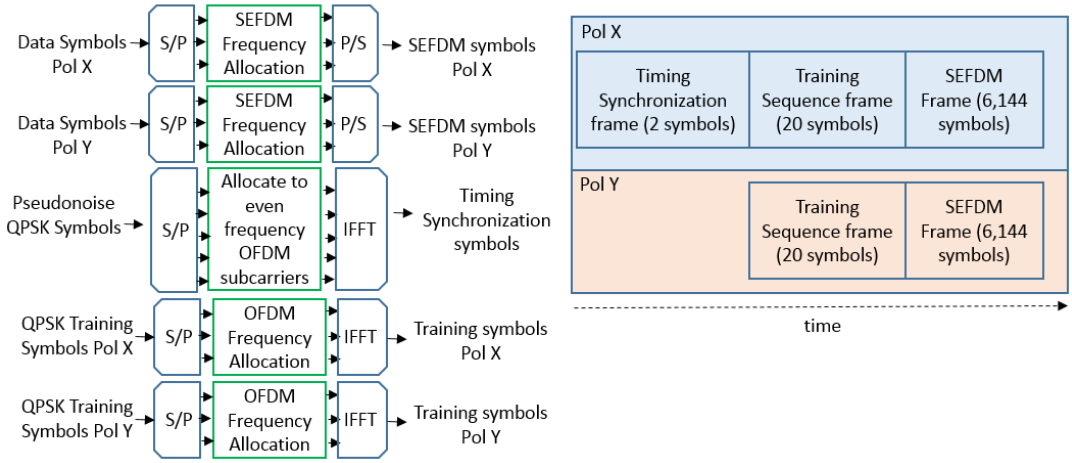

Figure 4.7: Simplified Block diagram of transmitter implementation (left) and the transmitted signal frame format.

on both polarizations. This is followed by a 6,144-symbol SEFDM data payload. A direct current (DC) pilot tone is also inserted on a single polarization at the transmitter to allow for frequency and phase offset correction at the receiver [159].

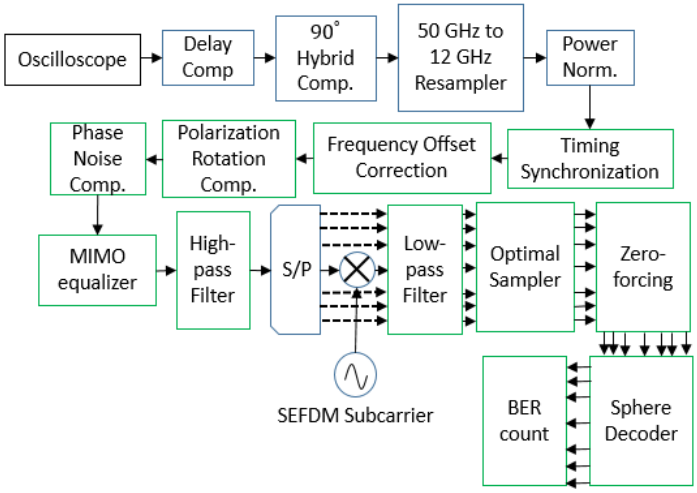

Figure 4.8: Block diagram of receiver digital signal processing.

Fig. 4.8 shows the DSP chain at the receiver-end of the DP-CO-SEFDM system. Firstly, the captured waveform from the oscilloscope was compensated for the skew of the coherent receiver and the varying responsivities of the balanced PDs. Subsequently, signals are resampled at 12 GS/s, before the first-stage gain-control.

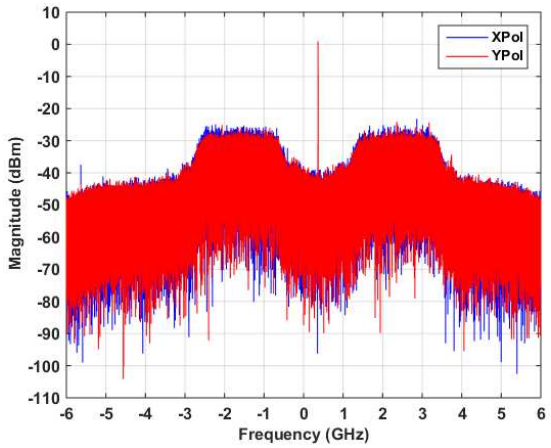

Figure 4.9: Received spectrum of 24 Gbit/s QPSK DP-CO-SEFDM, experimentally obtained after 80 km transmission at OSNR of 12.41 dB, with α=0.67.

4.3.1.1 Frame Timing synchronization

The Schmidl and Cox algorithm [160] was used for frame synchronization and to estimate the polarization angle of the received signal. As the timing synchronization symbol was only transmitted on one polarization, the angle could be estimated based on the distribution of the timing synchronization's energy across the two received polarization states.

4.3.1.2 Frequency Offset and Phase Noise Compensation

Before the polarization of the received signal was determined, the frequency offset was estimated using the DC pilot tone by performing a peak-search of the spectrum of the received signal, shown in Fig. 4.9. After polarization rotation compensation, the time resolved phase noise was estimated by digitally filtering out the DC pilot and the conjugate of the estimate was subsequently applied to the complex signal.

4.3.1.3 Channel Equalization

Fig. 4.10 depicts the channel equalization process. OFDM training symbols were used to estimate the channel response using the least squares method [161]. A MIMO equalizer was then used to compensate for the channel response of the SEFDM payload.

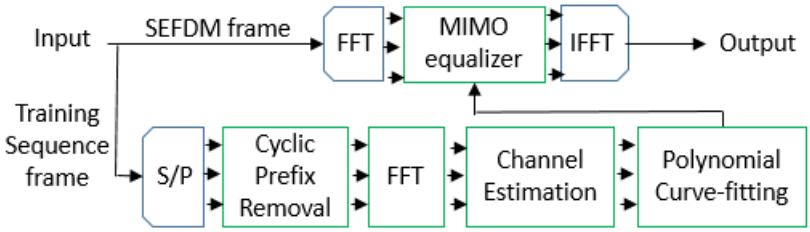

Figure 4.10: Block diagram of DP-CO-SEFDM MIMO equalizer.

As there is a frequency difference between the OFDM training sequence and SEFDM subcarriers, where the latter is a function of α, the estimated channel response was first interpolated using a second order polynomial in the frequency domain. Compensation was then performed on the entire frame.

The signal was then high-pass filtered to remove the DC pilot tone optical carrier and prevent from interfering with the ZF decoder. The SEFDM carriers were then demultiplexed and a matched filter was applied before down-sampling to one sample per symbol. The optimal sampling time was determined through an auto-correlation of the match-filtered samples. The deterministic ICI was subsequently compensated by applying a ZF detector whose coefficients were calculated from knowledge of the cross-correlation of the sub-carriers [54]. This process was followed by a sphere decoder, as described in [54] and [38].

4.3.2 Experimental Setup

A schematic of the DP-CO-SEFDM transmission system is illustrated in Fig. 4.11. The output of an ECL with a linewidth of 100 kHz was passed directly into an integrated dual polarization IQ modulator. The transmitted SEFDM signal comprises two SEFDM symbols each has 8 sub-carriers and each sub-carrier carries a single QPSK symbol. The signal occupying a total bandwidth ranging from 6 GHz (α=1) to 4.02 GHz (α=0.67) in each polarization. A conservatively set guard band of 1.85 GHz around DC was used to allow for the insertion of a DC pilot and to separate the positive and negative frequency sub-carriers in order to ease the detection process and

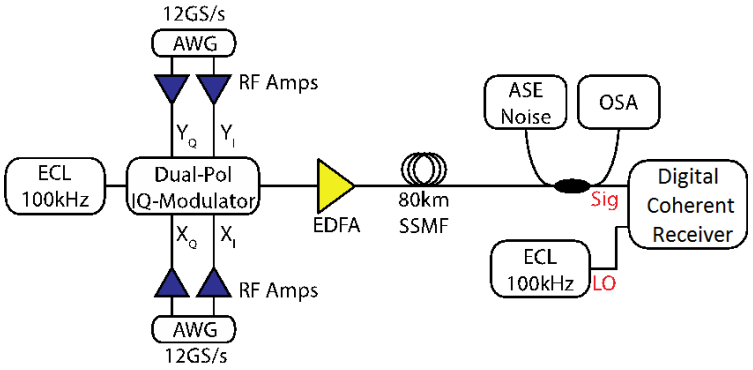

Figure 4.11: Experimental setup of DP-CO-SEFDM transmission system.

reduce the SEFDM detector complexity. The IQ components of the DP-CO-SEFDM signal were pre-emphasized to overcome the electrical response of the transmitter before being loaded onto a pair of AWG operating at 12 GS/s. Linear electrical amplifiers increased the voltage swing of the multi-level electrical drive signals before they were applied to the modulator. A DC pilot tone was inserted by slightly detuning the bias of the IQ modulator (3.2% of Vpi, relative to the modulator null point), as described in [162].

The DP-CO-SEFDM signal was amplified to overcome the insertion loss of the integrated modulator before propagating over 80 km of SSMF, which exhibited a span loss of 15.4 dB. The transmitted channel was coherently detected using a polarization diverse coherent receiver, which utilized a second 100 kHz ECL as a LO. The received signal was captured using a 50 GS/s real-time sampling oscilloscope with a 16 GHz analogue electrical bandwidth. For B2B error analysis, the output of the EDFA was passed directly into the digital coherent receiver and an ASE noise source was used to vary the OSNR. The DSP implementation was performed offline using MATLAB

4.3.3 Experimental Results

Fig. 4.12 and Fig. 4.13 show experimentally obtained results of the DP-CO-SEFDM signal for B2B and 80 km link configurations, respectively. The number of test-bits per burst was 393,216 bits. QPSK with α values of 1, 0.8, and 0.67 along with 8QAM with

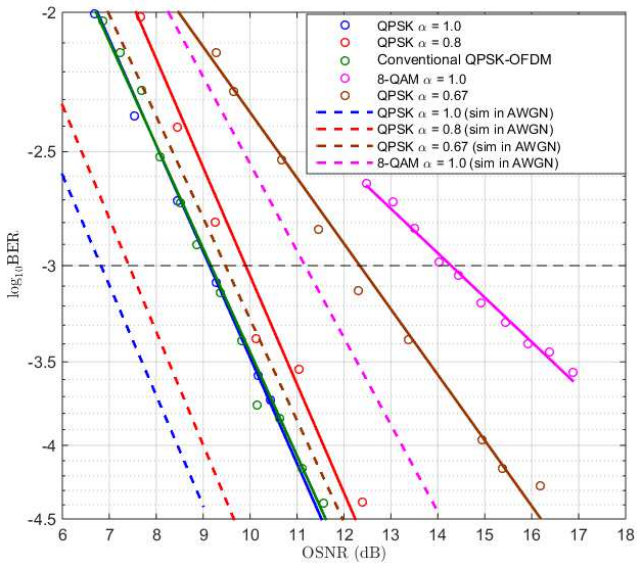

Figure 4.12: BER as a function of OSNR, obtained experimentally using a back-to-back setup, along with simulated performance in ideal AWGN channel (no optical impairments) at various values of α.

α of 1 were analyzed. It should also be deduced that DP-CO-SEFDM with α of 1 simply represents DP-OFDM with identical settings. In addition, a QPSK based conventional DP-OFDM configuration, which required periodic pilot symbols, was also analyzed as a performance reference. DP-CO-SEFDM was configured to transmission rate of 24 Gbit/s using 16 sub-carriers. Transmitting at the same bit-rate, the conventional DP-OFDM used 256 sub-carriers, 16 of which were uniformly-spaced pilot sub-carriers. In Fig. 4.12, simulated results of SEFDM performance in AWGN channel under various values of α are also shown for reference. The simulations were performed using 6,553,600 test-bits per burst.

Observing the experimental B2B results shown in Fig. 4.12, an OSNR of 9.1 dB is required to achieve a BER of 10^{-3} for QPSK based DP-OFDM, i.e., DP-CO-SEFDM when α was 1. This increased to 12.3 dB as bandwidth was reduced by 33% by using DP-CO-SEFDM when α was 0.67, thus representing an additional implementation penalty of 3.2 dB. Similarly, the experimental findings from the 80 km transmission link in Fig. 4.13, reveals this implementation penalty to be 3.26 dB. It should be

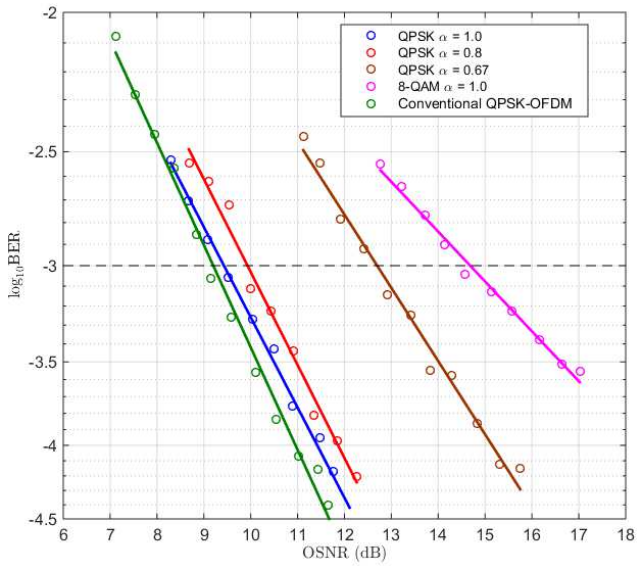

Figure 4.13: BER as a function of OSNR, obtained experimentally using 80 km transmission setup at various values of α.

noted that in the simulated AWGN channel, the additional implementation penalty is a smaller value of 2.65 dB. This suggests that the penalty from optical channel varies with α.

The spectral efficiency of QPSK based SEFDM with α of 0.67 is 2.99 bit/s/Hz. This is approximately the same to 3 bit/s/Hz spectral efficiency of 8QAM based OFDM, i.e., SEFDM with α of 1. Hence, the performance comparison between these two cases is of interest. From Fig. 4.12, experimental results in B2B configuration at BER of 10^{-3} show that QPSK based DP-CO-SEFDM with α of 0.67 outperformed 8QAM based DP-OFDM, giving performance gain of 1.94 dB. Furthermore, observing Fig. 4.13, this performance gain in 80 km link is found to be 2 dB. It can be concluded that at a given spectral efficiency in a dual polarization coherent optical channel, and with equivalent level of impairment correction, SEFDM with a lower order modulation scheme can provide better performance relative to OFDM with a higher order modulation scheme.

The performance of DP-CO-SEFDM's MIMO equalizer can be evaluated by comparing the BER results with and without polarization rotation and PMD. This is equivalent to considering the performance difference between B2B and 80 km link con-

figurations, since the former excluded both effects from the channel. Using the conventional DP-OFDM, where there is no frequency difference between the OFDM training sequence and SEFDM sub-carriers as reference, the performance difference at the BER of 10^{-3} between the B2B and 80 km transmission is only 0.02 dB. As for QPSK DP-CO-SEFDM, the estimated channel response was interpolated as described in Section 4.3.1.3, the performance differences are larger, specifically, 0.29 dB for α of 1, and 0.34 dB for α of 0.67. This penalty is also observed in 8QAM DP-CO-SEFDM with α of 1, giving a performance difference of 0.4 dB. These findings imply that channel estimation in DP-CO-SEFDM using the described configuration introduces a small performance penalty relative to the conventional DP-OFDM.

4.4 Conclusions

Two optical systems are experimentally evaluated in this chapter. Firstly, a single sideband DDO-SEFDM system with various bandwidth compression factors was tested. Relative to DDO-OFDM, up to 20 percent bandwidth saving may be obtained with negligible performance loss. For higher bandwidth saving, we experimentally show that a 4QAM DDO-SEFDM system may be constructed to have a similar spectral efficiency to that of 8QAM DDO-OFDM but with better error performance. Then, the proposed CO-SEFDM system demonstrates that for the same level of impairment correction, and approximately the same spectral efficiency, QPSK based DP-CO-SEFDM can outperform 8QAM based DP-CO-OFDM. This is the first experimental demonstration of these systems that save bandwidth in both the electrical and optical domains and may be used in future optical multicarrier experimental systems to improve spectral efficiency when small error performance degradation may be tolerated.

Chapter 5

Beyond LTE-Advanced: Practical Implementation of Bandwidth Compressed Carrier Aggregation

5.1 Introduction

The demand for broadband service is growing exponentially and the third generation partnership project (3GPP) is committed to establishing new standards to satisfy this requirement. Long term evolution (LTE) release 8 [1] was proposed and has been commercialized. In order to achieve a higher data rate, LTE-Advanced release 10 [15] was proposed and many new features have been standardized such as CA, enhanced MIMO and CoMP. Among these techniques, CA [163][164][165][166] is the distinct one. A system with aggregated bandwidth is composed of many component carriers (CCs). The bandwidth of each CC can be 1.4, 3, 5, 10, 15 or 20 MHz which are all defined in LTE release 8/9 since LTE-Advanced intends to provide backward compatibility to LTE. With the combination of 5 CCs of 20 MHz, LTE-Advanced can support a maximum 100 MHz aggregated bandwidth.

There are several benefits of the CA technique introduced in LTE-Advanced:

- **Lower Speed DAC.** In terms of a wide band signal, a typical DAC is not fast enough to support such a wide bandwidth. Therefore, multiple lower speed DACs can be used instead of a single high speed one. In such a way, a lower speed DAC is required to operate at the bandwidth of each CC, which is approximately scaled down by a factor equal to the number of CCs. This releases the DAC bandwidth bottleneck requirement.

- **Simplified Signal Processing.** Signal generation will be simplified by using multiple shorter IFFTs instead of a single long IFFT. In addition, channel estimation and signal detection become simpler by operating independently on each CC.

- **Multiuser Diversity.** Different CCs have different center frequencies. For different moving users, their Doppler shifts are different. This indicates that at different frequency bands users could experience different channel distortions. A CA system will allow each user to select its own preferred CCs based on their fading channel condition.

- **Lower PAPR.** Since the number of sub-carriers in each CC is reduced, the PAPR of each band is therefore reduced. The nonlinearity issue from power amplifier (PA) could be solved.

- **Easy Deployment.**

  Network operators can increase their network throughput and capacity through minor software upgrade. This is a cost effective solution since hardware has already been implemented over multiple frequencies.

The flexible use of legacy fragmented frequency bands in CA introduces a potential way to support a wider transmission bandwidth. However, this benefit is subject to spectrum availability. In this chapter, we combine respective advantages from both CA and SEFDM. CA is a bandwidth extension scheme while SEFDM is a bandwidth

compression technique. The combination of these two techniques results in more aggregated CCs in a given bandwidth. On one side, a higher throughput is achieved without consuming extra bandwidth. On the other side, more users (more CCs) can share the same bandwidth. Theoretical work is firstly presented, then in order to evaluate the technique in a more realistic RF scenario, an LTE-Advanced based CA-SEFDM experimental testbed is demonstrated where more CCs can be aggregated in a given bandwidth with negligible performance degradation. The experimental testbed consists of one 3026C digital RF signal generator, one 3035C RF digitizer, one Spirent VR5 channel emulator and two DSP processing blocks. The 3026C module is used at the transmitter to convert a digital signal to an RF signal; the VR5 can emulate various real-time fading channels and the 3035C is a module at the receiver side and is integrated in the same Aeroflex PCI extensions for instrumentation (PXI) with the 3026C module. The 3035C module captures the RF signal and converts it back to baseband. Finally, the baseband signal is delivered to the DSP block for signal detection. In this experiment, the signal format is configured following LTE release 10 with minor adjustments. Moreover, in order to emulate a real wireless environment, a real-time LTE fading channel model termed Extended Pedestrian A (EPA) [167] with 5 Hz Doppler shift is configured in the VR5. Thus, CSI is not known at the receiver side and the multipath fading channel has to be estimated using real-world channel measurements and further used to compensate for distorted signals.

5.2 Principle of CA-SEFDM

LTE-Advanced provides many different carrier aggregation scenarios to increase the system bandwidth beyond 20 MHz. CCs can be aggregated contiguously in the same band (intra-band contiguous CA), or non-contiguous in the same band (intra-band non-contiguous CA), or in different bands (inter-band non-contiguous CA). Each aggregated CC can have a different bandwidth. From the perspective of digital signal processing, there is no obvious difference among them. However, from an RF implementation

perspective [164][165][166], the intra-band contiguous CA is the easiest type. In this case, a single RF filter and a single IFFT/FFT can be used to reduce implementation complexity. However, it requires a wider bandwidth RF filter. For non-contiguous CA scenario either in the same band or different bands, several RF filters and IFFTs/FFTs have to be used. In this section, to simplify our demonstration, we employ the intra-band contiguous CA scheme. There are many transmitter architectures for the scenario. The stage where CCs are combined leads to alternative architectures [168]. For the sake of simplicity, we employ a conventional CA transmitter architecture as introduced in [168]. In this architecture, CCs are combined at digital baseband before DAC, which means a single IFFT is adopted.

In a typical CA-OFDM scenario, many CCs are aggregated to expand the bandwidth. Some practical challenges such as Doppler frequency shift and frequency aliasing for implementing CA are discussed in [169]. Simulation results show that the Doppler shift has limited impact while frequency aliasing will generate much more interference between adjacent component carriers. Therefore, a 10% frequency gap [1] is necessarily introduced as a protection guard band between two CCs. Our proposal is to compress both the signal band and the protection band. Thus, we can aggregate more CCs in a given bandwidth resulting in a more spectrally efficient transmission. The general CA-SEFDM idea is illustrated in Fig. 5.1. At the first stage, a single sub-carrier with 15 kHz baseband bandwidth is generated. The violation of the orthogonality principle leads to the new SEFDM signal as illustrated at the second stage in Fig. 5.1. Both OFDM and SEFDM sub-carriers packing schemes are demonstrated for the purpose of comparison. Through orthogonal multiplexing, several sub-carriers are orthogonally packed at each frequency with 15 kHz sub-carrier spacing. On the other hand, after non-orthogonal multiplexing, sub-carriers are packed more densely, thus the spacing between adjacent sub-carriers is smaller than 15 kHz. The spectra show that the SEFDM can provide spectrum compression by positioning sub-carriers closer. In time domain, both OFDM and SEFDM symbols are transmitted satisfying the Nyquist ISI-free cri-

terion. In frequency domain, sub-carriers in SEFDM are compressed and no longer orthogonal, thus ICI is introduced. It is evident from the second stage of Fig. 5.1 that by multiplexing the same number of sub-carriers (i.e. transmitting the same amount of data), SEFDM occupies less bandwidth than OFDM. Furthermore, at the third stage, the signal spectra for OFDM and SEFDM are illustrated and confirm that the signal bandwidth is compressed in SEFDM. This result provides an approach to enhance CA scenario and the way for the enhancement is shown at the final stage. Comparing two CA scenarios, it is inferred that the data rate of CA-SEFDM is increased by aggregating more CCs while maintaining the same data rate per sub-carrier. Therefore, for the same bandwidth allocation, CA-SEFDM offers a higher throughput than CA-OFDM.

5.3 MultiPath Fading Channel

In a single carrier communication system, each data symbol is modulated on one carrier which occupies the whole available bandwidth. In a multicarrier communication system, the entire bandwidth is decomposed into several (i.e. N) sub-carriers where each one occupies $\frac{1}{N}$ of the original bandwidth. Therefore, the period of one symbol of multicarrier signals is N times the symbol period of single carrier signals. The longer symbol period indicates the higher resilience to ISI.

The wireless signal propagates via multiple paths because of reflection, diffraction and scattering. These effects lead to the multi-path fading channel where each path experiences different attenuation, time delays and phases. At the receiver, many copies of a signal are superimposed resulting in the interference. The first kind of channel is a static channel named frequency selective channel due to the fact that the transmitter and receiver are both static. The second type is the time variant channel where a relative movement exists between the transmitter and the receiver.

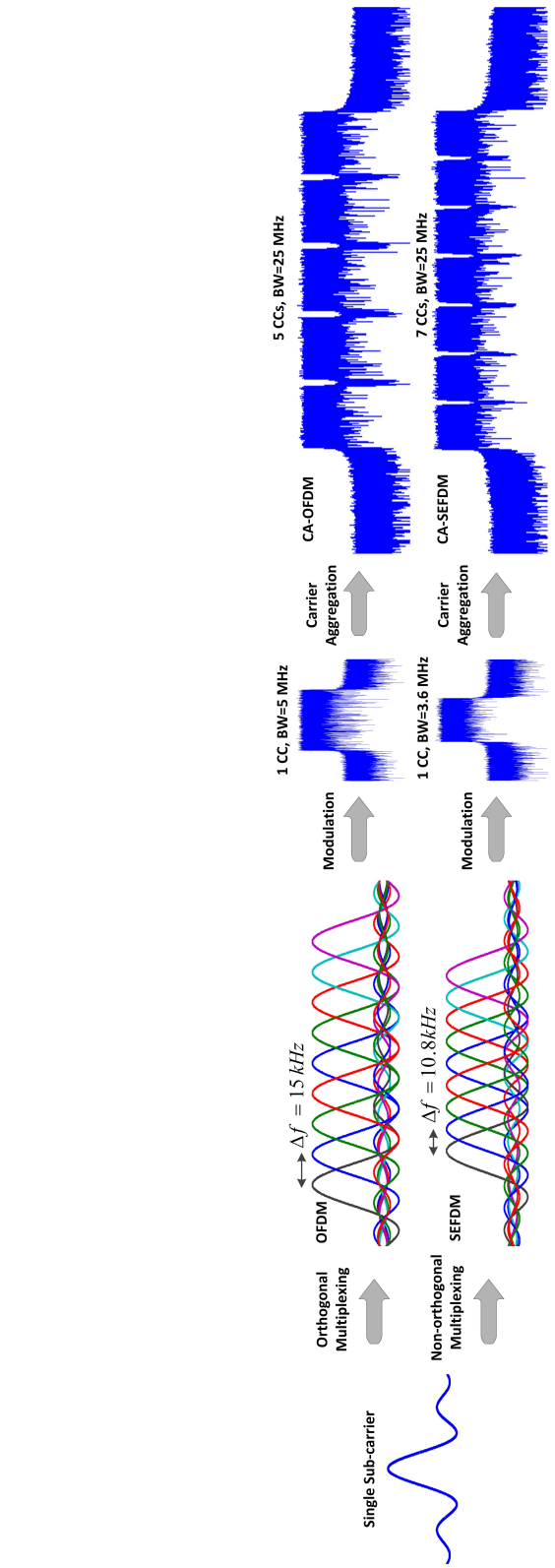

Figure 5.1: Extension to wider channel bandwidth by means of carrier aggregation for both OFDM and SEFDM. CC indicates component carrier. BW is the channel bandwidth including data bandwidth and 10% protection bandwidth.

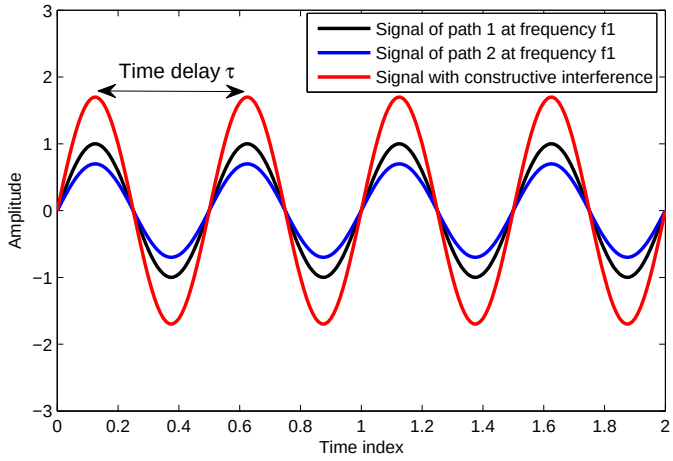

(a) Constructive interference.

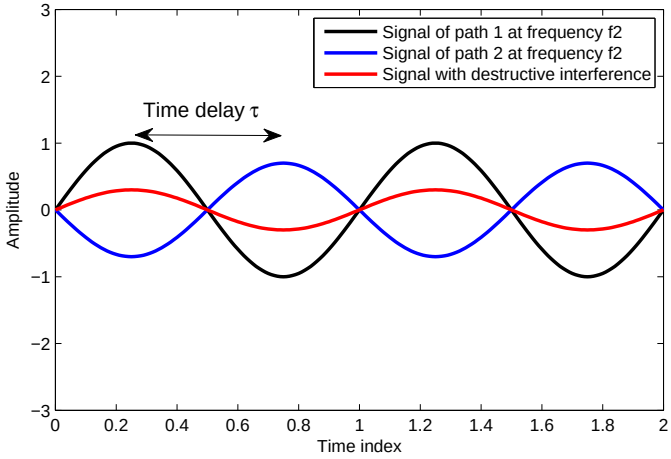

(b) Destructive interference.

Figure 5.2: Illustration of multipath distortion with constructive and destructive interference.

5.3.1 Frequency Selective Channel

The frequency selective nature is related to the time delay between different signal propagation paths reaching the receiver. Due to time dispersion among different multipaths, channel response varies with frequency leading to frequency selective channel. Assuming a fixed time delay τ, the superimposition of many copies of a signal could be either constructive or destructive, depending on their wavelengths. The difference

is illustrated in Fig. 5.2. The time delay is fixed and set to be τ for both insets. It is clearly seen that the time delay in Fig. 5.2(a) leads to a constructive superimposition at frequency f_1 while a destructive interference at frequency f_2 in Fig. 5.2(b). Therefore, the time delay causes different frequency signals adding either constructively or destructively, making the channel frequency selective.

The delay spread, D, is the time interval between the first arrived signal and the last arrived copy. Since the signal power is mainly concentrated in the first few paths, D_{RMS}, which is defined as root mean square (RMS) delay spread, is usually used. The coherence bandwidth, B_c, is a measure of the range of frequencies over which the channel can be considered flat. In other words, coherence bandwidth is the range of frequencies over which two frequency components have a strong potential for amplitude correlation. In general [170], the coherence bandwidth of a wireless channel is inversely proportional to its RMS delay spread as

$$B_c \approx \frac{1}{D_{RMS}} \tag{5.1}$$

Based on the experimental data from [171][172], the coherence bandwidth is empirically defined as

$$B_c \approx \begin{cases} \frac{1}{50 D_{RMS}} & \eta = 0.9 \\ \frac{1}{5 D_{RMS}} & \eta = 0.5 \end{cases} \tag{5.2}$$

where η indicates frequency correlation. If the coherence bandwidth is defined as the bandwidth over which the frequency correlation is above 0.9, then the first equation of (5.2) is derived. If the requirement is relaxed such as the frequency correlation is 0.5, then the second equation of (5.2) is derived. A frequency non-selective channel indicates the bandwidth of a signal is smaller than the coherence bandwidth. In other words, the symbol period should be much longer than the delay spread time indicating the current symbol does not affect the next symbol too much. Thus, the effect of ISI would not be significant. However, this is indeed difficult to achieve for a single carrier system where

frequency selective always occurs. In a single carrier system, each symbol is modulated on one carrier occupying the entire bandwidth which is significantly greater than the coherence bandwidth. This can also be proved in the time-domain since the symbol period is much smaller than the delay spread time. In a multicarrier system, the entire bandwidth is divided and distributed to several sub-carriers. Therefore, the spacing of each sub-carrier is much smaller than the coherence bandwidth making the multicarrier system more resistant to frequency selective channels.

5.3.2 Time Variant Channel

The time variation of a channel is related to the relative movement between a transmitter and a receiver. Depending on the value of Doppler spread, the signal is determined to experience fast or slow fading. The maximum frequency shift (i.e. Doppler spread) due to the movement is calculated as

$$f_m = \frac{v}{\lambda} = \frac{v f_{RF}}{c} \tag{5.3}$$

where λ is the wavelength of a transmitted signal equals to $\lambda = \frac{c}{f_{RF}}$ where c is the light speed and f_{RF} is the signal transmission frequency referred to RF; v is the movement velocity of the receiver. Hence, the frequency shift f_θ in different multi-path with the reaching angle θ is easily derived as

$$f_\theta = f_m cos\theta \tag{5.4}$$

Many copies of a signal come through different paths with different frequencies are combined at the receiver leading to a special spectrum termed Doppler spectrum. The power fluctuates at different frequency shifts, and the range of non-zero power in the power spectrum is referred to the Doppler spread. The multiple copies of signals are superimposed upon each other resulting in spatial interference. With the movement of the transmitter or the receiver, it experiences different frequencies and phases which are

defined as 'fading'. A fast fading channel can cause severe signal distortions since one SEFDM/OFDM symbol could experience different channel conditions. More specifically, a portion of one SEFDM/OFDM symbol experiences one channel while the rest experiences another channel. In this case, a conventional channel equalizer can not compensate for this distortion. In order to determine whether a channel is fast or slow fading, a concept termed coherence time is defined as the approximated inverse of the Doppler spread, which is expressed as

$$T_c \approx \frac{1}{f_m} \tag{5.5}$$

where the coherence time indicates a time period over which the channel is considered to be invariant. A short description of the coherence time is shown in the following. Assuming a signal $x(t)$ is transmitted at time t_1 experiencing a channel impulse response $h_{t_1}(t)$, meanwhile, a copy of this signal is transmitted at time t_2 experiencing a channel impulse response $h_{t_2}(t)$. Without considering channel distortions, at the receiver, the two signals are received as

$$y_{t_1}(t) = x(t - t_1) * h_{t_1}(t) \tag{5.6}$$

$$y_{t_2}(t) = x(t - t_2) * h_{t_2}(t) \tag{5.7}$$

where the notation $'*'$ denotes the convolution operation. A channel would be considered time invariant only if $\Delta h(t) = h_{t_2}(t) - h_{t_1}(t)$ is small. Then, the coherence time is defined as $T_c = t_2 - t_1$. On the basis of the above analysis, to avoid the fast fading, the symbol period must be smaller than the coherence time T_c.

Coherence time is the time duration over which two received signals have a strong potential for amplitude correlation. It should be noted that (5.5) is derived assuming the Rayleigh faded signal varies very slowly. In the condition of a fast variation scenario, if the coherence time is defined as the time over which the time correlation is 0.5, the 50% coherence time [170] is defined as

$$T_c \approx \frac{9}{16\pi f_m} \tag{5.8}$$

A common definition of coherence time is to use the geometric mean of (5.5) and (5.8), which is given as

$$T_c \approx \sqrt{\frac{1}{f_m}\frac{9}{16\pi f_m}} \approx \frac{1}{f_m}\sqrt{\frac{9}{16\pi}} \approx \frac{0.423}{f_m} \tag{5.9}$$

5.3.3 Summary

To sum up, the coherence bandwidth B_c determines a channel to be frequency selective or frequency non-selective (i.e. frequency flat). Therefore, in order to get a frequency non-selective channel, the signal bandwidth should be much smaller than the coherence bandwidth. Otherwise, the signal would experience a frequency selective channel. In a single carrier system, the symbol period is much shorter since each symbol occupies the entire bandwidth. In this case, a significant ISI is introduced. In a multicarrier system, the sub-carrier spacing is configured to be smaller than the coherence bandwidth to make a sub-carrier experiencing frequency flat channel. Furthermore, the CP is required to be much longer than the delay spread to prevent ISI. Hence, according to the above analysis, the CP length should be as long as possible and the sub-carrier spacing should be as small as possible. However, a small sub-carrier spacing results in severe ICI in a time variant channel. To summarize the above analysis, a transmitted signal is subject to frequency selective or frequency flat channel under the following conditions:

$$frequency\ flat: \begin{cases} B_c \gg B_{signal} \\ D_{_{RMS}} \ll T_{signal} \end{cases} \tag{5.10}$$

$$frequency\ selective: \begin{cases} B_c < B_{signal} \\ D_{_{RMS}} > T_{signal} \end{cases} \tag{5.11}$$

where assuming two variables a and b, then the notation $a \gg b$ means that a is much greater than b, the notation $a \ll b$ means that a is much less than b, the notation $a > b$ means that a is greater than b, the notation $a < b$ means that a is less than b, B_c is the coherence bandwidth, D_{RMS} is the RMS delay spread, B_{signal} is the bandwidth of one symbol and T_{signal} is the symbol period.

On the other hand, the coherence time T_c determines a channel fading to be fast or slow. A slow fading indicates that signal period is much smaller than the coherence time, otherwise, it is a fast fading channel. Hence, the symbol period should be as small as possible. In other words, the signal bandwidth should be made as large as possible. In a single carrier system, it is easily to be achieved since the signal occupies the entire bandwidth. However, in a multicarrier system, on the basis of the requirement, the sub-carrier spacing should be made as large as possible, which conflicts with the conclusion in the last paragraph. The sub-carrier spacing should be carefully considered in a time variant and frequency selective channel. In particular, the multicarrier system has a immunity against the deep fading since only some of the sub-carriers would experience severe distortions. However, in a single carrier system, the signal would be severely distorted since only one carrier is adopted. To summarize the above analysis, a transmitted signal is subject to fast or slow fading channel under the following conditions:

$$slow\ fading: \begin{cases} T_c \gg T_{signal} \\ f_m \ll B_{signal} \end{cases} \tag{5.12}$$

$$fast\ fading: \begin{cases} T_c < T_{signal} \\ f_m > B_{signal} \end{cases} \tag{5.13}$$

where assuming two variables a and b, then the notation $a \gg b$ means that a is much greater than b, the notation $a \ll b$ means that a is much less than b, the notation $a > b$ means that a is greater than b, the notation $a < b$ means that a is less than b, T_c is the

coherence time, f_m is the Doppler spread, B_{signal} is the bandwidth of one symbol and T_{signal} is the symbol period.

Therefore, the configuration of signal bandwidth is a trade-off between ISI and ICI for both single carrier systems and multicarrier systems. In particular, for a multicarrier communication system, the sub-carrier spacing should be carefully designed to balance the effect of ISI and ICI. This could be one reason why LTE adopts 15 kHz sub-carrier spacing. In addition, based on the above analysis, there are four combinations of different channels, frequency flat slow fading; frequency flat fast fading; frequency selective slow fading; frequency selective fast fading.

5.4 LTE Physical Layer Specifications

OFDM is selected as the physical layer technique in the LTE release 8 [1] together with MIMO, which can either improve spectral efficiency (space multiplexing) or enhance signal robustness (space diversity). The work in this thesis is focused on multicarrier transmission, thus, only OFDM is described here and MIMO will not be considered in this section.

LTE frame structure is shown in Fig. 5.3 where one frame of length 10 ms consists of 10 subframes. T_s=32.55 ns indicates sample time period which in frequency domain corresponds to 30.72 MHz. Furthermore, each subframe can be divided into 2 time slots with each accounting for 0.5 ms. Each time slot is composed of either seven (normal CP) or six (extended CP) OFDM symbols. In this section, only normal one is presented.

In Fig. 5.3, the useful symbol time is 66.7 us, which covers 2048 samples. In a normal CP mode, the first symbol has a CP of length 5.2 us=$160 \times T_s$ and the remaining six symbols have a CP of length 4.7 us=$144 \times T_s$. The reason for this is to make sure one time slot has 15360 samples. In an extended version, the CP is extended to 512 samples, which is longer than a normal one. The normal one is used in the condition of urban areas, small cells and high data rate applications. The extended one

is for rural areas, large cells and low data rate applications.

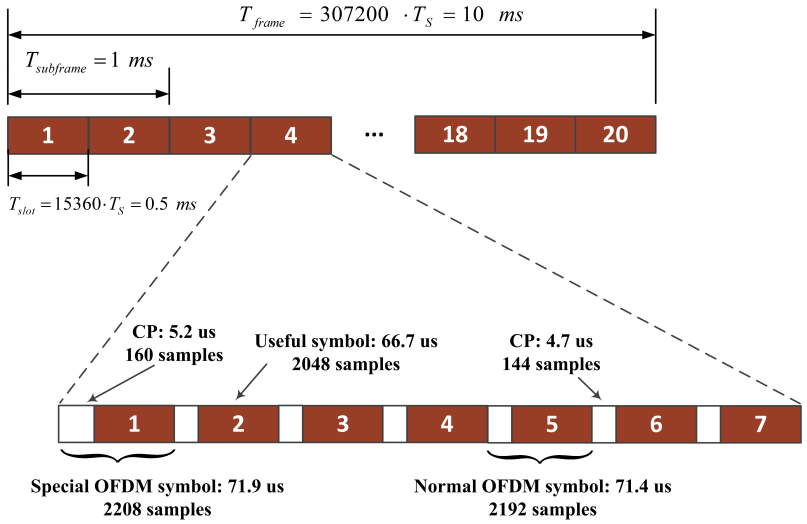

Figure 5.3: Frame structure type 1 (FDD frame).

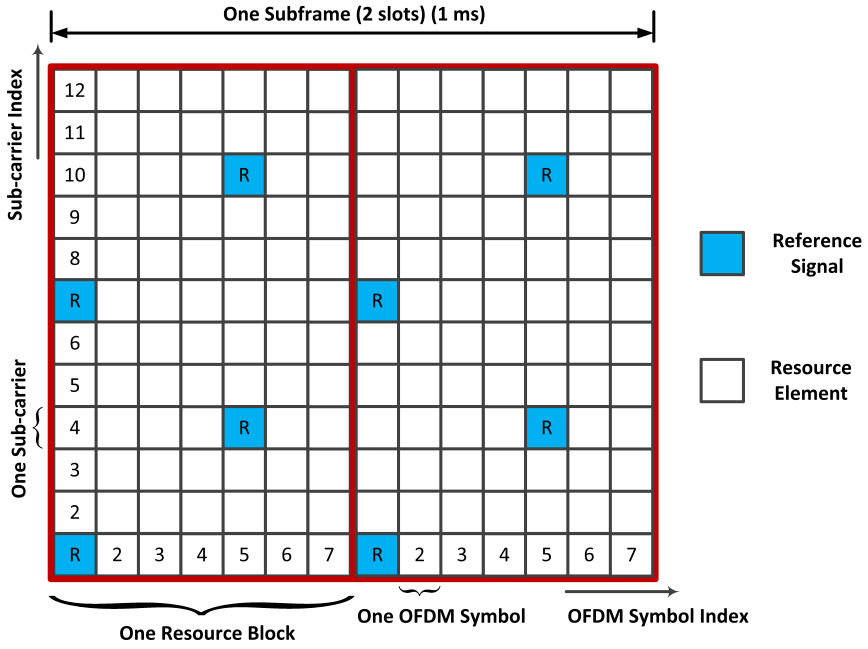

Figure 5.4: OFDM resource block and resource element definition for a one antenna LTE system with normal CP mode.

The LTE time-frequency grid is shown in Fig. 5.4. The x-axis indicates OFDM

symbols in time-domain while the y-axis means sub-carriers in frequency-domain. One resource element indicates one M-QAM symbol modulated on one sub-carrier. Resource block is the smallest component can be operated in LTE. Each resource block consists of 12 sub-carriers (1.e. 180 kHz) and 7 OFDM symbols. Therefore, with different number of sub-carriers, the number of resource blocks are different, which can be noticed in Table. 5.1.

Table 5.1 presents physical layer specifications for LTE downlink FDD mode. It should be noted that DC sub-carrier is not used and 10% of sub-carriers are not used on both sides of the channel. In other words, the occupied data bandwidth is roughly 90% of the channel bandwidth.

Table 5.1: LTE Downlink Physical Layer Specifications

Channel Bandwidth (MHz)	1.25	2.5	5	10	15	20
Sampling Frequency (MHz)	1.92	3.84	7.68	15.36	23.04	30.72
FFT Size	128	256	512	1024	1536	2048
Occupied Sub-carriers (inc. DC)	76	151	301	601	901	1201
Guard Sub-carriers	52	105	211	423	635	847
Number of Resource Blocks	6	12	25	50	75	100
Occupied Channel Bandwidth (MHz)	1.140	2.265	4.515	9.015	13.515	18.015
1^{st} CP Length	10	20	40	80	120	160
Remaining CP Length	9	18	36	72	108	144

5.4.1 Time-Frequency Requirements of the LTE Resource Block

The pilot locations are studied detailedly in [173]. The pilot location in time-domain is configured based on coherence time (it is calculated according to the Doppler spread). Its location in frequency-domain is based on the coherence bandwidth (it is calculated according to the time delay spread).

5.4.1.1 Resource Block Size

Coherence bandwidth B_c is calculated according to (5.2) with η=0.5 in the typical urban (TU) channel model with a 1.07 us delay spread [174]. Then, the coherence

bandwidth is approximated to be $B_c = \frac{1}{5D} \approx 187kHz$. Therefore, the bandwidth of one resource block should be within 187 kHz to make sure a flat channel response. In LTE, this value is rounded to be 180 kHz. Considering the 15 kHz sub-carrier spacing, the number of sub-carriers within one resource block is $180/15 = 12$.

In terms of coherence time, taking into account the peak mobility speed associated with a high speed train (roughly 300-350 km/h), together with a 2.6 GHz RF carrier, the Doppler frequency is approximated to be 843 kHz, which is calculated according to (5.3). Then based on (5.9), the coherence time is $\frac{0.423}{843} \approx 0.5ms$. To make the channel time invariant over one resource block, the time period of one resource block should be within 0.5 ms.

5.4.1.2 Sub-Carrier Spacing

The size of one resource block is configured and fixed based on multiplath fading conditions. It is evident that CP consumes additional radio resources. A solution is to aggregate more sub-carriers with smaller sub-carrier spacing Δf in a given bandwidth. Thus, the time period of one OFDM symbol is increased. However, it increases the sensitivity of OFDM to frequency offset and fast fading. In LTE, the sub-carrier spacing is 15 kHz since it may simplify the implementation of WCDMA/HSPA/LTE multimode terminals [175]. Typically, the FFT size is a power of two, multiplying with 15 kHz sub-carrier spacing, the sampling rate is $f_s = \Delta f \cdot N_{FFT}$ leading to a multiple or sub-multiple of the WCDMA/HSPA chip rate f_{cr}=3.84 MHz. Then, multi-mode WCDMA/HSPA/LTE terminals can straightforwardly be implemented with a single clock circuitry.

5.4.1.3 Carrier Raster

The location of LTE center carriers in frequency domain could be positioned anywhere as explained in [176]. Mobile terminals have to search for a carrier within the supported frequency bands when they are switched on. In order to save time and avoid unnecessary

search, a set of frequencies are limited to be searched within the supported frequency bands. Therefore, in LTE supported frequency bands, carriers exist on a 100 kHz carrier raster, which is expressed as $m \times 100$ kHz where m are integers.

In the carrier aggregation scenario, multiple CCs are put together. In order to be compatible with legacy terminals (e.g. support below LTE-Advanced standard), each CC should be centered on the 100 kHz carrier raster. Additionally, the sub-carrier spacing is defined as 15 kHz. Therefore, the gap between adjacent CCs should be a multiple of 15 kHz in order to preserve orthogonally of the sub-carriers. Overall, the center carrier spacing between different CCs should be a multiple of 300 kHz [176], which is the smallest carrier spacing being a multiple of both 100 kHz (the carrier raster) and 15 kHz (the sub-carrier spacing).

5.5 SEFDM Time-Frequency Requirements

Fading channels introduce random ICI in a wireless communication system. In order to eliminate this effect, a proper channel estimation algorithm has to be adopted. For an OFDM system, a single tap frequency-domain channel estimation algorithm is applied. However, for SEFDM, due to the self-created ICI, the typical OFDM approach does not work. Some related work [177][45] has been done to resolve this issue in SEFDM. A time-domain channel estimation and a frequency-domain joint channel equalization/detection were proposed in [177] where an SEFDM pilot symbol is used to estimate CSI, which is termed full channel estimation (FCE). However, due to non-orthogonal packing of sub-carriers in SEFDM, pilot tones (reference signals) within one SEFDM pilot symbol interfere with each other leading to inaccurate estimate of CSI. In [45], an enhanced method termed PCE was investigated. This scheme is a time-domain estimation/equalization algorithm. Based on the analysis in [45], there are a number of sub-carriers mutually orthogonal even if they are not adjacent. Therefore, the main idea of the PCE is to send pre-determined pilot tones on those mutually orthogonal sub-carriers. By using this method, ICI can be reduced within the pilot symbol. Thus,

the channel can be estimated more accurately.

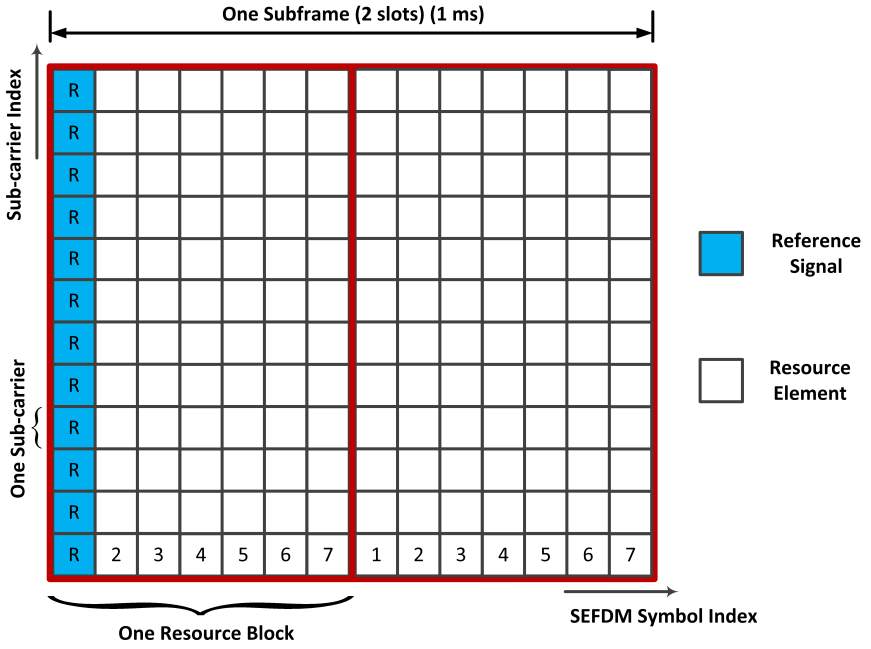

Figure 5.5: SEFDM resource block definition and location of reference signals for a single antenna system.

In this work, we adopt the typical FCE to estimate CSI and equalize the channel in time-domain, which indicates pilot tones are modulated on all sub-carriers instead of the mutually orthogonal ones. Reference signals are no longer reliable to be used to estimate channels. Therefore, in SEFDM, we define a new structure of one subframe in Fig. 5.5 to effectively recover non-orthogonal signals. It is similar to the LTE one except that the first SEFDM symbol is reserved as a pilot symbol instead of reference signals distributed within one LTE subframe. Based on the knowledge of the pilot symbol, the receiver can extract CSI and compensate for one subframe. Assume the channel is fixed within one subframe indicating all the SEFDM symbols in one subframe experience the same characterized channel. After 13 SEFDM symbols, a new pilot symbol is inserted in a second subframe. In this case, a more accurate CSI can be obtained via averaging two estimations from two pilot symbols of adjacent subframes. It is evident that this pilot structure makes SEFDM suitable for slow fading channel with severe frequency

selective channel. In other words, it works in a deep fading and slow changing channel.

5.6 Channel Estimation

Channel estimation algorithms used in OFDM are comprehensively investigated in [178]. The loss of orthogonality in SEFDM leads to ICI which affects the accuracy of channel estimation. It is difficult to use directly a single-tap frequency-domain equalizer to compensate for channel fading.

Channel estimation is required in a practical system, due to RF effects such as multipath fading channel, imperfect timing synchronization and phase offset. However, estimation of the channel in the case of SEFDM signals is challenged by the non-orthogonal structure of the sub-carriers in the system. The typical OFDM channel estimation algorithm is not applicable. Therefore, an SEFDM time-domain channel estimation technique is presented to overcome the discussed design challenge.

The concept of SEFDM time-domain channel estimation/equalization is described in the following. Let's assume that the length of CP is N_{CP}. After passing through a multipath fading channel, the received samples Y_{CP} can be expressed in matrix format as

$$Y_{CP} = \mathbf{H}X_{CP} + Z_{CP} \tag{5.14}$$

where X_{CP} is the transmitted signal including both useful data and CP, $\mathbf{H}$ is a $U \times U$ channel matrix, where $U = Q + N_{CP}$ and Z_{CP} is the AWGN of length U. At the receiver, after the removal of CP, the channel matrix $\mathbf{H}$ is transformed to a circulant matrix and, using (2.10), the signal vector is represented by

$$Y_c = \mathbf{H_c}X + Z = \mathbf{H_c}\mathbf{F}S + Z \tag{5.15}$$

where Y_c, X and Z are the sample vectors after truncating the first N_{CP} samples of Y_{CP}, X_{CP} and Z_{CP}, respectively. $\mathbf{F}$ is the $Q \times N$ sub-carrier matrix and $\mathbf{H_c}$ is a $Q \times Q$

circulant matrix, thus its first column gives all the information needed to construct the matrix. After demodulation, the signal vector is expressed as

$$R_c = \mathbf{F}^*\mathbf{H_c}\mathbf{F}S + \mathbf{F}^*Z = \mathbf{G}S + Z_{\mathbf{F}^*} \tag{5.16}$$

According to the characteristic of the circulant matrix $\mathbf{H_c}$, for orthogonal multicarrier signals (e.g. OFDM), $\mathbf{G}$ is a diagonal matrix. Thus, the channel can be estimated through a single tap frequency-domain estimator. However, this is not the case in SEFDM since there are off-diagonal elements in the matrix $\mathbf{G}$. This introduces both multiplicative (diagonal elements) and additive (off-diagonal elements) distortions. Therefore, in this work, we employ a time-domain estimation/equalization algorithm to estimate and compensate the channel response. For this purpose, pilot tones (reference signals) are modulated on non-orthogonal packed sub-carriers as illustrated in Fig. 5.5. Assuming P is the pilot vector, at the receiver, after CP removal, the faded signal is expressed as

$$Y_{c-pilot} = \mathbf{H_c}\mathbf{F}P + Z \tag{5.17}$$

In order to equalize the faded signal, we need to estimate the channel matrix $\mathbf{H_c}$ and compute its inverse. By rearranging (5.17), a new expression is shown as

$$Y_{c-pilot} = \mathbf{P}h + Z \tag{5.18}$$

where h is a $Q \times 1$ vector and $\mathbf{P}$ is a $Q \times Q$ circulant matrix whose first column is equal to the vector $X = \mathbf{F}P$. Therefore the matrix $\mathbf{P}$ is expressed as

$$\mathbf{P} = \begin{bmatrix} F_1 & F_Q & \cdots & F_2 \\ F_2 & F_1 & \ddots & \vdots \\ \vdots & \ddots & \ddots & F_Q \\ F_Q & \cdots & F_2 & F_1 \end{bmatrix} \begin{bmatrix} P & 0 & \cdots & 0 \\ 0 & P & \cdots & 0 \\ \vdots & \vdots & \ddots & \vdots \\ 0 & 0 & \cdots & P \end{bmatrix} \tag{5.19}$$

where F_i is the i^{th} row of the sub-carrier matrix $\mathbf{F}$. Then the estimate of h is expressed as

$$\hat{h} = \mathbf{P}^*(\mathbf{P}\mathbf{P}^*)^{-\mathbf{1}}Y_{c-pilot} \tag{5.20}$$

where $\hat{h}$ is the estimate of the first column of the matrix $\mathbf{H_c}$. Since $\mathbf{H_c}$ is a circulant matrix, then the matrix $\mathbf{H_c}$ can be regenerated via copying and shifting $\hat{h}$ repeatedly. The estimate matrix $\hat{\mathbf{H}}_\mathbf{c}$ is then inverted to give $\hat{\mathbf{H}}_\mathbf{c}^{-\mathbf{1}}$ and used to equalize the distorted SEFDM symbols in (8.9) as below

$$Y_{eq} = \hat{\mathbf{H}}_\mathbf{c}^{-\mathbf{1}}Y_c = \hat{\mathbf{H}}_\mathbf{c}^{-\mathbf{1}}\mathbf{H_c}\mathbf{F}S + \hat{\mathbf{H}}_\mathbf{c}^{-\mathbf{1}}Z \tag{5.21}$$

The equalized time-domain SEFDM sample vector Y_{eq} can also be expressed in terms of an error factor $\mathbf{\Psi} = \hat{\mathbf{H}}_\mathbf{c}^{-\mathbf{1}}\mathbf{H_c}$ matrix, attributed to the imperfect channel equalization process as

$$Y_{eq} = \mathbf{\Psi}\mathbf{F}S + \hat{\mathbf{H}}_\mathbf{c}^{-\mathbf{1}}Z \tag{5.22}$$

It is important to note that the noise itself is now enhanced by the multiplication with $\hat{\mathbf{H}}_\mathbf{c}^{-\mathbf{1}}$. Y_{eq} is then demodulated as in (5.23) giving the demodulated (and equalised) symbols vector R_{eq}

$$\begin{aligned} R_{eq} = \mathbf{F}^*Y_{eq} &= \mathbf{F}^*\mathbf{\Psi}\mathbf{F}S + \mathbf{F}^*\hat{\mathbf{H}}_\mathbf{c}^{-\mathbf{1}}Z \\ &= \mathbf{C}_\mathbf{\Psi}S + Z_{\mathbf{F}^*\hat{\mathbf{H}}_\mathbf{c}^{-\mathbf{1}}} \end{aligned} \tag{5.23}$$

where $\mathbf{C}_\mathbf{\Psi}$ is the correlation matrix contaminated by the error factor matrix $\mathbf{\Psi}$ and $Z_{\mathbf{F}^*\hat{\mathbf{H}}_\mathbf{c}^{-\mathbf{1}}}$ is the noise vector contaminated by the multiplicative factor $\mathbf{F}^*\hat{\mathbf{H}}_\mathbf{c}^{-\mathbf{1}}$. Compared with equation (2.23), it is apparent that in the condition of multipath fading, the signal is further distorted even if a channel equalization algorithm is adopted. Therefore, to ameliorate these degradation factors, employing an efficient signal detector is essential.

In order to evaluate the efficacy of the proposed time-domain channel estimation scheme, a static frequency selective channel [58] as shown in (8.13) is assumed.

$$h(t) = 0.8765\delta(t) - 0.2279\delta(t - T_s) + 0.1315\delta(t - 4T_s) - 0.4032e^{\frac{j\pi}{2}}\delta(t - 7T_s) \quad (5.24)$$

The mean squared error (MSE) is calculated and shown in Fig. 5.6. The MSE is calculated by

$$MSE = \frac{1}{n}\sum_{i=0}^{n-1}(\hat{h}_i - h_i)^2. \quad (5.25)$$

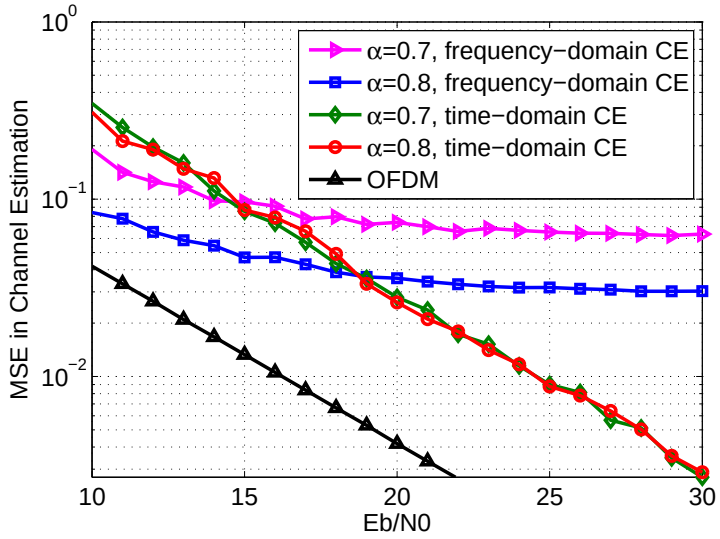

Figure 5.6: MSE of time-domain and frequency-domain channel estimation (CE) methods. FFT size is 128 and 9 samples are used as CP.

Results are compared to those of a frequency-domain channel estimator similar to that used in OFDM systems. For the frequency-domain channel estimation, expectedly the OFDM system results in better channel parameter estimates and therefore has a lower MSE values than those of the SEFDM system tested for different values of α. This illustrates that the loss of orthogonality in the SEFDM system impairs the performance

of the commonly used frequency-domain single tap channel estimation. It is evident that, with the increase of α, the SEFDM result approaches those of OFDM. Conversely, for the time-domain channel estimation, although the MSE values are still worse for SEFDM relative to those of OFDM, variation of α results in minimal variation of MSE values. It should be noted that at low E_b/N_o, the frequency-domain method provides a more accurate channel estimation than the time-domain one. At high E_b/N_o, since the typical frequency-domain method cannot effectively remove ICI, an error floor occurs. On the other hand, the time-domain method can mitigate the ICI effect, therefore, the time-domain method shows a lower MSE than the frequency-domain one. In addition, it is apparent that the OFDM system shows a lower MSE than the proposed SEFDM channel estimation scheme. The reason is attributed to the ill conditioning (i.e. self-created ICI as shown in (2.24)) of the SEFDM system. As shown in (5.19), the pilot symbols P are modulated on all sub-carriers.

5.7 Channel Equalization

In this section, a simple time-domain channel equalization which can compensate for the multiple path fading effect in SEFDM is studied. The original idea was proposed in [179] where an OFDM system associated with time-variant multipath channels are investigated. The time-domain channel equalization for SEFDM is mathematically expressed in (5.21). It is apparent that the size of the matrix $\hat{\mathbf{H}}_\mathbf{c}$ is proportional to a system size (e.g. the number of sub-carriers). In terms of a small size system, the computational complexity for the matrix inverse $\hat{\mathbf{H}}_\mathbf{c}^{-\mathbf{1}}$ is reasonable. But with the increase of the number of sub-carriers, the complexity will be significantly increased.

In order to reduce the complexity, this section applies a flexible method that decomposes the entire matrix $\hat{\mathbf{H}}_\mathbf{c}$ into multiple small matrices and computes matrix inverse for each. As explained before, $\hat{\mathbf{H}}_\mathbf{c}$ is a circulant matrix. It represents CSI such as path number, power and time delay of each path. From a transmitter side to a receiver side, a signal can experience various paths. The number of the different paths is infinite.

However, most energy of the signal is concentrated in a finite number of paths. Other paths that have very low energies are neglected. It is inferred that the matrix $\hat{\mathbf{H}}_\mathbf{c}$ is a sparse matrix where most of the energy is concentrated in the diagonal elements and their neighbouring non-diagonal elements. Since $\hat{\mathbf{H}}_\mathbf{c}$ is a sparse matrix, it is not efficient to compute the matrix inverse of the entire $\hat{\mathbf{H}}_\mathbf{c}$.

The effect of channel estimation is not the focus in this section, therefore, a perfect CSI is assumed at the receiver. In the following discussion, the perfect channel matrix $\mathbf{H}_\mathbf{c}$ is studied instead of $\hat{\mathbf{H}}_\mathbf{c}$. An efficient way is to transform the $Q \times Q$ matrix $\mathbf{H}_\mathbf{c}$ to multiple block diagonal matrices $\mathbf{A}$ of size $q \times q$. Hence, the matrix $\mathbf{H}_\mathbf{c}$ is converted to a new format as shown in (5.26).

$$\mathbf{H_c} = \begin{bmatrix} h_{1,1} & h_{1,2} & \cdots & h_{1,Q} \\ h_{2,1} & h_{2,2} & \ddots & \vdots \\ \vdots & \ddots & \ddots & h_{Q-1,Q} \\ h_{Q,1} & \cdots & h_{Q,Q-1} & h_{Q,Q} \end{bmatrix} \Rightarrow \overrightarrow{\mathbf{H}}_\mathbf{c} = \begin{bmatrix} \mathbf{A_1} & 0 & \cdots & 0 \\ 0 & \mathbf{A_2} & \cdots & 0 \\ \vdots & \vdots & \ddots & \vdots \\ 0 & 0 & \cdots & \mathbf{A_{Q-q+1}} \end{bmatrix} \tag{5.26}$$

where the small matrix $\mathbf{A_n}$ is a $q \times q$ matrix expressed as

$$\mathbf{A_n} = \begin{bmatrix} h_{n,n} & h_{n,n+1} & \cdots & h_{n,n+q-1} \\ h_{n+1,n} & h_{n+1,n+1} & \ddots & \vdots \\ \vdots & \ddots & \ddots & h_{n+q-2,n+q-1} \\ h_{n+q-1,n} & \cdots & h_{n+q-1,n+q-2} & h_{n+q-1,n+q-1} \end{bmatrix} \tag{5.27}$$

Therefore, the size of the matrix $\overrightarrow{\mathbf{H}}_\mathbf{c}$ in (5.26) is $\overrightarrow{Q} \times \overrightarrow{Q}$ where $\overrightarrow{Q} = (Q - q + 1) \times q$. In order to realize channel equalization in (5.21), the received symbol vector Y_c is converted to a new format as

$$Y_c \Rightarrow \overrightarrow{Y}_c = [B_1,\ B_2, ..., B_{Q-q+1}] \tag{5.28}$$

where B_n is a q-dimensional vector includes elements as

$$B_n = [Y_c(n),\ Y_c(n+1), ..., Y_c(n+q-1)] \tag{5.29}$$

Therefore, $\overrightarrow{Y}_c$ is a $\overrightarrow{Q}$-dimensional vector. The typical channel equalization in (5.21) can be transformed to

$$\overrightarrow{Y}_{eq} = \overrightarrow{\mathbf{H}}_{\mathbf{c}}^{-1} \overrightarrow{Y}_c \tag{5.30}$$

where

$$\overrightarrow{\mathbf{H}}_{\mathbf{c}}^{-1} = \begin{bmatrix} \mathbf{A_1}^{-1} & 0 & \cdots & 0 \\ 0 & \mathbf{A_2^{-1}} & \cdots & 0 \\ \vdots & \vdots & \ddots & \vdots \\ 0 & 0 & \cdots & \mathbf{A_{Q-q+1}^{-1}} \end{bmatrix} \tag{5.31}$$

It is inferred that due to the sparse characteristic of the channel matrix $\mathbf{H_c}$, the $Q \times Q$ matrix can be transformed to multiple $q \times q$ small matrices. Hence, the matrix inverse of the large channel matrix $\mathbf{H_c}$ is converted to the matrix inverse of multiple small channel matrices, indicating a greatly reduced computational complexity. Therefore, (5.30) can be further simplified to

$$\overrightarrow{Y}_n = \mathbf{A_n^{-1}} B_n \tag{5.32}$$

where $n \in [1, ..., Q-q+1]$. It is evident that the size of the multiplication is reduced indicating reduced computational complexity. We assume q is an even number in this section. For each multiplication in (5.32) with constraint $n \in [2, ..., Q-q]$, the middle (i.e. $q/2$) element is selected as one estimated symbol. For the first block multiplication (i.e. $n = 1$) and the last one (i.e. $n = Q-q+1$), the first $q/2$ and the last $1 + q/2$ elements are selected, respectively. Therefore, the estimated symbol vector Y_{eq} of size Q is expressed as

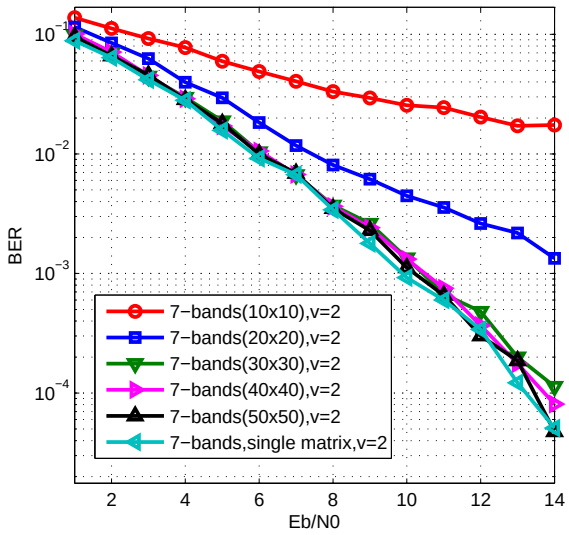

Figure 5.7: BER performance comparison for two channel equalization schemes.

$$Y_{eq} = [\overrightarrow{Y}_1(1), ..., \overrightarrow{Y}_1(q/2), \overrightarrow{Y}_2(q/2), ..., \overrightarrow{Y}_{Q-q}(q/2), \overrightarrow{Y}_{Q-q+1}(q/2), ..., \overrightarrow{Y}_{Q-q+1}(q)] \tag{5.33}$$

Simulations are investigated to demonstrate the benefit of the proposed multiple sub-matrix channel equalization method. A static frequency selective channel is used in the simulation shown as

$$h(t) = 0.8765\delta(t) - 0.2279\delta(t - T_s) + 0.1315\delta(t - 4T_s) - 0.4032e^{\frac{j\pi}{2}}\delta(t - 7T_s) \tag{5.34}$$

The system is configured based on the CA-SEFDM where the total bandwidth is 25 MHz with 7 CCs. The FFT size is 4096 and 288 samples are selected as CP. The modulation scheme is 4QAM. In a realistic CA-SEFDM system, one SEFDM symbol is reserved as the pilot symbol for every 13 data symbols. However, the purpose of this section is to show the benefit of the proposed channel equalization method. Therefore,

at the receiver side, a perfect CSI is assumed in order to neglect the channel estimation effect.

The comparison of the conventional single equalizer and the proposed multiple small equalizers are investigated in terms of execution time and BER performance. The proposed channel equalizer is evaluated with various sub-matrix sizes in order to find the balance between the execution time and the BER performance. For the conventional equalizer, it is realized by using the single large matrix inverse.

The effect of different sizes of the sub-matrix is illustrated in Fig. 5.7 where BER performance is studied. The conventional channel equalization result is included as a reference. For the 10×10 sub-matrix, the BER performance is far away from the conventional single matrix channel equalization result. Increasing the sub-matrix size to 20×20, the BER curve approaches the conventional single one but the performance gap is still large. By increasing the sub-matrix size to 30×30, the performance is identical to the typical one. With further increase to 40×40 or 50×50, the performance is fixed and identical to the typical one. It is concluded that the 30×30 sub-matrix is sufficient to get optimal performance.

Table 5.2: Execution Time of Two Channel Equalization Schemes

Sub-matrix	10×10	20×20	30×30	40×40	50×50
	0.0845 sec	0.0960 sec	0.1070 sec	0.1322 sec	0.1564 sec
Single Matrix	6.7235 sec				

The benefit of the sub-matrix concept is shown in Table. 5.2 where the execution time of the two channel equalization schemes is compared. Various sub-matrix sizes are studied in the first two rows of Table. 5.2. It is apparent that the smaller the sub-matrix size, the less execution time is required. With the increase of the sub-matrix size, the execution time is increased. But compared to the conventional single large matrix, the proposed multiple sub-matrix channel equalization shows shorter execution time. To sum up, the newly proposed multiple sub-matrix channel equalizer achieves the same performance with a significantly reduced complexity.

5.8 Experimental Setup

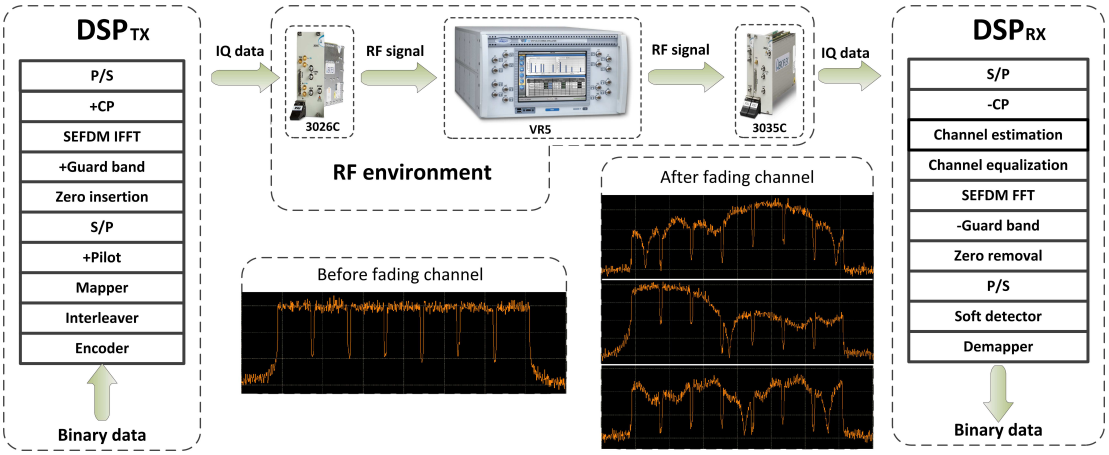

Figure 5.8: Experimental setup for CA-SEFDM transmission in the LTE EPA5 fading channel. Resolution bandwidth (RBW) for each spectrum is 1 kHz. Three screenshots of spectra are randomly obtained to illustrate fading channel characteristics. The frequency for central CC is 2 GHz, carrier frequencies for other CCs can be obtained by shifting $\alpha \times 5$ MHz=3.6 MHz.

This section presents the first experimental evaluation of SEFDM together with CA deployed in a real LTE wireless fading channel scenario. The experimental setup of CA-SEFDM with 7 CCs is illustrated in Fig. 5.8. To execute this experiment, both software and hardware are included in this testbed. The software consists of two DSP blocks, which carry out digital signal processing using Matlab at the transmitter and the receiver, respectively. The hardware consists of the 3026C RF signal generator, the 3035C RF digitizer and the VR5 channel emulator. Signal transmission, wireless channel and signal reception are all implemented in the RF environment.

The real experimental testbed is demonstrated in Fig. 5.9. The DSP transmitter and receiver are realized by Matlab in a PC. The Aeroflex PXI chassis consisting of a 3026C RF signal generator and a 3035C RF digitizer plays a key role in connecting the RF environment and the DSP environment. The RF signal from the 3026C RF signal generator is transmitted to the input of VR5 where its output is connected to the 3035C RF digitizer. The spectrum analyzer (e.g. Tektronix MDO4104-6 Mixed Do-

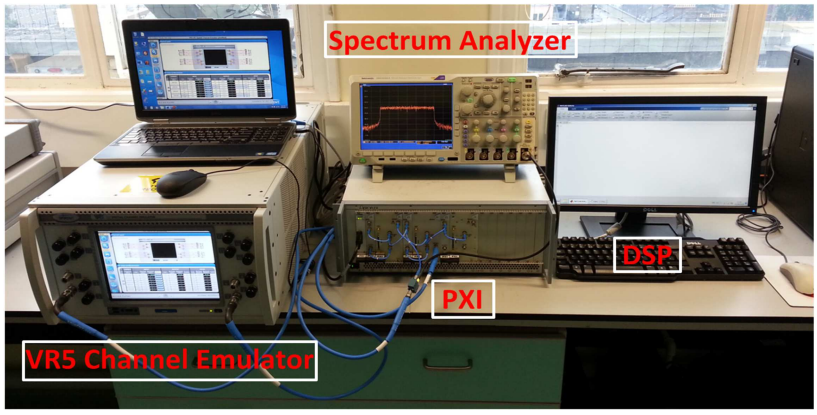

Figure 5.9: Demonstration of the real experimental setup.

main Oscilloscope) is used to evaluate frequency response of a signal after propagating through the VR5 channel emulator.

The PXI works as a transceiver whose carrier frequency ranging from 100 kHz to 6 GHz. Its modulation bandwidth is up to 90 MHz and with a maximum 512 MHz sampling rate. Each sample word consists of 14 bit I data, 14 bit Q data and 4 bit marker data.

The Spirent VR5 HD Spatial Channel Emulator [180] simplifies the testing of the cutting edge technologies such as MIMO over-the-air (OTA), LTE-Advanced, MIMO beamforming and IoT channel modeling. It provides a friendly graphical user interface (GUI) for users to set up a real time and complicated RF environment. VR5 supports a broad range of carrier frequencies up to 6 GHz and modulation bandwidth up to 100 MHz. There are several simplex (Input or Output only) and duplex (Input/Output) ports in the front panel of the VR5. After selecting the desired connection setup, these connections are automatically made inside the VR5. The propagation conditions like multi-path power delay profile of fading channel models can be edited and saved.

It should be noted that VR5 measures signal power and noise power on the output port, which indicates SNR measurement on the output port. In order to obtain E_b/N_o, a transform is needed. The relationship between E_b/N_o and E_s/N_o in dB is expressed as

$$E_s/N_o = E_b/N_o + 10log10(k) \tag{5.35}$$

where k is the number of information bits per symbol and it is related to modulation formats or the coding rate in a coded system. E_s is energy per symbol, E_b is energy per bit and N_o is noise density. Assume the modulation format is M-QAM and the coding rate is R_c, then the number of information bits per symbol is defined as

$$k = R_c \times log2(M) \tag{5.36}$$

The transform of E_s/N_o is shown as following

$$\begin{aligned} E_s/N_o &= 10log10((S \cdot T_{symbol})/(N/B)) \\ &= 10log10((T_{symbol} \cdot F_s)/(S/N)) \\ &= 10log10(T_{symbol}/T_{sample}) + SNR \end{aligned} \tag{5.37}$$

where S is the signal power, in watts, N is the noise power, in watts, B is the noise bandwidth, in Hertz, $F_s = B = 1/T_{sample}$ is the sampling frequency, in Hertz, T_{symbol} is the symbol period, in second and T_{sample} is the sampling period, in second. It should be noted the ratio of T_{symbol}/T_{sample} is equivalent to the oversampling ratio.

5.8.1 Transmitter

At the transmitter, a simple convolutional coding scheme is used for all the LTE-like experiments (OFDM and SEFDM) to allow fair comparisons. Therefore, the performance obtained is not optimized for each case and improved performance may be obtained if bespoke coding was designed for each case as suggested in [181]. The binary bit stream $\Upsilon = [\gamma_1, \gamma_2, ..., \gamma_\varepsilon]$ is first encoded in the encoder where a coding rate $R_{code} = 1/2$. The code used is a (7,5) recursive systematic convolutional (RSC) code of memory 2 with feedforward polynomial $G_1(D) = 1 + D + D^2$ and feedback polynomial $G_2(D) = 1 + D^2$

[145]. The bits in the coded vector $W = [w_1, w_2, ..., w_\eta]$ of length $\eta = \varepsilon/R_{code}$, are interleaved using a random interleaver $\mathbf{\Pi}$. The interleaved bits $\tilde{S}$ are mapped to the corresponding symbols $S = [s_1, s_2, ..., s_\Theta]$ of length $\Theta = \eta/log_2 O$, where O=4 is the constellation cardinality in this experiment. One uncoded pilot symbol is inserted at the beginning of each subframe (i.e. 13 complex coded symbols) and is used to estimate CSI, compensate for imperfect timing synchronization and LO phase offset. It should be noted that LTE release 8 defines 10% protection guard sub-carriers. Therefore, we should reserve a 10% gap between adjacent component carriers to combat the Doppler spread encountered in a real world fading channel. This is managed after a serial to parallel conversion by inserting zeros following useful data in each band. The guard band is the sub-carriers which are null for the purpose of oversampling. The modified stream appended with pilot symbols is modulated to specific frequencies by using IFFT operations. In order to combat multipath delay spread, a CP is added before S/P. The aforementioned processes are carried out offline in the Matlab environment (left hand block of Fig. 5.8). Subsequently, the I and Q data of the SEFDM signal are uploaded to the RF environment. In the RF domain, the Aeroflex 3026C converts the incoming baseband digital signal to an analogue one and up-converts the analogue signal to a 2 GHz frequency.

5.8.2 LTE Channel Model

There are three different multipath fading channel models defined in 3GPP technical recommendation (TR) 36.104 [167]. They are Extended Pedestrian A (EPA), Extended Vehicular A (EVA) and Extended Typical Urban (ETU). In the following experiment, we evaluate the performance of the CA-SEFDM system in the condition of the EPA channel model. Table 5.3 presents EPA channel Doppler frequency shift, relative power and delay values of each path.

The Spirent VR5 channel emulator can emulate any real-time wireless channels. In this experiment, we use the LTE EPA channel model [167]. This can be configured

Table 5.3: LTE EPA Fading channel model

Path	Doppler frequency	Relative power	Delay values
1	5 Hz	0.0 dB	0 ns
2	5 Hz	-1.0 dB	30 ns
3	5 Hz	-2.0 dB	70 ns
4	5 Hz	-3.0 dB	90 ns
5	5 Hz	-8.0 dB	110 ns
6	5 Hz	-17.2 dB	190 ns
7	5 Hz	-20.8 dB	410 ns

by setting the multipath power delay profile via the graphical user interface (GUI) on the channel emulator. A multipath frequency selective fading effect is reflected in frequency response magnitude. A real-world frequency response of a transmitted signal without multipath fading effect is shown in the left inset of Fig. 5.8. It is apparent that responses at each frequency within the whole bandwidth have the same power spectral magnitude. Multipath fading and Doppler shift effects resulting from user mobility lead to a frequency selective channel. After passing through the fading channel, it is observed that the channel gains at each frequency vary significantly. Since the channel responses vary in time, three faded spectra are randomly obtained to demonstrate fading channel characteristics.

5.8.3 Receiver

At the receiver side, after experiencing the EPA fading channel, the distorted analogue signals are down-converted to baseband and transformed back to digital I and Q signals in 3035C. This process includes down conversion and analogue to digital conversion. The captured signal is then transferred to the DSP_{RX} block for offline processing. The signal is first delivered to a serial to parallel (S/P) transform block and then the CP is stripped away. Due to the effects of multipath fading channel, phase and amplitude distortions are introduced and these impacts are estimated and equalized in the channel estimation and channel equalization modules, respectively. The compensated signal is demodulated in the FFT block and raw SEFDM symbols are obtained after the removal

of guard band and zeros. As mentioned before, sub-carriers are no longer orthogonally packed, ICI is introduced and can severely degrade the performance. Therefore, in order to recover SEFDM symbols from distortions and interference, a soft detector is employed after the P/S operation. Finally, the recovered complex symbols are demapped to a binary data stream for the following BER calculations.

5.9 Radio Frequency (RF) Effects

In our previous SEFDM simulations, an ideal condition that only AWGN channel is taken into account. A perfect RF scenario is assumed. However, in a real world wireless communication system, RF distortions result in signal degradations and further lead to performance loss. Thus, optimal performance obtained in an ideal simulation environment would not exist in a real world communication environment. RF impairments include nonlinear distortions from high power amplifier (HPA), IQ imbalance, frequency offset, phase noise, imperfect timing synchronization and sampling phase offset. These effects have been studied in detail in [182] [183] [184] [185] [186], while joint effect is more complicated since each impairment may strengthen each other and compensation for one effect could enhance the impact of others. In this section, taking into account equipments used in our experiment, RF impairments such as imperfect timing synchronization and sampling phase offset are considered, which make SEFDM systems more realistic.

5.9.1 RF Studies in A Bypass Channel

A bypass channel indicates a channel without AWGN and multipath effects. Thus, the RF effect can be studied more accurately. Fig. 5.10 shows OFDM constellations before and after compensations. Fig. 5.10(a) illustrates that without any compensation algorithms, constellation is like a circle. There are many reasons account for the constellation rotation. The first one is frequency offset. Techniques for its mitigation have been elaborately studied in [170]. Other possible factors are imperfect timing

synchronization, phase noise, LO phase offset and sampling phase errors.

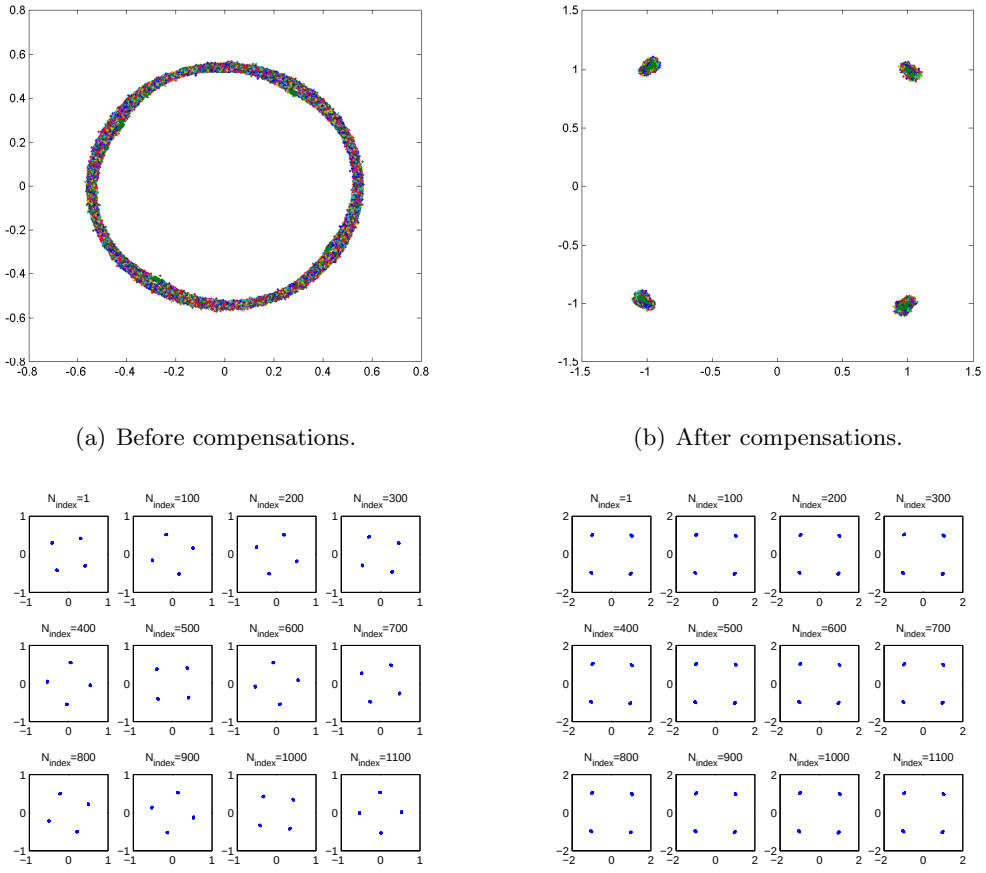

(a) Before compensations.

(b) After compensations.

(c) Before compensation on each sub-carrier.

(d) After compensation on each sub-carrier.

Figure 5.10: Practical constellation illustrations of OFDM amplitude/phase distortions and its compensations in a bypass channel. Sub-carrier indexes are clearly marked on each constellation diagrams in (c) and (d).

Since we don't know what kind of RF effects exist in the experiment, we firstly employ a classic one-tap frequency-domain ZF channel compensation method [11] to correct the rotations. As is shown in Fig. 5.10(b), the constellation rotations can be corrected. Four constellation points are clearly illustrated. Thus, it is proved that the testbed has no frequency offset issue since frequency offset cannot be straightforwardly compensated by the frequency-domain ZF method. However, it is difficult to separate imperfect timing synchronization, phase noise, LO phase offset and sampling phase

error since they all introduce time independent phase offset.

In order to get a detailed understanding of the reason for the constellation rotations, effects of constellation rotations for each sub-carrier are investigated. The result is shown in Fig. 5.10(c). The FFT size in the system is 2048 in which 1200 sub-carriers are used to transmit data, the rest are reserved for guard bands. In this investigation, 16 non-adjacent sub-carriers are selected with equal sub-carrier index gap, the sub-carrier indices are therefore $N_{index} = 1, 100, 200, ...1100$. In Fig. 5.10(c), we can see the phase offsets of constellation points on various sub-carriers are different. Constellations on sub-carriers corresponding to low frequencies rotate slightly while constellations on higher frequency sub-carriers experience a larger rotation. It seems that the rotation degree is proportional to the sub-carrier index. In addition, the rotation degree of the first sub-carrier is not zero, which indicates a fixed LO phase offset exists. It should be noted that for each sub-carrier, constellations are not time dependent like a circle, which further confirms no frequency offset exists. However, sampling phase offset could also exist.

SEFDM constellation performance is evaluated in Fig. 5.11. The bandwidth compression factor is α=0.8. Both constellation results before and after compensation are illustrated. It is evident that even without AWGN, the constellation seems to be affected by high interference. The reason for this is the self-created ICI introduced by SEFDM. In Fig. 5.11(a), the scattered constellation points result in a ball, which is totally different compared with the constellation circle shown in Fig. 5.10(a). By using the special time-domain SEFDM compensation algorithm [45], the rotated constellation points can be corrected in Fig. 5.11(b). The detailed investigations in terms of the SEFDM channel estimation and equalization algorithms have been done in section 5.6 and section 5.7. After compensations, the 4QAM constellation points are not easy to be recognized since it is severely affected by the self-created ICI. The interference introduced by non-orthogonal packed sub-carriers can be mitigated using the iterative interference cancellation scheme. In the following sections, detailed studies for each

factors are presented including mathematical explanations and practical results.

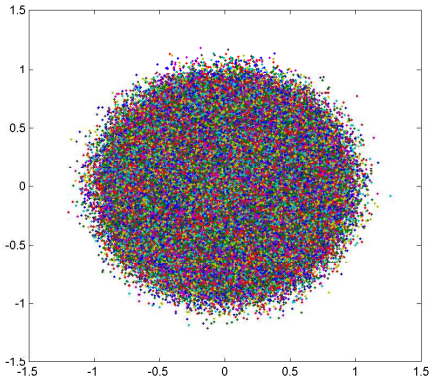

(a) Before compensations.

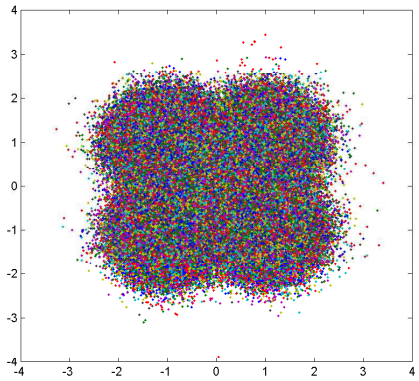

(b) After compensations.

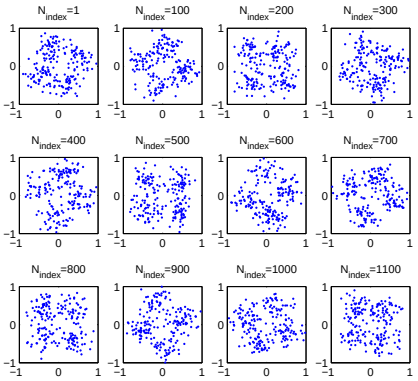

(c) Before compensation on each sub-carrier.

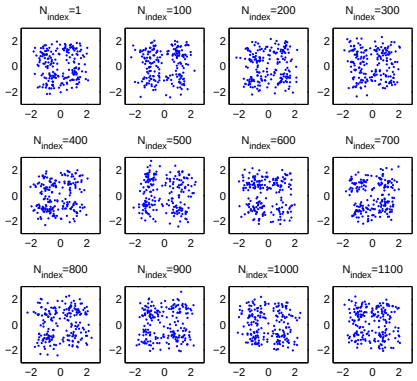

(d) After compensation on each sub-carrier.

Figure 5.11: Practical constellation illustrations of SEFDM (α=0.8) amplitude/phase distortions and its compensations in a bypass channel. Sub-carrier indexes are clearly marked on each constellation diagrams in (c) and (d).

5.9.2 Timing Synchronization

5.9.2.1 Symbol Time Offset

In order to properly demodulate and recover OFDM signals, the exact starting point of received data stream has to be located, which means correct symbol timing synchronization is required. The effects of symbol timing offset (STO) are mathematically presented in Table. 5.4. Note that the STO with δ in time domain results in the phase

offset of $2\pi k\delta/N$ in frequency domain, which is proportional to the sub-carrier index and the value of δ.

Table 5.4: The effects of STO

	Received signal	STO (δ)
Time domain	y[n]	x[n+δ]
Frequency domain	Y[k]	X[k]$e^{j2\pi k\delta/N}$

In a practical system, the starting point of a data stream is not always located accurately. The estimated starting point could be too early or too late. Thus, the effects would be different. Four cases [170] are illustrated in Fig. 5.12. The first case is that the estimated starting point is exactly the starting point of transmitted signals. The second case is that the estimated point is a little earlier, the third one is too earlier and the last one is a little later. It should be noted that multi-path delay is taken into account in Fig. 5.12 where τ is the maximum time delay. In the following, we will discuss these four different scenarios separately.

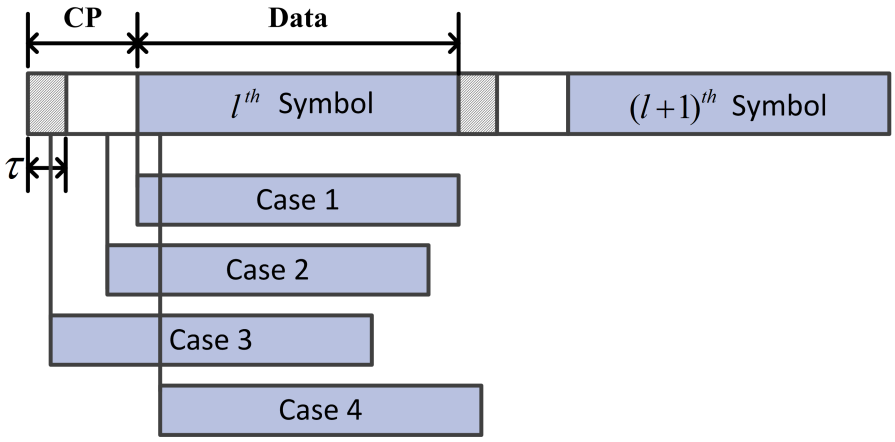

Figure 5.12: Four different cases of estimated starting point for an OFDM data stream.

Scenario 1: This is an ideal result that the estimated starting point is exactly the beginning of a transmitted OFDM signal. In this case, the OFDM symbols can be recovered with no compensation.

Scenario 2: This is the case that the estimated starting point is a little earlier, but

after the multipath delay τ range. The l^{th} OFDM symbol doesn't overlap with the $(l-1)^{th}$ OFDM symbol, which means no ISI is introduced. We mathematically show the frequency-domain signal after taking FFT of the time-domain received samples $x_l[n+\delta]$ for $n \in [0, N-1]$. The equation is expressed as:

$$\begin{aligned} Y_l[k] &= \frac{1}{N}\sum_{n=0}^{N-1} x_l[n+\delta]e^{-j2\pi nk/N} \\ &= \frac{1}{N}\sum_{n=0}^{N-1}\{\sum_{p=0}^{N-1} X_l[p]e^{j2\pi(n+\delta)p/N}\}e^{-j2\pi nk/N} \\ &= \frac{1}{N}\sum_{p=0}^{N-1} X_l[p]e^{j2\pi p\delta/N}\sum_{n=0}^{N-1} e^{j2\pi(p-k)n/N} \end{aligned} \tag{5.38}$$

where the second term in (5.38) can be transformed to

$$\begin{aligned} \sum_{n=0}^{N-1} e^{j2\pi(p-k)n/N} &= e^{j\pi(p-k)\frac{N-1}{N}} \cdot \frac{sin[\pi(k-p)]}{sin[\pi(k-p)/N]} \\ &= \begin{cases} N & for\ k = p \\ 0 & for\ k \neq p \end{cases} \end{aligned} \tag{5.39}$$

Substituting (5.39) into (5.38), we can get a new expression as

$$Y_l[k] = X_l[k]e^{j2\pi k\delta/N} \tag{5.40}$$

Observing (5.40), adjacent sub-carriers are still orthogonal while a phase offset exists and is proportional to the STO δ and the sub-carrier index k. This would result in constellation rotations as shown in Fig. 5.10(a). It is noted that the phase error can be compensated using the one-tap frequency-domain channel equalizer.

Scenario 3: This is the case that the estimated starting point is too earlier than the exact one. In this case, the l^{th} OFDM symbol overlaps with the $(l-1)^{th}$ OFDM

symbol. Thus, both ISI (from the $(l-1)^{th}$ symbol) and ICI are introduced.

Scenario 4: This is the case when the estimated starting point is a little later than the exact one. In this case, the captured signal consists of a part of the l^{th} OFDM symbol and a part of the $(l+1)^{th}$ OFDM symbol. Similar to Scenario 3, both ISI and ICI are introduced. A detailed mathematical explanation is referred to [170].

Considering our experiments and practical results from Fig. 5.10, the timing offset in Scenario 2 exists. This is due to the fact that a 'small' time delay exists in cables or wireless channels. In the experiment, timing synchronization is assisted in hardware using a trigger signal from PXI, which is directly delivered from the transmitter to the receiver through an internal short cable. However, the data signal is delivered through an external long cable. Therefore, the transmission timing difference due to different length of cables results in the timing synchronization error. Furthermore, if the signal is delivered through an even longer cable (several kilometres), the effect of time delay would be more serious. In that case, the effect of Scenario 3 would exist.

5.9.2.2 Compensation Schemes for STO

Based on the analysis of STO effects, STO can cause sub-carrier index dependent phase distortion, ISI and ICI. The first effect can be removed using channel equalization while the rest two factors cannot be corrected once it occurs. Therefore, the starting point of an OFDM frame has to be accurately estimated. In time domain, CP is a replica of the data in an OFDM symbol. Therefore, the correlation between the CP and the data part can be used for STO estimation. However, this method could be affected by multipath fading. In addition, training symbols consisting of two identical sequences are also applicable. This method introduces overhead, but it is robust against multipath fading effect. In frequency domain, since the phase rotation is proportional to the index of sub-carriers, STO can be estimated by comparing phase difference between symbols on two adjacent sub-carriers [170].

5.9.2.3 Imperfect Timing Synchronization

In order to further verify whether LO phase offset and sampling phase offset exist in the testbed, a specific number of received samples are manually shifted to locate the accurate starting point. If four constellation points are clearly and properly illustrated, which means no LO phase offset and sampling phase offset exist in the experiment. Otherwise, compensation algorithms have to be used to remove their effects. On the basis of the previous analysis, the estimated starting point is a little earlier than the exact starting point. Therefore, the following shift of the data stream is in the direction of left (advance the data stream).

1. **One Sample Shift Constellation**

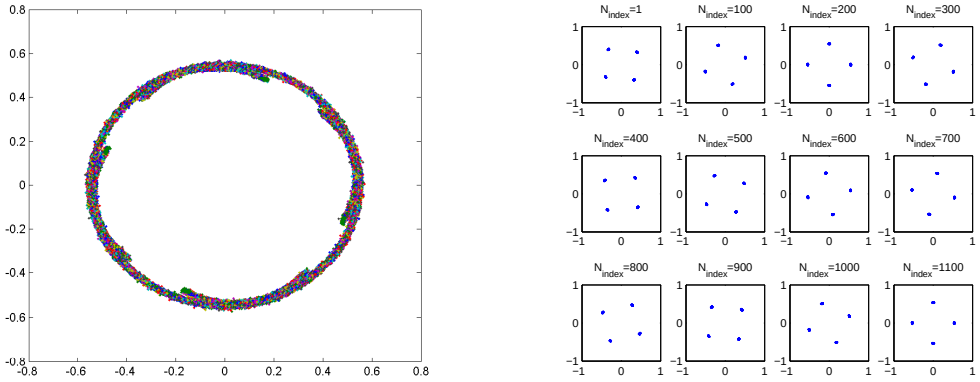

(a) One sample shift.

(b) One sample shift effect on each sub-carrier.

Figure 5.13: Constellation illustrations of one sample shift for OFDM.

Firstly, one sample is shifted and constellation for all sub-carriers and constellation for a subset of sub-carriers are illustrated in Fig. 5.13. It seems that the rotation is mitigated slightly but it is still a circle. Therefore, it is proved that one sample shift is not sufficient to remove the effect of imperfect timing synchronization. Finally, it should be noted that the rotation direction in Fig. 5.13(b) is clockwise due to the fact that the estimated starting point of the stream is earlier than the exact starting point of the data stream.

2. **Two Sample Shift Constellation**

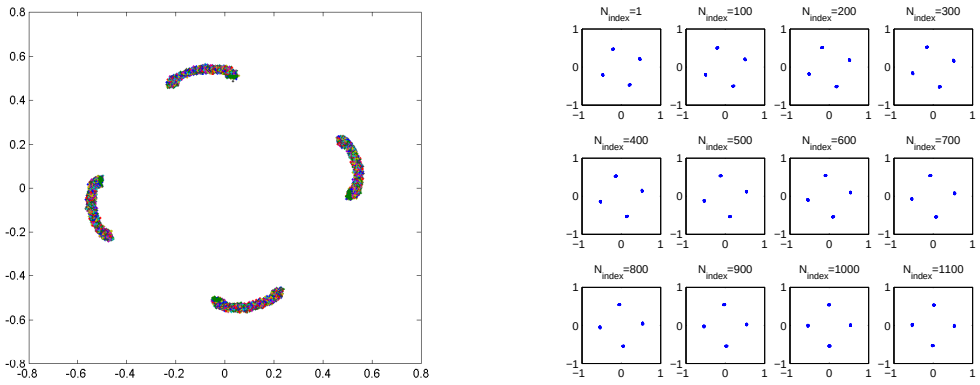

(a) Two samples shift.

(b) Two samples shift effect on each sub-carrier.

Figure 5.14: Constellation illustrations of two sample shift for OFDM.

In this part, two samples are shifted to get constellation results in Fig. 5.14.

Constellations become better than the one in Fig. 5.13. Four points are clearly recognized with small deviations in Fig. 5.14(a). This indicates that the imperfect timing synchronization effect is mitigated in some degree. The deviation is caused by a fractional sample shift, in other words, sampling phase offset exists. Furthermore, checking the constellation performance on each sub-carrier, It is apparent that rotation is fixed and rotation degrees for each sub-carrier are almost the same. This fixed rotation degree is caused by LO phase offset. Therefore, it is inferred that the experimental testbed has no frequency offset (no rotation circle on each sub-carrier); with imperfect timing synchronization (two samples shift or maybe random); with phase offset from local oscillator; with sampling phase offset.

3. **Three Sample Shift Constellation**

In order to make sure whether two sample shift is optimum, in Fig. 5.15, three samples are shifted. However, the constellation becomes worse again. It is impossible to recognize four points in this case, which indicates that an imperfect

timing synchronization is introduced again by advancing three samples. In addition, constellations on each sub-carrier are investigated, and again, rotation degrees on each sub-carrier are different. Finally, it should be noted that the rotation direction in Fig. 5.15(b) is anti-clockwise due to the fact that the estimated starting point of the stream is one sample later than the exact starting point of the data stream.

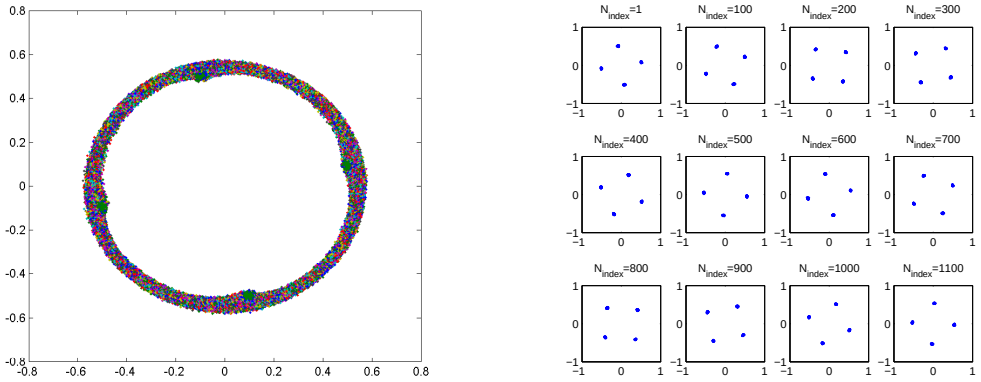

(a) Three samples shift.

(b) Three samples shift effect on each sub-carrier.

Figure 5.15: Constellation illustrations of three sample shift for OFDM.

5.9.3 Sampling Clock Phase Offset

Fig. 5.16 illustrates the cable connections of different modules on the front panel of PXI. The module labelled A is the power and digital signal provider. Digital signals from a PC will be delivered to this module via the serial interface. Module B,D,F are clock boards which provide external 10 MHz reference signal and LO signal to the 3026C RF signal generator and 3035C RF digitizer. Module C,G are signal receivers (digitizers) and module E is an RF signal generator. Although there are three separate clock boards, all the modules are synchronized by the 10 MHz reference signal from module B attempting to establish a frequency-offset-free situation. However, phase difference cannot be prevented since the LO frequency and sampling frequency are independently fed to module C and module E. LO phase offset leads to fixed constellation rotation and

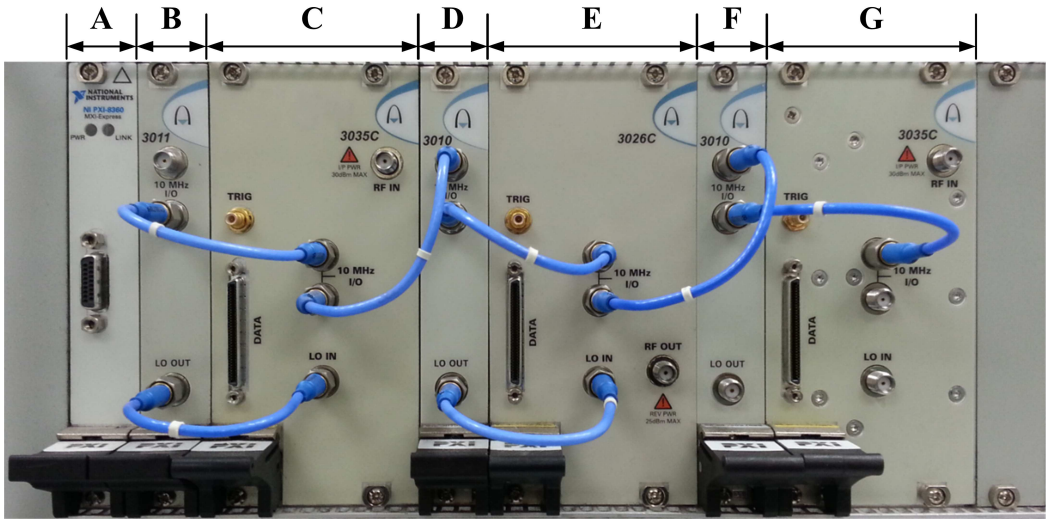

Figure 5.16: Cable connections on the front panel of PXI.

its compensation is straightforward using channel compensation algorithms. However, the sampling phase offset leads to a sub-carrier index dependent phase offset, which is constellation circle. Its effect and compensation will be explained in the following.

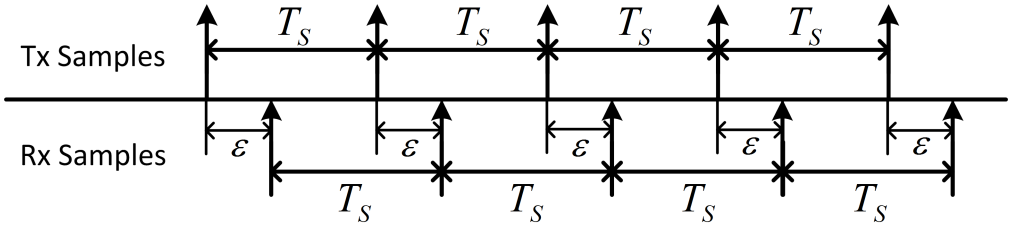

Figure 5.17: An illustration of sampling clock phase offset.

After manually correcting the imperfect timing synchronization by shifting two samples in section 5.9.2.3, a deviation still exists. The reason for this comes from fractional symbol timing offset or sampling phase offset. The principle of sampling phase offset is illustrated in Fig. 5.17. The start sampling point of the received sample stream is shifted by ε, which is shorter than one sample period. Thus, it cannot be compensated in time-domain by manually shifting one sample. The phase offset in a sampling clock can be viewed as the symbol timing error. In frequency domain, the effect is equiva-

lent to sub-carrier dependent phase offset. Since the effect of sampling phase offset is usually small, it is often treated as a part of imperfect timing synchronization, without requiring any additional phase offset compensation algorithms.

5.9.4 Joint RF Effects in A Frequency Selective Channel

In this section, joint effects from both RF and the frequency selective channel are investigated. Thus, the bypass channel is replaced by the frequency selective channel, which is described in (5.24). Results in Fig. 5.18(a) show that before channel equalization, constellation pionts are scattered and seriously interfered with each other.

The frequency selective channel introduces both amplitude and phase distortions. Thus, the constellation is no longer a circle and is scattered like a 'ball'. After the typical frequency-domain channel compensation, signals can be recovered with clear constellation points. Comparing the results of a bypass channel in Fig. 5.10(b) and the results in Fig. 5.18(b), it is evident that in the joint RF and frequency selective channel scenario, the signal is slightly distorted. The frequency selective channel has a additional negative impact on system performance. It is concluded that the joint effect significantly affect system performance and its effect is higher than the RF effect alone. The scattering condition can only be mitigated by using some signal detection algorithms at receiver side.

5.10 Experimental Results

5.10.1 Experimental Conditions

This experiment is carried out based on the setup shown in Fig. 5.8. As mentioned before, we use a single IFFT/FFT structure to generate and demodulate CA signals, respectively. Therefore, the IFFT/FFT size is larger than the one defined in LTE release 8. CA-SEFDM experimental system specifications are given in Table 5.5. In this experiment, a total of 25 MHz bandwidth is used instead of the maximum (100

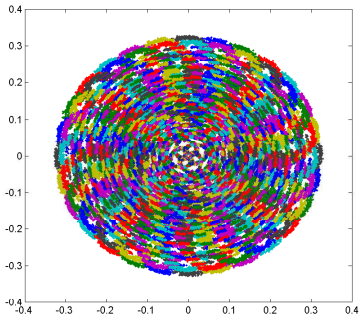

(a) Before compensations.

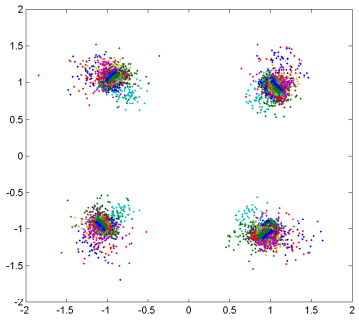

(b) After compensations.

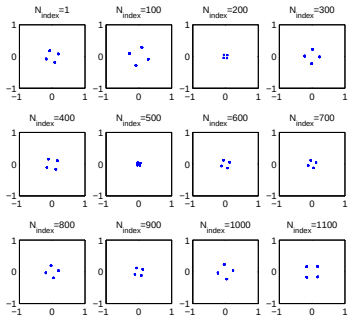

(c) Before compensation on each sub-carrier.

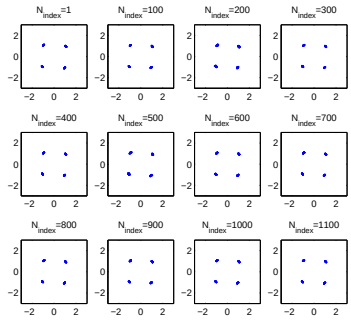

(d) After compensation on each sub-carrier.

Figure 5.18: Practical constellation illustrations of OFDM amplitude/phase distortions and its compensation in a joint RF and frequency selective scenario.

MHz) defined in LTE-Advanced. This is due to limitations of available instruments. Therefore, 5 CCs are aggregated with 5 MHz bandwidth for each in a CA-OFDM scenario or 7 CCs are aggregated with $\alpha\times$ 5 MHz bandwidth for each in a CA-SEFDM scenario. The central carrier frequency is set to be 2 GHz. Carrier frequencies of other CCs can be obtained by shifting $\alpha\times$ 5 MHz from the central carrier frequency. The system may be adapted to a higher bandwidth (e.g. 100 MHz) by replacing 5 MHz CCs with the 20 MHz ones at the expense of linear increase in complexity. A real-time LTE fading channel is configured with the use of the VR5 channel emulator. The channel specifications are shown in Table 5.3. Since different SEFDM symbols could experience channels with different phase and power distortions, therefore, we totally measure 6,500 CA-SEFDM symbols and compute their average bit error rate.

Table 5.5: Experimental system specifications

Parameters	**Values**
Central carrier frequency	2 GHz
Sampling frequency	61.44 MHz
CA channel bandwidth	25 MHz
Values of α	1 (OFDM); 0.84; 0.72
Number of CCs	5; 6; 7
Maximum effective bit rate	20.1 Mbps; 23.5 Mbps; 27.4 Mbps
Bandwidth of one CC	$\alpha\times$5 MHz
Sub-carrier baseband bandwidth	15 KHz
Sub-carrier spacing	$\alpha\times$15 KHz
IFFT/FFT size	4096
Occupied sub-carriers in one CC	301
Cyclic prefix	288
Modulation scheme	4QAM
Channel coding	(7,5) convolutional code
Coding rate	R_{code}=1/2

5.10.2 Error Performance

The iteration performance for three systems is studied in Fig. 5.19 where up to three iterations are tested. In terms of the CA-OFDM system with 5 CCs, it is evident that no iteration is required to get converged performance. However, for the CA-SEFDM system with 6 CCs, with one iteration, the performance can be slightly improved. Although the improvement is not obvious, in the following BER and effective spectral efficiency demonstrations, one iteration is used for the 6 CCs scenario. The second CA-SEFDM system employs 7 CCs indicating higher interference. As is shown in the first inset of Fig. 5.19, at least one iteration has to be used in the experiment to get converged performance.

As illustrated in Fig. 5.20, the performance in terms of BER is evaluated for three different systems. The first CA system is based on OFDM which packs 5 CCs. The second CA system is based on SEFDM, which can aggregate 6 CCs with each band compressed by $16\% = (1 - 0.84) \times 100\%$. Another system packs 7 CCs with a higher bandwidth compression corresponding to $28\% = (1 - 0.72) \times 100\%$. In Fig. 5.20, it is clearly seen that by using 6 CCs, the error performance is close (within 1.7dB) to that of

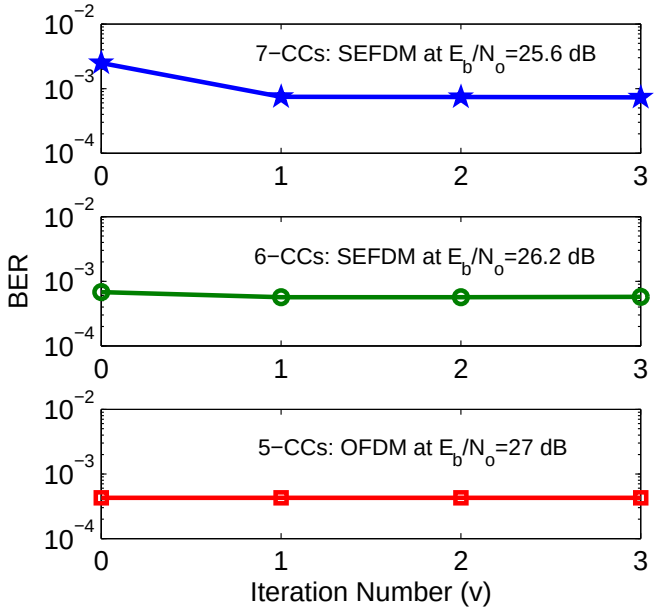

Figure 5.19: Iteration performance for three systems in the experiment environment.

the system with 5 CCs, occupying in the same bandwidth. This proves that occupying the same bandwidth, the CA with SEFDM scenario can transmit more data. In terms of the CA scenario with 7 CCs, even with a high level of bandwidth compression and therefore higher interference, the performance is still reasonably close to that of OFDM with some limited degradation (or power penalty) shown experimentally to be below 3 dB for all E_b/N_o values tested.

5.10.3 Spectral Efficiency

Although CA-SEFDM introduces slight performance degradation, Fig. 5.21 shows that CA-SEFDM outperforms CA-OFDM in terms of effective spectral efficiency, which is defined as the non-error bits per second per Hertz that can be achieved. In Fig. 5.21, spectral efficiencies are plotted for three different CA schemes at different E_b/N_o values. The effective spectral efficiency is defined as follows:

$$R_a = (1 - BER) \times R_{code} \times B_{(CC,OFDM)} \times N_{CC} \times log_2 O \tag{5.41}$$

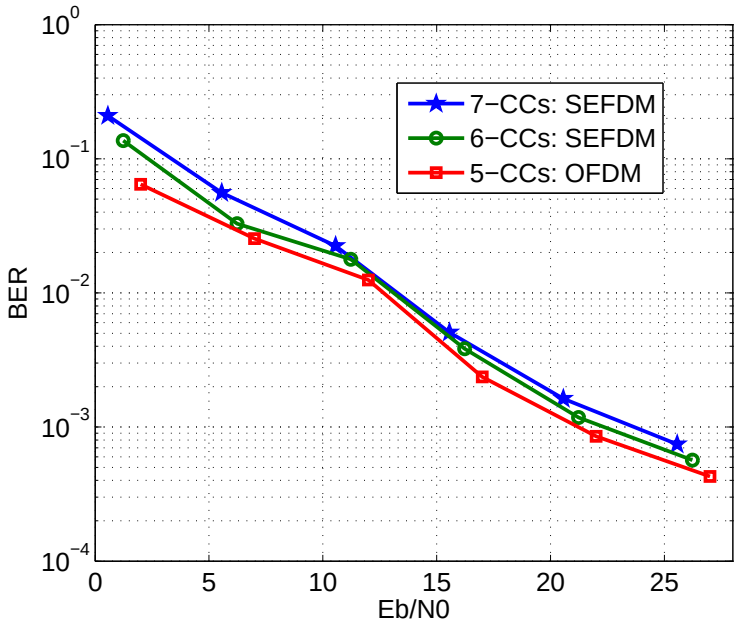

Figure 5.20: Performance of different CA-SEFDM systems operating in a real RF environment with the LTE EPA fading channel.

$$B = B_{(CC,OFDM)} \times N_{(CC,OFDM)} \tag{5.42}$$

$$SE = R_a/B \tag{5.43}$$

where R_a is transmission data rate, B is occupied bandwidth, SE is computed spectral efficiency, BER is the bit error rate at a specific E_b/N_o value, $(1-BER)$ indicates the probability of a non-error received bit stream, $B_{(CC,OFDM)}$ is the bandwidth of one CC in OFDM, N_{CC} is the number of CCs in either OFDM or SEFDM, $N_{(CC,OFDM)}$ is the number of CCs in OFDM and O is the constellation cardinality. Therefore, the spectral efficiency is computed as $SE = R_a/B$. It is apparent in Fig. 5.21 that spectral efficiencies of CA-SEFDM with different CCs are higher than that of CA-OFDM. This is because compared with CA-OFDM, in the CA-SEFDM scenario, more CCs are packed in a given bandwidth.

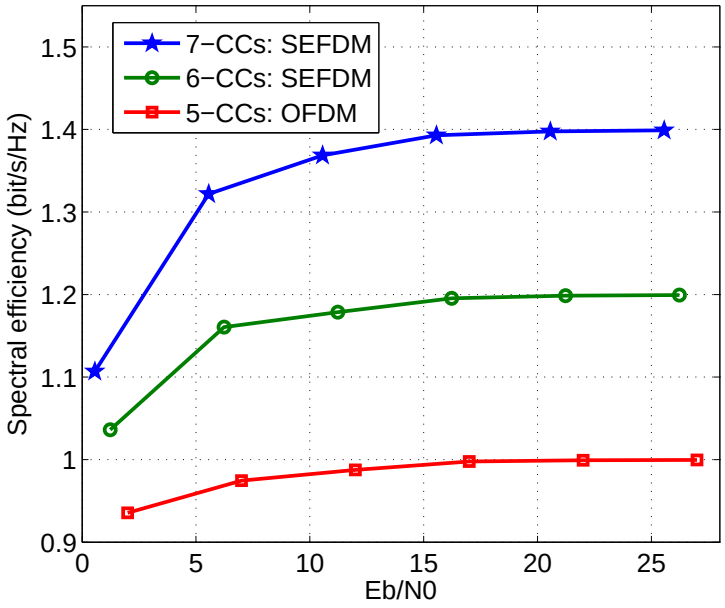

Figure 5.21: Effective spectral efficiency (bit/s/Hz) of different CA-SEFDM systems computed based on the BER information in Fig. 5.20 and system specifications in Table 7.1.

5.11 Promising Applications

Adding more antennas and increasing the occupied bandwidth of a signal are two approaches to improve data rate. However, due to terminal complexity, size and power consumption, it is difficult to further increase the number of antennas. Therefore, bandwidth extension (i.e. CA) is a better solution to achieve a high data rate transmission over a wider bandwidth by aggregating several legacy radio resources (i.e. component carriers). It is apparent that the data rate will scale linearly with the number of CCs. CA not only provides a solution of high data rate transmission, but also simplifies the receiver design. A typical OFDM symbol with a large number of sub-carriers requires complicated channel estimation and signal detection. In a CA-OFDM scheme, the entire spectrum is split into several CCs where simple channel estimation and signal detection can be employed for each. Furthermore, by using the CA scheme, lower speed DAC/ADCs are needed for each CC, which overcomes the ADC/DAC bandwidth bot-

tleneck issue [154]. In addition, a narrow band of CC could release the challenges of PAPR [168]. In a multiple access scenario, different users may experience different channel conditions leading to various signal-to-interference-plus-noise ratios (SINRs). Therefore, it would be more efficient to allow different users to select their own preferred CCs with better channel conditions. This opportunistic user scheduling refers to multiuser diversity [187]. CA-SEFDM inherits all the mentioned advantages of CA-OFDM and further brings new benefits. Two possible applications of CA-SEFDM are studied in the following.

5.11.1 Scenario I - enhanced throughput (TDMA)

In an OFDM system with a time division multiple access (TDMA) scenario, users are arranged in the time domain and the whole bandwidth is allocated to one user at one time. In a CA-OFDM system, multiple CCs (5 CCs in this work) are aggregated leading to a broadband service coming simultaneously from all 5 CCs. This means one user can get 5× throughput service. In order to get a higher throughput, the solution is either increasing the number of CCs or the total bandwidth. However, the maximum bandwidth in LTE-Advanced is 100 MHz. Therefore, aggregating more CCs in a limited bandwidth is a better solution. The way is to compress each CC and save bandwidth for additional CCs. In the CA-SEFDM scenario, 7 CCs are aggregated leading to a 7× throughput with no increase in the total bandwidth.

5.11.2 Scenario II - enhanced user multiplexing (FDMA)

The proposed compressed CA technique can also be applied in user multiplexing schemes. As different users in the same frequency band may have different SNR or signal-to-interference-plus-noise ratio (SINR), it would be more efficient to allow users to select their own preferred subset of sub-carriers with better channel conditions, rather than selecting a single user that occupies all the sub-carriers at the same time. In an OFDM system with a frequency division multiple access (FDMA) scenario termed OFDM-

FDMA (OFDMA), users are arranged in both the time and frequency domain. In this case, all users can share the same bandwidth. By using the SEFDM technique, we may introduce an enhanced user multiplexing scheme named SEFDM-FDMA (SEFDMA). Taking into account the OFDMA in a CA scenario, 5 CCs can be allocated to 5 different users at one time. However, in order to provide service to more users, CA-OFDMA has to provide more available bandwidths. In the CA-SEFDMA scheme, we compress each CC and integrate two more CCs in a given bandwidth. In other words, 2 more users can be served at one time. In terms of the multiuser diversity, since more CCs are introduced, each CC with a narrower bandwidth could experience a more flatter frequency response over the typical one. In other words, it has more user multiplexing flexibility, especially when the number of CCs increases. Our proposal is flexible in a CA scenario since the number of CCs in a given bandwidth can be dynamically configured based on users' requirements and fading channel conditions.

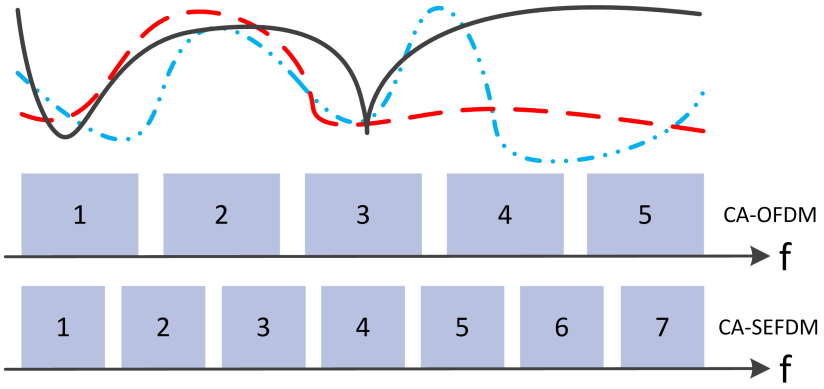

Identification		CA-OFDM	CA-SEFDM
User 1	———	2,4,5	2,3,5,6,7
User 2	-·-·-	2	3,5
User 3	— —	2	2,3

Figure 5.22: Example of user scheduling according to channel conditions.

The main purpose of the multiuser diversity is to allow each user to select its own preferred CCs based on their fading channel condition. Different users have different moving speed, hence, they experience different fading channels. Fig. 5.22 illustrates

an example that how users are scheduled according to fading channel conditions. In order to simplify the demonstration, three users are considered. Their channel states are shown in the figure represented by different frequency responses. The benefit of multiuser diversity is more obvious in a CA-SEFDM scenario since the bandwidth of each band is narrower than a band in OFDM. Therefore, the probability of experiencing fading channel for each SEFDM band is lower than that in OFDM. It is apparent that the radio resources are shared with different users based on different fading conditions. More specifically, depending on the channel SINR, different CCs will be allocated to different users. The channel user 1 experiences is marked with a black line where two deep fading points are observed. In terms of CA-OFDM, only CC(2,4,5) can be allocated due to their high channel SINR. The CC(1,3) are not used because of the deep fading effect. On the other hand, for CA-SEFDM, considering the same fading channel condition, CC(2,3,5,6,7) are available for user 1. It is because that the bandwidth of each CC is compressed, the effect of deep fading is confined to a small bandwidth CC. There would be more unaffected frequency resources that can be allocated to user 1. The allocation principle is the same for user 2 and user 3. It is noted that in the CA-OFDM scenario, both user 2 and user 3 are assigned with CC(2). It indicates only one user (either user 2 or user 3) can be served. However, in the case of CA-SEFDM, user 2 is assigned with CC(3,5) while CC(2,3) are allocated to user 3. Therefore, in the CA-SEFDM scenario, user 2 can use CC(5) and user 3 can use CC(2) indicating that both user 2 and user 3 can be served simultaneously with CC(3) allocated to other users. Based on the above analysis, it is apparent that in the same fading channel condition, CA-SEFDM can support user 1, user 2 and user 3 while in CA-OFDM only user 1 and user 2 (or user 3) can be served. It indicates that CA-SEFDM has an enhanced multiuser diversity leading to a more flexible multiuser scheduling ability.

5.12 Challenges of the Soft Detector

5.12.1 Computational Complexity

To simplify the following discussions, assume oversampling factor ρ=1 resulting in Q=N. In terms of a conventional CA-OFDM system, its experimental setup follows the same architecture as illustrated in Fig. 5.8 except that some modules are specially designed for CA-SEFDM. Firstly, due to the non-orthogonal packed sub-carriers in SEFDM, a typical IFFT based modulation or FFT based demodulation cannot be used straightforwardly. Moreover, the loss of orthogonality leads to ICI which affects the accuracy of channel estimation. Thus, it is difficult to use a single tap frequency-domain equalizer to compensate for multipath fading. Therefore, CSI in SEFDM is obtained through a time-domain ZF based channel estimation and further used to equalize distorted signals. Finally, in order to mitigate both self-created ICI and the ICI from multipath fading, a soft detector is introduced specially for SEFDM.

The computational complexity of various signal generation algorithms is shown in Table. 5.6. In a typical OFDM system, IFFT is an efficient method. For SEFDM, due to the violation of orthogonality, IFFT is not applicable. Several signal generation schemes for SEFDM are presented in Table. 5.6 with various computational complexities. A direct signal generation (applied to any α) according to (2.9) is shown firstly in the third column with a higher complexity than the IFFT one. Furthermore, in the next column, a single IFFT of N/α length is shown with reduced complexity. Then, a multiple IFFTs algorithm including c parallel IFFT blocks each of N points shows its competitive computational complexity. A more efficient algorithm termed 'pruned' IFFT operation was specially investigated for SEFDM in [46] where redundant operations like zero padding or zero insertion are skipped. The 'Pruned-S' indicates the pruned version of the single IFFT while the 'Pruned-M' indicates the multiple IFFTs one. It is apparent that the complexities of all the IFFT based SEFDM algorithms are dependent on both the number of sub-carriers N and the value of α.

Table 5.6: Complexity in number of complex operations for different signal generation algorithms.

Operations	**IFFT**	**Direct**	**Single**	**Multiple**	**Pruned – S**	**Pruned – M**
Multiplications	$\frac{N}{2} \times log_2 N$	N^2	$\frac{N}{2\alpha} \times log_2 \frac{N}{\alpha}$	$c \times (\frac{N}{2} \times log_2 N)$	$\frac{N}{2\alpha} \times log_2 N$	$c \times (\frac{N}{2} \times log_2 \frac{N}{c})$
Additions	$N \times log_2 N$	$N \times (N-1)$	$\frac{N}{\alpha} \times log_2 \frac{N}{\alpha}$	$c \times (N \times log_2 N)$	$\frac{N}{\alpha} \times log_2 N$	$c \times (N \times log_2 \frac{N}{c})$

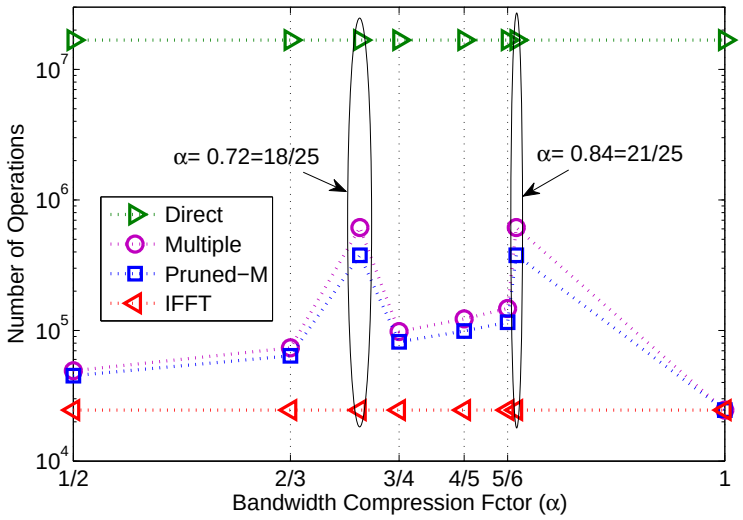

Figure 5.23: Computational complexity in terms of complex multiplication operations for different signal generation algorithms with IFFT size equals 4096 and various α.

Fig. 5.23 shows the computational complexity in terms of complex multiplication operations of several algorithms as a function of bandwidth compression factor α. Generally, the IFFT approach shows great benefit since it requires the least operations compared with other methods. The direct algorithm requires significantly more operations that is more than two orders of magnitude higher than the IFFT one. All IFFT-based SEFDM algorithms exhibit great operation reductions compared with the direct one. It should be mentioned that the computational complexities of the IFFT-based algorithms vary on the basis of α. On the other hand, the IFFT and the direct approaches are independent on α. Due to the extreme requirement of the values of $N/\alpha \in 2^{(\mathbb{N}_{>0})}$ in the single IFFT scheme, its practical use is prohibited. Therefore, the analysis of its complexity is not included in Fig. 5.23. It is evident that the computational complexity of the multiple IFFTs algorithm increases with bandwidth compression factor. This is attributed to the fact that the denominator (i.e. c) of bandwidth compression factor α on the x-axis increases. It is also proved in Table. 5.6 that the complexity is propositional to the value of c. Therefore, it is inferred that the multiple scheme

is applicable to a bandwidth compression factor with small denominators (i.e. c). In Fig. 5.23, in terms of the multiple algorithms including the pruned and non-pruned versions, two peaks are displayed. The reason for this is due to the large denominator (i.e. c=25) of the bandwidth compression factors. In our experiment, in order to demonstrate the idea of CA-SEFDM, the bandwidth compression factors are set to be 0.72 and 0.84 to satisfy the requirements of 7 and 6 aggregated CCs. In practice, the bandwidth compression factors can be selected around 0.72 and 0.84 since adjacent values in Fig. 5.23 show much lower complexity. In addition, the pruned version of the multiple IFFTs algorithm shows little benefit in complexity reduction compared to the non-pruned version. On the other hand, IFFT is a widely used algorithm in modern communication systems (e.g. OFDM), thus, due to the use of the multiple IFFTs algorithm, SEFDM shows its backward compatibility of OFDM.

Due to the self-created ICI, the conventional reference signals defined in LTE release 8 are not applicable to an SEFDM system. As illustrated in Fig. 5.5, a new pattern of reference signals is designed for SEFDM where a unique time-domain channel estimation and equalization are adopted. The computational complexity of the channel estimation and the channel equalization are highly dependent on the size of a system. For OFDM, a fading channel is estimated in the frequency-domain and a single tap frequency-domain equalizer is applied. Therefore, the computational complexity is proportional to the number of sub-carriers. However, for SEFDM, due to its time-domain channel estimation and equalization, the computational complexity is determined by the size of a $N \times N$ channel matrix. It is evident that SEFDM shows a higher computational complexity in terms of channel estimation/equalization than OFDM.

The main difference between SEFDM and OFDM is that SEFDM has a unique soft detector aiming to remove interference. In a normal communication system, FEC is required to eliminate bit errors. Therefore, the BCJR decoder is a common component to both OFDM and SEFDM. In addition, interleaving $\mathbf{\Pi}$ is an operation to improve

the performance of error correcting codes (ECC) by permutating a bit stream to avoid burst errors (e.g. caused by deep fading). At the receiver, a reverse operation termed deinterleaving $\mathbf{\Pi}^{-1}$ is required. However, SEFDM requires an additional interleaver in the soft detector for the purpose of iterative process. It is apparent that the interleaver $\mathbf{\Pi}$ within the SEFDM soft detector causes additional resource consumptions. The complexity of the FFT detector is related to Table. 5.6 since the basic operation within the FFT detector is IFFT based SEFDM signal generation. Table 5.7 shows the complexity of the FFT detector on the basis of the multiple IFFTs architecture. According to the mathematical analysis in section 3.4.2, the FFT detector consists of a simplified demodulator (3.27) and an interference generator (3.28). Additional operation is (3.31), whilst (3.32) has no computational cost.

Table 5.7: Complexity in number of complex operations per SEFDM symbol per iteration ($\rho = 1$)

Operations	**FFT Detector**
Multiplications in (3.27)	$c \times ((N/2) \times log_2 N)$
Additions in (3.27)	$c \times (N \times log_2 N)$
Multiplications in (3.28)	$(c-1) \times ((N/2) \times log_2 N)$
Additions in (3.28)	$(c-1) \times (N \times log_2 N)$
Multiplications in (3.31)	$(N/2) \times log_2 N$
Additions in (3.31)	$N \times log_2 N$

5.12.2 Processing Latency

In addition to the added computational complexity, the soft detector introduces a time delay due to the iterative architecture. The throughput is dependent on the number of iterations. The higher number of iterations, the smaller the throughput is achieved. A functional block diagram of the Turbo principle SEFDM soft detector simplified from Fig. 3.20 is shown in Fig. 5.24. Soft information is exchanged and updated between the FFT detector (including function A, B) and the BCJR decoder (function C) iteratively. After several iterations, the soft information remains the same and the converged performance is obtained.

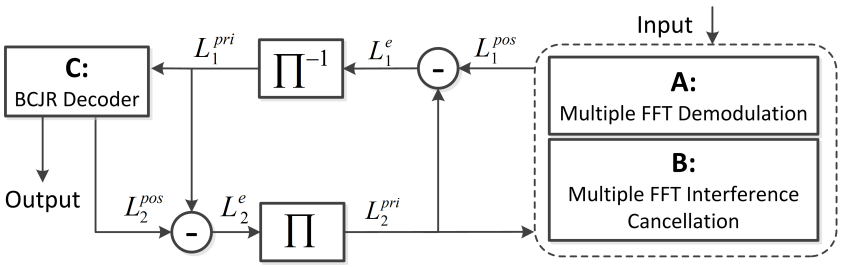

Figure 5.24: Functional block diagram of the Turbo-SEFDM soft detector.

Since we use a Turbo principle architecture, the interference canceller and demodulator are not activated simultaneously. Considering future hardware implementation, the FFT detector can reuse demodulation (function A) and interference cancellation (function B) through time multiplexing. The processing timing diagram of the reuse principle is shown in Fig. 5.25. The numbers next to the horizontal axis indicate processing time instants. The capital letters in each block indicate specific functions labelled in Fig. 5.24 and numbers after capital letters reflect SEFDM symbol index. In order to detect the first SEFDM symbol, the processing order is $A1 \rightarrow B1 \rightarrow C1 \rightarrow B1 \rightarrow C1$, which requires 5 time instants.

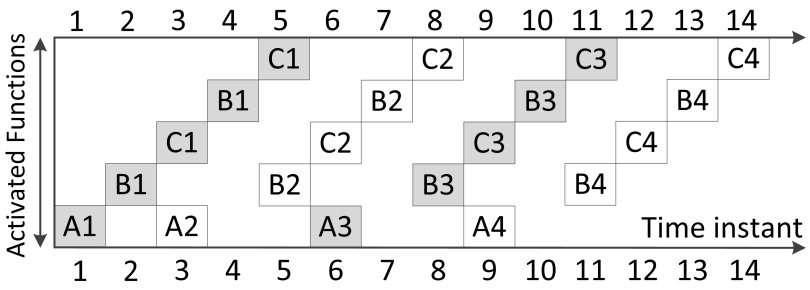

Figure 5.25: Processing timing diagram of the SEFDM soft detector. One iteration is defined by B1→B1 in this diagram.

In order to improve processing efficiency, the second symbol can be processed together with the first one. But it should be noted that A and B cannot be activated simultaneously while A/B and C can operate at the same time. This is because A and B share the same hardware resource, at any one time, there is only one function

can be activated. By using this scheme, the efficiency of is improved. Due to this reason, the second detected symbol is output at the 8^{th} time instant. Since it is not a fully pipelined structure, it cannot process data sequentially. The white area between symbol 1 and symbol 2 is reserved for iterations between function B and function C. In order to remove the white area in Fig. 5.25, a fully pipelined structure can be applied by occupying additional hardware resources for functions A, B and C. This is a trade-off between throughput and complexity. In particular, function A/B and function C are active at every time instant after the 3^{rd} time instant. Therefore, after the initial latency (5 time instants), one SEFDM symbol is detected every 3 time instants. It should be mentioned that the initial latency existing in the Turbo architecture is by no means removed even using a pipelined structure.

5.13 Comparison of Single Detector and Multiple Detectors

In this section, SEFDM is evaluated in the carrier aggregation scenario. Each band is termed one component carriers (CC). The purpose of this technique is to aggregate fragmented legacy LTE signal bands and obtain an extended wide bandwidth. In the LTE standard, a 10% protection guard band is introduced to mitigate the effect of Doppler shift. The bandwidth of the guard band is a multiple sub-carrier spacing. Therefore, in the typical CA-OFDM scenario, interband orthogonality maintains between adjacent CCs.

To detect the CA signal, two approaches can be employed. First, each CC is detected separately by using a simple detector. Second, a single complicated detector is used for the entire CCs. This section studies the effect of two scenarios. For CA-OFDM, in either cases, due to the interband orthogonality, interband interference can be avoided between the neighbouring CCs, despite the sub-carrier power leakage from neighbouring CCs. However, this is not the case for CA-SEFDM since sub-carriers are

non-orthogonally packed leading to interband non-orthogonality between adjacent CCs. Therefore, this section aims to investigate the effect of the interband non-orthogonality in the CA-SEFDM.

Systems in Fig. 5.26, Fig. 5.27 nd Fig. 5.28 are configured based on LTE release 8 [1] where 128 FFT size and 76 data sub-carriers are specified in one CC. The defined 10% protection guard band indicates 8 empty sub-carriers between neighbouring CCs. This separation mitigates the interband non-orthogonality effect.

The multiple detectors scenario is employed in Fig. 5.26 and Fig. 5.27. Fig. 5.26 presents BER performance of each CC in terms of the α=0.84 CA-SEFDM system. Each CC shows similar BER performance although with some fluctuations. The more smoother BER curve is obtained by averaging over 6 CCs. The similar result is observed in Fig. 5.27 where 7 CCs are evaluated. In order to compare the multiple detectors scenario and the single detector scenario within the CA-SEFDM system. BER performance of the two detection scenarios are shown in Fig. 5.28. It is evident that for both α=0.84 and α=0.72 CA-SEFDM systems, the multiple detectors scenario and the single detector scenario demonstrate very similar results.

In fact, the interband interference can further be eliminated using more empty sub-carriers indicating a wider protection guard band. According to LTE release 8, a different system specification is introduced in Fig. 5.29 where each CC employs 512 FFT size and 300 data sub-carriers. In this case, the 10% guard band approximately occupies 33 sub-carriers. Due to the increased protection gap, the effect of the out-of-sub-carrier power leakage from adjacent CCs is further mitigated. The performance is shown in Fig. 5.29 where it is evident that the multiple detectors scenario shows an improved performance which is identical to the single detector ones.

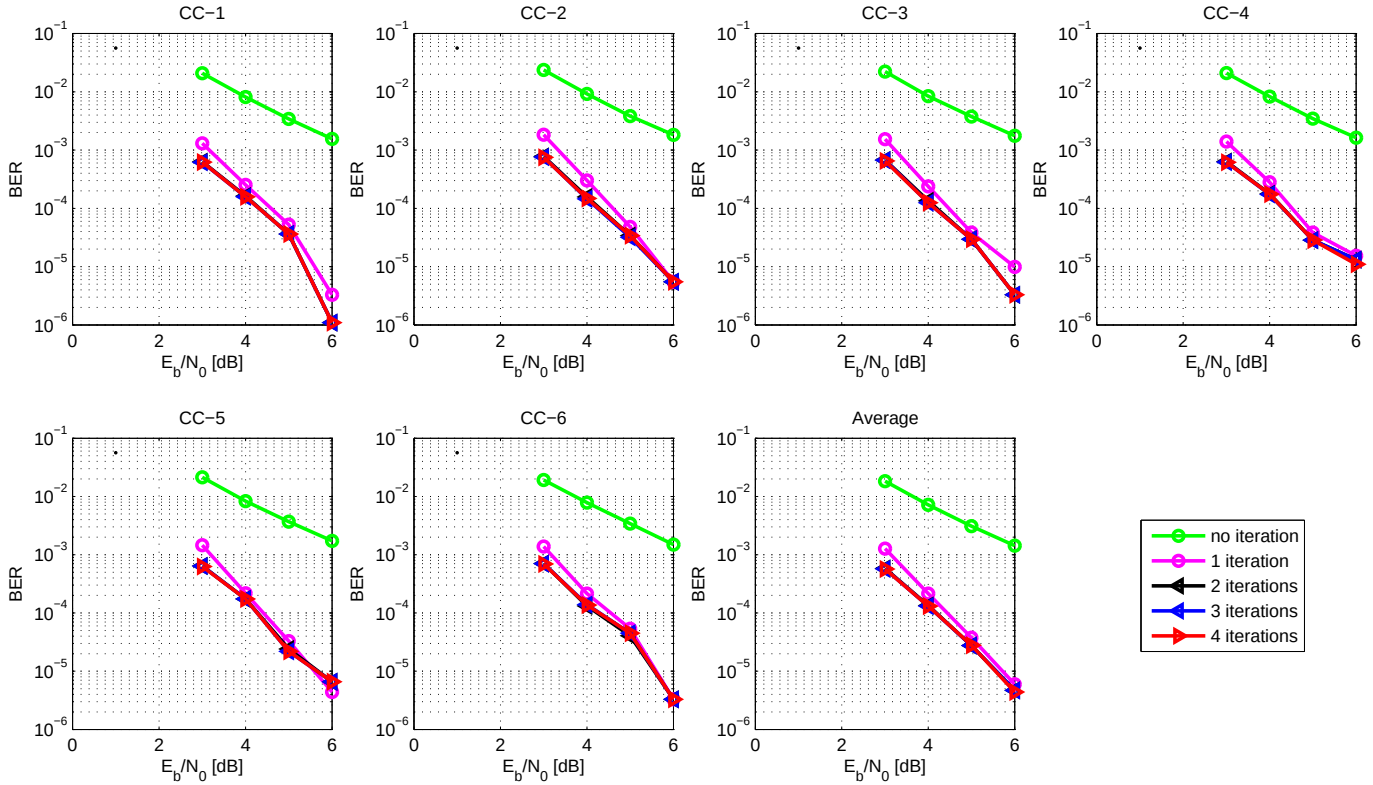

Figure 5.26: BER performance for each CC with various iterations in the CA-SEFDM system aggregated with 6 CCs. The multiple detectors scheme is employed. Average BER is provided by averaging BER on each CC. FFT size is 128.

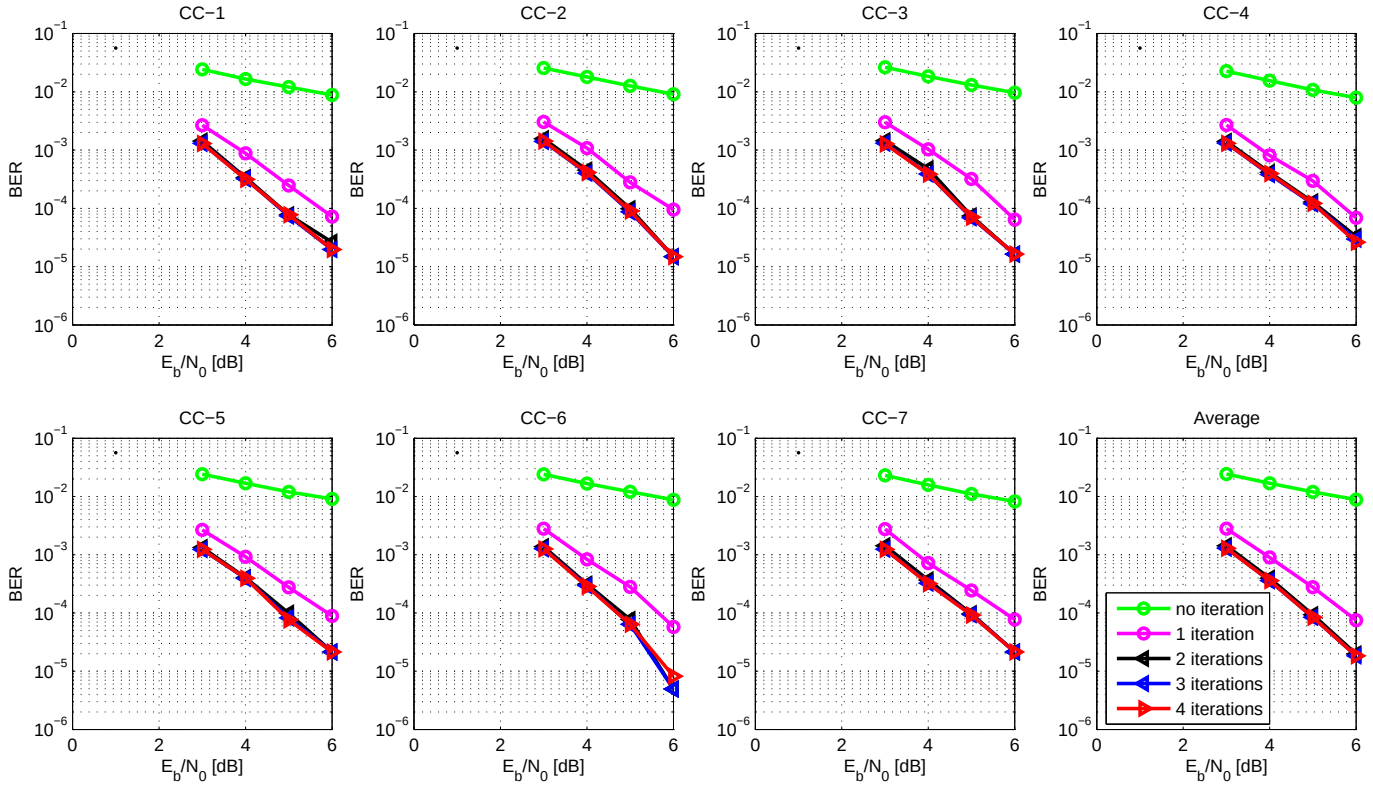

Figure 5.27: BER performance for each CC with various iterations in the CA-SEFDM system aggregated with 7 CCs. The multiple detectors scheme is employed. Average BER is provided by averaging BER on each CC. FFT size is 128.

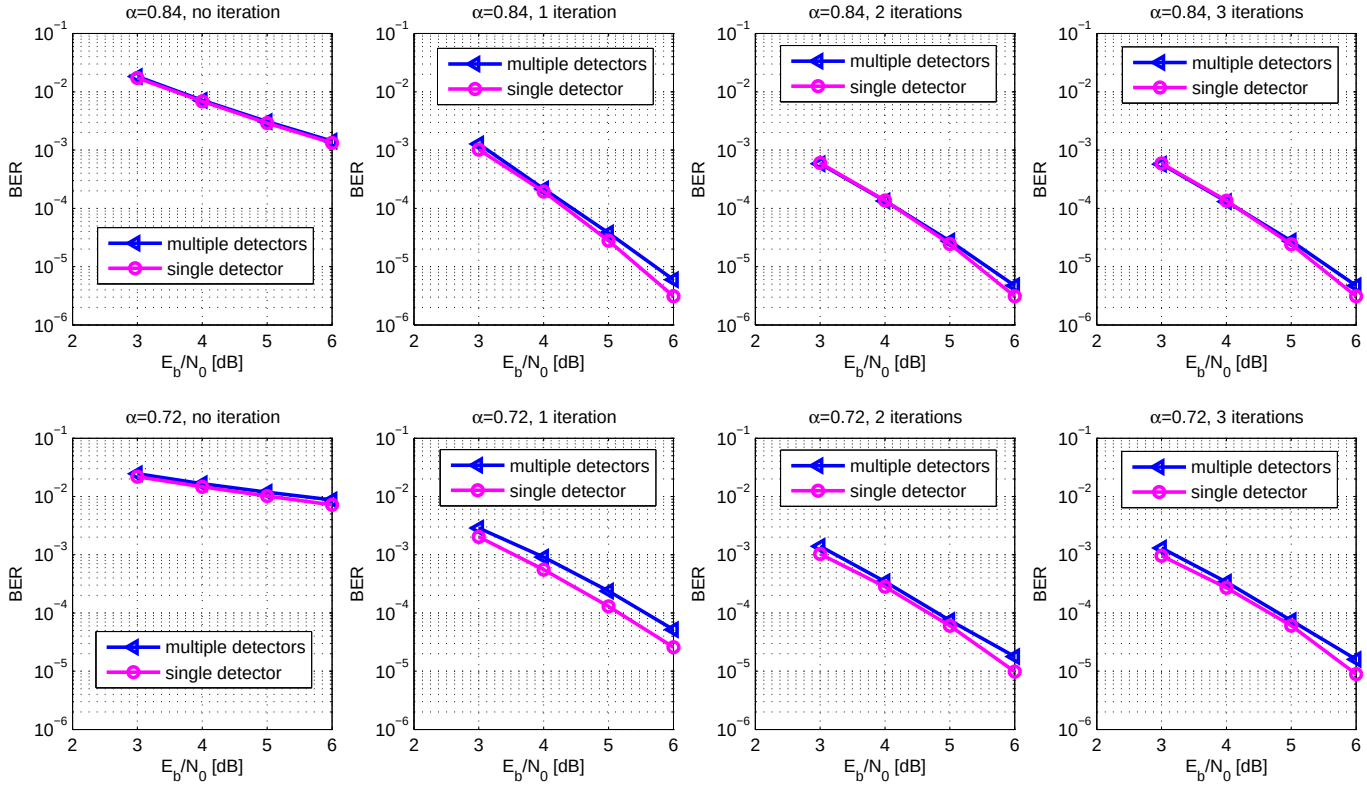

Figure 5.28: The comparison of BER performance in terms of multiple detectors and a single detector for two CA-SEFDM systems. FFT size is 128.

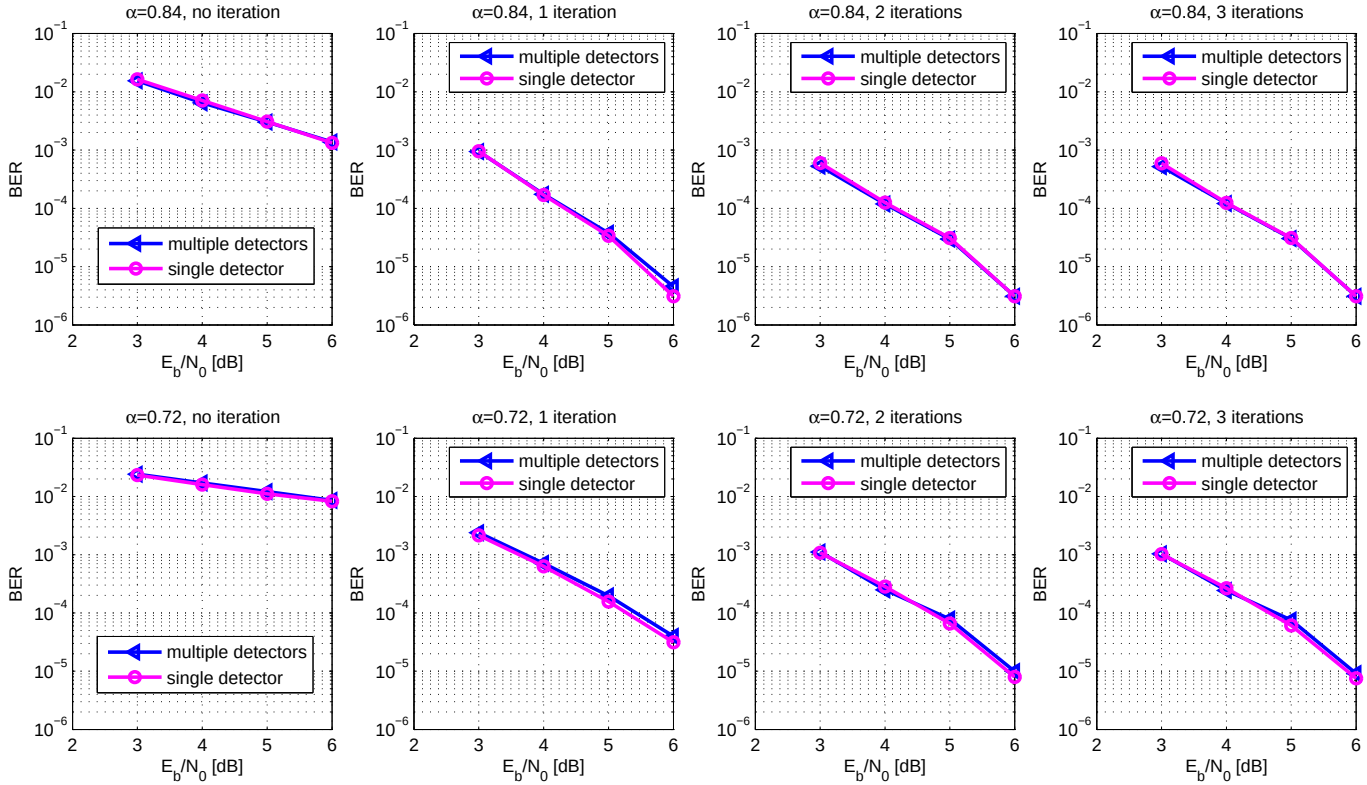

Figure 5.29: The comparison of BER performance in terms of multiple detectors and a single detector for two CA-SEFDM systems. FFT size is 512.

5.14 Conclusions

This chapter presents a practical experiment of the Turbo-SEFDM system in the LTE-Advanced scenario. Its principle is introduced followed by some key digital signal processing algorithms. Practical challenges are considered in the chapter where multipath effect, imperfect timing synchronization, sampling phase offset, LO phase offset and their joint impairments are experimentally studied. A realistic wireless channel is considered, with added noise and multipath fading which includes amplitude attenuation, phase distortion and propagation delay, since in a real RF environment, several distortions exist and their effects are not negligible. Impairments are demonstrated in the chapter in the form of constellation diagrams and spectra, which are useful to understand these effects and mitigate them. An experimental demonstration of an LTE-like SEFDM signal transmission over a realistic LTE EPA5 fading channel is presented. The SEFDM signal is constructed following the LTE downlink physical layer specifications, with a specially designed modification to allow for channel estimation. Performance is compared to signals with LTE specifications testbed in a realistic radio frequency (RF) environment. The testbed works at a 2 GHz frequency band and signal bandwidth is up to 25 MHz. The LTE VR5 multipath fading channel is adopted and the ZF based channel estimation/equalization is used to compensate for channel distortions. RF effects like phase offset and imperfect timing synchronization exist in the testbed. In addition, joint effects from the PXI and the channel emulator are investigated. All the mentioned effects can be compensated by using the ZF channel estimation/equalization.

Using signal structure based on LTE-Advanced and through some modifications of the pilot symbol structure, this work shows experimentally that compressing the subcarrier spacing within each CC by 16%, a CA-SEFDM system can integrate 6 CCs into the same 25 MHz bandwidth used for a CA-OFDM system with 5 CCs. Moreover, with further compression by 28%, one more CC can be aggregated. The superiority of CA-SEFDM is demonstrated by comparing it to CA-OFDM. Furthermore, two possible

scenarios are described for future applications of CA-SEFDM. These can be applied either by transmitting more data in a given bandwidth or allowing more users to share the same bandwidth. The CA-SEFDM scheme inherits all the benefits of CA-OFDM and introduces extra benefits such as low PAPR, relaxed requirements of DAC/ADC and enhanced multiuser diversity.

Chapter 6

Applications of Filtering in SEFDM: Nyquist-SEFDM

6.1 Introduction

Due to the scarcity of physical radio resources, cognitive radio (CR) was proposed to utilize frequency bands more efficiently, effectively improving the spectral efficiency. In a real wireless communication scenario, radio spectrum is not always occupied. The unused portion of the radio spectrum is termed "spectrum hole". More specifically, the spectrum hole is defined that in a period of time, the licensed spectrum assigned to a primary user (PU) is not utilized. Meanwhile, the unlicensed radio resources are overly used due to open access. In order to balance the workload and further improve spectral efficiency, CR allows secondary users (SUs) to access spectrum holes that are unutilized by PUs in a particular time period. In a CR scenario, an SU firstly detects available spectrum holes and then adopts a proper modulation scheme, signal band and transmission power to minimize the interference to PUs. In addition, a frequency gap is reserved between a PU and a SU to mitigate the interference.

Fig. 6.1 illustrates two CR scenarios. Assuming two PUs and the presence of a spectrum hole. In the first scenario, an SU with OFDM waveform is tested. It is apparent

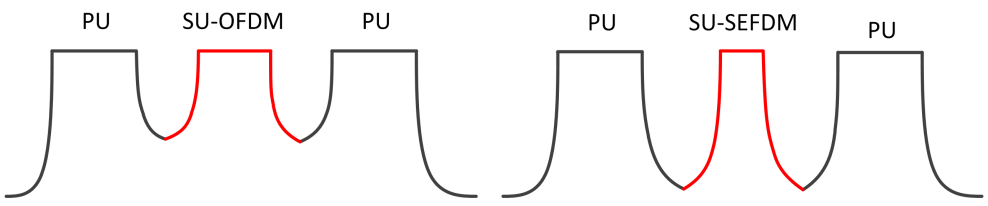

Figure 6.1: CR spectra occupation for both OFDM and SEFDM scenarios.

that due to the high out-of-band leakage of the OFDM spectrum, the SU introduces interference to the two PUs. In the second scenario, bandwidth is compressed in the SU-SEFDM. Thus, the frequency gap between the two PUs and the SU is expanded leading to a significant interference power reduction. This demonstrated the benefit of SEFDM in cognitive radio scenarios.

In [63] we reported that integrating more signal bands in a given bandwidth provides an efficient way to tackle the shortage of radio spectrum. The principle of a typical multiband OFDM system is to partition the entire signal band into multiple sub-bands where interband orthogonality remains between adjacent sub-bands. However, this is not the case for SEFDM systems since sub-carriers are no longer orthogonally packed, interband non-orthogonality is introduced. Moreover, the use of rectangular pulses in typical SEFDM systems results in high out-of-band power leakage and consequently in interference to adjacent frequency bands. Thus, a frequency gap has to be used as a protection gap which reduces spectral efficiency. Recently, a spectrally efficient concept, employing an root raised cosine (RRC) pulse shaping filter for each sub-carrier, demonstrated significant reduction of out-of-band power leakage, when applied to the multicarrier system termed GFDM [137]. However, because of the RRC filter shaping effects, ICI is introduced. Work in [137] has verified that with the assistance of a successive interference cancellation scheme, GFDM can achieve the same BER performance as that of the rectangular pulse shaped OFDM. Another filtering based system is FBMC. It copes with the ICI challenge by using OQAM [134] modulation scheme, where the real and imaginary parts of QAM complex symbols are separated by delaying the imag-

inary branch of a QAM symbol by half of symbol duration before passing through the pulse shaping filter. Thus, no successive interference cancellation is needed. It should be noted that contrary to SEFDM, the sub-carrier spacing of the GFDM/FBMC systems is still equal to the symbol rate. Since the out-of-band power is significantly suppressed in GFDM/FBMC, it would be spectrally advantageous to reduce the sub-carrier spacing below the symbol rate and reduce the out-of-band power at the same time. Therefore, the motivation of Nyquist-SEFDM is to create a spectrally efficient (i.e. saving bandwidth) system with reduced out-of-band power.

The comparisons of existing techniques are shown below indicating the motivation of work in this chapter, namely the application of filtering in SEFDM.

- **OFDM.** An existing 4th generation technique, has shortcomings such as high out-of-band power leakage.
- **FBMC and GFDM.** New physical layer multicarrier modulation schemes, employ novel pulse shaping filtering to each sub-carrier to cope with the aforementioned OFDM shortcomings.
- **SEFDM.** UCL designed bandwidth compressed multicarrier technique, compresses sub-carrier spacing below the symbol rate leading to improved spectral efficiency.
- **Nyquist-SEFDM.** A combined technique of Nyquist systems (similar to FBMC and GFDM) and SEFDM, saves bandwidth and reduces out-of-band power leakage. The reduced out-of-sub-carrier power leakage could simplify detection of SEFDM signals.

6.2 Methodology

This work aims to constrain the interference distributed across the SEFDM signal band only to neighbouring sub-carriers, hence simplifying signal detection. In a typical non-

shaped SEFDM system (i.e modulating signals are assumed to be ideally rectangular with sinc spectra), ICI is a result of all sidelobes of all non-orthogonally packed sub-carriers, due to the infinitely long sidelobes of the sinc spectra [99]. Optimizing the pulse shape and corresponding spectrum will be a reasonably simple, yet untested, approach to limit the interference in SEFDM.

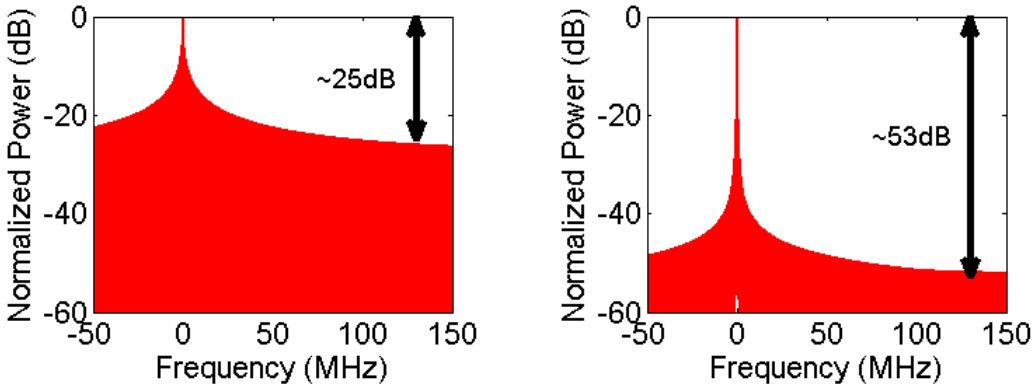

(a) No shaping.

(b) RRC shaping.

Figure 6.2: Single sub-carrier spectra of no shaping and RRC shaping. The roll-off factor of the RRC filter is γ=0.5 and the filter is truncated to six symbols.

The spectra of a non-shaped sub-carrier and an RRC shaped sub-carrier are shown in Fig. 6.2(a) and Fig. 6.2(b), respectively. It is apparent that the RRC shaped spectrum has a much lower out-of-band power leakage. The out-of-band power in Fig. 6.2(a) is approximately 25 dB below the spectral peak. Using RRC pulse shaping, in Fig. 6.2(b), such out-of-band power leakage is reduced by a further 28 dB. This comparison indicates that the interference from an RRC shaped sub-carrier is significantly reduced and it may only affects adjacent sub-carriers.

The idea of the Nyquist-SEFDM is illustrated in Fig. 6.3 where spectra of different systems are illustrated for the purpose of comparison. Fig. 6.3(a) is a typical OFDM spectrum with rectangular pulses, carrying 100 Msymbols/s, over 100 MHz bandwidth. The out-of-band power is approximately 15 dB below the spectral peak. Using RRC filtering, in Fig. 6.3(b), such out-of-band power leakage is reduced by a further 27 dB. Finally, for the same data rate, a rectangular pulse shaped SEFDM is shown

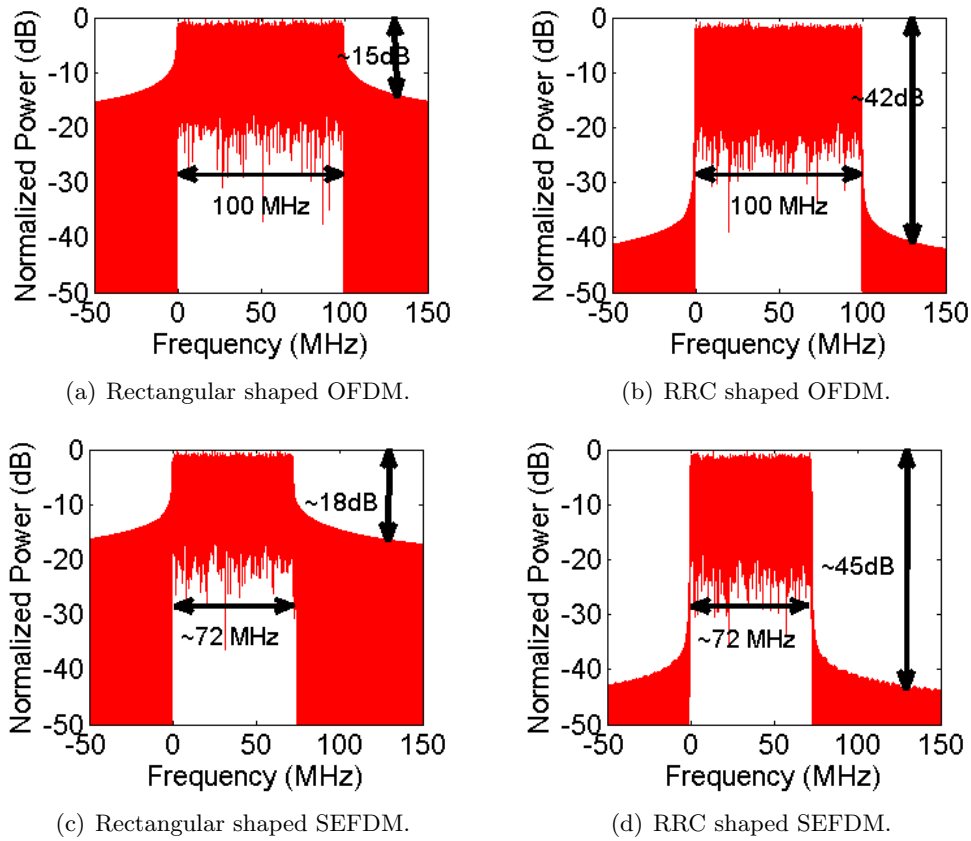

(a) Rectangular shaped OFDM.

(b) RRC shaped OFDM.

(c) Rectangular shaped SEFDM.

(d) RRC shaped SEFDM.

Figure 6.3: Bandwidth saving and out-of-band power reduction comparisons for various signals. Using the same number of sub-carriers, the bandwidth is compressed by 28% in SEFDM systems, the roll-off factor of the RRC filter is γ=0.5 and the filter is truncated to six symbols.

in Fig. 6.3(c) where the bandwidth is compressed to 72 MHz while the out-of-band power is reduced to -18 dB. This indicates that SEFDM is better than OFDM in both bandwidth saving and the out-of-band power suppression. Furthermore, the Nyquist-SEFDM spectrum is shown in Fig. 6.3(d) where the out-of-band power leakage is around -45 dB (i.e. the lowest one) over a 72 MHz compressed bandwidth.

Fig. 6.4 examines the characteristics of RRC time pulses. A sequence of 5 bits (10111) shaped with sinc pulses is used as an example. A perfect RRC pulse has infinite filter length. In order to make it realizable, a truncated version is desirable for the purpose of reducing computational complexity. The filter length or in other words the number of filter taps affects the frequency response. With fewer taps, more leakages

are introduced. The out-of-band power does not drop down as far as the one with large number of filter taps. In this figure, six symbols are truncated as the length of the RRC filter. In the first time instance as shown in Fig. 6.4(a), a positive sinc shaped pulse is used to represent a bit '1'. After T symbol period, a time shifted negative sinc shaped pulse is illustrated in Fig. 6.4(b) to signify a bit '0'. The overlapped pulse shaped signal is shown in Fig. 6.4(f). It is inferred from Fig. 6.4(f) that one individual pulse is overlapped and affected by adjacent pulses. But at the center of each time pulse, all other time pulses have zero amplitudes indicating no ISI. At the center of the first pulse (sample index=32×3=96), assume the signal amplitude is A. For the second pulse, at the center of the pulse (sample index=32×4=128), the amplitude is assumed to be -A. Since there is no ISI at the center of each sinc pulse, thus, in Fig. 6.4(f), at sample index=96 and sample index=128, the amplitudes are A and -A, respectively.

6.3 Interference Comparisons

In order to show the benefit of pulse shaping in SEFDM, Fig. 6.5 illustrates three-dimensional plots of interference patterns for various systems. The left hand side of the figure shows interference patterns for OFDM and SEFDM systems with no signal shaping. The right hand side of the figure shows corresponding interference patterns when RRC pulse shaping is used with roll-off factors γ=0.5. The numbers on the X-axis (indexed by x) and the Y-axis (indexed by y) correspond to sub-carrier indices. Both x and y scale range from 1 to N. The X-Y plane indicates the correlation between sub-carriers. The numbers on the Z-axis (indexed by z) indicate absolute values of the correlation coefficients. It should be noted that the auto correlation coefficients are denoted by $I(x, x)$ and the cross correlation coefficients are $I(x, y)$ indicating ICI. For clarity of the figures the number of sub-carriers is limited to N=16 and the auto correlation elements are removed (i.e. $I(x, x)$=0), thereby only the cross correlation values are shown.

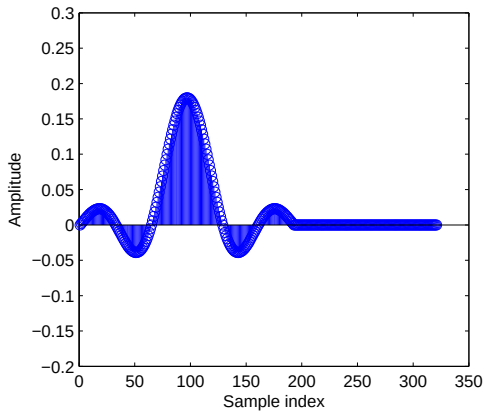

(a) 1^{st} pulse.

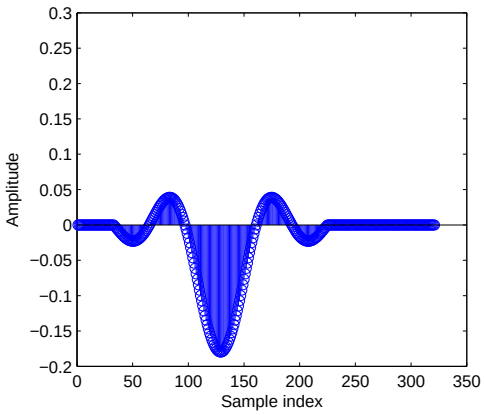

(b) 2^{nd} pulse.

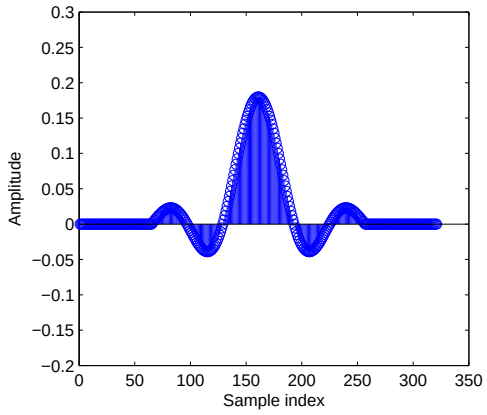

(c) 3^{rd} pulse.

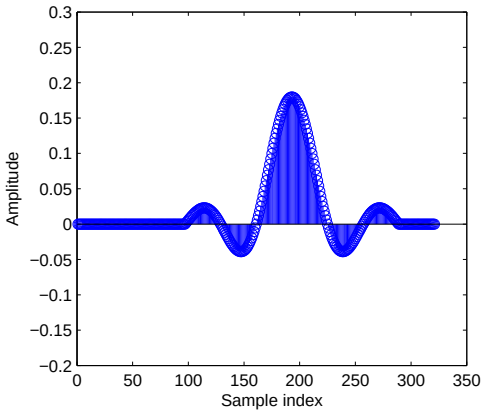

(d) 4^{th} pulse.

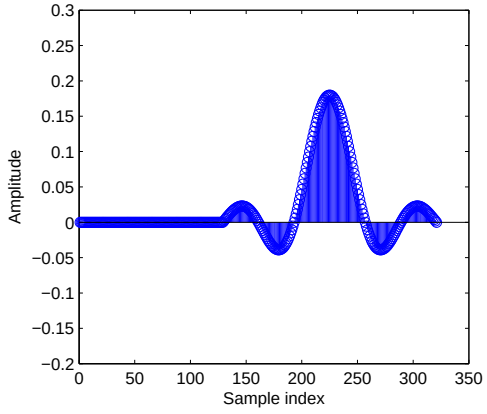

(e) 5^{th} pulse.

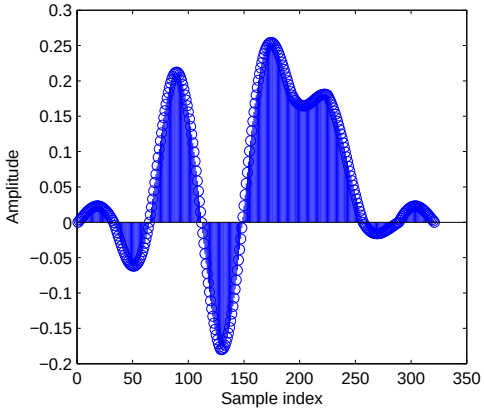

(f) Overlapped pulse.

Figure 6.4: Transmitting a sequence (1 0 1 1 1) by shaping each bit as a sinc pulse. The number of sub-carrier is 16, oversampling factor is 2, and sps (sample per symbol) for each span (symbol) is 32. The filter is truncated to be six symbols.

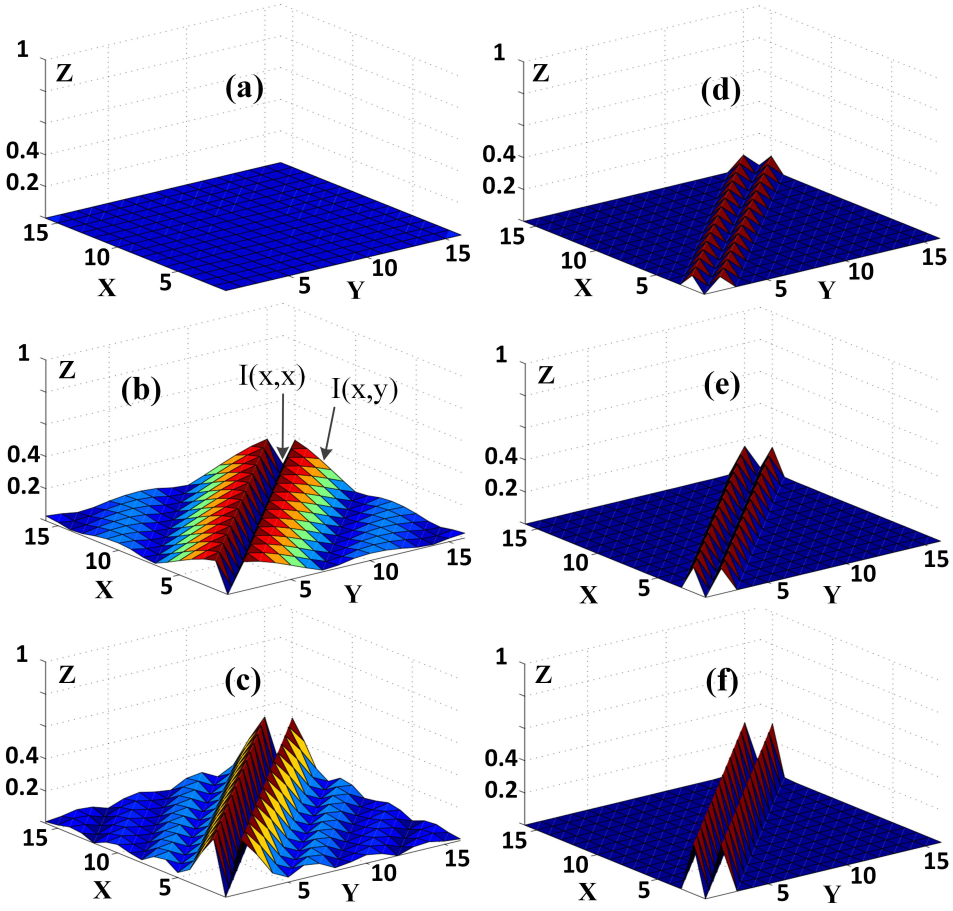

Figure 6.5: Three-dimensional interference comparison. (a) OFDM; (b) SEFDM α=0.84; (c) SEFDM α=0.72 and (d) OFDM with RRC shaping; (e) SEFDM α=0.84 with RRC shaping; (f) SEFDM α=0.72 with RRC shaping.

Fig. 6.5(a) expectedly shows no interference for the case of OFDM. Fig. 6.5(b) illustrates a non-shaped SEFDM system with 16% bandwidth compression (α=0.84). It is apparent that the interference is no longer zero and its values fluctuate since sub-carriers are no longer orthogonal. The interference levels clearly vary with the index (i.e frequency location) of the sub-carriers with highest levels evident for adjacent sub-carriers (at the center of the X-Y plane). The interference in a higher bandwidth compressed SEFDM system with 28% bandwidth compression (α=0.72) is shown in Fig. 6.5(c), where higher levels are noticed (relative to the two figures above) as the sub-carriers become more tightly packed and therefore interfere with higher powers

across the overall frequency band. Clearly, further bandwidth compression will result in more interference both from adjacent and non-adjacent sub-carriers.

When RRC pulse shaping is applied to an OFDM system in Fig. 6.5(d), limited levels of interference appear but only at the two adjacent sub-carriers. This is in contrast to the case of Fig. 6.5(a) where zero interference appears when no shaping is applied. Comparatively, when applying RRC pulse shaping to SEFDM, interference levels increase in proportion to the bandwidth compression levels as shown in Fig. 6.5(e) and Fig. 6.5(f). However, the interference becomes limited only to the adjacent sub-carriers, unlike the non-shaped SEFDM cases of Fig. 6.5(b) and 6.5(c), where interference occurs across all the sub-carriers space. Hence, advantageously moving away from the adjacent sub-carriers, interference is eliminated, even for the higher bandwidth compression case of Fig. 6.5(f).

6.4 Transceiver Design

6.4.1 Transmitter of Nyquist-SEFDM

A block diagram of the Nyquist-SEFDM transmitter is depicted in Fig. 6.6(a). Two scenarios are studied in this work. In scenarios A (uncoded scheme), the binary bit stream is directly mapped into QAM symbols. In scenarios B (coded scheme) [59], the binary bit stream is firstly convolutionally encoded in the encoder and then permuted through a random interleaver $\mathbf{\Pi}$. After that, complex symbols are obtained in the QAM mapper. Further processing is the same for both scenarios. After serial to parallel conversion, one data stream S is divided into N parallel branches; the n^{th} branch is denoted as S_n. In one branch, the complex data stream $S_n = [s_{n,0}, s_{n,1}, ...]$ is up sampled by a factor of Q leading to a new complex data vector $W_n = [w_{n,0}, w_{n,1}, ...]$ which is defined as

$$W_n[k] = \begin{cases} S_n[\frac{k}{Q}] & k \ mod \ Q = 0 \\ 0 & otherwise \end{cases} \tag{6.1}$$

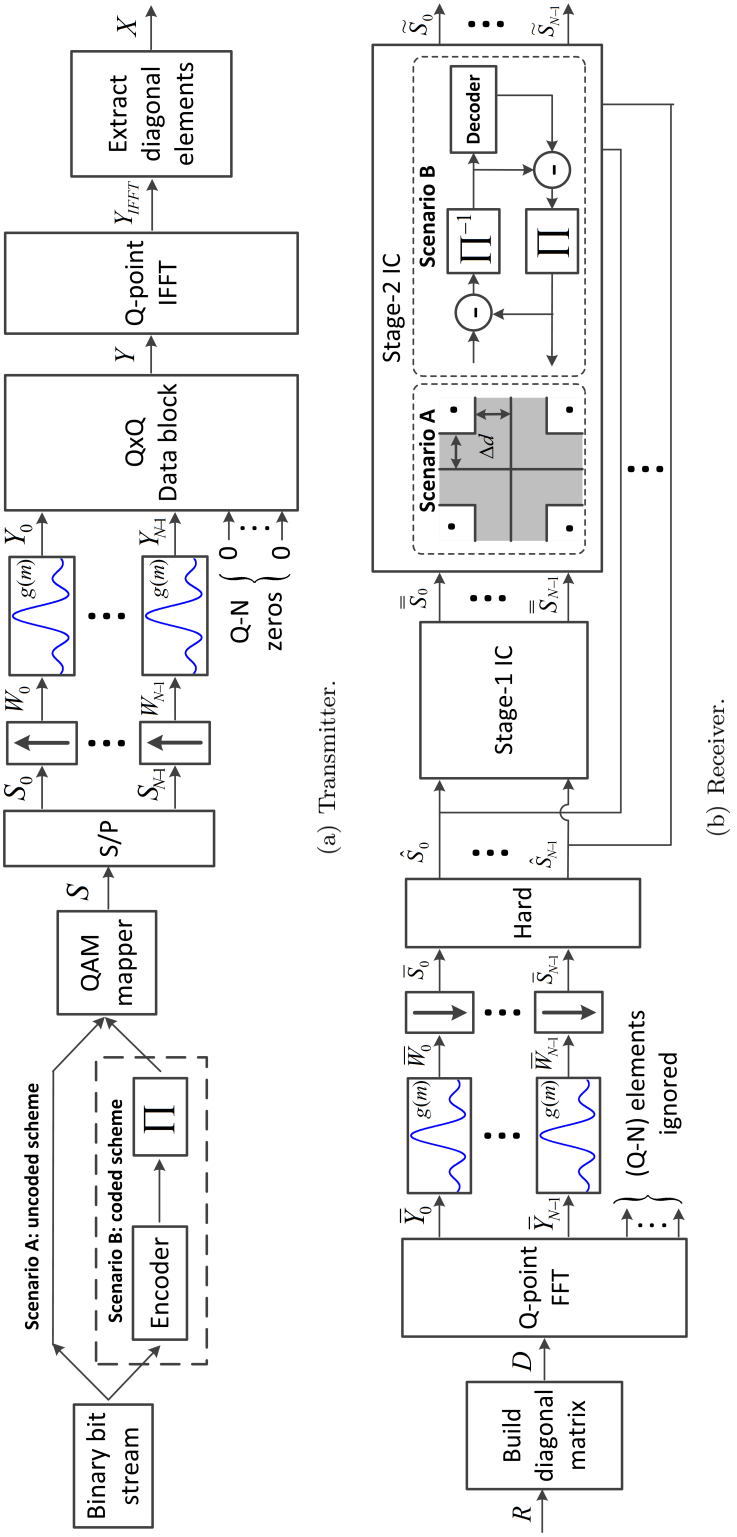

Figure 6.6: Block diagram of the Nyquist-SEFDM transceiver.

Thereafter, W_n is convolved with $g(m)$, which is the impulse response of each of the RRC filters, truncated to L symbols where each one contains Q samples. Therefore. The order of each filter is $U = Q \times L$ indicating $m = [0, 1, ..., U-1]$ and the output of each is Y_n, expressed as

$$Y_n = W_n * g(m) \tag{6.2}$$

where $*$ denotes convolution. After filtering, the pulse shaped data is up converted to sub-carrier frequency f_n.

Unlike rectangular pulse shaped systems, clearly the samples of one symbol no longer have equal values in the RRC filtered systems. Therefore, in Fig. 6.6(a), a $Q \times Q$ data block is introduced to buffer Q samples from each branch every T period. Assuming the data stream after the pulse shaping operation on the n^{th} branch is $Y_n = [y_{n,0}, y_{n,1}, ...]$, the $Q \times Q$ data matrix is defined as

$$\mathbf{Y} = \begin{bmatrix} y_{0,0} & y_{0,1} & \cdots & y_{0,Q-1} \\ y_{1,0} & y_{1,1} & \cdots & y_{1,Q-1} \\ \vdots & \vdots & \vdots & \vdots \\ y_{N-1,0} & y_{N-1,1} & \cdots & y_{N-1,Q-1} \\ 0 & 0 & \cdots & 0 \\ \vdots & \vdots & \vdots & \vdots \\ 0 & 0 & \cdots & 0 \end{bmatrix} \tag{6.3}$$

where $y_{n,k}$ indicates the k^{th} sample on the n^{th} sub-carrier frequency (branch). One row, $[y_{n,0}, y_{n,1}, ..., y_{n,Q-1}]$ contains time samples that will modulate one specific sub-carrier of frequency f_n and is defined as one sample vector. One column, the frequency vector $[y_{0,k}, y_{1,k}, ..., y_{N-1,k}, ..., 0]^{tr}$ of the data matrix contains time samples to be modulated at all carrier frequencies. The notation tr indicates the transpose operation. It should be noted that $Q - N$ additional branches are introduced via padding $Q - N$ zeros at the end of each frequency vector.

The up conversion of each branch is done by

$$X[k] = \sum_{n=0}^{Q-1} y_{n,k} \cdot \exp(\frac{j2\pi nk\alpha}{Q}) \tag{6.4}$$

where $n, k = [0, 1, ..., Q-1]$. The operation in (6.4) can be efficiently realized by IFFT either for OFDM (α=1) or SEFDM (α <1) [46]. In a rectangular pulse shaped system, the size of the data block is $Q \times 1$, since the elements of the sample vector $[y_{n,0}, ..., y_{n,Q-1}]$ have constant amplitude. Therefore, a single IFFT is operated every T time period. However, for the $Q \times Q$ data matrix, a single IFFT has to be activated every T/Q time period, requiring a higher processing speed IFFT. Alternatively, a single higher speed IFFT can be replaced by Q parallel lower speed IFFTs, which relaxes the requirement of processing speed at the expense of increased resource consumption.

It should be noted that the IFFT returns results for each column of the data block matrix. Therefore, a $Q \times Q$ matrix $Y_{_{IFFT}}$ is obtained after the IFFT processing. However, the useful data is only the diagonal elements of the matrix. Thus, extracting the diagonal elements from $Y_{_{IFFT}}$ is required to give the transmitted signal X as

$$X = diagonal\{IFFT(\mathbf{Y})\} = diagonal\{\mathbf{FY}\} \tag{6.5}$$

where the right hand side of (6.5) simply means that the process is equivalent to extracting the diagonal elements from sampled sub-carriers matrix $\mathbf{F}$ modulated by $\mathbf{Y}$.

Alternative and faster techniques for generating the same signals are given in [46] and utlize a pruned IFFT algorithm that can remove the redundant operations leading to reduced complexity.

6.4.2 Receiver of Nyquist-SEFDM

To illustrate the concept, a simple AWGN channel is used in this work. A block diagram of the Nyquist-SEFDM receiver is shown in Fig. 6.6(b). After propagating in

an AWGN channel, the received signal is expressed as

$$R = X + Z \tag{6.6}$$

where $R = [r_0, r_1, ...r_{Q-1}]$ is the received signal and Z denotes AWGN.

As shown at the transmitter side, the transmitted symbols X are the diagonal elements extracted from the $Q \times Q$ IFFT operated matrix Y_{IFFT}. Therefore, before the FFT operation at the receiver side, a diagonal matrix such as (6.7) is required to be built for every Q samples.

$$\mathbf{D} = \begin{bmatrix} r_0 & 0 & \cdots & 0 \\ \vdots & r_1 & \cdots & 0 \\ \vdots & \vdots & \ddots & \vdots \\ 0 & 0 & \cdots & r_{Q-1} \end{bmatrix} \tag{6.7}$$

Then, the demodulation can be expressed as:

$$\bar{y}_{n,k} = r_k \cdot \exp(\frac{-j2\pi nk\alpha}{Q}) \tag{6.8}$$

where $\bar{y}_{n,k}$ is an element of matrix $\bar{\mathbf{Y}}$ and $n, k = [0, 1, ..., Q-1]$. It should be noted that a Q-point FFT can be used in (6.8) either for OFDM (α=1) or SEFDM (α <1) [46]. Furthermore, (6.8) can be rearranged in a matrix form as:

$$\bar{\mathbf{Y}} = FFT(\mathbf{D}) = \mathbf{F}^* \mathbf{D} \tag{6.9}$$

where $\mathbf{F}^*$ is the conjugate of the sub-carrier matrix $\mathbf{F}$. It should be noted that the computational complexity can be reduced by skipping zero elements within the matrix $\mathbf{D}$ using the pruned FFT [46]. After the FFT, the last $Q - N$ elements of each output vector are ignored. Then, RRC filters identical to those used at the transmitter with $g(m)$, operate on the signals of each branch as in (6.10). This is followed by the down sampling operation as shown in (6.11).

$$\bar{W}_n = \bar{Y}_n * g(m) \tag{6.10}$$

$$\bar{S}_n[k] = \bar{W}_n[Q \times k] \tag{6.11}$$

Utilizing a hard decision module, initial estimates $\hat{S}$ are obtained. ISI and ICI exist in Nyquist-SEFDM due to the combine use of the RRC pulse shaping filter and the less than symbol rate packed sub-carriers. In order to obtain better BER performance, interference cancellation is required to remove the ICI effect. In a rectangular pulse shaped SEFDM system, interference to one sub-carrier comes from all other sub-carriers. However, for an RRC pulse shaped SEFDM system, due to the reduced out-of-band power, interference is mostly limited to neighbouring two sub-carriers resulting in relatively simplified interference cancellation.

The interference cancellation (IC) includes two stages. The first stage is a general IC module (stage-1 IC) and the second stage is a specially designed module (stage-2 IC) for Nyquist-SEFDM. Interference imposed on the n^{th} branch comes from the $(n-1)^{th}$ and the $(n+1)^{th}$ branches. Data streams $\hat{S}_{n-1}$ and $\hat{S}_{n+1}$ are extracted after the hard decision. After the up sampling and pulse shaping operations, two sequences are up converted to frequencies f_{n-1} and f_{n+1} multiplying with $e^{\frac{j2\pi(n-1)k\alpha}{Q}}$ and $e^{\frac{j2\pi(n+1)k\alpha}{Q}}$, respectively. This process is to model the interference superimposed on the targeted signal on the n^{th} branch. Therefore, before the demodulation of the received signal, R, interference is subtracted as

$$R_n = R - I_{n-1} - I_{n+1} \tag{6.12}$$

where R_n is the interference cancelled signal on the n^{th} branch, I_{n-1} is the modulated signal from the $(n-1)^{th}$ branch and I_{n+1} is the $(n+1)^{th}$ branch. After that, the interference cancelled data stream is down converted to baseband by multiplying R_n with $e^{\frac{-j2\pi nk\alpha}{Q}}$. After the subsequent pulse shaping and down sampling operations, the recovered data stream $\bar{\bar{S}}_n$ is obtained. The same interference cancellation operation

inside the stage-1 IC is repeated for the rest of $N-1$ branches. The stage-1 IC is very similar to the two-sided SIC proposed for GFDM [137]. However, unlike GFDM, the additional interference in SEFDM has to be removed using a specially designed SEFDM detector termed stage-2 IC.

Two scenarios are demonstrated in Fig. 6.6(b). The iterative soft demapping scheme termed ID in [52] is evaluated as the scenario A, with uncoded data. An adaptive decision threshold Δd is preferred. The principle of the ID scheme is firstly to decide less distorted symbols and then recover highly distorted symbols on the basis of the decided ones. It is concluded from [52] that the decision of one symbol is dependent on the recovered symbols from previous iterations. In order to improve the reliability of a decision after each iteration, coded data is used with Turbo equalizer [141][58] in scenario B, to improve the reliability of symbol decisions iteratively. Thus, BER performance is improved.

6.5 Performance Comparisons

This chapter aims to demonstrate the concept of the Nyquist-SEFDM. Therefore, a Nyquist-SEFDM system with 64 data sub-carriers and 4QAM modulation scheme is investigated in an AWGN channel. The efficacy of signal shaping of SEFDM is studied through simulating the error performance of different systems in two scenarios. Two specific bandwidth compression factors are selected according to the work [63]. For a more realistic wireless environment like multipath fading, an SEFDM experimental testbed has been recently reported in [63].

The RRC filter design is beyond the scope of this work. But it is necessary to evaluate the effect of different roll-off factors. The filter in this work is truncated to six symbols. In Fig. 6.7, the RRC pulse with γ=0.5 has the best performance. The performance becomes worse at both high and low γ. At high γ, more excess bandwidth is introduced leading to increased ICI. At low γ, more ISI is introduced due to the filter truncation. Therefore, in the following simulations, the roll-off factor γ is set to 0.5.

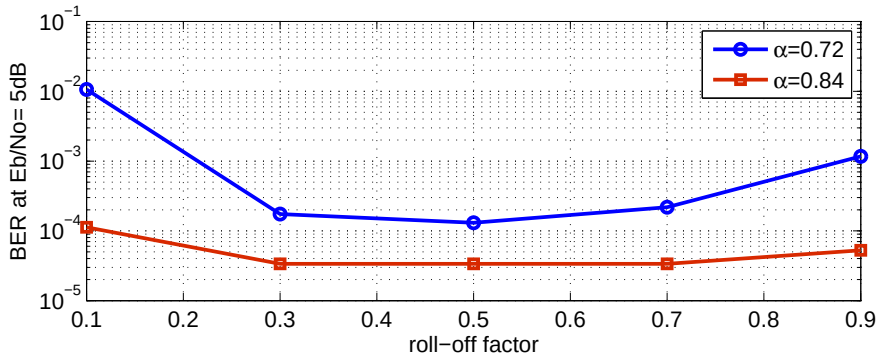

Figure 6.7: BER versus roll-off factors γ (scenario B).

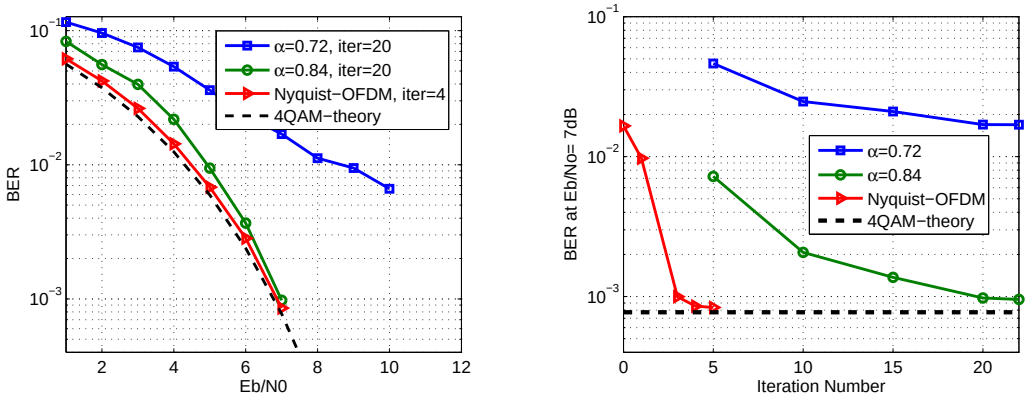

(a) BER performance.

(b) Iteration performance.

Figure 6.8: Performance (scenario A) for different pulse shaped systems.

Due to the use of RRC filter, interference is introduced in both Nyquist-OFDM and Nyquist-SEFDM systems. It is shown in Fig. 6.8(a) that four iterations are needed for the uncoded Nyquist-OFDM system to get converged performance. For Nyquist-SEFDM, more iterations are required to cope with the additional interference resulting from extra interference introduced by the closer packing of sub-carriers. The iteration numbers for different Nyquist-SEFDM systems are investigated in Fig. 6.8(b) where with 20 iterations and α=0.84, the performance approaches the theoretical one at around E_b/N_o=7dB. However, for α=0.72, even with 20 iterations, the performance is far away from the theoretical 4QAM one. This is due to the fact that with smaller α (i.e. higher bandwidth compression), more ICI is introduced in the system. This

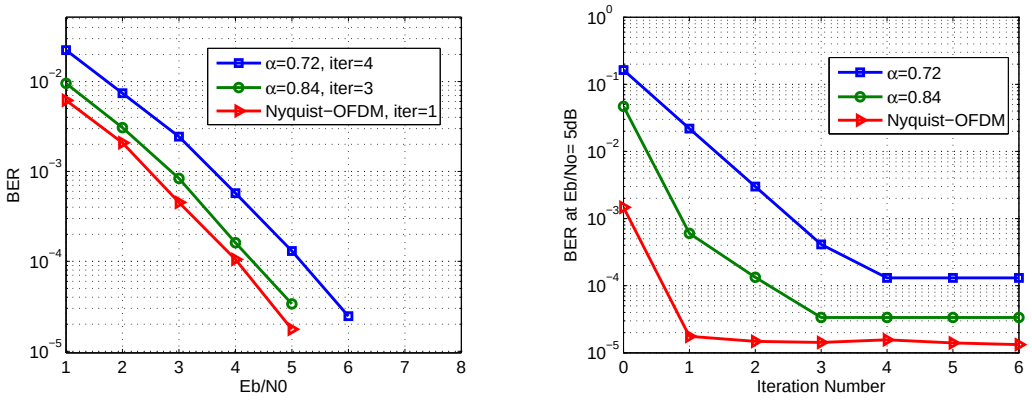

(a) BER performance. (b) Iteration performance.

Figure 6.9: Performance (scenario B) for different pulse shaped systems.

may be taken as a limitation of uncoded Nyquist-SEFDM when lower values of α are considered.

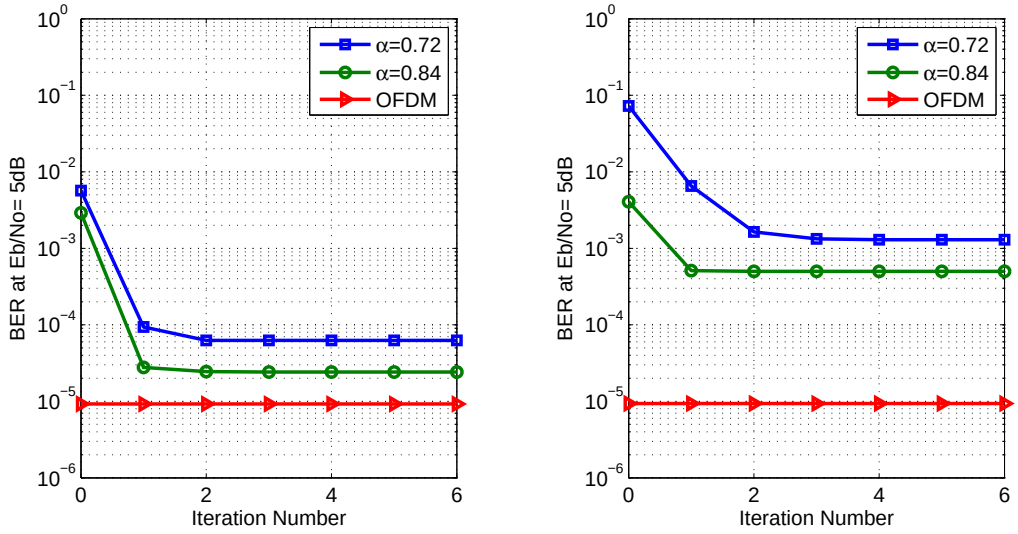

(a) Full-REC. (b) Partial-REC.

Figure 6.10: Convergence performance (scenario B) for full-REC and partial-REC systems.

The coded technique is studied and results are evaluated in Fig. 6.9. It is apparent that for both Nyquist-OFDM and Nyquist-SEFDM systems, the required iteration numbers are reduced significantly. This is due to the fact that more reliable esti-

mates are obtained after each iteration leading to an improved convergence speed. It is apparent that at BER=3×10^{-5} the performance gap between the α=0.84 and the Nyquist-OFDM one is approximately 0.3 dB. For α=0.72, the gap is 1.2 dB.

In a typical rectangular pulse shaped SEFDM system, interference to one sub-carrier comes from the rest N-1 (i.e. N is the total number of sub-carriers) sub-carriers. A signal detector has to cancel interference from the N-1 sub-carriers, which is complex. In the newly proposed Nyquist-SEFDM system, interference is constrained to neighbouring two sub-carriers leading to a much simpler interference cancellation scheme.

In order to demonstrate the effect of adjacent and non-adjacent interference, in Fig. 6.10, both full and partial signal detection are evaluated in terms of convergence behaviour for REC pulse shaped SEFDM systems. The full signal detection indicates that interference is removed from the N-1 sub-carriers while the partial signal detection means that only neighbouring interference is removed. The performance is tested at E_b/N_o=5dB. In Fig. 6.10(a), for both SEFDM with α=0.72 and 0.84, two iterations are sufficient to get converged performance. In Fig. 6.10(b), partial signal detection is evaluated for the same systems. One iteration is required for α=0.72 SEFDM while two iterations for α=0.84 SEFDM. It is clearly seen that the BER gap between SEFDM and OFDM in the partial-REC scenario is increased significantly compared to the full-REC scenario. Fig. 6.10 proves that interference to one sub-carrier comes not only from neighbouring sub-carriers but also from N-1 sub-carriers. In other words, for a rectangular pulse shaped system, interference has to be removed from N-1 sub-carriers.

Based on the iteration information obtained from Fig. 6.10, Fig. 6.11 compares different systems in terms of BER performance. In Fig. 6.11(a), it is apparent that the full-REC detection scheme without pulse shaping shows the best result since all the interference has been removed. When partial-REC detection scheme is applied, error performance suffers several dBs of degradation. However, when RRC shaping is used, applying the partial detection results in close performance to the one achieved using the full detection without signal shaping.

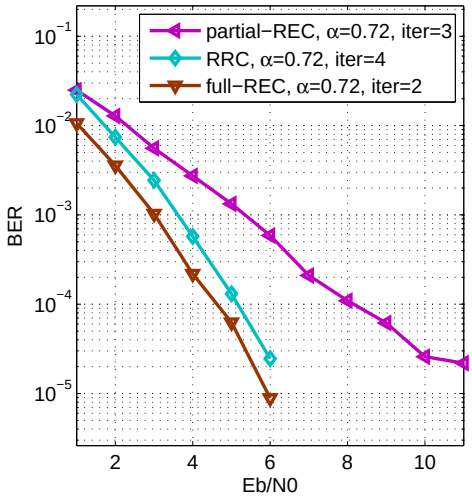

(a) α=0.72.

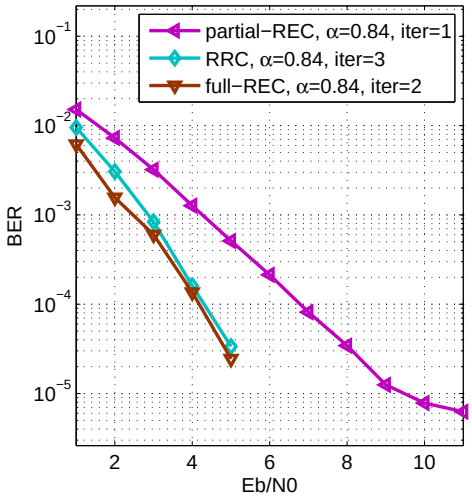

(b) α=0.84.

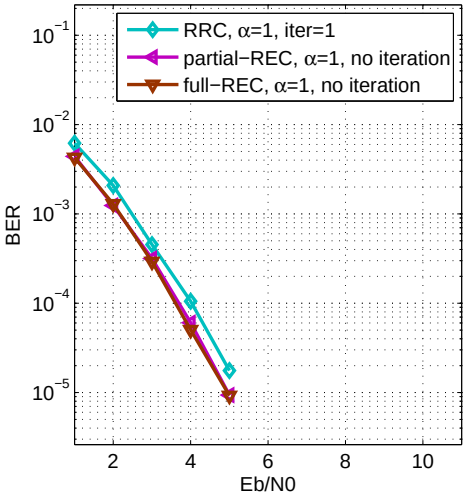

(c) α=1.

Figure 6.11: Performance comparisons for different systems with full/partial signal detection schemes in scenario B.

The same results are observed for α=0.84 in Fig. 6.11(b). However, due to the relaxed bandwidth compression compared to that in Fig. 6.11(a), the performance gap is narrowed and the required iteration number to achieve converged performance is reduced. The same comparison is studied for OFDM systems in Fig. 6.11(c). Due to the orthogonal property in an REC pulse shaped OFDM system, ICI doesn't exist.

Thus, the full-REC signal detection and the partial-REC signal detection shows the same BER result. In terms of an RRC pulse shaped OFDM system, because of pulse shaping filters, interference is re-introduced. Thus, it requires one iteration to get converged performance. To sum up, using RRC shaping results in interference limited to adjacent sub-carriers, which can be removed easily at the receiver with minimal performance degradation.

It can be seen from Fig. 6.11 that a narrow performance gap exists between the partial-RRC scheme and the full-REC scheme in both OFDM and SEFDM systems. It is because in Nyquist systems interference mainly comes from neighbouring sub-carriers. Therefore, the interference is only cancelled from two sub-carriers, which may not be sufficient. In addition, for Nyquist systems, joint effects from bandwidth compression factor α, roll-off factor γ, filter size and the number of detection iterations could affect the final performance, which needs further investigations.

6.6 Coexistence of 4G and Promising 5G Signals

The benefit of Nyquist-SEFDM is experimentally demonstrated in Fig. 6.12 where a non-shaped SEFDM signal and an RRC shaped SEFDM signal are compared. The bandwidth compression factor is set to α=0.72 which is derived from previous work [63]. It is apparent that the RRC pulse shaped SEFDM signal outperforms the non-shaped SEFDM signal in terms of the out-of-band power leakage by over 20 dB.

In Chapter 5, an LTE-Advanced technique, termed CA, has been explained and showed that it can aggregate multiple legacy radio bands to support higher data rates. However, typical rectangular signals (i.e. no signal shaping) are specified in LTE-Advanced. The high out-of-band power leakage of one CC poses harmful interference to adjacent CCs. Thus, a 10% protection gap is inserted between adjacent CCs resulting in an inefficient spectrum utilization. Using the pulse shaping concept in the CA scenario, the out-of-band power leakage of a CC would be reduced. Thus, the 10% protection gap could be removed leading to further improved spectral efficiency. Con-

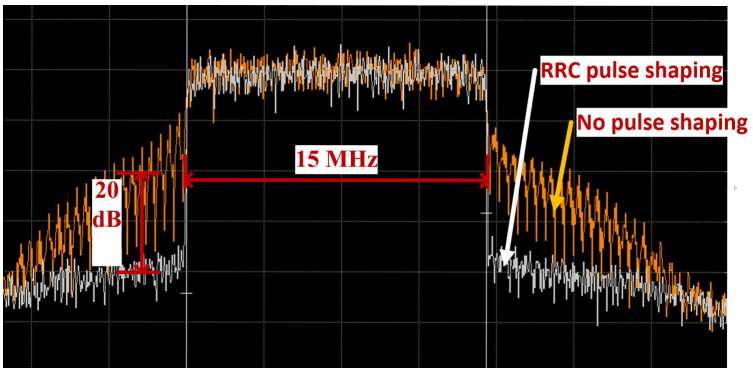

Figure 6.12: Measured spectra of SEFDM systems with two pulse shaping schemes. The center frequency is 2 GHz.

clusively, applying RRC pulse shaping in SEFDM is therefore beneficial in two aspects; it simplifies signal detection by reducing interference without degrading performance and improves spectral efficiency through out-of-band power suppression.

Practical evaluations of the proposed Nyquist-SEFDM are presented here in a carrier aggregation scenario. Signal is generated on the basis of the system block diagram in section 6.4.1. The reception part of Nyquist-SEFDM is skipped in this section due to multipath channel and RF challenges. The multipath effect is a complicated issue since both amplitude and phase can change at the same time. But using CP assistance, this issue would be solved. In addition, as explained in section 5.9, the testbed we are using introduces LO phase offset, sampling phase offset and phase errors from imperfect timing synchronization. These effects are equivalent to frequency-domain phase rotation. Since the phase rotation is proportional to sub-carrier frequency, the effect can be compensated using a frequency-domain equalization method as explained in [170].

This section will show the Nyquist-SEFDM signal effect on existing 4G signals. The coexistence experimental testbed is shown in Fig. 6.13 where the left inset is a real testbed setup and the right one is a framework illustration. In order to operate the experiment, two PXIs are required. The configurations of the two PXIs are shown in Table 6.1 where they have different carrier frequencies. One PXI is used as the signal transmitter for existing LTE OFDM signals and the other one is for promising 5G

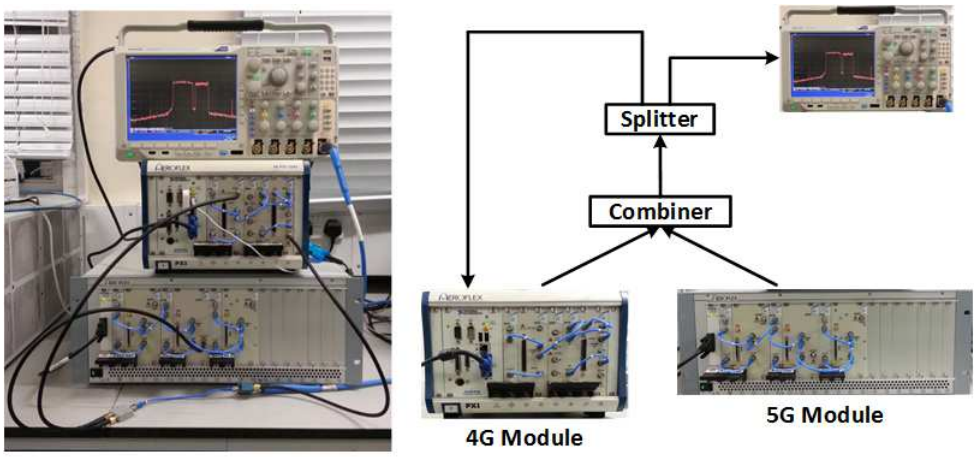

Figure 6.13: Practical 4G and 5G coexistence testbed setup.

signals. It should be noted that the 5G testbed configuration is flexible and it is easily reconfigured to another signal standards. The experiment here is to test the out-of-band power effect on existing 4G signals. Therefore, two signals would be aggregated very close with a 10% protection gap, which has been defined in LTE. Four aggregation scenarios are illustrated in Fig. 6.14 where they are noted as A,B,C,D.

Table 6.1: Experimental Testbed Specifications

Parameters	**4G Testbed(OFDM)**	**5G Testbed**
Sampling rate (MHz)	30.72	30.72
Carrier frequency (GHz)	2	2.018
Bandwidth (MHz)	18	15
FFT size	2048	128
Sub-carrier bandwidth (kHz)	15	240
Symbol rate per sub-carrier (kS/s)	15	240
Sub-carrier spacing (kHz)	15	$240\times\alpha$
Roll-off factor γ	None	0.5

- **Scenario A:**

  In this scenario, a future 5G signal format is assumed to be OFDM signal. A 10% protection gap, which is equal to 1.5 MHz, between the two signal bands is reserved. The right hand side spectrum clearly shows its out-of-band power

leakage. Constellation is the performance criteria that judges the interference effect. As explained above, at this stage, the defined 5G signal would not be recovered and the existing 4G signal performance would only be evaluated. Thus, the constellation on the right corresponds to the 4G signal band. In this comparison, we employe a bypass channel, which indicates no AWGN and no multipath effects. However, the constellation points are scattered, which is caused by the high out-of-band power leakage from the 5G signal band.

- **Scenario B:**

  The newly proposed Nyquist-OFDM signal is aggregated as the 5G candidate signal in this scenario. The protection gap is still 1.5 MHz. The out-of-band power leakage of this signal is significantly reduced. Therefore, the adjacent channel interference is therefore reduced. It can be observed from the right hand side signal spectrum. The constellation attached on the right also shows the significantly improved performance.

- **Scenario C:**

  This is the case that a typical SEFDM signal is designed for the 5G band. The protection gap is increased to 3 MHz due to the compressed bandwidth of the SEFDM signal band. The high out-of-band power leakage still exists since no pulse shaping is used. However, the effect would be mitigated in some degree. It is evident that the out-of-band power is not flat, which is inversely proportional to the frequency. This is due to non-ideal analogue filters. The benefit of using SEFDM signal in this case is that lower out-of-band interference power would be added to the 4G signal band due to the bandwidth compression. This can be observed from the corresponding constellation diagram. Although it is not clear, the scattering of each constellation point is mitigated.

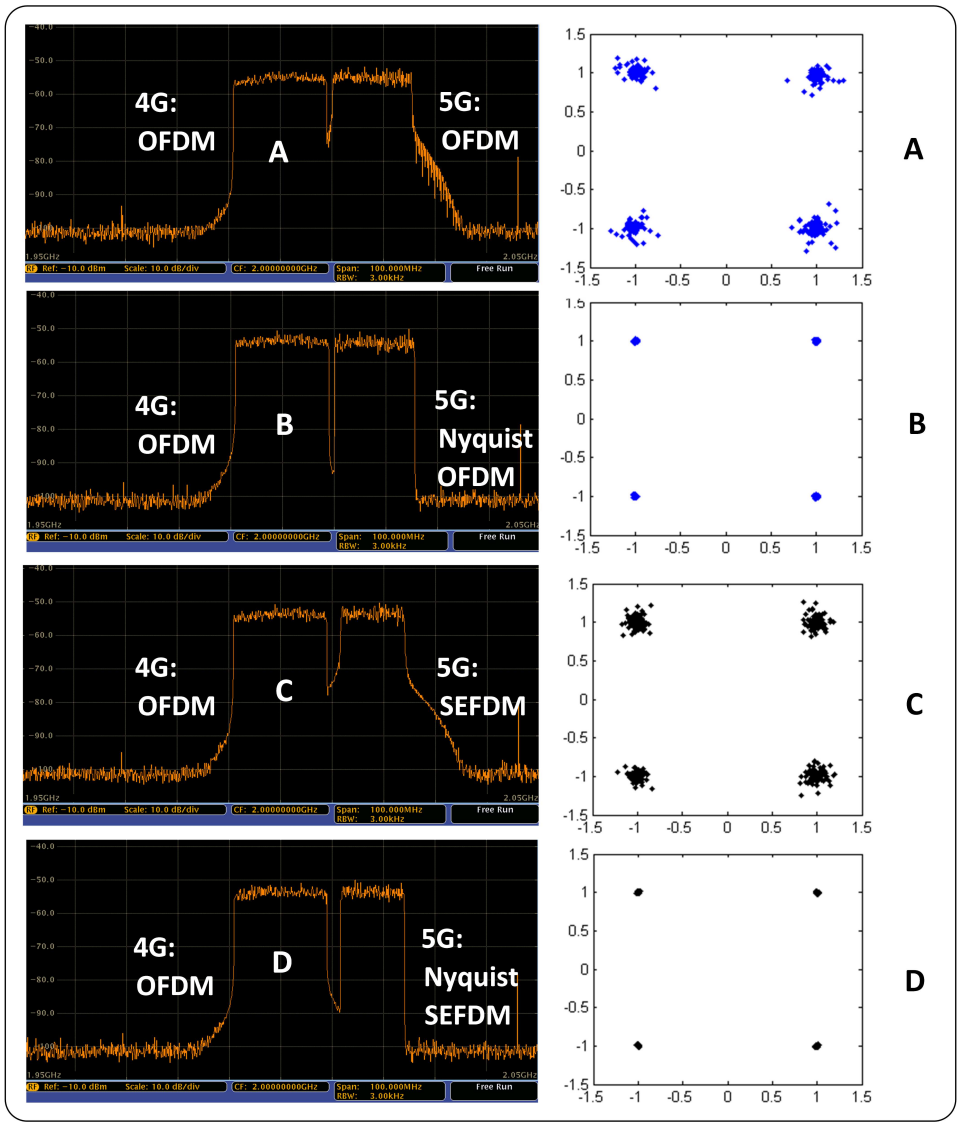

Figure 6.14: Four carrier aggregation scenarios for 4G and 5G signals coexistence testing.

- **Scenario D:**

  In the last scenario, we finally tested the newly proposed Nyquist-SEFDM signal, which compresses bandwidth and reduces out-of-band power leakage simultaneously. From the illustrated spectrum, the protection gap between two signal bands are extended. In a future system design, due to the extra bandwidth bonus, the right signal band could be shifted closer to the first signal band. Thus, the overall

occupied bandwidth would be compressed. The reduced out-of-band power benefit of this scenario is demonstrated in the constellation diagram, which is similar to the one in scenario B.

6.7 Over-the-Air Testing Using Software Defined Radio Devices

Experimental work discussed below is based on two independent USRP RIO 2953R platforms [188]. The actual setup, shown in Fig. 6.15, is designed to test the coexistence of SEFDM signal and LTE signal. LTE framework [189] is used as a tool to evaluate the proposed waveform. In this case, two USRPs, one implements SEFDM transceiver while the other one implements the LTE framework transceiver, are used to transmit over the air asynchronously operated.

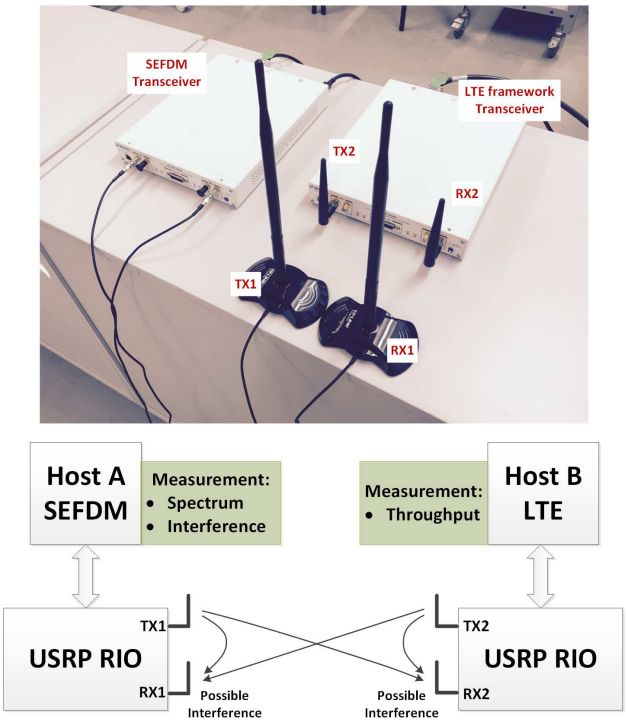

Figure 6.15: Double SEFDM/OFDM testbeds setup using USRP RIO for the evaluations of coexistence of SEFDM and LTE signals.

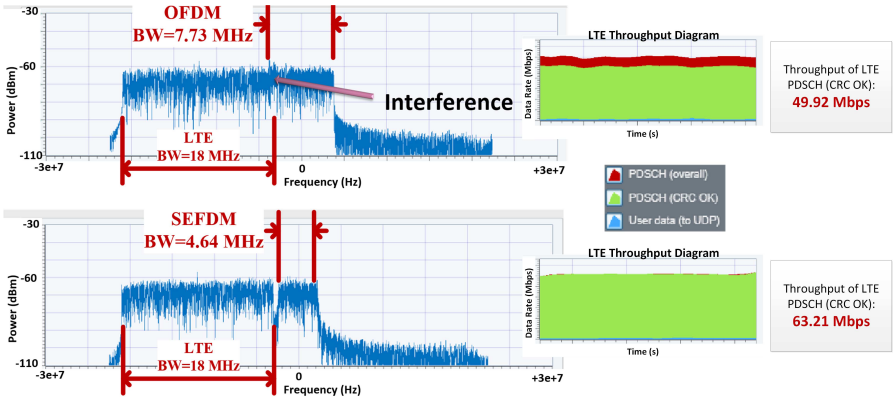

Figure 6.16: Coexistence of SEFDM/OFDM and LTE signals in a bandwidth limited scenario shown at baseband frequency.

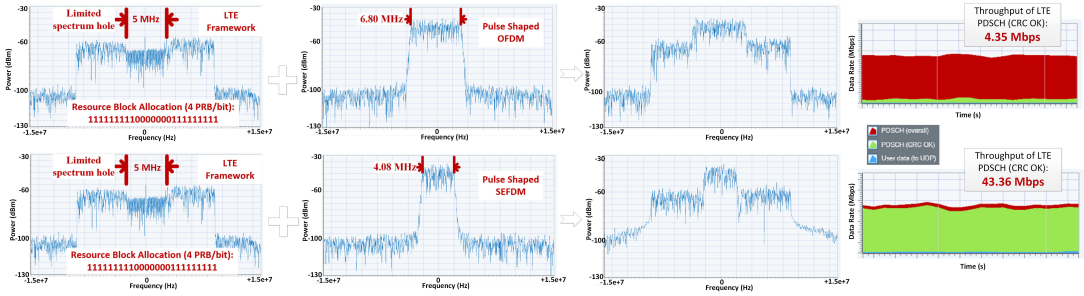

Figure 6.17: Coexistence of pulse shaped SEFDM/OFDM and LTE signals in a limited spectrum hole shown at baseband frequency.

The main benefit of this testbed is that the entire SEFDM system can be jointly implemented in software and hardware. LabVIEW is the software tool that implements part of the functions aligning with the FPGA integrated in the USRP RIO platform. A computer is connected to the USRP RIO and is used to generate the digital signals to be transmitted and to process received digital signals. The analogue signal processing is integrated in the USRP RIO device. The wireless signal transmission link is set up between USRP RF0 out port and RF1 in port via two omnidirectional antennas on each USRP with a 8 dBi peak gain in the azimuth plane. Two antennas are arranged with a line-of-sight (LOS) link and the spacing between the two antennas is 12cm and the antennas are placed 0.8 m above the floor. Two sets of Tx/Rx antennas are spaced approximately 14cm. Thus, possible interference would occur on RX ports of both

USRPs. Host A is for user defined SEFDM/OFDM signal generation and reception. The measured results include spectrum and interference effect. Host B is for LTE standardized signal transmission and reception. The physical USRP setup is shown in Fig. 6.15. Antennas are deployed in this experiment for the testing of a realistic wireless scenario.

This work is focused on coexistence performance with existing 4G LTE signals. Therefore, the detection of our designed SEFDM signal is skipped. Many efficient SEFDM signal detection schemes have been developed either based on uncoded [57] or coded [58][80] for various size systems.

Table 6.2: Experimental Testbed Specifications For Non-Pulse Shaped Systems

Parameters	**OFDM**	**SEFDM**
Central carrier frequency (GHz)	2.412	2.412
Modulation scheme	4QAM	4QAM
Sampling rate (MHz)	45	45
FFT size	1024	1024
Number of data sub-carriers	176	176
Bandwidth compression factor	1	0.6
Sub-carrier spacing (kHz)	44	26.4
Data bandwidth (MHz)	7.73	4.64
Data rate (Mbps)	15.46	15.46

Screenshots illustrating the coexistence performance are provided in Fig. 6.16 where two scenarios are considered. In the first scenario (top part of Fig. 6.16), OFDM (i.e. α=1) and LTE signals are transmitted and evaluated. The OFDM signal is configured based on Table 6.2, with associated spectrum clearly showing interference occurring due to the spectral overlap of the two signals. The LTE signal is degraded and this can be observed from the LTE throughput diagram where the red region in the figure indicates lower throughput measured through observation of the cyclic redundancy check (CRC) field of LTE data transmitted on the physical downlink shared channel (PDSCH) (overall) throughput and PDSCH (CRC OK) throughput. It indicates that the PDSCH transmission is not always correct. For this case throughput of the PDSCH (CRC OK) is measured to be 49.79 Mbps. Our proposed solution to use SEFDM signals

which, due to its reduced bandwidth, can avoid spectral overlap. The results are shown in the lower part of Fig. 6.16. The new SEFDM signal specifications are presented in Table 6.3. Due to the compressed bandwidth of SEFDM signals, a protection guard band is reserved between the LTE spectrum and the SEFDM spectrum. In the LTE throughput diagram, it is apparent that the received PDSCH transmission is almost free (no red region is observed) with a measured throughput of PDSCH (CRC OK), equals to 63.21 Mbps. This means that using SEFDM not only saves spectrum but improves throughput of an adjacent LTE system by a factor of 27%.

Table 6.3: Experimental Testbed Specifications For Pulse Shaped Systems

Parameters	**OFDM**	**SEFDM**
Central carrier frequency (GHz)	2.4	2.4
Modulation scheme	4QAM	4QAM
Sampling rate (MHz)	30	30
FFT size	128	128
Number of data sub-carriers	29	29
Roll-off factors	1	1
Bandwidth compression factor	1	0.6
Data bandwidth (MHz)	6.80	4.08
Data rate (Mbps)	13.60	13.60

Pulse shaping can cut the out-of-band power leakage leading to reduced interference to adjacent signals. Pulse shaping for SEFDM and GFDM has been conceptually studied in [76] and [137], respectively. Reusing the testbed in Fig. 6.15, the Nyquist-SEFDM and GFDM can be evaluated using antennas in a realistic wireless environment. It can be demonstrated that Nyquist-SEFDM can achieve the same benefits of GFDM [137] and will add additional interference avoidance benefit. Fig. 6.17 shows the performance of the coexistence of Nyquist-SEFDM/GFDM and LTE signals, with their system specifications shown in Table 6.3.

A sufficient spectrum hole indicates a wide enough notch that can be occupied by an additional signal band. To evaluate the benefit of Nyquist-SEFDM over Nyquist-OFDM (or GFDM), the LTE signal was modified to narrow the spectrum hole, indicating limited spectrum hole as shown in Fig. 6.17. The notch width maybe easily changed in

the experimental setup. In the first scenario, the sharp edge of the pulse shaped OFDM spectrum is due to the pulse shaping applied to each sub-carrier. The spectrum hole is emulated by deactivating some physical resource blocks (PRBs) of an LTE spectrum. The combination of the two signal bands leads to making new spectrum available. It is clearly seen that the Nyquist-OFDM spectrum overlaps the LTE one with interference introduced. The throughput, observed from the LTE throughput diagram, drops to 4.35 Mbps. This indicates that Nyquist-OFDM (or GFDM) has significant interference on the LTE signal even with reduced out-of-band leakage in a bandwidth limited scenario. In the second scenario, Nyquist-SEFDM shows its benefits. Although the spectrum notch is narrow, due to the bandwidth compression characteristic, interference can be avoided in the combined spectrum. Thus the LTE PDSCH (CRC OK) throughput is 43.36 Mbps, which is much higher than the one achieved in the first scenario by nearly one order of magnitude. Therefore, the benefits of using SEFDM in either rectangular shaped or RRC shaped systems are clear and have been summarized in Table 6.4. In both coexistence scenarios, SEFDM signals boost the LTE signal throughput greatly due to the interference avoidance coming from SEFDM bandwidth compression.

Table 6.4: Comparisons of Experimental LTE Signal Throughput

Parameters	**OFDM**	**SEFDM**
Traditional systems in Fig. 6.16 (Mbps)	49.92	63.21
Pulse shaped systems in Fig. 6.17 (Mbps)	4.35	43.36

6.8 Conclusions

For the purpose of reducing the out-of-band power leakage of SEFDM signals, a novel interference cancellation scheme for a waveform shaped signal was studied and verified considering future 5G requirements. The SEFDM system can transmit signals in a compressed bandwidth at the cost of self-created ICI. This work proposed a pulse shaping concept in SEFDM to suppress the interference caused by non-orthogonally packed sub-carriers. 3D interference patterns of various systems are studied and compared to show

the advantage of the pulse shaping idea. Detailed transmitter and receiver designs are investigated. Signal detection is simplified while the benefits of bandwidth saving and low out-of-band power leakage are presented. Two detection scenarios are considered. One uses uncoded data and the other applies coding and Turbo equalization. Results indicate that the uncoded iterative detection can effectively remove interference at the expense of high iteration numbers. With the coded Turbo equalization scheme, signal detection is simplified with fewer iterations.

In order to test and show the benefits of the pulse shaped SEFDM signal in a realistic RF environment, a coexistence experimental testbed, in which 4G and the pulse shaped signal are aggregated, was designed and tested. The main focus of the experiment is to investigate the out-of-band power leakage of promising 5G signals and their effects on existing 4G signals. Results indicate that the typical OFDM and SEFDM have high out-of-band power interference while the pulse shaped OFDM and the pulse shaped SEFDM (i.e. Nyquist-SEFDM) show significantly reduced out-of-band interference. In addition, the Nyquist-SEFDM introduces extra bandwidth saving benefit. Altogether, the signal studies show suitability for future communication systems where spectral efficiency and carrier aggregation are required to allow high data rate communication in an increasingly congested spectrum.

In addition, to test its over-the-air performance, several experiments based on the use of software defined radio equipment (national instruments USRP-RIO) were designed and reported in this chapter. Morreover, the signal coexistence scenario indicates that the pulse shaped Nyquist-SEFDM signal significantly outperforms GFDM signal in terms of BER performance in bandwidth limited scenarios.

Chapter 7

Millimeter Wave SEFDM: Practical Implementation for 60 GHz Band Indoor Transmission

7.1 Introduction

A proof-of-concept experiment on a SEFDM radio over fiber scheme with LTE type framing operating on a 2 GHz carrier has been presented in our previous work [62]. This chapter describes the benefits and challenges of using mm-wave systems and then moves on to the motivation of using RoF for 60 GHz mm-wave and SEFDM. Recalling that in the mm-wave frequencies range, there exists a wide unlicensed bandwidth while SEFDM is a bandwidth compression technique, the combination of the two allows a higher number of aggregated sub-carriers in a given bandwidth. This can be set in the system architecture, shown in Fig. 7.1, where more users (more signal bands) can share the same overall bandwidth. For each signal band, either in OFDM or SEFDM scenarios, the same number of sub-carriers are aggregated. It is evident that the bandwidth of each band in the SEFDM scenario is narrower than that of the OFDM one. In order to simplify the demonstration, one mobile station (MS) is assumed to

occupy the entire bandwidth in this experimental work. In an integrated multimode fiber (250 meters) and wireless (60 GHz over 3 meters) link, the work in this chapter demonstrates that the OFDM system achieves 2.25 Gbit/s while a bandwidth equivalent SEFDM can reach up to 3.75 Gbit/s.

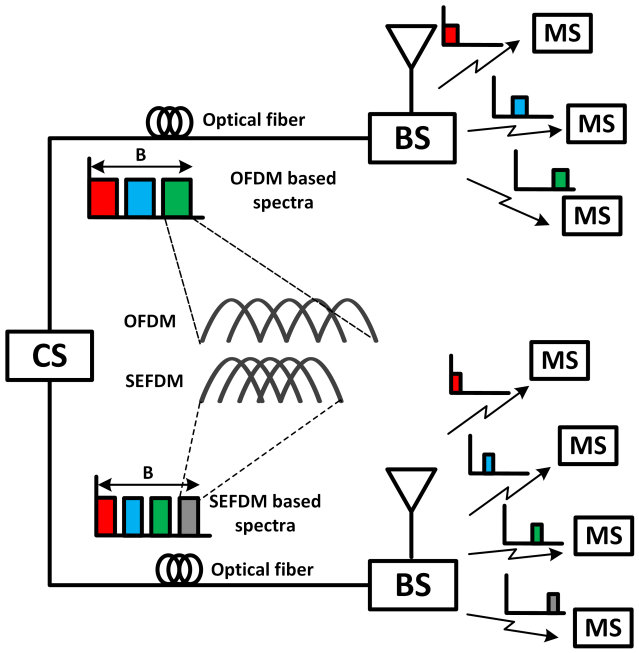

Figure 7.1: Application scenario of SEFDM in fiber wireless networks where CS indicates central station, BS indicates base station and MS indicates mobile station. Both OFDM and SEFDM sub-carrier packing schemes for each band are illustrated.

The experiment designed in this chapter offers the following benefits:

- Multimode fiber is employed for the preparation of future 5G applications.
- Photodiode is used to generate 60 GHz mm-wave signals from the beating of two optical signals, based on an uncorrelated remote heterodyne detection (RHD) concept. This optical domain carrier generation scheme is low-cost and can be easily modified by adjusting the two lasers wavelength separation to give different mm-wave carrier frequencies.
- The second tunable laser deployed in the BS or coherent RAU, after the SMF-

MMF-SMF fiber, brings many benefits. Firstly, it offers higher optical power due to no fiber noise addition. Secondly, it is easy to be integrated in an existing coherent passive optical network (PON) system. Thirdly, it can save optical bandwidth since only one laser carrier will be carried in the fiber. Last of all, there is no modal noise from the second laser.

- Envelope detector is used to down convert the 60 GHz millimeter wave signal to basedband. This is a low cost and robust technique, with high resistance to phase noise.

7.2 Millimeter Wave Benefits and Challenges

The current LTE system can offer data rates up to 300 Mb/s in the downlink and 75 Mb/s in the uplink [1]. The enhanced LTE-Advanced standard can support up to 3 Gb/s in the downlink and 1.5 Gb/s in the uplink, using carrier aggregation and MIMO techniques [15]. Although today's developed cellular 4G standards can significantly improve capacity and user throughput, current projections predict a rapidly growing wireless data traffic demand accompanied by new demanding wireless services in terms of bandwidth, capacity, coverage, and quality of service (QoS). Due to the limited available bandwidth at low frequencies, current existing wireless standards are unable to support such services. The increasing demands may be addressed by the utilization of millimeter-wave (mm-wave) (i.e. 30-300GHz) [13] radio frequencies, which have wider unlicensed signal bandwidths.

Unlicensed spectrum at 60 GHz [190] is popular and is in an active commercial deployment [191]. The 7 GHz wide continuous spectrum ranging from 57 GHz to 64 GHz is desirable for applications requiring high transmission bandwidth. Up to 7 Gbit/s data rate can be achieved in IEEE 802.11ad [192] aiming for the 60 GHz indoor communications.

In addition to the substantially rich available spectrum in the mm-wave band, the 60

GHz band also has some unique propagation characteristics that provides an excellent mechanism to combat interference and ensures high security [193]. The 60 GHz band was previously used in applications which require secure communication channels such as satellite-to-satellite communication systems. The secure communications at this frequency are limited by the high amount of electromagnetic energy absorption in the 60 GHz transmission spectrum, caused by oxygen molecules (O2), as illustrated in Fig. 7.2 [191]. It is apparent that attenuation values vary at different frequencies. The atmospheric loss peak value at 60 GHz is around 15 dB/km. This absorption shows an attenuation peak in Fig. 7.2 where the peak value is several orders of magnitude higher than those at lower microwave frequencies.

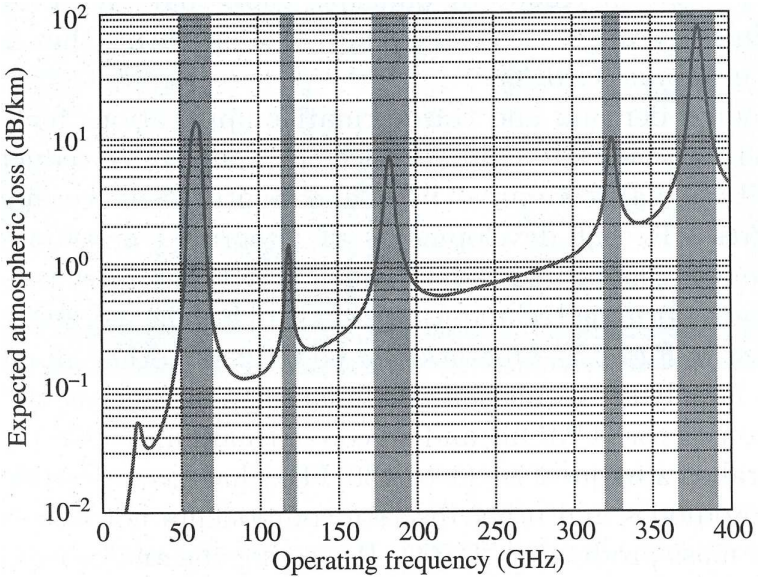

Figure 7.2: Atmospheric and molecular absorption at millimeter wave frequencies. The figure is reused from [191]

Therefore, unlike low frequency microwave signals, the 60 GHz signal cannot travel far beyond the intended receiver. The propagation characteristics at mm-wave frequencies limit their application to short distance wireless communication scenarios such as next generation 5G picocell/femtocell based mm-wave cellular networks, with ranges in the order of 10-200 m. This is the reason why 60 GHz communication is securely

guaranteed. This also explains the principle of satellite-to-satellite secure communications. This is due to the fact that the earth's atmosphere creates an absorption shield that prevents eavesdropping from earth based stations.

Due to the high carrier frequency and therefore short wavelength of millimeter wave frequency, a large number of mini antennas (e.g. phased array antennas) could be deployed to realize directional beamforming [14] in which effects of high path loss could be mitigated. Since information is transmitted through a narrow beam, the co-channel interference from adjacent channels or adjacent cells would be greatly reduced. Therefore, in an outdoor millimeter wave transmission scenario, a user can be switched to a further base station instead of a close one occupied by other users [194]. The reason for the new handover mechanism comes from the narrow beam. Another benefit introduced by beamforming is reduced signal power on each mini antenna, thus, the requirement of PA would be released. In addition, the multiple antenna design encourages the use of MIMO, which would further improve the spectral efficiency. In a backhaul transmission scenario, for typical microwave deployments, either a dish antenna or physical antenna alignment would be employed [195]. However, in a millimeter wave MIMO beamforming scenario, transmit beams could be adaptively modified electronically without physical readjustment. Moreover, millimeter waves could be used in backhaul transmission scenarios where high speed fiber is costly to deploy. It is also more competitive than a microwave backhaul transmission scenario due to the potentially high throughput and steerable operation.

To sum up, millimeter wave communications have the following advantages:

- A wider bandwidth allows higher data rates.
- The high absorption loss allows secure communication.
- The short range communications can extend existing 4G cellular architectures to future 5G picocell/femtocell networks. Thus, the frequency reuse efficiency is greatly improved.

- Beamforming is able to limit co-channel interference using narrow beams.
- The millimeter wave beam could be electronically adjusted and steered instead of physically adjusted in microwave using phased array antennas. Thus the deployment in a backhaul transmission scenario is simplified.

Despite the aforementioned benefits, millimeter wave also brings engineering challenges such as

- **DAC/ADC limit:**

  The use of wide spectra in millimeter wave scenarios brings hardware implementation challenges such as ADC/DAC design. A higher data rate indicating a higher sampling rate, therefore more complicated and costly DAC/ADC components. It should be noted that a high speed, high precision ADC is either not available or too costly and power hungry [196]. The available precision is severely limited at high sampling rate. It is shown in [196] that for large sampling rate, which is above 2MS/s, the precision falls off by 1 bit for every doubling of the sampling rate. Normally, two solutions exist for this challenge. The first one is to use a low precision ADC for the wide band millimeter wave communication. However, due to the reduced precision, performance maybe affected. The second solution is to use time interleaved ADC scheme, which combines multiple high precision, low sampling rate ADCs. This solution would maintain the performance while bring some new challenges such as increased hardware complexity and mismatch between sub ADCs.

- **High PAPR:**

  This is a common challenge assuming multicarrier signals are used in millimeter wave such as IEEE 802.11ad Wireless Gigabit Alliance (WiGig) standard. There are many existing solutions to reduce this effect, however, extra signal processing is required.

- **Coherence time and frequency:**

  Although beamforming can eliminate much of multipath in a millimeter wave scenario and therefore reduce time delay spread, the very wide signal bandwidth that may reach several gigahertz, with symbol periods in the order of 1-10 ns or less [195], necessitates very low delay spread values. Thus, both time delay spread and symbol period are reduced. It is inferred that frequency selective fading would still exist and proper equalizers and/or specially designed modulation schemes have to be considered. There are single carrier and multicarrier modulation schemes proposed for millimeter wave communications. Employing a single carrier scheme would have a more challenging issue, which is the shorter symbol period. The timing constraint is therefore tighter than a multicarrier one. However, multicarrier signals result in high PAPR, which lowers the efficiency of PA. There is a trade-off between single carrier and multicarrier techniques and new thoughts and insights are needed to make a judgement. Due to the shorter time delay spread, the channel coherence bandwidth of millimeter wave is wider than that of lower frequency microwave. However, using millimeter wave frequencies, even at a very low user velocity, may result in a very high Doppler shift. Thus the coherence time is very short. Therefore, a novel channel estimation/equalization scheme has to be designed to deal with the channel challenge.

- **Blockage:**

  The wavelength of the millimeter frequency is very short and its weak diffraction ability makes it sensitive to blockages [194] such as brick, concrete and rain drop. Therefore, the application scenario is possibly limited to indoor short-range LOS environments. In the near future, millimeter wave and microwave systems are expected to coexist [194]. As millimeter waves are sensitive to blockages, microwave can help to cover the shadowed areas behind blockages. Therefore, user mobility may result in high Doppler shift in a millimeter wave communication scenario, users may be switched to microwave frequencies.

- **Alignment sensitivity:**

  In order to use a narrow beam in millimeter wave scenarios, transmitters and receivers have to be accurately aligned in a stable link, otherwise, significant loss would occur. In addition, the alignment can be greatly affected by environmental factors such as wind. If millimeter wave transmitters and receivers are not installed on fixed and stable structures, due to the wind effect, the perfect alignment would disappear. Furthermore, some other factors such as buildings and trees would block the LOS communication and lead to further loss of alignment.

- **Maintenance and cost challenges:**

  As mentioned in the last shortcoming point, millimeter wave transmitters and receivers have to be aligned perfectly. Some natural or human factors would change the perfect alignment condition. Thus, realignment has to be operated. The realignment could be readjusted adaptively using some alignment tools, but this would be costly. If the alignment tool is broken, engineers would have to be involved and therefore additional cost. Therefore, the shortcomings mentioned above could prevent the use of millimeter in an outdoor environment and maybe an indoor LOS is a desired scenario.

7.3 Radio over Fiber in Millimeter Wave Systems

The mm-wave spectrum imposes several challenges due to its high transmission losses, which mandate a high density of radio access points. This imposes critical limitations in terms of complexity, increased cost, high power consumption/ backhaul radiation, distributed network upgrade and maintenance. This is in contrast to societal demands for reduced capital expenditure (CapEx), energy conservation (i.e. green communications) and a drastic reduction of backhaul radiation (i.e. health concerns).

In recent years, RoF [197] technology has emerged as a promising candidate in order to bridge the gap between optical & wireless networking. Such a hybrid system has

several advantages over typical stand alone fiber and wireless systems since it merges both optical and wireless benefits. On one hand, the fiber link provides low attenuation to mm-wave signals and the supported transmission distance can be significantly increased. On the other hand, the wireless link provides the flexibility of ubiquitous networking. Much research has been done, including in several EU funded projects, to target design in this area, the most prominent being; Building the Optical Network in Europe (BONE), Integrated PHOtonic mm-wave components and functions for BroAdband Connectivity (IPHOBAC, IPHOBAC-NG), Ultra wideband Radio Over Optical Fiber (UROOF), and Architectures for fLexible Photonics Home and Access networks (ALPHA).

RoF technology offers the conversion of complex densely distributed base station (BS) sites to simple remote antenna units (RAUs) connected to a central base station (CBS), using already deployed passive optical network (PON)-FTTx. Thus, complicated operations are concentrated at a CBS. In such cases, RoF technology eliminates the requirements for local oscillators, digital signal processors, and mixers at the RAUs, potentially leading to few tens of Watts power saving per RAU [198]. This approach can make use of widely deployed fiber to the home (FTTH) as an efficient way to provide backhaul to wireless BSs. Additionally, it can extend the coverage of a PON to support some areas which are not easily supported by fibers. Moreover, the RoF concept significantly reduces the overall cost in terms of CapEx and operating expenditure (OpEx), while optical functionality can be used for required mm-wave generation and/or beamforming. However, the critical factors which will determine the practical deployment of the RoF scenario are; the simplicity and compatibility of the optical components used with the standard TDM-PON or upcoming next generation WDM-NG-PON devices, and the cost-efficiency in terms of reuse of already installed infrastructures in the optical (e.g. PON) and wireless (e.g. LTE) domain. Typically, OFDM [199] signals are used in mm-wave RoF systems [200][201][202]. Firstly, OFDM is preferred due to its compatibility with emerging wireless standards. Secondly, OFDM

provides high spectral efficiency using orthogonally overlapping sub-carriers. Thirdly, OFDM can simultaneously mitigate dispersion effects from fiber links and multipath fading effects from wireless links.

In-line with the above, in this chapter an integrated PON/mm-wave wireless topology using single mode fiber to multimode fiber feeds is adopted [203], which can be used for cost-efficient beyond 4G in building extensions and small cell mobile backhaul/fronthaul communications. Such concepts are based on the reuse of PON fiber to the building (FTTB/FTTC) and indoor MMF deployments, including potential upgrade with next generation coherent WDM-PON. In the wireless domain, a beyond 4G topology, where mm-wave 5G cells will be overlaid by microwave 4G cells, is preferred so as the users will be able to use traditional 4G LTE based systems where the mm-wave link is shadowed.

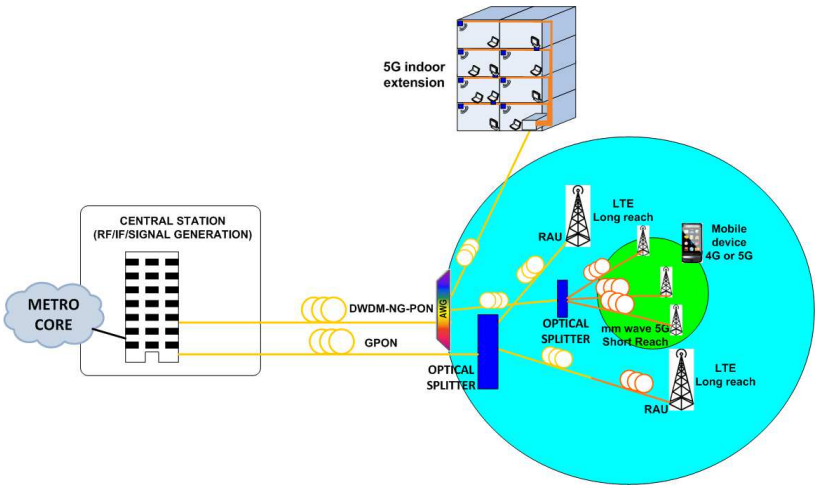

Figure 7.3: Proposed cost-efficient integrated PON/mm-wave wireless topology for beyond 4G (5G) deployment using SMF-MMF spans. AWG stands for arrayed waveguide gratings. RAU stands for remote antenna unit. PON stands for passive optical network. GPON stands for Gigabit-capable passive optical network. DWDM stands for dense wavelength division multiplexing.

A cost-efficient PON/mm-wave wireless converged system topology is depicted in Fig. 7.3 which can support mm-wave based 5G radio over fiber for indoor and small cell deployment. 5G specifications are still under consideration and the selection of exact

range of mm-wave frequency spectrum and operational bandwidth are still open issues. Notwithstanding, in the demonstrated experimental setup this work uses transmission in the 60GHz band, where a bandwidth up to 7 GHz has been allocated for use by the Gigbit/s WiFi services and this stands as an excellent opportunity to investigate further this band potentially for 5G mm-wave transmission, due to the availability of relevant experimental know-how and relative 60GHz components in the market, such as low cost 60GHz silicon-germanium (SiGe) BiCMOS amplifiers. Indeed, mm-wave (60GHz) has already been standardized or pre-standardized in WiFi hotpots (eg. IEEE 802.11ad and IEEE 802.15.3c). An interesting option will be to consider the 60 GHz for mm-wave 5G (or beyond 4G) as this facilitates integration of outdoor and indoor networking on a common air interface. In any case, our topology (as validated by the presented proof-of-concept experiments) can be easily adopted by future standardized mm-wave systems, with minor modifications, as the selection of mm-wave frequency comes at the RAUs (or coherent RAUs) with a second tunable laser (as it pre-exists in the coherent-PON configuration), while the central point is used for the IF/RF signal generation/distribution. Ongoing, all the required baseband/lower frequency (IF/RF) signal processing is performed at a central base station, which can be the standard optical line terminal (OLT), while high frequency components and optical amplifiers are not required. A low-bandwidth optical modulator or a directly modulated laser source can be used so as to generate the IF/RF modulated optical carrier accompanied by transmission in a SMF (or MMF) type link, using in both cases an SMF-pigtailed optical transmitter and receiver so as to fulfill relatively high bandwidth/ carrier 5G signals requirements. For the 4G case, a low bandwidth photodiode can be utilized at the RAU to convert directly the signal to the electronic domain, followed by an RF amplifier and an antenna. In the 5G scenario, the signal can be easily up converted from IF/RF to mm-wave (for example 60GHz or similar) using a second, simple, long-wavelength PON compatible (such as the laser used for IF generation at the coherent-PON) DFB laser source properly tuned (i.e separated by the required mm-wave frequency), and a high

speed SMF-pigtailed photodiode. This topology keeps the CS (OLT) configuration the same for the IF/RF signal generation using low cost components, while the selection of the service (4G or 5G) is performed at the receiver stage (RAU).

7.4 System Model

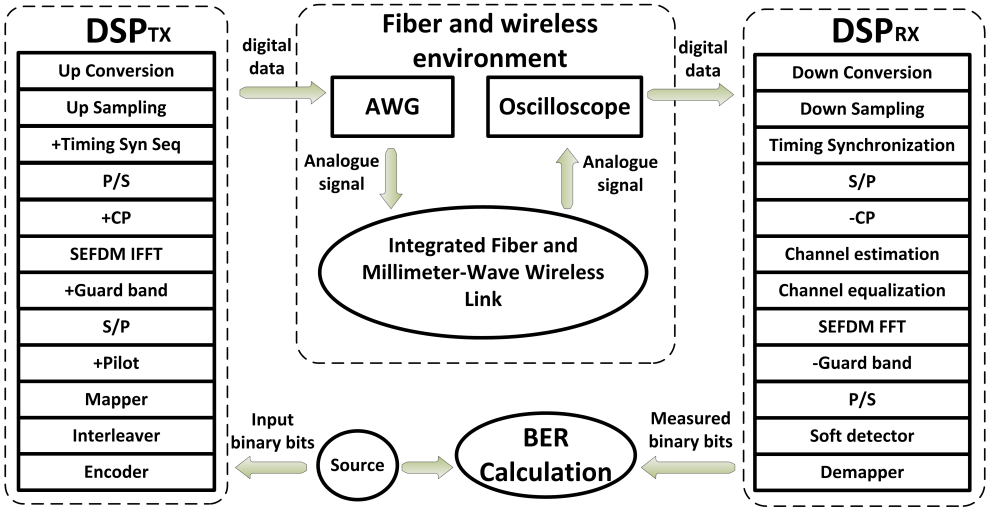

Figure 7.4: Block diagram of step-by-step digital signal processing operations for the mm-wave SEFDM transmission system.

To realize the mm-wave SEFDM experiment, new software and hardware setup were developed. The hardware testbed including analogue signal generation, integrated RoF and mm-wave wireless link and analogue signal reception will be described in section 7.5. This section focuses on the software testbed. The software consists of two digital signal processing (DSP) blocks for digital signal generation and digital signal reception, at the transmitter and the receiver, respectively. The DSP modules of the mm-wave SEFDM transmission system are depicted in Fig. 7.4.

In line with most of today's wireless systems, FEC, in the form of convolutional coding, is applied in this system to achieve coding gain. A simple, rate 1/2 RSC code [204] is used, which is similar to the code used in FTN [25] and wireless based SEFDM [63]. At the transmitter, the input binary bits are first encoded in the RSC encoder.

Then, a random interleaver $\mathbf{\Pi}$ is employed to permute the coded bits. Depending on the specific modulation format, the interleaved bits are mapped to the corresponding complex symbols. One uncoded pilot symbol is inserted at the beginning of each data stream and is used to estimate CSI, enabling compensation for wireless channel distortion, imperfect timing synchronization and sampling phase offset. After the S/P conversion, oversampling is operated by adding zeros (i.e. guard band). The data stream with pilot symbols is modulated using a purpose designed SEFDM IFFT block [46]. Then a CP is added at the beginning of each modulated symbol to combat multipath delay spread. In order to estimate the actual starting point of a data stream at the receiver, the Schmidl and Cox timing synchronization sequence [160] is added after the parallel-to-serial (P/S) conversion module.

In a direct detection optical system, to avoid the second-order IMD from the PD, a frequency gap [155] is introduced between the signal band and the optical carrier and is set to be at least equal to the bandwidth of the signal, as shown in Chapter 4. This is typically done in the analogue domain using an IQ mixer which up converts baseband I and Q signals to a real value signal at a radio frequency f_c. In this work, in order to simplify the optical testbed, the IQ mixer function is realized in the DSP testbed. After adding the timing sequence, a serial data stream is upsampled to 12 GHz (i.e. AWG sampling frequency). Subsequently, the I and Q data of the upsampled SEFDM signal are up converted to f_c=1.8 GHz as:

$$x_{up}(m) = \Re\{x(m)\}cos(2\pi f_c m) + \Im\{x(m)\}sin(2\pi f_c m) \tag{7.1}$$

where $\Re\{\cdot\}$ and $\Im\{\cdot\}$ indicate the real and imaginary part of a signal, m is the time sample index and $x(m)$ is the upsampled baseband SEFDM signal at the transmitter. Then the mixed real valued SEFDM signal $x_{up}(m)$ is uploaded in a digital form to the AWG which implements a digital to analogue conversion. Finally, the AWG analogue output signal is transmitted through the fiber/wireless environment. All the signal processing within the transmitter DSP block is operated offline in a Matlab environment.

At the receiver, a real-time oscilloscope captures the analogue signal and transforms it to digital samples, with a 50 GHz sampling frequency, to be delivered to the receiver DSP block for offline processing. The down conversion and down sampling functions are realized in the receiver DSP block. The down conversion is operated as

$$y_{down}(m) = y(m) \cdot e^{j2\pi f_c m} \tag{7.2}$$

where m is the receiver sample index which has a larger sample range due to unbalanced sampling frequencies of the oscilloscope (i.e. 50 GHz) and the AWG (i.e. 12 GHz). It should be noted that $y(m)$ is the real valued sample from the oscilloscope while $y_{down}(m)$ is a complex signal, which includes I and Q data. After the down conversion and down sampling, the accurate starting point of the data stream is estimated according to the Schmidl and Cox algorithm [160]. In the mm-wave radio environment, the channel introduces amplitude attenuation, phase distortion and propagation delay. Additionally, imperfect timing synchronization leads to an inaccurate estimate of the starting point of a data stream. A small time offset results in the rotation of the constellation and degrades system performance, which, for design purposes, may be considered as an additional channel imperfection that can be corrected using channel equalization. For the purpose of channel compensation, a parallel signal is obtained after the S/P block and the CP is stripped away. Then, a time-domain channel estimation algorithm, based on that described in Chapter 5, is employed to extract the CSI which is further used to equalize the distorted symbols. The compensated signal is demodulated using either the single FFT or the multiple FFTs methods [46]. After the removal of guard band and P/S conversion, a soft detector [58] is needed to recover SEFDM symbols from interference. Then, the recovered complex symbols are demapped to binary bits. Finally, the measured binary bits are compared with the original input binary bits for the BER calculation. The same system setup is also used for OFDM signals.

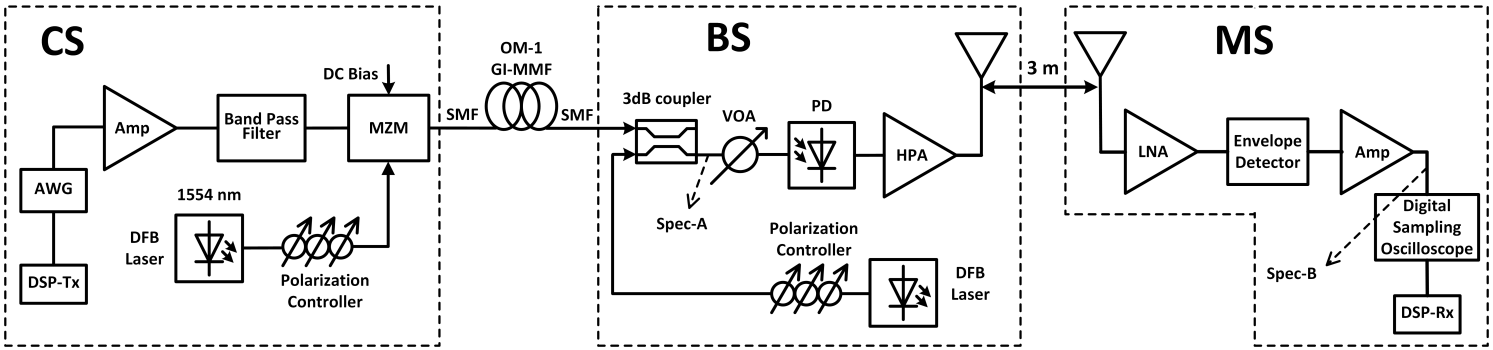

(a) Block diagram of the experimental setup.

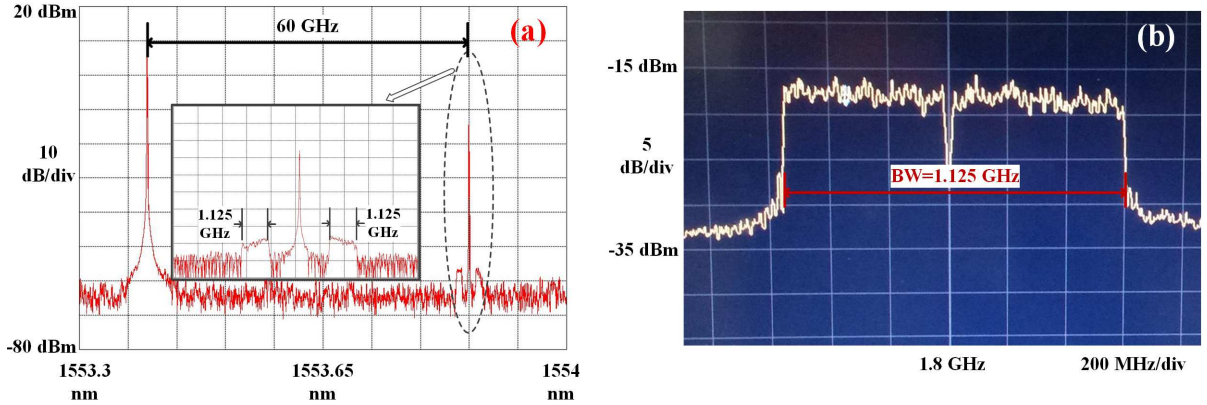

(b) Optical and electrical spectra illustration.

Figure 7.5: Experimental setup for SEFDM signal transmission over a 60 GHz millimeter-wave radio over fiber transmission link.

7.5 Experimental Setup

In this section, the mm-wave SEFDM signal transmission is experimentally tested in an indoor propagation environment using the testbed shown in Fig. 7.5(a), with the parameters shown in Table 7.1. The 4QAM modulated SEFDM/OFDM signals of 1.125 GHz bandwidth, with different bit rates; specifically 2.25 Gbit/s for OFDM, 2.8 Gbit/s for α=0.8 and 3.75 Gbit/s for α=0.6 are generated offline in the DSP-Tx module in Fig. 7.4. Data streams are generated by assembling up to 10^6 coded bits per stream (over 6,250 OFDM/SEFDM symbols), with three additional uncoded symbols inserted at the start of an entire data stream; two symbols for timing synchronization and one symbol for channel estimation. BER measurements were taken for each transmitted stream and repeated several times for verification of measurement accuracy. Data stream samples are then uploaded to a Tektronix 7122B AWG operating at a sampling rate of 12 GS/s. After a 20 dB gain amplifier and a band-pass filter, the resulting signals are modulated onto an optical carrier using a DFB laser at around 1554 nm and an intensity modulator biased at quadrature point. This results in an optical DSB signal at the output of a 3 GHz bandwidth MZM. The optical signal is then transmitted over a 250 meters OM-1 MMF span, coupled using single mode fiber (SMF) connectors at both ends. An SMF-MMF(OM-1)-SMF link [203] is preferred to achieve a restricted mode launch condition, thus improving the bandwidth length product of graded index (GI)-MMFs, which is in the order of 500/160 MHz.km at 1310/850 nm, when operating in an overfilled launch condition (OFL). In the recent work [71], a description of a purely optical system (that does not include the 60 GHz mm-wave link) is included as a first step towards the design of the 60 GHz system which is briefly described in the same reference.

At the BS, a second uncorrelated DFB laser, tuned to 60 GHz below the optical frequency of the first DFB laser is combined in the 3 dB coupler with the DSB optical signal. The combined signal is attenuated using a variable optical attenuator (VOA) and delivered to a 70 GHz bandwidth photodiode. It is well-known that the phase noise of the optical carrier generated by the beating of two uncorrelated optical sources, as

Table 7.1: Experimental system specifications

Parameters	**Values**
Millimeter wave frequency	60 GHz
Intermediate frequency	1.8 GHz
Baseband signal sampling frequency	3 GHz
Bandwidth of baseband signal	1.125 GHz
AWG sampling frequency	12 GHz
Oscilloscope sampling frequency	50 GHz
Length of MMF fiber	250 meters
Distance of mm-wave wireless link	3 meters
Modulation scheme	4QAM
IFFT/FFT size	128
Data sub-carriers	48; 60; 72; 80
Sub-carrier baseband bandwidth	23.4 MHz
Sub-carrier spacing	$\alpha\times$23.4 MHz
Cyclic prefix	10
Channel coding	(7,5) RSC code
Coding rate	R_{code}=1/2

it is the case for the remote heterodyne detection scheme used in this experiment, may manifest itself in the broadening of the spectral linewidth. In the presence of phase noise, a carrier-recovery circuit might have difficulties in tracking rapid phase variations, resulting in degradation of the detection performance. Alternatively, these phase-noise effects can be avoided at baseband by utilizing an envelope detector with sufficient IF bandwidth [205]. The measured optical spectrum at the VOA input is shown in Fig. 7.5(b) (a) where two wavelengths are shown with a 60 GHz separation. The detailed DSB signal spectrum is also illustrated in the inset of the same figure. The 60 GHz mm-wave signal can be generated at the 70 GHz square-law photodiode based on an uncorrelated remote heterodyne detection (RHD) scheme. This optical scheme is of low-cost and can be easily used for existing 4G or future 5G mm-wave signal by adjusting the laser separation to any required carrier frequencies.

A pair of 60 GHz parabolic (Cassegrain) antennas operating in the frequency range of 50-75 GHz which have 30 dBi gain; and 3 dB beamwidth of 3.1° are employed and shown in Fig. 7.6. In addition, a 30 dB gain V-band HPA at the transmitter and a 30

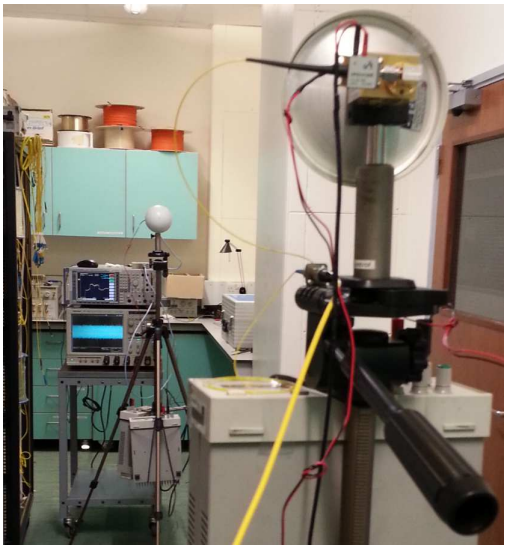

Figure 7.6: Experimental demonstration of the antenna deployment.

dB gain V-band low noise amplifier (LNA) at the receiver are used. Having propagated through a 3 meter mm-wave wireless link, the received 60 GHz mm-wave signal is down-converted to a 1.8 GHz intermediate frequency (IF) using a waveguide coupled 3 GHz bandwidth envelope detector, which is tolerant to phase noise impairment. The IF signal is captured by a real-time digital oscilloscope and the measured electrical spectrum is illustrated in Fig. 7.5(b) (b) where the signal bandwidth is 1.125 GHz. Finally, the captured signal is processed offline in the DSP-Rx module as detailed in Fig. 7.4.

The system parameters used in this experiment are given in Table 7.1. In this experiment, a total of 1.125 GHz data bandwidth is used. The number of data sub-carriers is different for the OFDM and SEFDM systems. For OFDM, 48 data sub-carriers are used while with higher bandwidth compression levels in SEFDM systems, more data sub-carriers (e.g. 60 for α=0.8, 72 for α=0.67 and 80 for α=0.6) are aggregated.

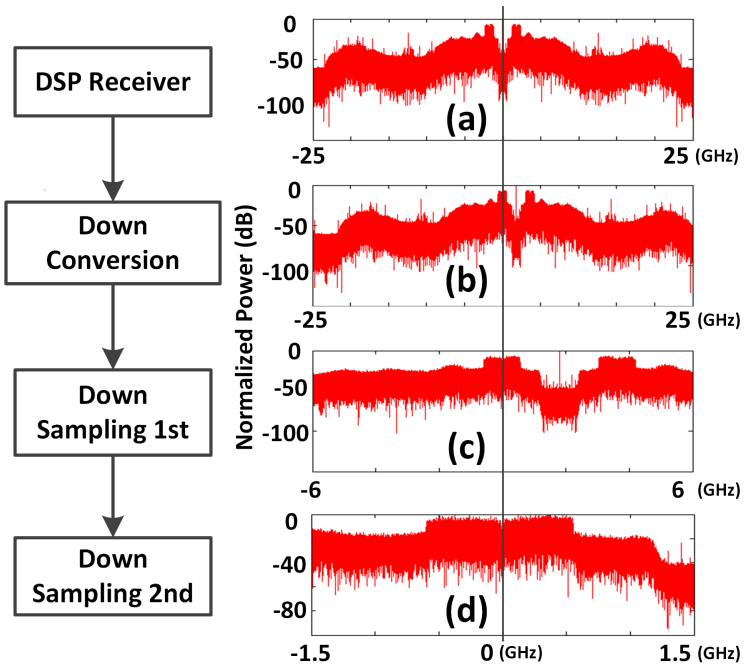

Figure 7.7: Signal spectra at different receiver stages.

7.6 Results and Discussion

As mentioned before, in order to simplify the optical testbed, up sampling and up conversion to IF are moved to the digital domain and performed by the DSP elements in Fig. 7.4. Electrical spectra at different receiver stages are shown by the insets in Fig. 7.7. For the illustration, only OFDM spectra are shown here. First, the received spectrum from the 50 GS/s real-time oscilloscope is shown in Fig. 7.7 (a). The overall frequency range is 50 GHz indicating the sampling frequency of the oscilloscope. Two peaks are observed indicating double sideband signal with 1.125 GHz bandwidth for each one. After down conversion, one side band is moved to baseband as shown in Fig. 7.7 (b). Due to the unbalanced sampling frequency (12 GHz AWG and 50 GHz oscilloscope), two-stage down sampling is required. The first stage is from 50 GHz to 12 GHz in Fig. 7.7 (c) and the second one is from 12 GHz to 3 GHz in Fig. 7.7 (d). Then the baseband signal is timing synchronized for subsequent signal processing.

Measured receiver constellation diagrams for OFDM and SEFDM (i.e. α=0.8)

signals are illustrated in Fig. 7.8 in the form of constellation density plots. Two channel compensation scenarios are considered to recover the rotated constellation points. For the OFDM signal, a typical frequency-domain channel compensation algorithm is employed. For the SEFDM signal, an additional time-domain channel compensation scheme is also tested. The purpose of the comparison is to show the effects of two channel compensation schemes on the SEFDM signal.

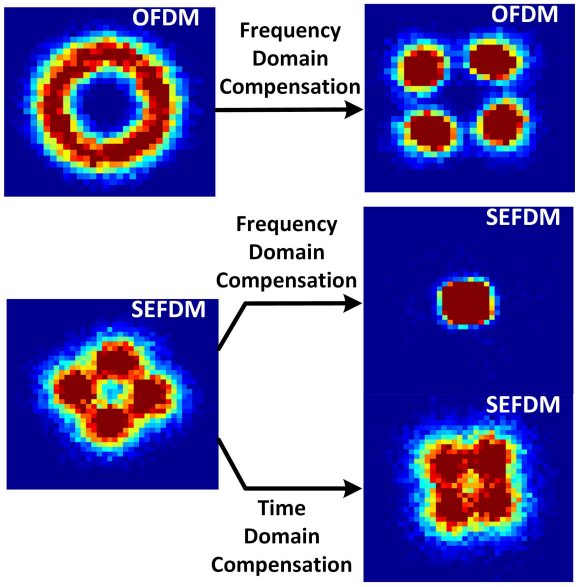

Figure 7.8: Constellation diagrams for OFDM and SEFDM (i.e. α=0.8) signals before and after channel compensation.

It is evident that due to sampling phase offset and imperfect timing synchronization, both the original OFDM and SEFDM signal constellation points are scattered and overlapped. For OFDM, before channel compensation, the constellation points rotate in phase and appear as a circle. After applying frequency-domain channel compensation, the phase rotation can be mitigated and the constellation points are clearly distinguishable. However, for the SEFDM signal, following the same frequency-domain channel compensation, the phase ambiguity is not mitigated. The constellations are no longer recoverable. This is because the non-orthogonality between sub-carriers results in compensation failure. The constellation recovery can be achieved using the afore-

mentioned time-domain channel compensation. Hence, the recovered constellation is recognized. It should be noted that compared to the recovered OFDM, the SEFDM with time-domain channel compensation shows more scattered constellation points due to the self-created ICI of SEFDM signals. The intrinsic ICI will be mitigated using the soft signal detection mechanism [58].

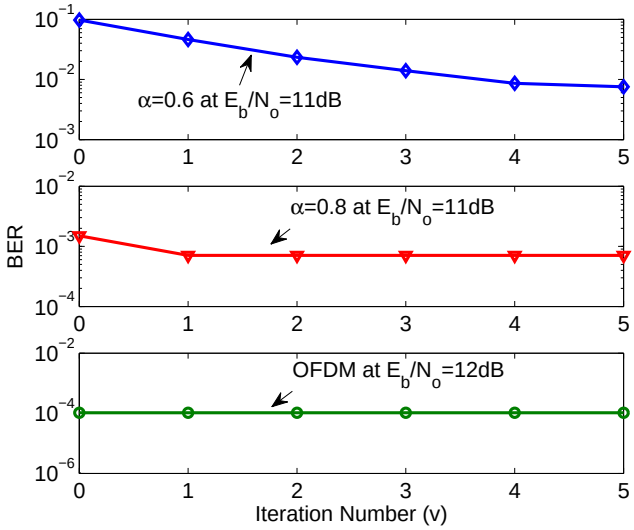

Figure 7.9: BER convergence performance of SEFDM signals over the integrated 60 GHz mm-wave and fiber transmission link.

The iteration performance is evaluated in Fig. 7.9 in terms of the number of iterations (v). It is evident that no iterations are needed for the OFDM system. However, for SEFDM systems, in order to get converged performance, extra iterations are required to deal with the interference introduced by the closer packing of sub-carriers. Thus, SEFDM requires additional computations to get converged performance. For α=0.8, one iteration is sufficient while four iterations are needed for α=0.6. This is due to the fact that with smaller α (i.e. higher bandwidth compression), more ICI is introduced. The computational complexity for SEFDM is flexible based on variable implementation methods such as pruned and non-pruned FFT operations. The detailed analysis of complexity can be found in [46][58].

BER performance was measured and shown in Fig. 7.10. Two typically used FEC limits [157] are indicated in the figure to facilitate comparison of power penalties when SEFDM is used. It is clearly seen that by using α=0.8, the BER performance is close to that of the 4QAM modulated OFDM system. This proves that occupying the same bandwidth, the SEFDM system can transmit more data. For the SEFDM system with a higher level of bandwidth compression such as α=0.6 and therefore higher interference, the performance is degraded with an approximately 3 dB power penalty relative to OFDM, at all values measured for BER below 2×10^{-2} as shown in the figure. In addition, two systems with equal spectral efficiencies operating in the same bandwidth are evaluated. The first is an OFDM system with 8QAM modulated symbols and the second is a 4QAM SEFDM system of α=0.67. The results, also plotted in Fig. 7.10, clearly show that the α=0.67 SEFDM outperforms OFDM of equal spectral efficiency with 1 dB gain. It is also worth noting that the case of α=0.6 also outperforms the 8QAM OFDM in both spectral efficiency and BER performance. In other words, the above indicates that a lower order modulation format, with the advantage of increased bit rate, can replace a higher order one without compromising BER performance.

Due to unreliable transmission links, errors are introduced. Therefore, the effective bit rate, which is related to BER values, is smaller than the theoretical one. The effective gross bit rate is defined as the non-error bits per second that can be achieved including overhead (i.e. symbols used for channel estimation, syncronization), CP and coding redundancy bits. Effective gross bit rates are plotted for three different systems at different E_b/N_o values in Fig. 7.11 following the calculation as

$$R_d = \frac{1}{\alpha} \times (1 - BER) \times B \times log_2 O \tag{7.3}$$

where B is data bandwidth, BER is the bit error rate at a specific E_b/N_o value, $(1 - BER)$ indicates the probability of a non-error received bit stream and O is the constellation cardinality. For the 4QAM cases studied, Table 7.2 shows the SEFDM benefits in terms of spectral efficiencies and achievable bit rates, for different bandwidth

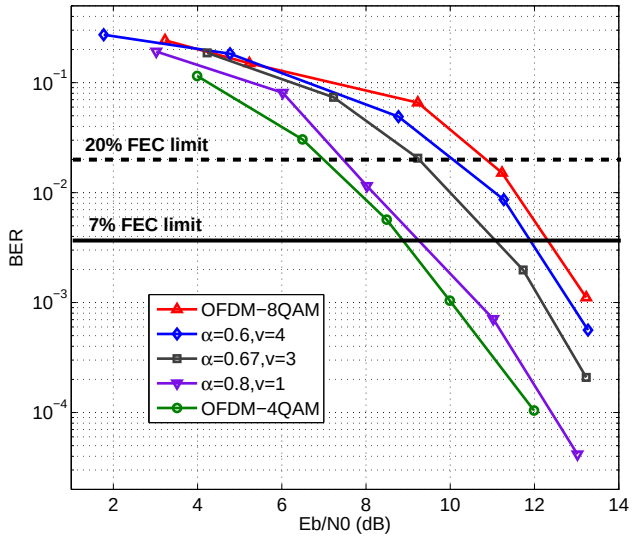

Figure 7.10: BER performance of SEFDM signals at 60 GHz mm-wave frequency through 3 meters wireless and 250 meters MMF fiber transmission with 4QAM symbols.

compression factors and associated number of sub-carriers. Although SEFDM shows slight performance degradation, it is apparent in Fig. 7.11 that the gross bit rates of 4QAM SEFDM with different bandwidth compression factors are higher than that of 4QAM OFDM. This is because compared to OFDM, in the SEFDM scenario, more sub-carriers are packed into a given bandwidth with a much closer sub-carrier spacing. For higher order modulation formats such as 8QAM, a spectral efficiency equivalent 4QAM shows a higher bit rate due to the 1 dB performance gain achieved in Fig. 7.10.

Table 7.2: Gross spectral efficiency and bit rate comparisons (4QAM-1.125 GHz bandwidth)

Parameter	**OFDM**	**SEFDM**		
α	1	0.8	0.67	0.6
Data sub-carriers	48	60	72	80
Spectral efficiency (bit/s/Hz)	2.0	2.5	3.0	3.3
Bit rate (Gbit/s)	2.25	2.80	3.38	3.75

In addition, net bit rates are also illustrated in Fig. 7.11 for SEFDM and OFDM after removing the CP and coding redundancy bits. We note that the pilot symbol and

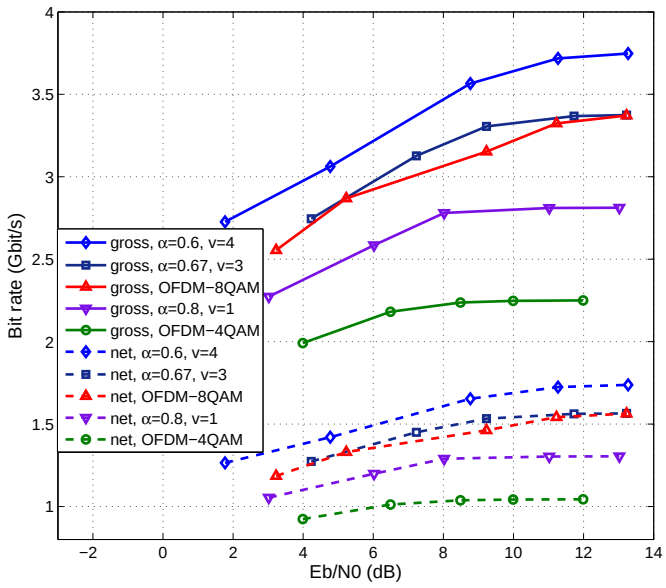

Figure 7.11: Gross and net bit rates of SEFDM signals at 60 GHz mm-wave through 3 meters wireless and 250 meters MMF fiber transmission with 4QAM symbols.

the timing sequence are used only once at the beginning of a data stream and therefore have minimal contribution to the size of the overhead and a negligible effect on the calculation of net bit rate.

7.7 Conclusions

The low frequency such as LTE frequency offers limited data rate due to the lack of bandwidth at low frequency. In order to achieve higher data rate, a wider bandwidth has to be explored. This is the motivation to use the millimeter wave band since a wide unlicensed spectrum exists. The millimeter wave frequency offers many other benefits such as secure communications, reduced co-channel interference, improved frequency reuse feasibility and MIMO antenna deployment. Meanwhile, the millimeter wave frequency also brings challenges such as complicated DAC/ADC design, strict requirement of coherence time and frequency, blockage and alignment sensitivity.

The deployment of millimeter wave transmission imposes challenges due to its high transmission loss. Therefore, a large number of radio access points are needed which complicates the entire system design. RoF is considered to be a solution that combines both optical and wireless benefits. Thus, the hybrid RoF can jointly deal with challenges from optical fiber and wireless channels. It has already been proved that SEFDM signals can save both optical and wireless bandwidths. In order to solve part of the aforementioned millimeter wave transmission issues and maintain its benefits, SEFDM signals are practically studied in the RoF scenario due to its benefits such as less sensitivity to frequency offset, lower PAPR and released requirement of DAC/ADC.

Experimental results obtained from a world first 60 GHz SEFDM testbed demonstrate the efficacy of SEFDM through showing that the bit rate can be increased whilst maintaining the same bandwidth, at the expense of some power penalty. For a 4QAM OFDM system, occupying 1.125 GHz bandwidth, the gross bit rate can reach 2.25 Gbit/s at E_b/N_o=12 dB, while, for similar E_b/N_o values in an SEFDM system, compressing the sub-carrier spacing by 20%, it can achieve 2.8 Gbit/s. With further bandwidth compression of 40%, results show that up to 3.75 Gbit/s can be achieved at the expense of a loss (around 3 dB) in error performance and additional computational complexity. In addition, the two spectral efficiency equivalent systems 4QAM SEFDM and 8QAM OFDM are experimentally demonstrated. The SEFDM system is shown to outperform the 8QAM OFDM with 1 dB performance gain. All experimental results were obtained by testing signals over a wireless channel using a pair of antennas operating in the 60 GHz mm-wave band.

Chapter 8

Low Complexity SEFDM Design: Precoding and Self Interference Cancellation

8.1 Introduction

High throughput enhanced mobile broadband (eMBB) service is one requirement for future wireless networks. In future 5G networks, a thousand-fold wireless traffic increase is predicted from 2020, originating from over 50 billion connected devices [16]. Such massive device connection and communication, termed massive machine-type communication (mMTC), will be associated with the continuously emerging IoT. Currently, 80% of IoT applications require terminals with low power consumption, with an average battery life expectancy reaching 10 years [206].

Hence, IoT devices have to be able to set up a reliable communication with simplified signal processing. Thus, their batteries lifetime would be extended. The other key requirement for future 5G networks is that it should be able to provide a very low level of latency communication link. However, the complicated signal processing at the receiver could add delays significantly. To sum up, an increase of data rates and a

ultra-reliable and low-latency communication (URLLC) service are equally important for the next generation networks.

To overcome the aforementioned challenges, two solutions are provided; one is to gather distributed complicated signal processing work together in a form of cloud-radio access networks (C-RAN) [207]; the other one is to design new algorithms that can simplify receiver side signal processing. This chapter will investigate the second solution that signals would be modified at the transmitter and relax the receiver side complexity. This is an efficient power saving technique for down-link transmission since a BS can handle complicated signal processing while the battery use in a mobile terminal is limited. In addition, latency would be reduced as well since additional hardware in a BS can be used.

A simple precoding scheme such as single-carrier-frequency division multiple access (SC-FDMA) have been standardized in 4G LTE. There are three distinct characteristics of SC-FDMA; it is a multiple access technique; it is a single carrier technique and it is a precoded technique. The reason for the 'single carrier' is that SC-FDMA carries data symbols over a group of sub-carriers rather than individual sub-carriers in OFDM. In MIMO scenarios, linear precoding schemes based on channel inversion show the least complexity while the performance is far from optimal. Their non-linear substitutes such as dirty paper coding (DPC) [208], VP [209] and Tomlinson-Harashima precoding (THP) [210] can significantly improve the performance. However, their complexity is much higher than the linear ones.

In this chapter, two specially designed schemes are investigated for SEFDM. The first one is based on repetition coding in which two identical symbols will be modulated on two adjacent sub-carriers with opposite weighting factors such as '+1' and '-1'. The other one is to distribute signal power based on eigenvalue decomposition. Some sub-carriers are associated with high eigenvalues indicating high CIR while others will have low CIR. The scheme is to transmit information data on those high CIR sub-carriers.

8.2 Precoding: Power Redistribution

The precoding makes use of eigenvalue decomposition investigated for SEFDM in [37], which would redistribute the power on each sub-carrier after symbol demodulation at the receiver. Depending on the percentage of bandwidth compression, some sub-carriers would experience power enhancement while others would experience power attenuation. The original precoding work in [37] aimed to transmit data on both strong sub-carriers (i.e. high sub-carrier to interference ratio (ScIR)) and weak sub-carriers (i.e. low ScIR). As mentioned in [37], simple detectors such as ZF can be applied for the strong channels while high performance detectors such as ML are used for the weak channels. However, this approach requires the increase of complexity at the receiver, which does not satisfy the initial purpose of precoding. It should be noted that the approach of [37] is only applicable to small size systems. With the increase of system size, the detection for the weak channels becomes exponentially complicated. This section concerns the simplification and optimization of the precoding scheme, in a static frequency selective channel.

8.2.1 Principle

Precoding concept can make use of ICI information at the transmitter and simplify the design of the receiver. As mentioned in section 2.5, the correlation matrix $\mathbf{C}$ characterizes the interference among the sub-carriers. The matrix can be diagonalized using eigenvalue [1] decomposition [211] as

$$\mathbf{C} = \mathbf{U}\mathbf{\Lambda}\mathbf{U}^{*} \tag{8.1}$$

where $\mathbf{U}$ is a unitary matrix and $\mathbf{U}^{*}$ is its conjugate transpose with the property as $\mathbf{U}^{*}\mathbf{U} = \mathbf{I}$ where $\mathbf{I}$ is an identity matrix and $\mathbf{\Lambda}$ is a diagonal matrix that contains the eigenvalues $diagonal(\mathbf{\Lambda}) = [\lambda_1, \lambda_2, ..., \lambda_N]$ of $\mathbf{C}$.

[1] An eigenvalue and eigenvector of a square matrix $\mathbf{A}$ are a scalar λ and a nonzero vector x so that $\mathbf{A}x = \sigma x$.

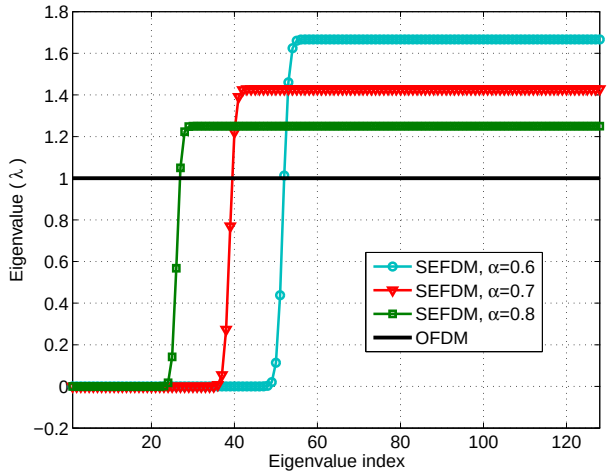

Figure 8.1: Eigenvalue versus eigenvalue index. A total number of N=128 sub-carriers are tested.

The eigenvalues, calculated according to (8.1), are illustrated in Fig. 8.1 where OFDM and SEFDM systems are compared. It is noted that for an OFDM system with N sub-carriers, all eigenvalues have equal amplitude, which is equal to 'one'. For SEFDM systems, αN of the eigenvalues will have values greater than 'one' while the remaining $(1-\alpha)N$ eigenvalues can take very small values. It can be inferred that SEFDM detection systems that rely on matrix inversion will result in poor BER performance due to those small eigenvalues.

The main idea of the precoding system, discussed here, is to recover a signal vector in which signal power is redistributed according to the eigenvalues. Small eigenvalues, therefore low ScIR, indicate weak channels and high eigenvalues, therefore high ScIR, indicate strong channels. Therefore, the precoding method leads to high performance for the strong channels while it lowers the performance for the weak channels.

The original transmitted symbols vector S is multiplied by the unitary matrix $\mathbf{U}$. Thus, the precoded symbols vector $\bar{S}$ is expressed as

$$\bar{S} = \mathbf{U}S \tag{8.2}$$

where the power of the precoded symbols vector is calculated as

$$\|\bar{S}\|^2 = S^*\mathbf{U}^*\mathbf{U}S = \|S\|^2 \tag{8.3}$$

where S^* is conjugate transpose of S, showing that the total power of the transmitted symbols is maintained after multiplying with a unitary matrix $\mathbf{U}$. Then, the precoded symbols are modulated using IFFT [46] as

$$X = \mathbf{F}\bar{S} \tag{8.4}$$

After transmitting X through an AWGN channel, denoted by Z, the received signal is expressed as

$$Y = X + Z \tag{8.5}$$

After demodulation, at the receiver, using an FFT [46], the collected statistic vector R is derived as

$$R = \mathbf{F}^*(X + Z) = \mathbf{F}^*\mathbf{F}\bar{S} + \mathbf{F}^*Z = \mathbf{C}\bar{S} + Z_{\mathbf{F}^*} \tag{8.6}$$

where R is an N-dimensional vector of demodulated symbols, $Z_{\mathbf{F}^*}$ is the AWGN correlated with the conjugate sub-carriers.

Removal of precoding is done in a de-precoding stage, which is effected by left multiplying (8.6) with $\mathbf{U}^*$, a new vector $\bar{R} = [\bar{r}_1, \bar{r}_2, ..., \bar{r}_N]$ is obtained as

$$\begin{aligned} \bar{R} &= \mathbf{U}^*R \\ &= \mathbf{U}^*\mathbf{C}\bar{S} + \mathbf{U}^*Z_{\mathbf{F}^*} \\ &= \Lambda\mathbf{U}^*\bar{S} + Z_{\mathbf{U}^*} \\ &= \Lambda S + Z_{\mathbf{U}^*} \end{aligned} \tag{8.7}$$

Equation (8.7) indicates that the power is re-distributed on each M-QAM symbols S based on the eigenvalues $diagonal(\mathbf{\Lambda}) = [\lambda_1, \lambda_2, ..., \lambda_N]$. Then vector scaling is operated

as

$$\hat{s}_i = \bar{r}_i/\lambda_i \tag{8.8}$$

where $i \in [(1-\alpha) \times N + 1, N]$. It is inferred that the scaling operation in (8.8) would enchance the noise effect on the sub-carriers associated with small eigenvalues while it lowers the noise effect on the sub-carriers associated with high eigenvalues. Thus, the first $(1-\alpha) \times N$ sub-carriers result in low performance while the rest $\alpha \times N$ sub-carriers lead to better performance. In this work, the $\alpha \times N$ sub-carriers carry user data while redundant data for precoding is modulated on the $(1-\alpha) \times N$ sub-carriers.

Since a portion of sub-carriers are effectively used for user data, symbol rate is reduced by a factor of $(1-\alpha)$, but since the bandwidth is compressed by a factor of $(1-\alpha)$, the spectral efficiency is not changed. In order to have a fair comparison where equal occupied bandwidth is used for SEFDM and OFDM, a higher number of sub-carriers are aggregated in the SEFDM system leading to an improved symbol rate.

8.2.2 Design Verification and Testing

The simulation setup of the joint waveform and precoding system is shown in Fig. 8.2. In this section, signals are tested over the same bandwidth. Therefore, the total number of sub-carriers is $\frac{N}{\alpha}$, which is inversely proportional to the bandwidth compression factor. At the transmitter, a bit stream is mapped onto a symbol stream in the mapping block based on a specific modulation format (e.g. M-QAM). After S/P conversion, multiple symbol blocks $\tilde{S}$ are obtained with each consisting of N M-QAM symbols. $(\frac{1}{\alpha}-1)\times N$ redundant symbols, of the same modulation format of the data, are randomly generated and then inserted at the beginning of each symbol block $\tilde{S}$ leading to multiple symbol blocks S in which $\frac{N}{\alpha}$ M-QAM symbols are aggregated. The precoding follows the operations described in section 8.2.1. A guard band is added on both sides of each precoded symbol before the IFFT [46] for oversampling and protection purposes. The modulated signal, after CP addition, is then P/S converted and finally delivered through a channel.

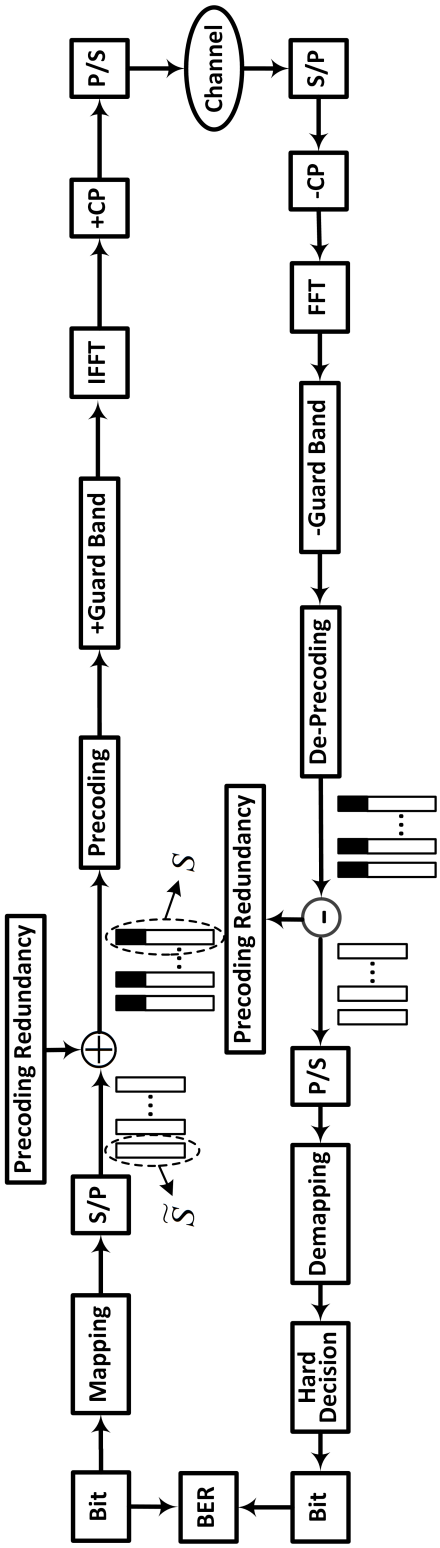

Figure 8.2: Simulation block diagram of the precoding scheme of SEFDM.

At the receiver, the S/P converted signal is CP removed and demodulated using a specially designed FFT algorithm [46] followed by guard band removal. The de-precoding follows the operations in section 8.2.1 where matrix multiplication and vector scaling operation are required. The precoding redundancy is removed to recover the information data. After P/S conversion, demapping and hard decision processing, the receiver bit stream is recovered. Finally, BER will be calculated by comparing the receiver bit stream to that of the transmitter.

Table 8.1: Simulation System Specifications

Parameters	**OFDM**	**SEFDM**
Sampling rate (MHz)	30.72	30.72
Bandwidth (MHz)	18	18
FFT size	2048	2048
Symbol rate per sub-carrier (kS/s)	15	15
Sub-carrier spacing (kHz)	15	15×α
Bandwidth compression factor α	1	0.8, 0.7, 0.6
Guard band sub-carriers	848	548, 334, 48
Number of data sub-carriers	1200	1500, 1714, 2000
Modulation scheme (M-QAM)	64, 16, 4	128, 64, 32, 16, 8, 4
Precoding redundancy	0	300, 514, 800
Effective symbol rate (MS/s)	18	18

The simulation parameters for both OFDM and precoded SEFDM systems are shown in Table 8.1. In this work, and without loss of generality, SEFDM systems are designed to be compatible with existing LTE OFDM systems [1]. By reconfiguring the guard band sub-carriers length (e.g. 548 for α=0.8, 334 for α=0.7 and 48 for α=0.6), three SEFDM systems of equal bandwidth are studied. LTE defined modulation formats such as 64QAM, 16QAM and 4QAM are tested for OFDM systems. For the purpose of fair and sufficient comparisons, various modulation formats ranging from 4QAM to 128QAM are evaluated for SEFDM systems.

At first, PAPR is evaluated for both OFDM and SEFDM signals. The complementary cumulative distribution function (CCDF) is used as a way to analyze the probability of PAPR being higher than a predefined threshold γ. Fig. 8.3 presents

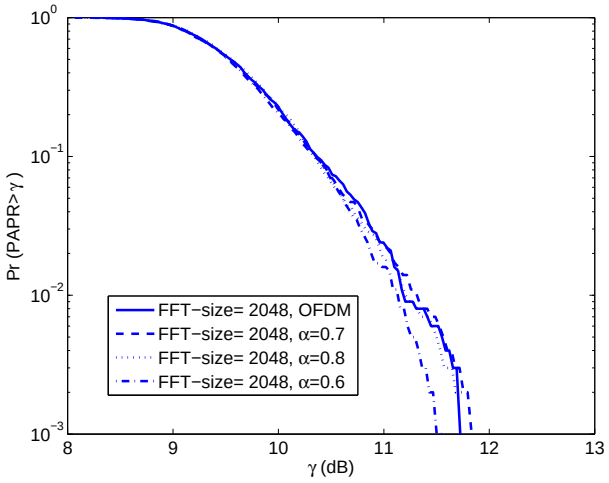

Figure 8.3: CCDF of PAPR for precoded SEFDM and OFDM signals modulated with 4QAM symbols.

four systems, one is OFDM and the other three are SEFDM with various α values. Results indicate that although more sub-carriers are aggregated in SEFDM systems, the probability of PAPR exceeding the threshold γ is close or even lower than that of OFDM.

8.2.2.1 AWGN Scenario

The BER comparisons of the conventional OFDM and the precoded SEFDM are investigated by considering Fig. 8.4, where the effect of different bandwidth compression factors of the precoded SEFDM is evaluated. It is worth noting that the E_b values shown in the figure are for effective bit energies, averaged over the total number of bits, which include the redundancy bits. For α=0.8, the BER performance is approximately 1 dB better than the conventional OFDM, for all the modulation formats studied. Reducing the bandwidth compression factor α to 0.7, the BER curve moves away from the OFDM one with further 0.5 dB improvement. With further reduction of α to 0.6, the performance is further improved and 2 dB gain is achieved compared with the OFDM result. It is concluded that by using the same modulation format, therefore

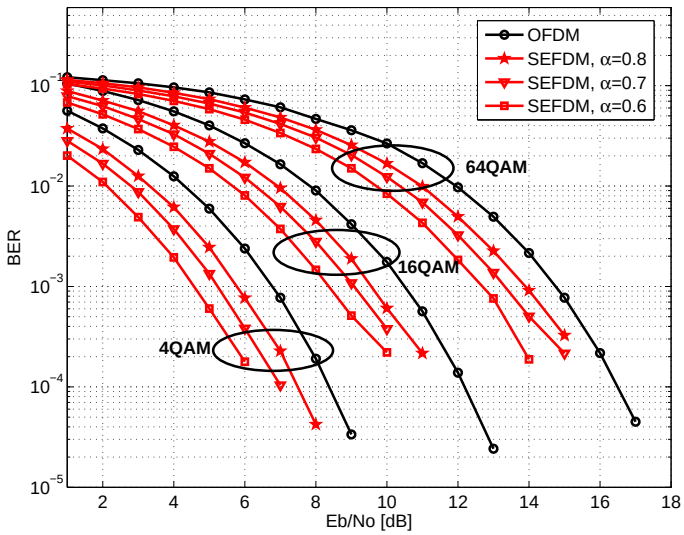

Figure 8.4: BER versus effective E_b/N_o comparisons in AWGN channel under various bandwidth compression factors.

the same spectral efficiency, the precoded SEFDM outperforms OFDM with flexible performance gains, which are related to the values of bandwidth compression factor α. This counterintuitive result of improvement of the error performance with reduction of alpha is due to the fact that lower values of alpha require higher levels of precoding and a higher number of subcarriers, each modulated with symbols that have the same energy per symbol before precoding and different powers after precoding but still resulting in a transmitted signal power that is inversely proportional to α. Therefore the apparent improvement in performance of 8.4 comes at the expense of larger FFT sizes and smaller guard band sub-carriers. Finding an optimum value of alpha that trades transmission power versus error performance is an interesting research question and its study is proposed as a subject of future investigation.

The benefit of the precoded SEFDM in terms of data rate improvement is presented in Fig. 8.5 where three additional modulation formats; 128QAM, 32QAM and 8QAM are tested. It is apparent that the 8QAM modulated SEFDM signal has close performance to that of the 4QAM modulated OFDM signal. Since each of the 8QAM symbol

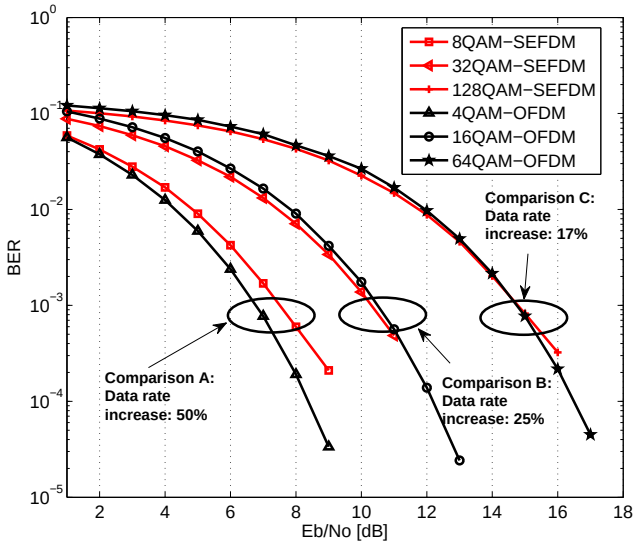

Figure 8.5: Bit rate comparisons of α=0.6 precoded SEFDM and OFDM in the condition of various modulation formats.

has 3 bits and each 4QAM symbol has 2 bits, therefore, the data rate is improved by $50\% = (3/2 - 1) \times 100\%$. With the increase of modulation format order, the data rate improvement is still evident in SEFDM but with reduced benefits. For example, comparing the 32QAM modulated SEFDM signal and the 16QAM modulated OFDM signal, the data rate is increased by $25\% = (5/4 - 1) \times 100\%$. Furthermore, with higher modulation formats such as 128QAM modulated SEFDM signal and 64QAM modulated OFDM signal, the percentage is reduced to around $17\% = (7/6 - 1) \times 100\%$. To summarize, the tested precoded SEFDM system can achieve the same performance compared to an OFDM system while achieving increased data rates, which are jointly set by modulation formats and bandwidth compression factors.

8.2.2.2 Multipath Propagation Scenario

In this section, a perfect CSI is assumed at the receivers for both OFDM and SEFDM in order to mitigate the effect of channel estimation. For detailed description of a time-domain channel estimation algorithm of SEFDM, readers are referred to the work

in [77]. This section will briefly present the principle of the time-domain channel equalization for SEFDM and frequency-domain channel equalization for OFDM.

Considering a joint multipath and AWGN channel, the receiver side distorted signal after CP removal [77] is expressed as

$$Y_c = \mathbf{H_c}X + Z = \mathbf{H_c}\mathbf{F}S + Z \tag{8.9}$$

where Y_c is a vector of length Q. The channel $\mathbf{H_c}$ is a $Q \times Q$ circulant matrix, which is a truncated (i.e. removing CP effect) version of a channel Toeplitz matrix $\mathbf{H}$ shown in [77]. After demodulation, which is effectively a multiplication of Y_c with the conjugate sub-carrier matrix $\mathbf{F}^*$, the signal vector is expressed as

$$R = \mathbf{F}^*\mathbf{H_c}\mathbf{F}S + \mathbf{F}^*Z = \mathbf{G}S + Z_{\mathbf{F}^*}. \tag{8.10}$$

For orthogonal multicarrier signals (e.g. OFDM), $\mathbf{G}$ is a diagonal matrix. Thus, the channel can be estimated and compensated through a one tap frequency-domain equalizer. However, this is not the case in SEFDM since there are off-diagonal elements in the matrix $\mathbf{G}$. This introduces both multiplicative (diagonal elements) and additive (off-diagonal elements) distortions. Therefore, OFDM and SEFDM have different solutions to compensate for channel effects.

For OFDM, channel equalization with perfect CSI is operated as

$$\hat{s}_i = r_i/g_i, i = 0, 1, ..., N-1 \tag{8.11}$$

where $\hat{s}_i$ is the i^{th} element of estimate $\hat{S}$, r_i is the i^{th} element of R and g_i is the i^{th} element of $diagonal(\mathbf{G})$.

For SEFDM, the known channel matrix $\mathbf{H_c}$ is inverted to give $\mathbf{H_c^{-1}}$ and used to equalize the distorted SEFDM symbols in the time domain in (8.9) as

$$\begin{aligned} Y_{eq} = \mathbf{H_c^{-1}} Y_c &= \mathbf{H_c^{-1}} \mathbf{H_c} \mathbf{F} S + \mathbf{H_c^{-1}} Z \\ &= \mathbf{F} S + Z_{\mathbf{H_c^{-1}}} \end{aligned} \tag{8.12}$$

Then, following the operations in (8.6), (8.7) and (8.8), SEFDM symbols will be recovered.

To test this, a static frequency selective channel, obtained from [147], is used in the simulation as

$$\begin{aligned} h(t) = 0.8765\delta(t) - 0.2279\delta(t - T_s) + 0.1315\delta(t - 4T_s) \\ -0.4032e^{\frac{j\pi}{2}}\delta(t - 7T_s) \end{aligned} \tag{8.13}$$

where T_s is the sampling period, which can be calculated according to the system specifications in Table 8.1. The spectra of OFDM and precoded SEFDM signals distorted by the static channel are shown in Fig. 8.6 where the occupied bandwidth is 18 MHz for both cases. Although both spectra have the same frequency response, the OFDM spectrum aggregates N sub-carriers while the SEFDM one aggregates $\frac{N}{\alpha}$ sub-carriers.

For the OFDM signals, after symbol mapping, each symbol is modulated on a separate sub-carrier. In the precoded SEFDM signals, after symbol mapping, the precoding operation will spread each symbol over multiple sub-carriers, which indicates multiple sub-carriers will carry one symbol. Hence, in a frequency selective channel, the precoded SEFDM will offer improved frequency diversity.

In order to explore fully the benefits of precoded SEFDM in the static frequency selective channel, various modulation formats ranging from 4QAM to 128QAM are tested with results showing in Fig. 8.7. For the same modulation formats, it is clear that the error performance of precoded SEFDM signals shows several dBs of advantage compared to that of the OFDM signals. When a precoded SEFDM signal is used, ap-

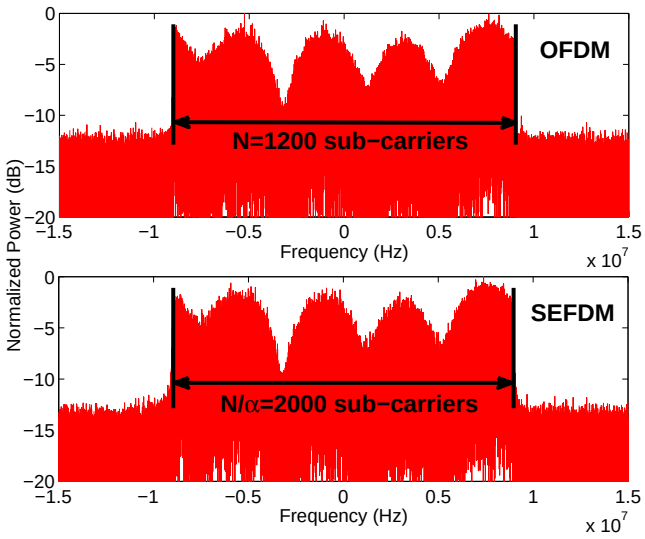

Figure 8.6: Spectra of OFDM and α=0.6 SEFDM signals after the static frequency selective channel. Occupying the same bandwidth, a total number of N=1200 data sub-carriers are aggregated for OFDM and N/α=2000 data sub-carriers for SEFDM.

plying a higher modulation format leads to almost identical error performance at low Eb/No and much better performance at high Eb/No. This is due to the effect of pre-coding leading to BER curves slope difference where the slope of the SEFDM curves is greater than that of the OFDM curves. One achievement is the comparison of 128QAM SEFDM and 16QAM OFDM. It is noted that below Eb/No=19dB, the OFDM system outperforms the SEFDM system while beyond Eb/No=19dB, the 128QAM SEFDM starts performing better than the 16QAM OFDM one.

The reason for such performance improvement is attributed to the fact that this joint compressed waveform and precoding scheme provides frequency diversity in frequency selective channels, since not only channel effects are spread over all sub-carriers, but also only a portion (i.e. $(100 \times \alpha)\%$) of sub-carriers carry information data and these are the ones benefitting most from the precoding and eigenvalue decomposition process.

The precoding technique can achieve better performance since it can exploit the frequency diversity. In realistic communication systems, Turbo error correcting codes are commonly used due to their powerful error correction capability over multipath

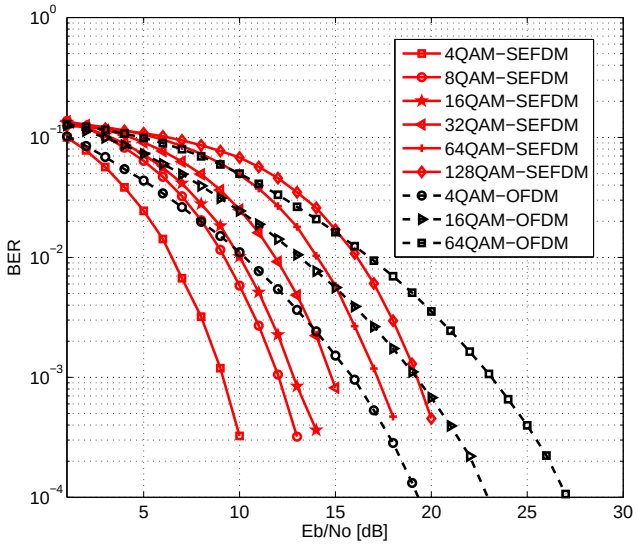

Figure 8.7: BER comparisons of α=0.6 precoded SEFDM signals and OFDM signals in a static frequency selective channel.

channels. Fig. 8.8 further explores performance in a Turbo coding scenario to verify that the precoding technique can still have advantages when used in conjunction with Turbo coding.

For the simulation, a rate 1/3 parallel concatenated Turbo code with polynomials $G_1(D) = 1+D^2+D^3$ and $G_2(D) = 1+D+D^3$, derived from LTE [212], are used for both cases; the typical OFDM and precoded SEFDM. Both systems are tested in the same frequency selective channel scenario used to obtain the results of the uncoded systems of Fig. 8.7. The 64QAM modulated OFDM signals with three and eight iterations are evaluated. It is evident that both have the same error performance. This indicates that three iterations are sufficient to achieve optimal BER performance and increasing the number of iterations will not have any added benefit. Meanwhile, the precoded SEFDM signal with the same modulation scheme is tested using also three and eight iterations. The two tested SEFDM cases perform better than the typical OFDM cases by several dBs. Three iterations are sufficient to obtain better performance relative to the typical OFDM cases and further performance gain can be achieved for eight

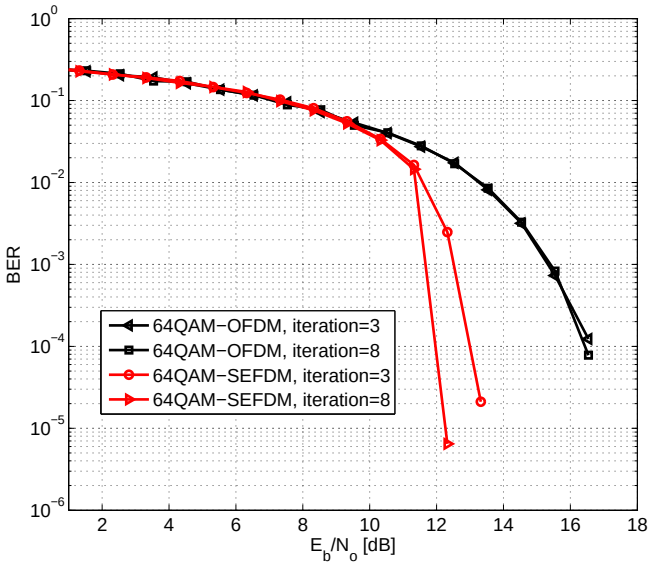

Figure 8.8: Turbo coded BER comparisons of α=0.6 precoded SEFDM signals and OFDM signals in a static frequency selective channel.

iterations. It is inferred from the above simulations that the use of Turbo coding can improve the performance of both systems and the performance gain achieved by the precoded SEFDM signal is still maintained.

8.2.3 Applications in Copper Access Networks

The requirement of high data rate service accelerates the development of last mile access techniques. Fiber networks can support very high throughput data services and many deployment models [213] such as FTTH, fiber to the building (FTTB), fiber to the cabinet (FTTC) and fiber to the distribution point (FTTdp) are being used today. In addition, since the 1990s, the rapid deployment of copper access networks motivates digital subscriber line (DSL) to be a successful fixed broadband access technique. There are approximately 300 million legacy DSL lines [214] deployed worldwide. The efficient use of the existing resources would significantly cut the deployment cost and time to market. The FTTH is a desired approach to serve high data rates service to users. However, the construction cost is significantly high since the fiber has to be connected

to each house. In order to evolve smoothly to FTTH, a cost efficient and fast time-to-market approach is "fiber-in copper-out". Two key hybrid fiber-copper architectures have been summarized in [215] where solutions include FTTC with vectoring very-high-bit-rate digital subscriber line 2 (VDSL2) and FTTdp [216] with G.fast (fast access to subscriber terminals), developed by British Telecommunications and reported in [217].

Among DSL techniques, VDSL2 has been widely used for a decade due to its high data rate and bandwidth, which is up to 30 MHz. However, the main issue is the crosstalk between twisted pairs copper lines. According to research results in [213][215], longer copper length and higher frequency result in higher crosstalk interference. In addition, the Huawei report [214] indicates that a larger number of copper lines also cause higher crosstalk. The "reach vs. rate" comparisons of different copper access techniques have been studied in the Huawei report [214] and are reproduced in Fig. 8.9. It is clearly seen that G.fast expands the occupied bandwidth to achieve higher data rates at the cost of reduced transmission distance.

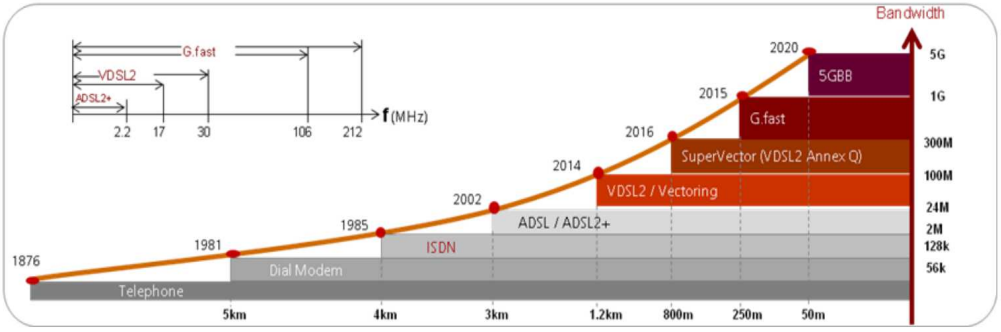

Figure 8.9: Development of copper access techniques. This figure is reused from a Huawei technical report [214].

The crosstalk is divided into near-end crosstalk (NEXT) and far-end crosstalk (FEXT). The NEXT is the interference between downstream signals and upstream signals of different twisted pairs while FEXT is the interference between downstream signals of different twisted pairs or between upstream signals of different twisted pairs. The VDSL2 is implemented based on the frequency division duplexing (FDD) scheme

where upstream signals and downstream signals use different frequencies. Thus, the NEXT can be avoided to some extent. However, the FEXT cannot be eliminated since downstream signals of different pairs or upstream signals of different pairs occupy the same frequency band. To deal with the issue, vectoring techniques [214] are considered. Unlike the FDD used in VDSL2, G.fast employs time division duplexing (TDD) scheme [213] to simplify the analog front-end and adjust the ratio between downstream and upstream rates. Since both the downstream and upstream signals use the same frequency, the NEXT have to be avoided by fixing the upstream/downstream ratio for all twisted pairs [213].

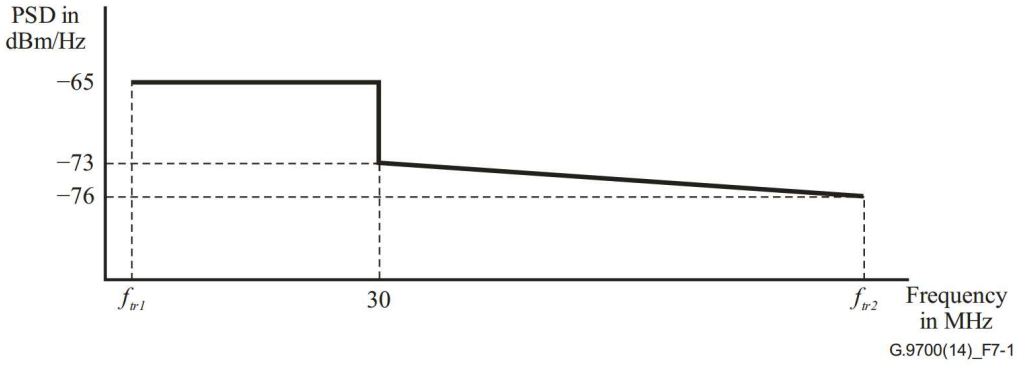

Figure 8.10: In-band limit PSD mask for 106 MHz profile. f_{tr1}=2 MHz, f_{tr2}=106 MHz and maximum aggregate transmit power = +4 dBm. The PSD figure is reused from ITU-T G.9700.

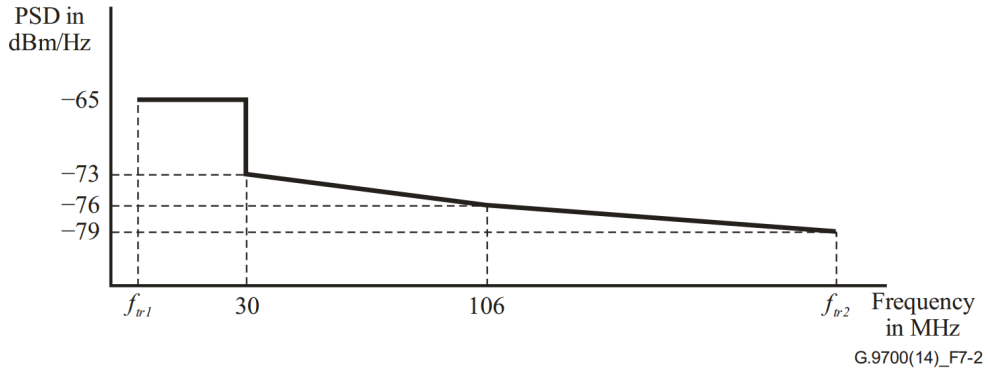

Figure 8.11: In-band limit PSD mask for 212 MHz profile. f_{tr1}=2 MHz, f_{tr2}=212 MHz. The PSD figure is reused from ITU-T G.9700.

The detailed information of G.fast is referred to [217]. The main work here is to propose an SEFDM system deployment idea that can bring benefits to copper access networks. The power spectral density (PSD) masks of G.fast are specified in [218] where two spectral profiles are shown in Fig. 8.10 and Fig. 8.11, respectively. It is clearly seen that for both cases the PSD is flat ranging from 2 MHz to 30 MHz. Beyond 30 MHz, the PSD is reduced to -76 dBm/Hz at 106 MHz and -79 dBm/Hz at 212 MHz. Therefore, the special spectral mask motivates the use of SEFDM signals by compressing signal bandwidth below 30 MHz. Assume an OFDM signal that occupies a 35 MHz bandwidth ranging from 2 MHz to 37 MHz. Since 37 MHz is beyond 30 MHz, part of the OFDM signal would be distorted. However, compressing bandwidth by 20%, the new signal would be within the 30 MHz spectral edge. Therefore, the quality of the signal maybe improved by avoiding the frequency range associated with low SNR.

8.3 Self Interference Cancellation

The self interference cancellation scheme was firstly proposed in [219] for the purpose of mitigating frequency offset in an OFDM system. The general principle of the cancellation scheme is to modulate the same symbol onto adjacent two sub-carriers (or a group of more than two sub-carriers) with opposite weighting coefficients (e.g. '+1' and '-1') in order to minimize the ICI caused by the channel frequency errors. Thus, the ICI can be self cancelled at the transmitter. At the receiver, using a linear combination scheme, ICI could be further removed. An SEFDM signal has a similar effect of OFDM frequency offset since sub-carriers are packed non-orthogonally intentionally. Therefore, the cancellation scheme may be applicable for SEFDM systems.

It has been shown in Fig. 2.3, Fig. 2.4 and Fig. 2.5 that the desired SEFDM signal power is dominant while with fluctuating interference power. The ICI components are relatively stable. Thus, modulating the same complex symbol onto adjacent two sub-carriers (or a group of more than two sub-carriers) with opposite weighting

coefficients could minimize the ICI effect since ICI signals from adjacent sub-carriers will be mutually cancelled.

8.3.1 Principle and Performance

The basic idea is to arrange symbols as $S(1) = -S(0)$, $S(3) = -S(2)$,..., $S(N-1) = -S(N-2)$, thus the new version of the first demodulated symbol is given as

$$R'(0) = \sum_{k=0\&k=even}^{N-2} S(k)[\mathbf{C}(0,k) - \mathbf{C}(0,k+1)] + Z_{\mathbf{F}^*}(0) \tag{8.14}$$

where the ICI component in this case is expressed as

$$\mathbf{C}'(0,k) = \mathbf{C}(0,k) - \mathbf{C}(0,k+1) \tag{8.15}$$

In addition, the second demodulated symbol is defined in (8.16) with its ICI component in (8.17).

$$R'(1) = \sum_{k=0\&k=even}^{N-2} S(k)[\mathbf{C}(1,k) - \mathbf{C}(1,k+1)] + Z_{\mathbf{F}^*}(1) \tag{8.16}$$

$$\mathbf{C}'(1,k) = \mathbf{C}(1,k) - \mathbf{C}(1,k+1) \tag{8.17}$$

Focusing on the first symbol, a new CIR is expressed as

$$CIR = \frac{|\mathbf{C}(0,0) - \mathbf{C}(0,1)|^2}{\sum_{k=2\&k=even}^{N-2} |\mathbf{C}(0,k) - \mathbf{C}(0,k+1)|^2} \tag{8.18}$$

The aforementioned ICI cancellation is operated at the transmitter and it is noted as 'Tx-cancellation'. In order to further improve the performance, a joint transmitter and receiver ICI cancellation scheme, noted as 'Tx-Rx-cancellation', is presented in the following. The solution is to add weighting factors in front of each demodulated symbol. Specifically, the data on the k^{th} sub-carrier is multiplied by '+1' while the data on the $(k+1)^{th}$ sub-carrier is multiplied by '-1'. Then the summation of them

results in a new expression as

$$\begin{aligned} R''(0) &= R'(0) - R'(1) \\ &= \sum_{k=0\&k=even}^{N-2} S(k)[\mathbf{C}(0,k) - \mathbf{C}(0,k+1) - \mathbf{C}(1,k) + \mathbf{C}(1,k+1)] + Z'_{\mathbf{F}^*}(0) \end{aligned} \tag{8.19}$$

where $Z'_{\mathbf{F}^*}(0) = Z_{\mathbf{F}^*}(0) - Z_{\mathbf{F}^*}(1)$. Since $\mathbf{C}$ is a Toeplitz matrix, therefore $\mathbf{C}(0,k)$=$\mathbf{C}(1,k+1)$. A new expression is given as

$$R''(0) = \sum_{k=0\&k=even}^{N-2} S(k)[2\mathbf{C}(0,k) - \mathbf{C}(0,k+1) - \mathbf{C}(1,k)] + Z'_{\mathbf{F}^*}(0) \tag{8.20}$$

where a new ICI component is $\mathbf{C}''(0,k) = 2\mathbf{C}(0,k) - \mathbf{C}(0,k+1) - \mathbf{C}(1,k)$ and a new CIR expression is defined as

$$CIR = \frac{|2\mathbf{C}(0,0) - \mathbf{C}(0,1) - \mathbf{C}(1,0)|^2}{\sum_{k=2\&k=even}^{N-2} |2\mathbf{C}(0,k) - \mathbf{C}(0,k+1) - \mathbf{C}(1,k)|^2} \tag{8.21}$$

Two ICI components have been studied so far. The comparison of them is included in Fig. 8.12 and Fig. 8.13. Two different bandwidth compression factors such as α=0.8 and α=0.6 are tested and each figure includes three different self cancellation schemes.

In Fig. 8.12, when n=0, $|\mathbf{C}(0,n)|$ indicates desired signal while ICI components are conditioned by $n > 0$. It is evident that the Tx-Rx-cancellation scheme has the highest desired signal power and the Tx-cancellation one is in the middle and the standard SEFDM is the lowest one. In terms of ICI components, which remove the n=0 component, they all have similar ICI signal powers. It should be noted that the Tx-Rx-cancellation scheme and the Tx-cancellation scheme only take even values, and the number of the interference signals is reduced to half compared to the standard SEFDM one leading to the improved CIR performance of Fig. 8.14. Therefore the total ICI signal power is much smaller than that in a standard SEFDM system since the number of ICI signals is reduced.

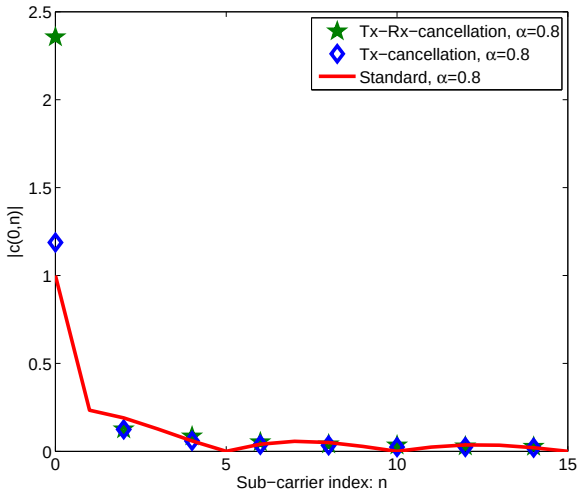

Figure 8.12: Comparisons of three different systems in terms of desired and undesired power contributions to the first demodulated symbol $R(0)$, for α=0.8.

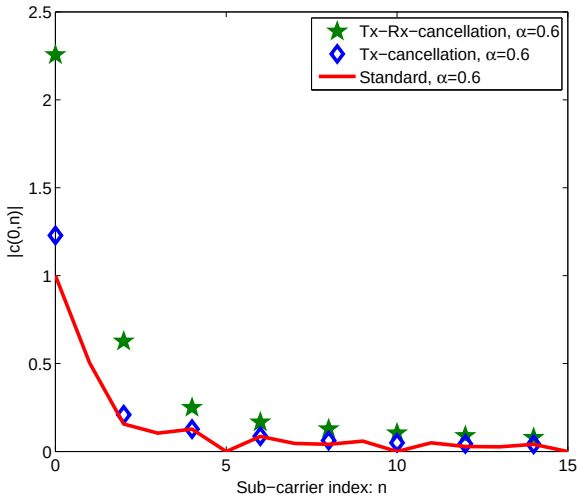

Figure 8.13: Comparisons of three different systems in terms of desired and undesired power contributions to the first demodulated symbol $R(0)$, for α=0.6.

In addition, in Fig. 8.13, a smaller bandwidth compression factor α is used and therefore a different result is observed. The desired signal power follows the conclusion in Fig. 8.12 while the ICI signal power is different among three different self interference

cancellation schemes. It is apparent that the Tx-cancellation scheme shows a similar interference power with the standard one while the Tx-Rx-cancellation scheme presents a higher interference power such as the second star notation.

Finally, the different desired and undesired power contributions are studied in the form of CIR. The standard SEFDM is included as a reference. Both the Tx cancellation and the Tx-Rx cancellation schemes show improved CIR relative to the standard SEFDM one. The Tx-Rx cancellation one offers more than two orders of magnitude CIR improvement within the range from α=0.7 to α=0.9. This is due to the increased desired signal power as shown in Fig. 8.12. However, below α=0.7, Tx cancellation scheme starts to show a higher CIR. The reason can be inferred by considering Fig. 8.13 where the interference from the Tx-Rx cancellation scheme is much higher than that of the Tx cancellation SEFDM for α=0.6.

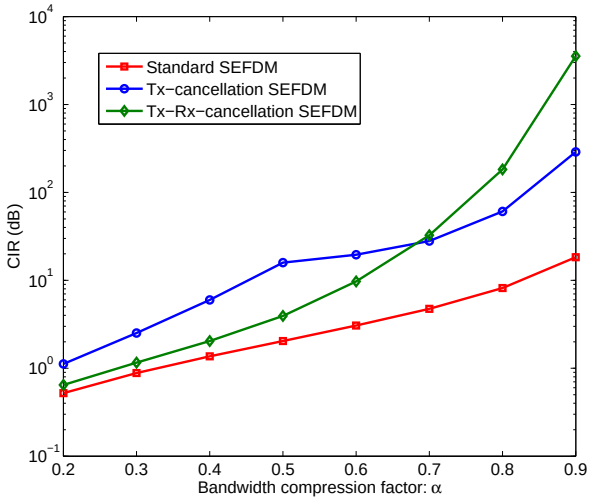

Figure 8.14: CIR comparisons for three different systems with N=16 sub-carriers over various bandwidth compression factors α.

Constellation quality is used for an initial assessment the performance of the self interference cancellation scheme. Fig. 8.15 shows different 16QAM constellation patterns for SEFDM signals with 20% bandwidth compression (i.e. α=0.8). Fig. 8.15 (a) shows a typical constellation diagram with no interference cancellation. It is clearly

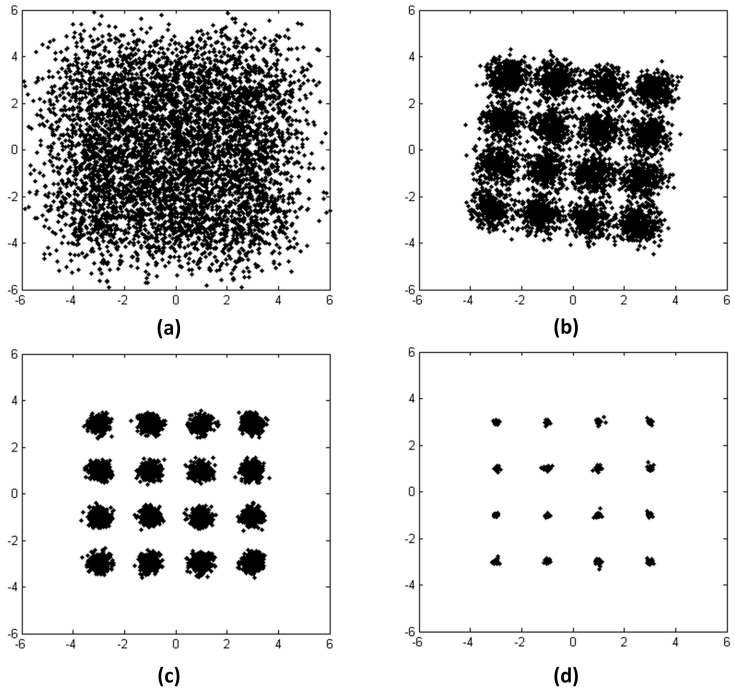

Figure 8.15: Constellation illustrations for 16QAM SEFDM with α=0.8. (a) No cancellation; (b) Tx cancellation; (c) Tx-Rx cancellation; (d) Tx-Rx-ID cancellation.

seen that the constellation points scatter significantly due to the self-created ICI and the high density of the 16QAM constellation points. It is expected that the signal associated with this constellation cannot be recovered easily. Fig. 8.15 (b) presents a better constellation diagram due to the use of transmitter self interference cancellation scheme. However, a fixed phase rotation of the constellation is observed. This can be compensated at the receiver by self interference cancellation technique, which is shown in Fig. 8.15 (c). The quality of the constellation is greatly improved since the scattering and the phase rotation have been compensated. The results also verify the conclusion obtained from figure 8.14 where the CIR of the tx-rx self interference cancellation scheme is much higher than others at α=0.8. In order to get further improved constellation performance, the advanced soft demapping derived from work [52] is tested in Fig. 8.15 (d) where a much better constellation pattern can be obtained.

Fig. 8.16 presents the BER simulation results of SEFDM systems with the self

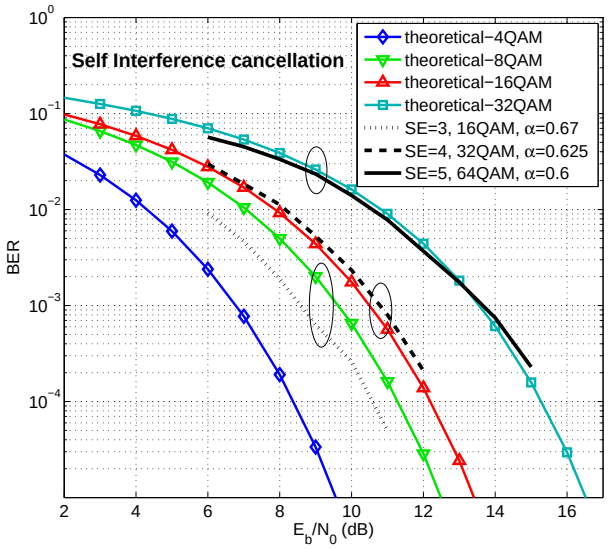

Figure 8.16: BER comparisons of self interference cancellation SEFDM systems and ZF based OFDM systems in various spectral efficiencies.

Table 8.2: Achievable Spectral Efficiency

Parameters	**16QAM**
Raw spectral efficiency	4 bit/s/Hz
SelfIC spectral efficiency	2 bit/s/Hz
SelfIC with SEFDM signals (33% bandwidth saving)	3 bit/s/Hz $\Longleftrightarrow$ 8QAM OFDM

interference cancellation scheme. OFDM systems with ZF detectors are included for comparisons. They are denoted as "theoretical-MQAM". AWGN channel is used here and multipath fading effects are not considered. In terms of SEFDM, a pair of two symbols are grouped resulting in halved data rate. It should be noted that the self interference cancellation is similar to repetition coding since a symbol is effectively transmitted twice by being modulated onto two adjacent sub-carriers with opposite signs. Thus, the spectral efficiency is halved. In order to have fair comparisons, systems with the same achievable spectral efficiency have to be compared. Thus, modulation formats and bandwidth compression factors should be flexible for SEFDM. One example of the

achievable spectral efficiency for SEFDM is presented in Table 8.2. Results indicate that the interference cancellation technique can mitigate the self-created ICI to some extent. It is clearly seen that SEFDM outperforms OFDM at spectral efficiency equals 3 bit/s/Hz. For other spectral efficiency values, SEFDM shows the same performance as that of OFDM. The results are expected since higher constellation density introduces higher interference and the ICI level is beyond the correction capability. With further bandwidth compression, further performance loss is expected.

8.3.2 Over-the-Air Testing of Self Interference Cancellation Scheme

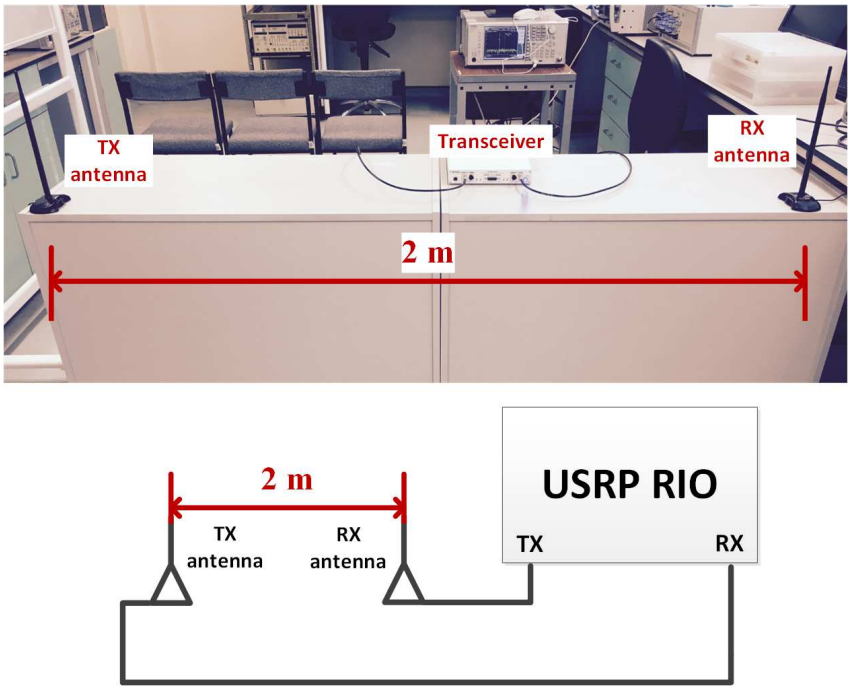

Figure 8.17: Single SEFDM/OFDM testbed setup using USRP RIO.

The experimental setup is designed on a single USRP based SEFDM/OFDM platform. The actual setup is shown in Fig. 8.17, where one USRP RIO 2953R [188] is used as a transceiver. In order to extend the coverage of the transmit and receive antennas, a 5 m RF coaxial cable with negligible attenuation is connected between the Tx antenna (or Rx antenna) and the USRP RF0 out port (or RF1 in port). Two antennas are

arranged with a LOS link and the spacing between the two antennas is 2 m, with the antennas being placed 0.8 m above the floor. The experiment is operated according to the system specifications in Table. 8.3 where the central carrier frequency is set to be the free license 2.4 GHz and other parameters are mostly set based on LTE standard. The table indicates that transmitting the same amount data per second, SEFDM signal occupies narrow bandwidth. For a more detailed description of the USRP operations, section 6.7 gives a comprehensive explanation.

Table 8.3: Experimental Testbed Specifications For Single USRP Systems

Parameters	**OFDM**	**SEFDM**
Central carrier frequency (GHz)	2.4	2.4
Modulation scheme	4QAM	4QAM
Sampling rate (MHz)	7.68	7.68
FFT size	1024	1024
Number of data sub-carriers	600	600
Bandwidth compression factor	1	0.8
Sub-carrier spacing (kHz)	15	12
Channel bandwidth (MHz)	5	4
Data bandwidth (MHz)	4.5	3.6
Data rate (Mbps)	9	9

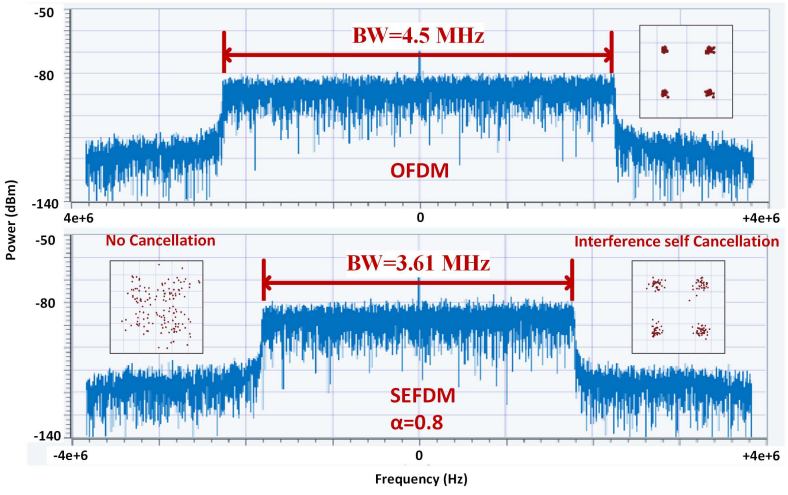

Figure 8.18: Baseband OFDM (top) and SEFDM (bottom) spectra on a single USRP RIO device.

Screenshots illustrating the single device performance are studied and are provided in Fig. 8.18. Firstly, a typical OFDM spectrum together with a constellation pattern, following LTE specifications, are illustrated. The data occupied bandwidth is 4.51 MHz, which is equivalent to one of the LTE requirements [1]. Second, the same data was used to generate an SEFDM signal with a bandwidth compression factor α=0.8, as evaluated in Fig. 8.18. It is clearly seen that the occupied signal bandwidth is compressed and the constellation points are becoming scattered with the reduction of α. Without self interference cancellation, the constellation points are scattered greatly. After the use of the cancellation method, the constellation performance is similar to the OFDM one.

8.4 Conclusions

This section reported two new design concepts for low complexity SEFDM transceivers. Firstly, a precoded architecture is evaluated in realistic channel scenarios. This scheme utilized eigenvalue decomposition to allocate information data on the sub-carriers associated with high eigenvalues, which in turn are related to the bandwidth compression factor. Due to the constructive power introduced by those high eigenvalues, the receiver design is significantly simplified. Several simulations are evaluated in different conditions to demonstrate the benefits of the precoded SEFDM. In AWGN channel, for same condition of modulation format and occupied bandwidth, the proposed precoded SEFDM systems perform much better than its OFDM equivalent. In a frequency selective channel, different modulation formats are presented to show the advantage of the precoded SEFDM. The precoding operation introduces frequency diversity since one symbol will be modulated on multiple sub-carriers. Thus, the precoded SEFDM would be more robust in frequency selective channels. Results show that for the same bandwidth a 128QAM precoded SEFDM system outperforms a 16QAM OFDM one by offering 75% bit rate increase. Since error correcting codes improve performance in multipath channel scenarios, Turbo coding BER performance comparisons are in-

vestigated in this work. Results indicate that significant coding gains are achieved for both systems whilst maintaining the power advantage of the precoded SEFDM over OFDM. In order to have a fair comparison, the precoded SEFDM and the typical OFDM systems, both modulated by 64QAM symbols, are tested in a predefined frequency selective channel. Using 64QAM modulated symbols, the precoded SEFDM outperforms the typical OFDM by several dBs.

The second scheme, termed self interference cancellation, aims to transmit data, having the same absolute amplitude but opposite signs, on adjacent sub-carriers. This solution has some tradeoffs in terms of complexity and spectral efficiency. The benefit is its low complexity compared to post interference cancellation schemes. Typical SEFDM signal detectors such as SD and FSD are too complicated to implement in systems requiring large number of sub-carriers or high order QAM modulation constellation due to multiplication and matrix inverse operations. However, the tested self interference cancellation scheme almost follows the typical OFDM operations. It should be noted that using a group of two symbols, the spectral efficiency is halved. Therefore, achievable spectral efficiency is studied for this scheme. Results indicate that this solution is specially suitable for low order modulation formats. For achievable spectral efficiency equals 3 bit/s/Hz, SEFDM outperforms typical OFDM. For other achievable spectral efficiency values, SEFDM and OFDM have close BER performance. In addition, this work has been designed experimentally and integrated in USRP verifying the concept through simple constellation observations. Based on the practical results, it is concluded that the self interference cancellation method can bring benefits to SEFDM signals in a single USRP point-to-point communication scenario.

Chapter 9

Conclusions

Future communication systems will aim to maximize data throughput without compromising the scarcely available spectrum. SEFDM is one such system where orthogonality is intentionally violated to improve spectral efficiency at the expense of self-created ICI. A model of an efficient signal generator has been mathematically analyzed and further implemented on FPGA and VLSI platforms. Linear and non-linear detectors for small size uncoded SEFDM systems were proposed by previous researchers and their limitations were presented in Chapter 2. For SEFDM systems with a large number of sub-carriers and high order modulation formats, the topic of efficient signal detection still remains open and untackled. Therefore, this thesis proposed and explored several efficient SEFDM system models and further experimentally evaluated such systems in both optical testbeds, wireless testbeds and combinations of these.

Chapter 3 presented three novel signal detection schemes for ICI mitigation of SEFDM signals. An optimized iterative detector (ID) assisted by the soft demapping scheme was first described. This outperforms linear detectors such ZF and TSVD. A hybrid detector combining both ID and FSD results in much better performance while maintaining acceptable complexity. However, the ID-FSD detector is only applicable to small size systems. The ICI introduced within SEFDM is proportional to the number of sub-carriers, which poses great challenge to SEFDM implementation and a restric-

tion of its potential use in future practical systems. Therefore, a detector for large size SEFDM systems with good error performance is highly desirable. Block-SEFDM is the technique proposed in this thesis to modify the sub-carrier locations at the transmitter. The whole spectrum band is divided into several blocks and symbols in each block can be detected separately leading to reduced complexity. This technique is applicable to large size non-orthogonal systems, which in this thesis are tested with up to 128 sub-carriers. Furthermore, an efficient detector termed BED is proposed and shown to have much improved performance when compared to other detectors used for SEFDM. Simulation shows several dB performance gain is achieved for various bandwidth compression factors. This is the first SEFDM attempt to employ more than one hundred sub-carriers whilst performance is maintaining. In order to further reduce the complexity and improve the reliability of signal detection, an efficient soft detector, that is specially proposed for SEFDM systems consisting of a large number of sub-carriers, were designed and tested. The convolutional coding is used with a purpose designed efficient soft detector. Simulation results show that in the presence of a frequency selective channel, relative to OFDM, the soft detector would allow up to 40% bandwidth saving with less than 1.1 dB degradation and 45% of bandwidth with a penalty of 1.6 dB in the case of 1024 non-orthogonal sub-carriers while maintaining acceptable implementation complexity.

Chapter 4 presents applications of SEFDM in the optical domain. Two optical systems were designed and reported. The 10 Gb/s DDO-SEFDM optical experiment can improve spectral efficiency in both the electrical and optical domains. It is experimentally shown that for bandwidth saving up to 20% or signalling rate up to 25%, after transmission over 80 km of single mode fiber, it can achieve the same performance as DDO-OFDM. This is the first experimental verification of 25% optical faster than the Nyquist principle. Furthermore, for approximately the same spectral efficiency, 4QAM DDO-SEFDM outperforms the standard 8QAM DDO-OFDM by 1.6 dB. It is experimentally shown that a lower-order modulation format can achieve a better performance

by replacing a higher order one. The coherent system experiment (CO-SEFDM) shows the transmission of a 24 Gb/s DP-CO-SEFDM signal over 80 km of SSMF. It is shown that QPSK based DP-CO-SEFDM, achieves a 2 dB gain in OSNR performance relative to an otherwise equivalent 8QAM, which has approximately the same spectral efficiency.

Chapter 5 introduces a new framework to increase the number of component carriers (CCs), in a carrier aggregation (CA) system, within a limited bandwidth and without changing the transmission rate per sub-carrier, by using bandwidth compressed SEFDM signals. Results illustrate that overall bit rate can be increased whilst maintaining the same bandwidth. Experimental results show that by compressing each CC by 16%, a CA-SEFDM system can integrate 6 CCs. Moreover, with further compression by 28%, one more CC can be aggregated. Compared with CA-OFDM, which is used in LTE-Advanced systems, the equivalent SEFDM shows that a significant spectral efficiency improvement is achieved at small performance loss. In a real RF experiment, imperfect timing synchronization, sampling phase offset and LO offset will distort signals at the receiver. These effects have been studied and solutions have been provided. In addition, the self-created ICI results in poor channel estimation. In this work, CSI is derived from a zero forcing based time-domain channel estimation algorithm. Experimental results show that up to 40% bit rate increase can be achieved at the cost of small power penalty (below 3 dB). Such experimental results were obtained by testing signals over an LTE channel generated using a commercially available channel emulator operating in the 2 GHz band. This chapter discusses the implementation complexity and shows that the benefits achieved in CA-SEFDM are at the cost of additional computational complexity.

In Chapter 6, a new waveform termed Nyquist-SEFDM was proposed, theoretically studied and practically verified that it can simultaneously save bandwidth and reduce out-of-band power leakage. Bandwidth saving is achieved by packing sub-carriers at frequencies below the symbol rate, spectral efficiency is improved at the cost of self-

created ICI, and out-of-band power suppression is achieved by shaping each sub-carrier with an RRC filter, which introduces new interference. The doubly created interference and its effects are studied under two scenarios. Uncoded detectors are firstly studied followed by coded ones with Turbo equalization. Results show that in order to get converged BER performance, high iterations are needed for the uncoded scenario while fewer iterations for the coded one. In a coexistence scenario of 4G and 5G signals, the newly proposed waveform shows a significant reduced out-of-band interference, therefore it could be well suited to application scenarios such as cognitive radio and spectrum aggregation. This chapter also shows over-the-air testing of SEFDM signals on commercially deployed USRP devices. Two USRPs are tested together. Coexistence evaluations show that SEFDM can avoid interference on the top of LTE signals leading to improved video quality. Specifically, pulse shaping brings new benefits to SEFDM in scenarios where the spectrum is limited. All the results are obtained via realistic over-the-air software defined radio testing, using commercially available USRP devices.

The combination of wireless and optical transmission was investigated in a millimeter wave scenario in Chapter 7 in detail. The data rate can be increased greatly within a limited bandwidth and without changing the transmission rate per sub-carrier, by using SEFDM signals. However, the improved data rate was achieved at the expense of some power penalty. Considering 4QAM modulation scheme, compressing sub-carrier spacing by 20% therefore aggregating more sub-carriers in a given bandwidth, the bit rate is improved by 25%. For higher bandwidth compression up to 40%, approximately 67% more data can be delivered at the cost of roughly 3 dB power penalty and additional computational complexity. In order to have a more convincing comparison, two systems with equal spectral efficiency are set up and compared. The system using bandwidth compressed SEFDM signals outperforms its equivalent 8QAM OFDM by 1 dB. All the experiments are operated in a realistic environment with a pair of 60 GHz antennas and optical fibers. Indeed, the achieved performance is not surprising since previous experiments in the optical or wireless domains have shown the efficiency

and practicability of these systems. The main concern is the system complexity, which should be considered and dealt with in near future.

Chapter 8 considered the simplification of SEFDM transceiver design. The effective interference, which is contributed by all sub-carriers, has to be minimized and this results in a receiver of significant complexity. In order to mitigate the interference and simplify the receiver design, two promising solutions are proposed and tested. Firstly, a precoding technique, based on eigenvalue decomposition of the sub-carrier correlation matrix, is utilised. A new signal model, which occupies the same bandwidth, is tested for the precoded SEFDM without requiring a complex detection algorithm. Results show that due to the bandwidth compression benefit, SEFDM is able to offer constructive power distribution to a portion of its sub-carriers, which indicates an improved performance on those sub-carriers. In a frequency selective channel, simulation results show that a 128QAM signal using the precoded SEFDM scheme outperforms a 16QAM OFDM signal. This is due to the benefit of frequency diversity that specially exists in the precoded SEFDM. Secondly, a repetition coding based new solution was tested. The system principle was explained and simulations show that the self interference cancellation SEFDM results in better BER performance compared to that of an OFDM system of the same achievable spectral efficiency. However, the improved performance of both solutions comes with cost. The first solution requires SVD computation, which consumes extra computational resources. The performance of the second solution is improved at the expense of repeated symbol transmission, thus, the achievable spectral efficiency is halved. Its performance can be further improved using a group of three symbols at the cost of further reduced spectral efficiency. This chapter also shows over-the-air testing of SEFDM signals on commercially available software defined radio (USRP devices). Single USRP is used to test the self interference cancellation idea. Results show that the self interference cancellation method can efficiently remove interference showing clear and recognizable constellation diagrams.

To sum up, the thesis reported the design of optimal system models that can recover

complex SEFDM signals (e.g. LTE-like signals). Both conceptual and experimental tests are investigated. The first part, including Chapter 2 and Chapter 3, mainly focuses on theoretical studies of efficient detectors or system models for SEFDM. The second part, of Chapter 4 to Chapter 8 is dedicated to practical implementations in both the optical and wireless domain. It should be noted that the second part contributes to future 5G systems developments. Many real world impairments are considered, such as multipath fading, phase offset, imperfect timing synchronization and poor channel estimation/equalization. It is worth mentioning that it is for the first time that SEFDM was implemented in optical experimental testbeds. Moreover, it is also the first time to set up SEFDM experiments in LTE, LTE-Advanced, millimeter wave and pulse shaping scenarios.

9.1 Future Work

Despite contributions reported in this work, the design of efficient detectors for large size SEFDM systems is still an attractive research topic. In addition, the work in this thesis paves the way for many other research directions. Below is a list of topics considered for future work.

- **Filtered Block-SEFDM**

  The principle of Block-SEFDM has been explained in Chapter 3 in which the entire signal band is separated into multiple sub-bands and one sub-carrier is reserved between two adjacent sub-bands for out-of-band interference mitigation. However, the spectral efficiency is reduced since the guard band cannot be used for data transmission. In order to mitigate the interband interference, the pulse shaping concept explained in Chapter 6 could be employed for each sub-band. Thus, the out-of-band power leakage of each sub-band is suppressed without any spectral efficiency loss. Adjacent sub-bands can be packed next to each other without a protection gap between each.

- **Copper Access Applications**

  This topic has been mentioned in section 8.2.3. Its technical background is based on the precoding scheme of section 8.2.1. The main idea of using SEFDM signals in copper access scenario is to avoid the significant channel attenuation and cope with severe cross talk. The way to do this is through bandwidth compression of multicarrier systems.

- **Iteration Control of the ID Signal Detection**

  According to section 3.2, a uncertainty interval is defined and narrowed linearly after each iteration. In order to achieve the best performance, the number of iterations should be large enough. This causes processing delay and poses great challenges to hardware implementation. It may be beneficial to relax the iteration numbers and optimize the iteration process using a nonlinear uncertainty interval based on an exponential function in a form as

$$f(x) = a^x \tag{9.1}$$

  where the base a could be greater than one or smaller than one. Normally, the above equation is expressed as a natural exponential function if the form of e^x. Therefore, the convergence would be faster using a nonlinear scheme that in the beginning of several iterations the uncertainty interval is relatively wider than that in the last few iterations.

- **Cancellation Carriers for Out-Of-Band Power Suppression**

  Chapter 6 showed that the high sidelobe of a sub-carrier can be suppressed using pulse shaping filters. However, this method is too complicated due to the convolution operations at transmitter and receiver. A simpler method to suppress the sidelobe was proposed in [220] where a number of predefined sub-carriers are inserted at the edge of an OFDM spectrum. These special sub-carriers are called

cancellation carriers. They are determined based on the principle that the power of the sidelobe of a transmitted signal is the minimum one. This method has been theoretically analyzed for GFDM in [221]. Therefore, it is worth trying the CC method in SEFDM systems.

Appendix A

Abbreviations

3GPP	third generation partnership project
4G	4^{th} generation
5G	5^{th} generation
ADC	analog-to-digital conversion
AED	accumulated euclidean distance
ASE	amplified spontaneous emission
ASIC	application specific integrated circuit
AWG	arbitrary waveform generator
AWGN	additive white Gaussian noise
A/D	analog-to-digital
B2B	back-to-back
BCF	bandwidth compression factor
BCJR	Bahl-Cocke-Jelinek-Raviv
BDM	bit division multiplexing
BED	block efficient detector
BER	bit error rate
Block-SEFDM	block-spectrally efficient frequency division multiplexing
BPSK	binary phase shift keying

BS	base station
BSS	best solution selector
BU	butterfly unit
CapEx	capital expenditure
CA	carrier aggregation
CBS	central base station
CC	component carriers
CCDF	complementary cumulative distribution function
CCs	component carriers
CD	chromatic dispersion
CDMA	code division multiple access
CIR	carrier-to-interference power ratio
CMOS	complementary metal-oxide-semiconductor
CoMP	coordinated multiple point
CO-SEFDM	coherent optical-SEFDM
CP	cyclic prefix
CPE	common phase error
CRVD	conventional real valued decomposition
CR	cognitive radio
CS	central station
CSI	channel state information
CSPR	carrier to signal power ratio
C-RAN	cloud-radio access networks
DAC	digital-to-analogue conversion
DC	direct current
DCT	discrete cosine transform
DDC	digital down-conversion
DDO-OFDM	directed detection optical-OFDM

DDO-OFDM	direct detection optical-OFDM
DDO-SEFDM	directed detection optical-SEFDM
DFB	distributed feedback
DFT	discrete Fourier transform
DOFDM	dense orthogonal frequency division multiplexing
DP	dual polarization
DPC	dirty paper coding
DSB	double sideband
DSL	digital subscriber line
DSP	digital signal processors
DVB	digital video broadcast
D/A	digital-to-analog
ECC	error correcting codes
ECL	external-cavity laser
EDFA	erbium doped fiber amplifier
eMBB	enhanced mobile broadband
EPA	extended pedestrian A
FBMC	filterbank based multicarrier
FCE	full channel estimation
FD	fixed detector
FDD	frequency division duplexing
FDM	frequency division multiplexing
FDMA	frequency division multiple access
FE	full expansion
FEC	forward error correction
FEXT	far-end crosstalk
FF	flip-flop
FFT	fast Fourier transform

FOFDM	fast orthogonal frequency division multiplexing
FPGA	field programmable gate array
FrFT	fractional Fourier transform
FSD	fixed sphere decoding
FSD-MNSF	FSD-modified-non-sort-free
FSD-NSF	FSD-non-sort-free
FSD-SF	FSD-sort-free
FTN	faster than Nyquist
FTTB	fiber to the building
FTTC	fiber to the cabinet
FTTdp	fiber to the distribution point
FTTH	fiber to the home
GB	guard band
GFDM	generalized frequency division multiplexing
GUI	graphical user interface
HC-MCM	high compaction multicarrier communication
HPA	high power amplifier
IC	integrated circuit
ICI	inter carrier interference
ID	iterative detection
IDCT	inverse discrete cosine transform
IDFT	inverse discrete Fourier transform
ID-FSD	iterative detection-FSD
ID-SD	ID-sphere decoding
IF	intermediate frequency
IFFT	inverse fast Fourier transform
IFrFT	inverse fractional Fourier transform
IMD	intermodulation distortion

IoT	internet of things
IOTA	isotropic orthogonal transform algorithm
IP	intellectual property
ISI	inter symbol interference
LDPC	low density parity check
LLR	log-likelihood ratio
LNA	low noise amplifier
LO	local oscillator
LOS	line-of-sight
LTE	long term evolution
LTE-Advanced	long term evolution-advanced
LUT	look up table
MA	multiple access
MASK	m-ary amplitude shift keying
MCM	multicarrier modulation
MC-CDMA	multi-carrier code division multiple access
MF	matched filter
MIMO	multiple input multiple output
ML	maximum likelihood
MLSD	maximum likelihood sequence detection
MMF	multi-mode fiber
MMSE	minimum mean squared error
mMTC	massive machine-type communication
MNSF	modified-non-sort-free
MOFDM	masked-OFDM
MRVD	modified real valued decomposition
MS	mobile station
MSE	mean squared error

MTC	machine-type communication
MUSA	multi-user shared access
MZM	Mach-Zehnder modulator
NB-IoT	narrow-band IoT
NEXT	near-end crosstalk
NOFDM	non-orthogonal frequency division multiplexing
NOMA	non-orthogonal multiple access
NP	non-polynomial
NSF	non-sort-free
NWDM	Nyquist wavelength division multiplexing
Nyquist-SEFDM	Nyquist-spectrally efficient frequency division multiplexing
OBM-OFDM	orthogonal band multiplexed OFDM
OF	optical filter
OFDM	orthogonal frequency division multiplexing
OFDMA	OFDM-FDMA
OMA	orthogonal multiple access
OpEx	operating expenditure
OQAM	offset-QAM
OSNR	optical signal-to-noise ratio
OSSB	optical single sideband
OTA	over-the-air
Ov-FDM	Overlapped FDM
O-SEFDM	optical-spectrally efficient frequency division multiplexing
O-FOFDM	optical-fast orthogonal frequency division multiplexing
O-OFDM	optical-orthogonal frequency division multiplexing
PA	power amplifier
PAPR	peak-to-average power ratio
PCE	partial channel estimation

PD	photodiode
PDF	probability density function
PDMA	polarisation division multiple access
PDM-OFDM	polarization-division multiplexing-OFDM
PDM-SEFDM	polarization-division multiplexing-SEFDM
PDSCH	physical downlink shared channel
PE	processing element
PED	partial Euclidean distance
PMD	polarization mode dispersion
PON	passive optical network
PSD	power spectral density
PU	primary user
PXI	PCI extensions for instrumentation
P/S	parallel-to-serial
QAM	quadrature amplitude modulation
QoS	quality of service
QPSK	quadrature phase-shift keying
RAUs	remote antenna units
RBW	resolution bandwidth
RF	radio frequency
RMS	root mean square
RoF	radio-over-fiber
ROM	read only memory
RRC	root raised cosine
RSC	recursive systematic convolutional
RTL	register transfer level
RVD	real valued decomposition
ScIR	sub-carrier to interference ratio

SCMA	sparse code multiple access
SC-FDMA	single-carrier-frequency division multiple access
SD	sphere decoding
SDP	semidefinite programming
SDR	software defined radio
SEFDM	spectrally efficient frequency division multiplexing
SEFDMA	SEFDM-FDMA
SelfIC	self interference cancellation
SF	sort-free
SIC	successive interference cancellation
SiGe	silicon-germanium
SINR	signal-to-interference-plus-noise ratio
SMF	single mode fiber
SNR	signal-to-noise ratio
SP	shortest-path
SSB	single-sideband
SSBI	signal-signal beat interference
SSMF	standard single mode fiber
STBC	space time block coding
STO	symbol timing offset
SU	secondary user
SVD	singular value decomposition
S/P	serial-to-parallel
TDD	time division duplexing
TDMA	time division multiple access
TFP	time frequency packing
THP	Tomlinson-Harashima precoding
TSVD	truncated singular value decomposition

TSVD-FSD	truncated singular value decomposition-fixed sphere decoding
UFMC	universal-filtered multicarrier
URLLC	ultra-reliable and low-latency communication
USRP	universal software radio peripheral
VDSL	very-high-bit-rate digital subscriber line
VDSL2	very-high-bit-rate digital subscriber line 2
VHDL	very high speed integrated circuit hardware description language
VLC	visible light communication
VLSI	very large scale integration
VOA	variable optical attenuator
VP	vector perturbation
VSSB-OFDM	virtual single-sideband OFDM
WCDMA	wideband code division multiple access
WiFi	wireless fidelity
WiGig	Wireless Gigabit Alliance
WiMAX	Worldwide interoperability for Microwave Access
WSS	wavelength selective switch
ZF	zero forcing
ZP	zero padding

Appendix B

Optics Express Paper: Reach Enhancement in Optical Fiber Transmission

The paper attached here has been submitted to Optics Express in August 2017 and is under review. It reports reach enhancement in nonlinear optical fiber transmission using SEFDM signals.

Appendix C

Research Images as Art - Kaleidoscope of Radio Signals

This was a poster submission to a competition of research images of art, held at UCL in 2016. The patterns were simulated using multicarrier signals constellation based on those of Chapter 5 of this thesis.

The flower patterns shown in Fig. C.1 indicate the motion of radio signals, which are generally propagated over noisy, interfered and attenuated wireless channels. A constellation diagram, represented by constellation points, is used to evaluate the signal quality. Noise scatters constellation points; interference results in circular and spreading constellation points and attenuation causes expansion and shrink of constellation points. The combination of these effects displays diversified flower patterns and therefore the motion of the world.

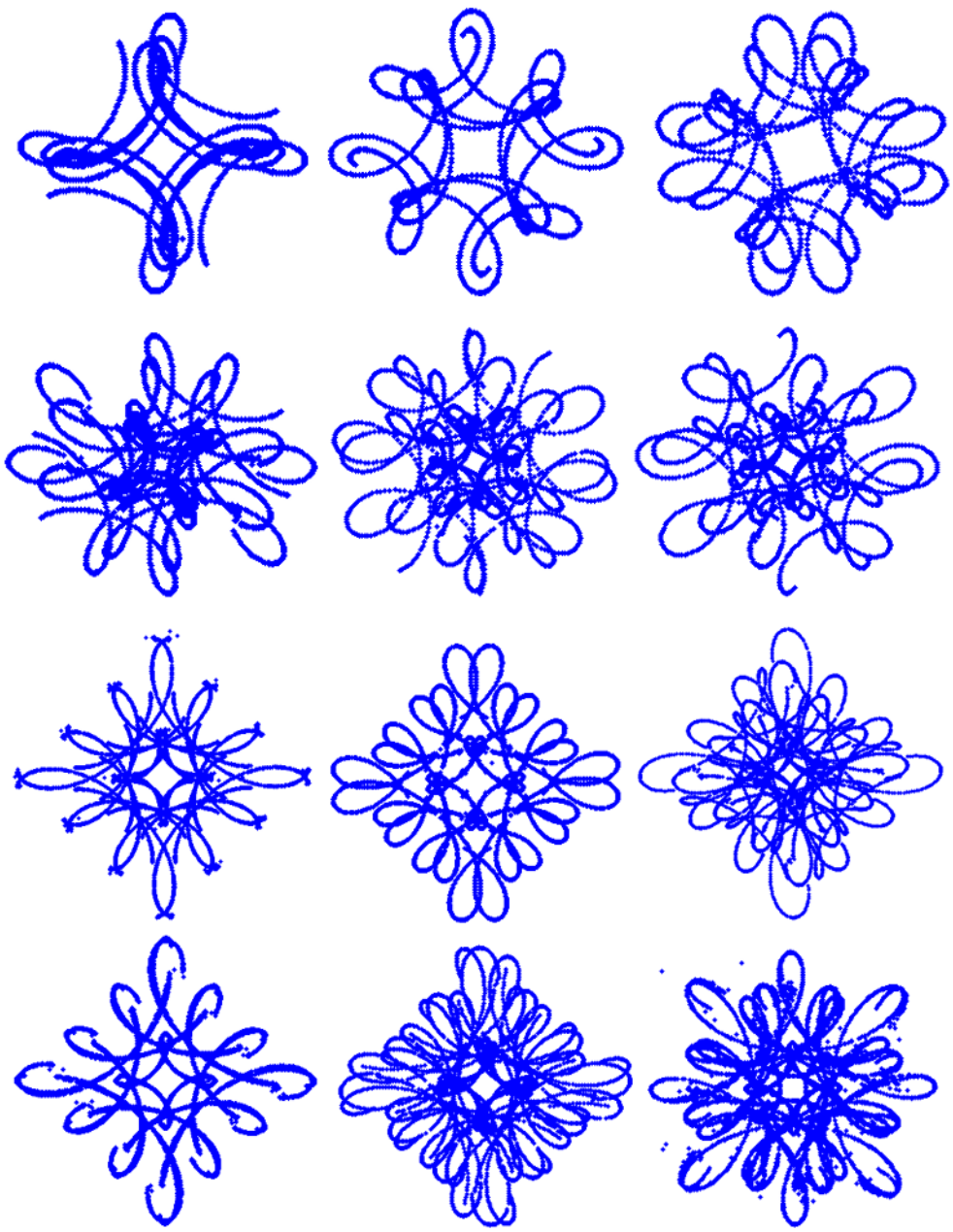

Figure C.1: Radio signal constellation patterns after wireless channel propagation.

List of References

[1] 3GPP TS 36.300 version 8.12.0 Release 8. Evolved universal terrestrial radio access (E-UTRA) and evolved universal terrestrial radio access network (E-UTRAN); overall description; stage 2 (release 8). April 2010.

[2] 3GPP TR 36.912 v.13.0.0. Feasibility study for further advancements for E-UTRA (LTE-Advanced). Rel. 13, Dec. 2015.

[3] J.G. Andrews, S. Buzzi, Wan Choi, S.V. Hanly, A Lozano, AC.K. Soong, and J.C. Zhang. What will 5G be? *Selected Areas in Communications, IEEE Journal on*, 32(6):1065–1082, June 2014.

[4] G. Wunder, P. Jung, M. Kasparick, T. Wild, F. Schaich, Yejian Chen, S. Brink, I Gaspar, N. Michailow, A Festag, L. Mendes, N. Cassiau, D. Ktenas, M. Dryjanski, S. Pietrzyk, B. Eged, P. Vago, and F. Wiedmann. 5GNOW: non-orthogonal, asynchronous waveforms for future mobile applications. *Communications Magazine, IEEE*, 52(2):97–105, February 2014.

[5] A Zakrzewska, S. Ruepp, and M.S. Berger. Towards converged 5G mobile networks-challenges and current trends. In *ITU Kaleidoscope Academic Conference: Living in a converged world - Impossible without standards?, Proceedings of the 2014*, pages 39–45, June 2014.

[6] Yuya Saito, Anass Benjebbour, Yoshihisa Kishiyama, and Takehiro Nakamura. System-level performance evaluation of downlink non-orthogonal multiple access

(NOMA). In *Personal Indoor and Mobile Radio Communications (PIMRC), 2013 IEEE 24th International Symposium on*, pages 611–615, Sept 2013.

[7] A Sahin, I Guvenc, and H. Arslan. A survey on multicarrier communications: Prototype filters, lattice structures, and implementation aspects. *Communications Surveys Tutorials, IEEE*, 16(3):1312–1338, Third 2014.

[8] R. R. Mosier and R. G. Clabaugh. Kineplex, a bandwidth-efficient binary transmission system. *American Institute of Electrical Engineers, Part I: Communication and Electronics, Transactions of the*, 76(6):723–728, Jan 1958.

[9] Robert W. Chang. Synthesis of band-limited orthogonal signals for multichannel data transmission. *Bell System Technical Journal, The*, 45(10):1775–1796, Dec 1966.

[10] S. Weinstein and P. Ebert. Data transmission by frequency-division multiplexing using the discrete Fourier transform. *Communication Technology, IEEE Transactions on*, 19(5):628–634, October 1971.

[11] T. Hwang, C. Yang, G. Wu, S. Li, and G. Y. Li. OFDM and its wireless applications: A survey. *IEEE Transactions on Vehicular Technology*, 58(4):1673–1694, May 2009.

[12] E. Larsson, O. Edfors, F. Tufvesson, and T. Marzetta. Massive MIMO for next generation wireless systems. *Communications Magazine, IEEE*, 52(2):186–195, February 2014.

[13] T. S. Rappaport, S. Sun, R. Mayzus, H. Zhao, Y. Azar, K. Wang, G. N. Wong, J. K. Schulz, M. Samimi, and F. Gutierrez. Millimeter wave mobile communications for 5G cellular: It will work! *IEEE Access*, 1:335–349, May 2013.

[14] W. Roh, Ji-Yun Seol, JeongHo Park, Byunghwan Lee, Jaekon Lee, Yungsoo Kim, Jaeweon Cho, Kyungwhoon Cheun, and F. Aryanfar. Millimeter-wave beamform-

ing as an enabling technology for 5G cellular communications: theoretical feasibility and prototype results. *Communications Magazine, IEEE*, 52(2):106–113, February 2014.

[15] 3GPP TR 36.913 v.10.0.0. Requirements for further advancements for evolved universal terrestrial radio access (E-UTRA) (LTE-Advanced). Rel. 10, Apr. 2011.

[16] H. A. U. Mustafa, M. A. Imran, M. Z. Shakir, A. Imran, and R. Tafazolli. Separation framework: An enabler for cooperative and D2D communication for future 5G networks. *IEEE Communications Surveys Tutorials*, 18(1):419–445, Firstquarter 2016.

[17] B. Farhang-Boroujeny. OFDM versus filter bank multicarrier. *Signal Processing Magazine, IEEE*, 28(3):92–112, May 2011.

[18] V. Vakilian, T. Wild, F. Schaich, S. Ten Brink, and J.-F. Frigon. Universal-filtered multi-carrier technique for wireless systems beyond LTE. In *Globecom Workshops (GC Wkshps), 2013 IEEE*, pages 223–228, Dec 2013.

[19] N. Michailow, M. Matthe, I.S. Gaspar, A.N. Caldevilla, L.L. Mendes, A. Festag, and G. Fettweis. Generalized frequency division multiplexing for 5th generation cellular networks. *Communications, IEEE Transactions on*, 62(9):3045–3061, Sept 2014.

[20] J.E. Mazo. Faster-than-Nyquist signaling. *Bell Syst. Tech. J*, 54(8):1451–1462, 1975.

[21] M.R.D. Rodrigues and Izzat Darwazeh. Fast OFDM: a proposal for doubling the data rate of OFDM schemes. In *International conference on Telecommunications*, volume 3, pages 484–487, 2002.

[22] Fuqin Xiong. M-ary amplitude shift keying OFDM system. *IEEE Trans. Commun.*, 51(10):1638–1642, 2003.

[23] Wang Jian, Yang Xun, Zhang Xi-lin, and Daoben Li. The prefix design and performance analysis of DFT-based overlapped frequency division multiplexing (OvFDM-DFT) system. In *3rd Int. Workshop on Signal Design and Its Applicat. in Commun.*, pages 361–364, Chengdu, IWSDA, September 2007.

[24] M.R.D. Rodrigues and Izzat Darwazeh. A spectrally efficient frequency division multiplexing based communications system. In *Proc. 8th Int. OFDM Workshop*, pages 48–49, Hamburg, 2003.

[25] J.B. Anderson, F. Rusek, and V. Öwall. Faster-than-Nyquist signaling. *Proceedings of the IEEE*, 101(8):1817–1830, 2013.

[26] A. Barbieri, D. Fertonani, and G. Colavolpe. Time-frequency packing for linear modulations: spectral efficiency and practical detection schemes. *Communications, IEEE Transactions on*, 57(10):2951–2959, October 2009.

[27] Hosein Nikopour and Hadi Baligh. Sparse code multiple access. In *Personal Indoor and Mobile Radio Communications (PIMRC), 2013 IEEE 24th International Symposium on*, pages 332–336, Sept 2013.

[28] Yuya Saito, Anass Benjebbour, Yoshihisa Kishiyama, and Takehiro Nakamura. System-level performance evaluation of downlink non-orthogonal multiple access (NOMA). In *Personal Indoor and Mobile Radio Communications (PIMRC), 2013 IEEE 24th International Symposium on*, pages 611–615, Sept 2013.

[29] S. Hara and R. Prasad. Overview of multicarrier CDMA. *Communications Magazine, IEEE*, 35(12):126–133, Dec 1997.

[30] I. Kanaras, A. Chorti, M.R.D. Rodrigues, and I. Darwazeh. A combined MMSE-ML detection for a spectrally efficient non orthogonal FDM signal. In *Broadband Communications, Networks and Systems, 2008. BROADNETS 2008. 5th International Conference on*, pages 421–425, Sept 2008.

[31] I. Kanaras, A. Chorti, M.R.D. Rodrigues, and I. Darwazeh. Spectrally efficient FDM signals: bandwidth gain at the expense of receiver complexity. In *Communications, 2009. ICC '09. IEEE International Conference on*, pages 1–6, June 2009.

[32] I. Kanaras, A. Chorti, M. Rodrigues, and I. Darwazeh. Investigation of a semidefinite programming detection for a spectrally efficient FDM system. In *Personal, Indoor and Mobile Radio Communications, 2009 IEEE 20th International Symposium on*, pages 2827–2832, Sept 2009.

[33] A. Chorti and I. Kanaras. Masked M-QAM OFDM: A simple approach for enhancing the security of OFDM systems. In *Personal, Indoor and Mobile Radio Communications, 2009 IEEE 20th International Symposium on*, pages 1682–1686, Sept 2009.

[34] I. Kanaras, A. Chorti, M. Rodrigues, and I. Darwazeh. A new quasi-optimal detection algorithm for a non orthogonal spectrally efficient FDM. In *Communications and Information Technology, 2009. ISCIT 2009. 9th International Symposium on*, pages 460–465, Sept 2009.

[35] S. Isam and I. Darwazeh. Simple DSP-IDFT techniques for generating spectrally efficient FDM signals. In *Communication Systems Networks and Digital Signal Processing (CSNDSP), 2010 7th International Symposium on*, pages 20–24, July 2010.

[36] A. Chorti, I. Kanaras, M.R.D. Rodrigues, and I. Darwazeh. Joint channel equalization and detection of spectrally efficient FDM signals. In *Personal Indoor and Mobile Radio Communications (PIMRC), 2010 IEEE 21st International Symposium on*, pages 177–182, Sept 2010.

[37] S. Isam and I Darwazeh. Precoded spectrally efficient FDM system. In *Personal Indoor and Mobile Radio Communications (PIMRC), 2010 IEEE 21st International Symposium on*, pages 99–104, Sept 2010.

[38] I. Kanaras, A. Chorti, M.R.D. Rodrigues, and I. Darwazeh. A fast constrained sphere decoder for ill conditioned communication systems. *Communications Letters, IEEE*, 14(11):999–1001, November 2010.

[39] S. Isam, I. Kanaras, and I. Darwazeh. A truncated SVD approach for fixed complexity spectrally efficient FDM receivers. In *Wireless Communications and Networking Conference (WCNC), 2011 IEEE*, pages 1584–1589, March 2011.

[40] S. Isam and I. Darwazeh. Peak to average power ratio reduction in spectrally efficient FDM systems. In *Telecommunications (ICT), 2011 18th International Conference on*, pages 363–368, May 2011.

[41] S. Isam and I. Darwazeh. Design and performance assessment of fixed complexity spectrally efficient FDM receivers. In *Vehicular Technology Conference (VTC Spring), 2011 IEEE 73rd*, pages 1–5, May 2011.

[42] M.R. Perrett and I. Darwazeh. Flexible hardware architecture of SEFDM transmitters with real-time non-orthogonal adjustment. In *Telecommunications (ICT), 2011 18th International Conference on*, pages 369–374, May 2011.

[43] R.C. Grammenos, S. Isam, and I. Darwazeh. FPGA design of a truncated SVD based receiver for the detection of SEFDM signals. In *Personal Indoor and Mobile Radio Communications (PIMRC), 2011 IEEE 22nd International Symposium on*, pages 2085–2090, Sept 2011.

[44] N. Ahmad, S. Kamilah Syed-Yusof, N. Fisal, K. Anwar, and T. Matsumoto. Soft-feedback MMSE equalization for non-orthogonal frequency division multiplexing (n-OFDM) signal detection. In *Smart Antennas (WSA), 2012 International ITG Workshop on*, pages 248–255, March 2012.

[45] S. Isam and I. Darwazeh. Robust channel estimation for spectrally efficient FDM system. In *Telecommunications (ICT), 2012 19th International Conference on*, pages 1–6, April 2012.

[46] P.N. Whatmough, M.R. Perrett, S. Isam, and I. Darwazeh. VLSI architecture for a reconfigurable spectrally efficient FDM baseband transmitter. *Circuits and Systems I: Regular Papers, IEEE Transactions on*, 59(5):1107–1118, May 2012.

[47] M.R. Perrett, R.C. Grammenos, and I. Darwazeh. A verification methodology for the detection of spectrally efficient FDM signals generated using reconfigurable hardware. In *Communications (ICC), 2012 IEEE International Conference on*, pages 3686–3691, June 2012.

[48] R.C. Grammenos and I. Darwazeh. Hardware implementation of a practical complexity spectrally efficient FDM reconfigurable receiver. In *Personal Indoor and Mobile Radio Communications (PIMRC), 2012 IEEE 23rd International Symposium on*, pages 2401–2407, Sept 2012.

[49] Tongyang Xu, Ryan C Grammenos, and Izzat Darwazeh. FPGA implementations of real-time detectors for a spectrally efficient FDM system. In *Telecommunications (ICT), 2013 20th International Conference on*, pages 1–5, May 2013.

[50] R.C. Grammenos and I. Darwazeh. Performance trade-offs and DSP evaluation of spectrally efficient FDM detection techniques. In *Communications (ICC), 2013 IEEE International Conference on*, pages 4781–4786, June 2013.

[51] S. Chatzinotas, S. K. Sharma, and B. Ottersten. Frequency packing for interference alignment-based cognitive dual satellite systems. In *2013 IEEE 78th Vehicular Technology Conference (VTC Fall)*, pages 1–7, Sept 2013.

[52] Tongyang Xu, Ryan C Grammenos, Farokh Marvasti, and Izzat Darwazeh. An improved fixed sphere decoder employing soft decision for the detection of non-

orthogonal signals. *Communications Letters, IEEE*, 17(10):1964–1967, October 2013.

[53] P. Kumar A. Shetty V. Prasshanth S. Sriram, N. Vijayakumar and K. Narayanankutty. Spectrally efficient multi-carrier modulation using Gabor transform. *Wireless Engineering and Technology*, 4(2):112–116, Mar 2013.

[54] I. Darwazeh, Tongyang Xu, Tao Gui, Yuan Bao, and Zhaohui Li. Optical SEFDM system; bandwidth saving using non-orthogonal sub-carriers. *Photonics Technology Letters, IEEE*, 26(4):352–355, Feb 2014.

[55] I. Darwazeh, Tongyang Xu, Tao Gui, Yuan Bao, and Zhaohui Li. Optical spectrally efficient FDM system for electrical and optical bandwidth saving. In *Communications (ICC), 2014 IEEE International Conference on*, pages 3432–3437, June 2014.

[56] Tongyang Xu and Izzat Darwazeh. M-QAM signal detection for a non-orthogonal system using an improved fixed sphere decoder. In *9th IEEE/IET International Symposium on Communication Systems, Networks & Digital Signal Processing 2014 (CSNDSP14)*, pages 623–627, Manchester, United Kingdom, July 2014.

[57] Tongyang Xu and Izzat Darwazeh. Multi-Band reduced complexity spectrally efficient FDM systems. In *9th IEEE/IET International Symposium on Communication Systems, Networks & Digital Signal Processing 2014 (CSNDSP14)*, pages 904–909, Manchester, United Kingdom, July 2014.

[58] T. Xu and I. Darwazeh. A soft detector for spectrally efficient systems with non-orthogonal overlapped sub-carriers. *Communications Letters, IEEE*, 18(10):1847–1850, Oct 2014.

[59] Tongyang Xu and I. Darwazeh. Spectrally efficient FDM: spectrum saving technique for 5G? In *5G for Ubiquitous Connectivity (5GU), 2014 1st International Conference on*, pages 273–278, Nov 2014.

[60] Sergey V. Zavjalov, Sergey B. Makarov, and Sergey V. Volvenko. *Application of Optimal Spectrally Efficient Signals in Systems with Frequency Division Multiplexing*, pages 676–685. Springer International Publishing, Cham, 2014.

[61] V.O. Rashich and A.V. Rashich. Asymptotically optimal algorithm for OFDM-signal reception under AWGN and OFDM interference shifted in frequency. In *Communications and Networking (BlackSeaCom), 2015 IEEE International Black Sea Conference on*, pages 5–8, May 2015.

[62] S. Mikroulis, Tongyang Xu, J.E. Mitchell, and I. Darwazeh. First demonstration of a spectrally efficient FDM radio over fiber system topology for beyond 4G cellular networking. In *Networks and Optical Communications - (NOC), 2015 20th European Conference on*, pages 1–5, June 2015.

[63] Tongyang Xu and Izzat Darwazeh. Bandwidth compressed carrier aggregation. In *IEEE ICC 2015 - Workshop on 5G & Beyond - Enabling Technologies and Applications (ICC'15 - Workshops 23)*, pages 1107–1112, London, United Kingdom, June 2015.

[64] Dmitrii K. Fadeev and Andrey V. Rashich. Optimal input power backoff of a nonlinear power amplifier for SEFDM system. In *Internet of Things, Smart Spaces, and Next Generation Networks and Systems - 15th International Conference, NEW2AN 2015, and 8th Conference, ruSMART 2015, St. Petersburg, Russia, August 26-28, 2015, Proceedings*, pages 669–678, 2015.

[65] Sergey V. Zavjalov, Sergey B. Makarov, Sergey V. Volvenko, and Wei Xue. Waveform optimization of SEFDM signals with constraints on bandwidth and an out-of-band emission level. In *Internet of Things, Smart Spaces, and Next Generation Networks and Systems - 15th International Conference, NEW2AN 2015, and 8th Conference, ruSMART 2015, St. Petersburg, Russia, August 26-28, 2015, Proceedings*, pages 636–646, 2015.

[66] D. Rainnie, Yi Feng, and J. Bajcsy. On capacity merits of spectrally efficient FDM. In *Military Communications Conference, MILCOM 2015 - 2015 IEEE*, pages 581–586, Oct 2015.

[67] S. V. Zavjalov, S. B. Makarov, and S. V. Volvenko. Duration of nonorthogonal multifrequency signals in the presence of controlled intersymbol interference. In *2015 7th International Congress on Ultra Modern Telecommunications and Control Systems and Workshops (ICUMT)*, pages 49–52, Oct 2015.

[68] Alexandr B. Kislitsyn and Andrey V. Rashich. *Using the DFT-Based Detection Method for ASK-Manipulated SEFDM Signals*, pages 612–620. Springer International Publishing, Cham, 2015.

[69] Wei Xiang, Kan Zheng, and Xuemin Shen. *Key Enabling Technologies for 5G Mobile Communications*. Springer, 2016.

[70] Fa-Long Luo and Charlie Zhang. *Signal Processing for 5G: Algorithms and Implementations*. Wiley, 2016.

[71] Spiros Mikroulis, Tongyang Xu, and Izzat Darwazeh. Practical demonstration of spectrally efficient FDM millimeter-wave radio over fiber systems for 5G cellular networking. In *Proc. SPIE*, volume 9772, pages 97720I–1–97720I–8, 2016.

[72] D. Nopchinda, T. Xu, R. Maher, B.C. Thomsen, and I. Darwazeh. Dual polarization coherent optical spectrally efficient frequency division multiplexing. *Photonics Technology Letters, IEEE*, 28(1):83–86, Jan 2016.

[73] T. Xu and I. Darwazeh. Experimental validations of bandwidth compressed multicarrier signals. In *2016 IEEE 17th International Symposium on A World of Wireless, Mobile and Multimedia Networks (WoWMoM)*, pages 1–10, June 2016.

[74] E. O. Antonov, A. V. Rashich, D. K. Fadeev, and N. Tan. Reduced complexity tone reservation peak-to-average power ratio reduction algorithm for SEFDM

signals. In *2016 39th International Conference on Telecommunications and Signal Processing (TSP)*, pages 445–448, June 2016.

[75] J. Huang, Q. Sui, Z. Li, and F. Ji. Experimental demonstration of 16-QAM DD-SEFDM with cascaded BPSK iterative detection. *IEEE Photonics Journal*, 8(3):1–9, June 2016.

[76] T. Xu and I. Darwazeh. Nyquist-SEFDM: pulse shaped multicarrier communication with sub-carrier spacing below the symbol rate. In *2016 10th International Symposium on Communication Systems, Networks and Digital Signal Processing (CSNDSP)*, pages 1–6, July 2016.

[77] T. Xu, S. Mikroulis, J. E. Mitchell, and I. Darwazeh. Bandwidth compressed waveform for 60-GHz millimeter-wave radio over fiber experiment. *Journal of Lightwave Technology*, 34(14):3458–3465, July 2016.

[78] Y. Wang, Y. Zhou, T. Gui, K. Zhong, X. Zhou, L. Wang, A. P. T. Lau, C. Lu, and N. Chi. Efficient MMSE-SQRD-based MIMO decoder for SEFDM-based 2.4-Gb/s-spectrum-compressed WDM VLC system. *IEEE Photonics Journal*, 8(4):1–9, Aug 2016.

[79] W. Ozan, K. Jamieson, and I. Darwazeh. Truncating and oversampling OFDM signals in white Gaussian noise channels. In *2016 10th International Symposium on Communication Systems, Networks and Digital Signal Processing (CSNDSP)*, pages 1–6, July 2016.

[80] H. Ghannam and I. Darwazeh. Comparison of turbo decoder and Turbo equalizer for spectrally efficient FDM system. In *2016 10th International Symposium on Communication Systems, Networks and Digital Signal Processing (CSNDSP)*, pages 1–6, July 2016.

[81] Y. Wang, Y. Zhou, T. Gui, K. Zhong, X. Zhou, L. Wang, A. P. T. Lau, C. Lu, and N. Chi. SEFDM based spectrum compressed VLC system using RLS time-

domain channel estimation and ID-FSD hybrid decoder. In *ECOC 2016; 42nd European Conference on Optical Communication*, pages 1–3, Sept 2016.

[82] A. Gelgor, A. Gorlov, and V. P. Nguyen. The design and performance of SEFDM with the Sinc-to-RRC modification of subcarriers spectrums. In *2016 International Conference on Advanced Technologies for Communications (ATC)*, pages 65–69, Oct 2016.

[83] Ji Zhou, Yaojun Qiao, Zhanyu Yang, and Erkun Sun. Faster-than-Nyquist non-orthogonal frequency-division multiplexing based on fractional Hartley transform. *Opt. Lett.*, 41(19):4488–4491, Oct 2016.

[84] H. Liu, L. Liu, and P. Wang. Spectrally efficient nonorthogonal frequency division multiplexing with index modulation. In *2016 17th International Conference on Parallel and Distributed Computing, Applications and Technologies (PDCAT)*, pages 290–293, Dec 2016.

[85] S. V. Zavjalov, S. V. Volvenko, and S. B. Makarov. A method for increasing the spectral and energy efficiency SEFDM signals. *IEEE Communications Letters*, 20(12):2382–2385, Dec 2016.

[86] T. Xu and I. Darwazeh. A joint waveform and precoding design for non-orthogonal multicarrier signals. In *2017 IEEE Wireless Communications and Networking Conference (WCNC)*, pages 1–6, March 2017.

[87] T. Xu and I. Darwazeh. Transmission experiment of bandwidth compressed carrier aggregation in a realistic fading channel. *IEEE Transactions on Vehicular Technology*, 66(5):4087–4097, May 2017.

[88] H. Ghannam and I. Darwazeh. Signal coding and interference cancellation of spectrally efficient fdm systems for 5g cellular networks. In *2017 24th International Conference on Telecommunications (ICT)*, pages 1–6, May 2017.

[89] Ji Zhou, Yaojun Qiao, Zhanyu Yang, Qixiang Cheng, Qi Wang, Mengqi Guo, and Xizi Tang. Capacity limit for faster-than-Nyquist non-orthogonal frequency-division multiplexing signaling. *Scientific Reports*, 7, 2017.

[90] T. Fagorusi, Y. Feng, and J. Bajcsy. An architecture for non-orthogonal multi-carrier faster-than-Nyquist transmission. In *2017 15th Canadian Workshop on Information Theory (CWIT)*, pages 1–5, June 2017.

[91] Y. Feng and J. Bajcsy. Information rate of multi-antenna spectrally-efficient FDM communication. In *2017 15th Canadian Workshop on Information Theory (CWIT)*, pages 1–5, June 2017.

[92] T.Xu, T.Xu, P.Bayvel, and I.Darwazeh. Reach enhancement in optical fiber transmission using non-orthogonal signals with sub-carrier spacing below symbol rate. *Opt. Express*, 2017.

[93] Tongyang Xu and Izzat Darwazeh. Bit precision study of a non-orthogonal iterative detector with FPGA modelling verification. In *2017 IEEE 28th Annual International Symposium on Personal, Indoor, and Mobile Radio Communications (PIMRC) - Track 1 on "Fundamentals and PHY" (IEEE PIMRC 2017 Track 1)*, Montreal, Canada, October 2017.

[94] Tongyang Xu and Izzat Darwazeh. Experimental Over-The-Air testing for coexistence of 4G and a spectrally efficient Non-Orthogonal signal. In *2017 IEEE 28th Annual International Symposium on Personal, Indoor, and Mobile Radio Communications (PIMRC) - "Fundamentals and PHY" (IEEE PIMRC 2017 Track 1)*, Montreal, Canada, October 2017.

[95] Tongyang Xu and Izzat Darwazeh. Multi-Sphere decoding of block segmented SEFDM signals with large number of sub-carriers and high modulation order. In *The International Conference on Wireless Networks and Mobile Communications (WINCOM'17) (WINCOM'17)*, Rabat, Morocco, November 2017.

[96] J.G. Proakis and M. Salehi. *Digital Communications*. McGraw-Hill, 2008.

[97] S. Isam. *Spectrally Efficient FDM Communication Signals and Transceivers: Design, Mathematical Modeling and System Optimization*. PhD thesis, University College London - Department of Electronic and Electrical Engineering, October 2011.

[98] S. Kandhi. Design radix-4 64-point pipeline FFT/IFFT processor for wireless application. In *International Journal of Engineering Inventions (IJEI)*, pages 67–70, September 2013.

[99] S. Isam and I. Darwazeh. Characterizing the intercarrier interference of non-orthogonal spectrally efficient FDM system. In *Communication Systems, Networks Digital Signal Processing (CSNDSP), 2012 8th International Symposium on*, pages 1–5, July 2012.

[100] B. Hassibi and H. Vikalo. On the sphere-decoding algorithm I. expected complexity. *Signal Processing, IEEE Transactions on*, 53(8):2806–2818, Aug 2005.

[101] A. Burg, M. Borgmann, M. Wenk, M. Zellweger, Wolfgang Fichtner, and H. Bolcskei. VLSI implementation of MIMO detection using the sphere decoding algorithm. *Solid-State Circuits, IEEE Journal of*, 40(7):1566–1577, July 2005.

[102] C. Studer, A. Burg, and H. Bolcskei. Soft-output sphere decoding: algorithms and VLSI implementation. *Selected Areas in Communications, IEEE Journal on*, 26(2):290–300, February 2008.

[103] A. Burg, M. Wenk, M. Zellweger, M. Wegmueller, N. Felber, and W. Fichtner. VLSI implementation of the sphere decoding algorithm. In *Solid-State Circuits Conference, 2004. ESSCIRC 2004. Proceeding of the 30th European*, pages 303–306, Sept 2004.

[104] P. Bhagawat, R. Dash, and Gwan Choi. Architecture for reconfigurable MIMO detector and its FPGA implementation. In *Electronics, Circuits and Systems,*

2008. ICECS 2008. 15th IEEE International Conference on, pages 61–64, Aug 2008.

[105] Mikel Mendicute, Luis G. Barbero, Gorka L, John S. Thompson, Jon Altuna, and Vicente Atxa. Real-time implementation of a sphere decoder-based MIMO wireless system. In *EURASIP European Signal Processing Conference (EUSIPCO '06), Invited Paper, Florence, Italy*, Sept 2006.

[106] Qingwei. Li and Zhongfeng. Wang. New sphere decoding architecture for MIMO systems. In *13th NASA Symposium on VLSI Design, Post Falls, Idaho, USA*, June 2007.

[107] Yuping Zhang and K.K. Parhi. Parallel architecture of list sphere decoders. In *Circuits and Systems, 2007. ISCAS 2007. IEEE International Symposium on*, pages 2096–2099, May 2007.

[108] Yuping Zhang, J. Tang, and K.K. Parhi. Low complexity radius reduction method for list sphere decoders. In *Signals, Systems and Computers, 2006. ACSSC '06. Fortieth Asilomar Conference on*, pages 2200–2203, Oct 2006.

[109] Jin Lee and Sin-Chong Park. Novel techniques of a list sphere decoder for high throughput. In *Advanced Communication Technology, 2006. ICACT 2006. The 8th International Conference*, volume 3, pages 3 pp.–1787, Feb 2006.

[110] Jin Lee, Sin-Chong Park, and Sungchung Park. A pipelined VLSI architecture for a list sphere decoder. In *Circuits and Systems, 2006. ISCAS 2006. Proceedings. 2006 IEEE International Symposium on*, pages 4 pp.–, May 2006.

[111] Weiyu Xu, Youzheng Wang, Zucheng Zhou, and Jing Wang. A computationally efficient exact ML sphere decoder. In *Global Telecommunications Conference, 2004. GLOBECOM '04. IEEE*, volume 4, pages 2594–2598 Vol.4, Nov 2004.

[112] Jin Lee, Hyung Soon Kim, and Sin-Chong Park. Parallel architecture for sphere decoder with runtime constraint. In *Consumer Communications and Networking Conference, 2008. CCNC 2008. 5th IEEE*, pages 181–184, Jan 2008.

[113] Chia-Hsiang Yang and D. Markovic. A multi-core sphere decoder VLSI architecture for MIMO communications. In *Global Telecommunications Conference, 2008. IEEE GLOBECOM 2008. IEEE*, pages 1–6, Nov 2008.

[114] B.M. Hochwald, C.B. Peel, and A.L. Swindlehurst. A vector-perturbation technique for near-capacity multiantenna multiuser communication-part II: perturbation. *Communications, IEEE Transactions on*, 53(3):537–544, March 2005.

[115] M. Barrenechea, L. Barbero, M. Mendicute, and J. Thompson. Design and hardware implementation of a low-complexity multiuser vector precoder. In *Design and Architectures for Signal and Image Processing (DASIP), 2010 Conference on*, pages 160–167, Oct 2010.

[116] L.G. Barbero and J.S. Thompson. Fixing the complexity of the sphere decoder for MIMO detection. *Wireless Communications, IEEE Transactions on*, 7(6):2131–2142, June 2008.

[117] L.G. Barbero and J.S. Thompson. Rapid prototyping of a fixed-throughput sphere decoder for MIMO systems. In *Communications, 2006. ICC '06. IEEE International Conference on*, volume 7, pages 3082–3087, June 2006.

[118] L.G. Barbero and J.S. Thompson. Extending a fixed-complexity sphere decoder to obtain likelihood information for Turbo-MIMO systems. *Vehicular Technology, IEEE Transactions on*, 57(5):2804–2814, Sept 2008.

[119] Guanghui Li, Xin Zhang, Sheng Lei, Cong Xiong, and Dacheng Yang. An early termination-based improved algorithm for fixed-complexity sphere decoder. In *Wireless Communications and Networking Conference (WCNC), 2012 IEEE*, pages 624–629, April 2012.

[120] P. Bhagawat, S. Ekambavanan, S. Das, G. Choi, and Khatri.S. VLSI implementation of a staggered sphere decoder design for MIMO detection. In *Forty-Fifth Annual Allerton Conference*, September 2007.

[121] Kwan wai Wong, Chi ying Tsui, R.S.-K. Cheng, and Wai-Ho Mow. A VLSI architecture of a K-Best lattice decoding algorithm for MIMO channels. In *Circuits and Systems, 2002. ISCAS 2002. IEEE International Symposium on*, volume 3, pages III–273–III–276 vol.3, 2002.

[122] M. Wenk, M. Zellweger, A. Burg, N. Felber, and Wolfgang Fichtner. K-Best MIMO detection VLSI architectures achieving up to 424 Mbps. In *Circuits and Systems, 2006. ISCAS 2006. Proceedings. 2006 IEEE International Symposium on*, pages 4 pp.–1154, May 2006.

[123] Chung-An Shen and A.M. Eltawil. A radius adaptive K-Best decoder with early termination: Algorithm and VLSI architecture. *Circuits and Systems I: Regular Papers, IEEE Transactions on*, 57(9):2476–2486, Sept 2010.

[124] S. Mondal, A. Eltawil, Chung-An Shen, and K.N. Salama. Design and implementation of a sort-free K-Best sphere decoder. *Very Large Scale Integration (VLSI) Systems, IEEE Transactions on*, 18(10):1497–1501, Oct 2010.

[125] I. Kanaras. *Spectrally Efficient Multicarrier Communication Systems: Signal Detection, Mathematical Modelling and Optimisation.* PhD thesis, University College London - Department of Electronic and Electrical Engineering, June 2010.

[126] J. Zhao and A.D. Ellis. A novel optical fast OFDM with reduced channel spacing equal to half of the symbol rate per carrier. In *Optical Fiber Communication (OFC), collocated National Fiber Optic Engineers Conference, 2010 Conference on (OFC/NFOEC)*, pages 1–3, 2010.

[127] Jian Zhao, S.K. Ibrahim, D. Rafique, P. Gunning, and Andrew D. Ellis. Symbol synchronization exploiting the symmetric property in optical fast OFDM. *Photonics Technology Letters, IEEE*, 23(9):594–596, May 2011.

[128] Jian Zhao and Andrew D. Ellis. Discrete-Fourier transform based implementation for optical fast OFDM. In *Optical Communication (ECOC), 2010 36th European Conference and Exhibition on*, pages 1–3, Sept 2010.

[129] D. Dasalukunte, F. Rusek, and V. Öwall. An iterative decoder for multicarrier faster-than-Nyquist signaling systems. In *Communications (ICC), 2010 IEEE International Conference on*, pages 1–5, May 2010.

[130] D. Dasalukunte, F. Rusek, and V. Öwall. Multicarrier faster-than-Nyquist transceivers: Hardware architecture and performance analysis. *Circuits and Systems I: Regular Papers, IEEE Transactions on*, 58(4):827–838, April 2011.

[131] D. Dasalukunte, F. Rusek, and V. Öwall. An 0.8-mm^2 9.6-mw iterative decoder for faster-than-Nyquist and orthogonal signaling multicarrier systems in 65-nm CMOS. *Solid-State Circuits, IEEE Journal of*, 48(7):1680–1688, July 2013.

[132] T.J. Richardson and R.L. Urbanke. The capacity of low-density parity-check codes under message-passing decoding. *Information Theory, IEEE Transactions on*, 47(2):599–618, Feb 2001.

[133] Jian Zhao and A. D. Ellis. Offset-QAM based coherent WDM for spectral efficiency enhancement. In *Optical Express*, volume 19, pages 14617–14631, July 2011.

[134] P. Siohan, C. Siclet, and N. Lacaille. Analysis and design of OFDM/OQAM systems based on filterbank theory. *Signal Processing, IEEE Transactions on*, 50(5):1170–1183, May 2002.

[135] Jian Zhao. DFT-based offset-QAM OFDM with arbitrary orthogonal waveform generation. In *Optical Communication (ECOC 2013), 39th European Conference and Exhibition on*, pages 1–3, Sept 2013.

[136] G. Fettweis, M. Krondorf, and S. Bittner. GFDM - generalized frequency division multiplexing. In *Vehicular Technology Conference, 2009. VTC Spring 2009. IEEE 69th*, pages 1–4, April 2009.

[137] R. Datta, N. Michailow, M. Lentmaier, and G. Fettweis. GFDM interference cancellation for flexible cognitive radio PHY design. In *Vehicular Technology Conference (VTC Fall), 2012 IEEE*, pages 1–5, Sept 2012.

[138] F. Schaich and T. Wild. Waveform contenders for 5G: OFDM vs. FBMC vs. UFMC. In *Communications, Control and Signal Processing (ISCCSP), 2014 6th International Symposium on*, pages 457–460, May 2014.

[139] L.G. Barbero and J.S. Thompson. Rapid prototyping of a fixed-throughput sphere decoder for MIMO systems. In *Communications, 2006. ICC '06. IEEE International Conference on*, volume 7, pages 3082 –3087, june 2006.

[140] IEEE standard for information technology–telecommunications and information exchange between systems local and metropolitan area networks–specific requirements–part 11: Wireless LAN medium access control (MAC) and physical layer (PHY) specifications–amendment 4: Enhancements for very high throughput for operation in bands below 6 GHz. *IEEE Std 802.11ac-2013 (Amendment to IEEE Std 802.11-2012, as amended by IEEE Std 802.11ae-2012, IEEE Std 802.11aa-2012, and IEEE Std 802.11ad-2012)*, pages 1–425, Dec 2013.

[141] J. Hagenauer. The turbo principle: tutorial introduction and state of the art. In *Proc. Int. Symp. Turbo Codes*, pages 1–11, Sept 1997.

[142] L. Bahl, J. Cocke, F. Jelinek, and J. Raviv. Optimal decoding of linear codes for minimizing symbol error rate (Corresp.). *Information Theory, IEEE Transactions on*, 20(2):284–287, Mar 1974.

[143] C. Berrou, A. Glavieux, and P. Thitimajshima. Near shannon limit error-correcting coding and decoding: Turbo-codes. 1. In *Communications, 1993. ICC '93 Geneva. Technical Program, Conference Record, IEEE International Conference on*, volume 2, pages 1064–1070 vol.2, May 1993.

[144] C. Berrou and A. Glavieux. Near optimum error correcting coding and decoding: turbo-codes. *Communications, IEEE Transactions on*, 44(10):1261–1271, Oct 1996.

[145] B.M. Hochwald and S. Ten Brink. Achieving near-capacity on a multiple-antenna channel. *Communications, IEEE Transactions on*, 51(3):389–399, March 2003.

[146] L. Hanzo, T. H. Liew, B. L. Yeap, R. Y. S. Tee, and S. X. Ng. *Turbo coding, turbo equalization and space-time coding: EXIT-chart-aided near-capacity designs for wireless channels*. John Wiley and Sons, Ltd, second edition, 2011.

[147] Xianbin Wang, P. Ho, and Yiyan Wu. Robust channel estimation and ISI cancellation for OFDM systems with suppressed features. *Selected Areas in Communications, IEEE Journal on*, 23(5):963–972, May 2005.

[148] S. Mehmood, D. Dasalukunte, and V. Öwall. Hardware architecture of IOTA pulse shaping filters for multicarrier systems. *Circuits and Systems I: Regular Papers, IEEE Transactions on*, 60(3):733–742, March 2013.

[149] S.J. Savory. Digital coherent optical receivers: Algorithms and subsystems. *Selected Topics in Quantum Electronics, IEEE Journal of*, 16(5):1164–1179, 2010.

[150] A. Ali, J. Leibrich, and W. Rosenkranz. Spectral efficiency and receiver sensitivity in direct detection Optical-OFDM. In *Optical Fiber Communication - incudes post deadline papers, 2009. OFC 2009. Conference on*, pages 1–3, 2009.

[151] J. Armstrong. OFDM for optical communications. *Lightwave Technology, Journal of*, 27(3):189–204, 2009.

[152] Wei-Ren Peng, Bo Zhang, Kai-Ming Feng, Xiaoxia Wu, A.E. Willner, and Sien Chi. Spectrally efficient direct-detected OFDM transmission incorporating a tunable frequency gap and an iterative detection techniques. *Lightwave Technology, Journal of*, 27(24):5723–5735, 2009.

[153] Shuto Yamamoto, K. Yonenaga, A. Sahara, F. Inuzuka, and Atsushi Takada. Achievement of subchannel frequency spacing less than symbol rate and improvement of dispersion tolerance in optical OFDM transmission. *Lightwave Technology, Journal of*, 28(1):157–163, 2010.

[154] W. Shieh and I. Djordjevic. *OFDM for Optical Communications*. ELSEVIER Inc., 2010.

[155] B. Schmidt, A.J. Lowery, and J. Armstrong. Experimental demonstrations of electronic dispersion compensation for long-haul transmission using direct-detection optical OFDM. *Lightwave Technology, Journal of*, 26(1):196–203, 2008.

[156] Wei-Ren Peng, I. Morita, H. Takahashi, and T. Tsuritani. Transmission of high-speed ($>$ 100 Gb/s) direct-detection optical OFDM superchannel. *Lightwave Technology, Journal of*, 30(12):2025–2034, 2012.

[157] F. Chang, K. Onohara, and T. Mizuochi. Forward error correction for 100 G transport networks. *IEEE Communications Magazine*, 48(3):S48–S55, March 2010.

[158] D. Bailey and P. Swarztrauber. The fractional Fourier transform and applications. *SIAM Review*, 33(3):389–404, 1991.

[159] Sander L. Jansen, Itsuro Morita, Noriyuki Takeda, and Hideaki Tanaka. 20-Gb/s OFDM transmission over 4,160-km SSMF enabled by RF-pilot tone phase noise

compensation. In *Optical Fiber Communication Conference and Exposition and The National Fiber Optic Engineers Conference*, page PDP15. Optical Society of America, 2007.

[160] T.M. Schmidl and D.C. Cox. Robust frequency and timing synchronization for OFDM. *Communications, IEEE Transactions on*, 45(12):1613–1621, Dec 1997.

[161] Xiang Liu and Fred Buchali. A novel channel estimation method for PDM-OFDM enabling improved tolerance to WDM nonlinearity. In *Optical Fiber Communication - incudes post deadline papers, 2009. OFC 2009. Conference on*, pages 1–3, March 2009.

[162] R. Maher, Kai Shi, S.J. Savory, and B.C. Thomsen. Fast wavelength switching digital coherent OFDM transceiver. In *Optical Communication (ECOC 2013), 39th European Conference and Exhibition on*, pages 1–3, Sept 2013.

[163] M. Iwamura, K. Etemad, Mo-Han Fong, R. Nory, and R. Love. Carrier aggregation framework in 3GPP LTE-advanced [WiMAX/LTE update]. *Communications Magazine, IEEE*, 48(8):60–67, August 2010.

[164] K.I. Pedersen, F. Frederiksen, C. Rosa, H. Nguyen, L.G.U. Garcia, and Yuanye Wang. Carrier aggregation for LTE-advanced: functionality and performance aspects. *Communications Magazine, IEEE*, 49(6):89–95, June 2011.

[165] Dongwoon Bai, Cheolhee Park, Jungwon Lee, Hoang Nguyen, J. Singh, A. Gupta, Zhouyue Pi, Taeyoon Kim, Chaiman Lim, Min-Goo Kim, and Inyup Kang. LTE-advanced modem design: challenges and perspectives. *Communications Magazine, IEEE*, 50(2):178–186, February 2012.

[166] C.S. Park, L. Sundstrom, A. Wallen, and A. Khayrallah. Carrier aggregation for LTE-advanced: design challenges of terminals. *Communications Magazine, IEEE*, 51(12):76–84, December 2013.

[167] 3GPP Evolved Universal Terrestrial Radio Access (E-UTRA) TS 36.104 V10.2.0. Base station (BS) radio transmission and reception. May 2011.

[168] S. Bassam, Wenhua Chen, M. Helaoui, and F. Ghannouchi. Transmitter architecture for CA: carrier aggregation in LTE-advanced systems. *Microwave Magazine, IEEE*, 14(5):78–86, July 2013.

[169] Guangxiang Yuan, Xiang Zhang, Wenbo Wang, and Yang Yang. Carrier aggregation for LTE-advanced mobile communication systems. *Communications Magazine, IEEE*, 48(2):88–93, February 2010.

[170] Yong Soo Cho., Jaekwon Kim., and Won Yong Yang. Chung-Gu Kang. *MIMO-OFDM Wireless Communications with MATLAB*. John Wiley & Sons (Asia) Pte Ltd, 2010.

[171] Q.T. Zhang and S.H. Song. Exact expression for the coherence bandwidth of rayleigh fading channels. *Communications, IEEE Transactions on*, 55(7):1296–1299, July 2007.

[172] T. S. Rappaport, S. Y. Seidel, and K. Takamizawa. Statistical channel impulse response models for factory and open plan building radio communicate system design. *IEEE Transactions on Communications*, 39(5):794–807, May 1991.

[173] M.K. Ozdemir and H. Arslan. Channel estimation for wireless OFDM systems. *Communications Surveys Tutorials, IEEE*, 9(2):18–48, Second 2007.

[174] G. Ku and J. Walsh. Resource allocation and link adaptation in LTE and LTE-Advanced: A tutorial. *Communications Surveys Tutorials, IEEE*, PP(99):1–1, 2014.

[175] Erik. Dahlman, Stefan. Parkvall, Johan. Sköld, and Per. Beming. *3G evolution: HSPA and LTE for mobile broadband*. Elsevier Ltd., 2007.

[176] Erik. Dahlman, Stefan. Parkvall, and Johan. Sköld. *4G LTE/LTE-Advanced for Mobile Broadband*. Elsevier Ltd., 2011.

[177] A. Chorti, I. Kanaras, M.R.D. Rodrigues, and I. Darwazeh. Joint channel equalization and detection of spectrally efficient FDM signals. In *Personal Indoor and Mobile Radio Communications (PIMRC), 2010 IEEE 21st International Symposium on*, pages 177–182, Sept 2010.

[178] Y. Shen and E. Martinez. Channel estimation in OFDM systems. Technical report, Freescale Semiconductor, lnc., 2006.

[179] Won Gi Jeon, Kyung Hi Chang, and Yong Soo Cho. An equalization technique for orthogonal frequency-division multiplexing systems in time-variant multipath channels. *Communications, IEEE Transactions on*, 47(1):27–32, Jan 1999.

[180] Spirent Communications plc. VR5 HD Spatial Channel Emulator. http://www.spirent.com/Products/VR5.

[181] P. Banelli, S. Buzzi, G. Colavolpe, A. Modenini, F. Rusek, and A. Ugolini. Modulation formats and waveforms for 5G networks: Who will be the heir of OFDM?: An overview of alternative modulation schemes for improved spectral efficiency. *Signal Processing Magazine, IEEE*, 31(6):80–93, Nov 2014.

[182] G. Fettweis, M. Lohning, D. Petrovic, Marcus Windisch, P. Zillmann, and W. Rave. Dirty RF: a new paradigm. In *Personal, Indoor and Mobile Radio Communications, 2005. PIMRC 2005. IEEE 16th International Symposium on*, volume 4, pages 2347–2355 Vol. 4, Sept 2005.

[183] T.C.W. Schenk, P.F.M. Smulders, and E. Fledderus. Multiple carriers in wireless communications - curse or blessing? In *NERG: Tijdschrift Ned. Elektron & Radiogenoot*, pages 112–123, 2005.

[184] A.G. Armada. Understanding the effects of phase noise in orthogonal frequency division multiplexing (OFDM). *Broadcasting, IEEE Transactions on*, 47(2):153–159, Jun 2001.

[185] A.G. Armada and M. Calvo. Phase noise and sub-carrier spacing effects on the performance of an OFDM communication system. *Communications Letters, IEEE*, 2(1):11–13, Jan 1998.

[186] L. Litwin and M. Pugel. The principles of OFDM. Technical report, RF signal processing, 2001.

[187] Anritsu. Understanding LTE-Advanced carrier aggregation. Technical report, Anritsu, September 2013.

[188] National Instruments. USRP-RIO-2953R, Software Defined Radio Reconfigurable Device. http://sine.ni.com/nips/cds/view/p/lang/en/nid/213005.

[189] National Instruments. LabVIEW Communications LTE Application Framework. http://sine.ni.com/nips/cds/view/p/lang/en/nid/213083.

[190] T.S. Rappaport, J.N. Murdock, and F. Gutierrez. State of the art in 60-GHz integrated circuits and systems for wireless communications. *Proceedings of the IEEE*, 99(8):1390–1436, Aug 2011.

[191] T.S. Rappaport, R.W. Heath, R.C. Daniels, and J.N. Murdock. *Millimeter Wave Wireless Communications*. Prentice–Hall, 2014.

[192] IEEE standard for information technology–telecommunications and information exchange between systems–local and metropolitan area networks–specific requirements-part 11: Wireless LAN medium access control (MAC) and physical layer (PHY) specifications amendment 3: Enhancements for very high throughput in the 60 GHz band. *IEEE Std 802.11ad-2012 (Amendment to IEEE Std 802.11-2012, as amended by IEEE Std 802.11ae-2012 and IEEE Std 802.11aa-2012)*, pages 1–628, Dec 2012.

[193] Heinz Willebrand. Advantages of the 60 GHz frequency band and new 60 GHz backhaul radios. Technical report, LightPointe Communications Inc.

[194] T. Bai, A. Alkhateeb, and R. W. Heath. Coverage and capacity of millimeter-wave cellular networks. *IEEE Communications Magazine*, 52(9):70–77, September 2014.

[195] A. L. Swindlehurst, E. Ayanoglu, P. Heydari, and F. Capolino. Millimeter-wave massive MIMO: the next wireless revolution? *IEEE Communications Magazine*, 52(9):56–62, September 2014.

[196] J. Singh, S. Ponnuru, and U. Madhow. Multi-Gigabit communication: the ADC bottleneck. In *2009 IEEE International Conference on Ultra-Wideband*, pages 22–27, Sept 2009.

[197] V.A. Thomas, M. El-Hajjar, and L. Hanzo. Performance improvement and cost reduction techniques for radio over fiber communications. *Communications Surveys Tutorials, IEEE*, 17(2):627–670, Secondquarter 2015.

[198] Y. Yang, C. Lim, and A. Nirmalathas. Radio-over-fiber as the energy efficient backhaul option for mobile base stations. In *Microwave Photonics, 2011 International Topical Meeting on Microwave Photonics Conference, 2011 Asia-Pacific, MWP/APMP*, pages 242–245, Oct 2011.

[199] L. L. Hanzo, M. Münster, B. J. Choi, and T. Keller. *OFDM and MC-CDMA for broadband multi-user communications, WLANs and broadcasting.* Wiley-IEEE Press, 2003.

[200] E. P. Martin, T. Shao, V. Vujicic, P. M. Anandarajah, C. Browning, R. Llorente, and L. P. Barry. 25-Gb/s OFDM 60-GHz radio over fiber system based on a gain switched laser. *Journal of Lightwave Technology*, 33(8):1635–1643, April 2015.

[201] M. Weiss, A. Stohr, F. Lecoche, and B. Charbonnier. 27 Gbit/s photonic wireless 60 GHz transmission system using 16-QAM OFDM. In *Microwave Photonics, 2009. MWP '09. International Topical Meeting on*, pages 1–3, Oct 2009.

[202] A. Kanno, K. Inagaki, I. Morohashi, T. Sakamoto, T. Kuri, I. Hosako, T. Kawanishi, Y. Yoshida, and K. i. Kitayama. 40 Gb/s W-band (75-110 GHz) 16-QAM radio-over-fiber signal generation and its wireless transmission. In *Optical Communication (ECOC), 2011 37th European Conference and Exhibition on*, pages 1–3, Sept 2011.

[203] S. Mikroulis, M. P. Thakur, and J. E. Mitchell. Evaluation of OOK and OFDM on an SMF-MMF-SMF link targeting a PON/60-GHz topology for beyond 4G. *IEEE Photonics Technology Letters*, 28(4):449–452, Feb 2016.

[204] C. Berrou and A. Glavieux. Near optimum error correcting coding and decoding: turbo-codes. *IEEE Transactions on Communications*, 44(10):1261–1271, Oct 1996.

[205] O. Omomukuyo, M.P. Thakur, and J.E. Mitchell. Simple 60-GHz MB-OFDM ultrawideband RoF system based on remote heterodyning. *Photonics Technology Letters, IEEE*, 25(3):268–271, Feb 2013.

[206] Huawei Technologies Co., Ltd. NB-IOT, Accelerating Cellular IOT. http://www.huawei.com/minisite/hwmbbf15/en/nb-iot-accelerating-cellular-iot.html, 2015.

[207] A. Checko, H. L. Christiansen, Y. Yan, L. Scolari, G. Kardaras, M. S. Berger, and L. Dittmann. Cloud RAN for mobile networks–a technology overview. *IEEE Communications Surveys Tutorials*, 17(1):405–426, Firstquarter 2015.

[208] M. Costa. Writing on dirty paper (Corresp.). *IEEE Transactions on Information Theory*, 29(3):439–441, May 1983.

[209] J. Maurer, J. Jalden, D. Seethaler, and G. Matz. Vector perturbation precoding revisited. *IEEE Transactions on Signal Processing*, 59(1):315–328, Jan 2011.

[210] C. Windpassinger, R. F. H. Fischer, T. Vencel, and J. B. Huber. Precoding in multiantenna and multiuser communications. *IEEE Transactions on Wireless Communications*, 3(4):1305–1316, July 2004.

[211] Gilbert Strang. *Introduction to linear algebra*. Wellesley–Cambridge Press, 2009.

[212] 3GPP TS 36.212 v.12.2.0. Evolved universal terrestrial radio access (E-UTRA); multiplexing and channel coding. Rel. 12, Oct. 2014.

[213] M. Timmers, M. Guenach, C. Nuzman, and J. Maes. G.fast: evolving the copper access network. *IEEE Communications Magazine*, 51(8):74–79, August 2013.

[214] Huawei. Vectoring technology white paper. Technical report, Huawei Technologies Co., Ltd., July 2015.

[215] J. Maes and C. J. Nuzman. The past, present, and future of copper access. *Bell Labs Technical Journal*, 20:1–10, 2015.

[216] J. R. Schneir and Y. Xiong. Cost assessment of FTTdp networks with G.fast. *IEEE Communications Magazine*, 54(8):144–152, August 2016.

[217] ITU-T Rec. G.9701. Fast access to subscriber terminals (G.fast) - physical layer specification. Dec. 2014.

[218] ITU-T Rec. G.9700. Fast access to subscriber terminals (G.fast) - power spectral density specification. Apr. 2014.

[219] Yuping Zhao and S.-G. Haggman. Intercarrier interference self-cancellation scheme for OFDM mobile communication systems. *Communications, IEEE Transactions on*, 49(7):1185–1191, Jul 2001.

[220] S. Brandes, I. Cosovic, and M. Schnell. Reduction of out-of-band radiation in OFDM systems by insertion of cancellation carriers. *Communications Letters, IEEE*, 10(6):420–422, June 2006.

[221] R. Datta and G. Fettweis. Improved ACLR by cancellation carrier insertion in GFDM based cognitive radios. In *Vehicular Technology Conference (VTC Spring), 2014 IEEE 79th*, pages 1–5, May 2014.